Active and passive reduction of high order modes in the gravitational wave detector GEO 600

Von der QUEST-Leibniz-Forschungsschule
der Gottfried Wilhelm Leibniz Universität Hannover
zur Erlangung des Grades

Doktor der Naturwissenschaften
– Dr. rer. nat. –

genehmigte Dissertation
von

Dipl.-Phys. Holger Wittel

geboren am 16. Juni 1984 in Hannover

2015

Referent:	Prof. Dr. Karsten Danzmann (Leibniz Universität Hannover)
Korreferent:	Dr. Stefan Hild (University of Glasgow)
Korreferent:	Prof. Dr. Kenneth A. Strain (University of Glasgow)
Tag der Promotion:	30.10.2015

Abstract

The interferometric gravitational wave detector GEO 600 has faced many challenges with light being scattered into high order modes (HOMs). HOMs have been observed to add noise into the gravitational wave measurement and to degrade the performance of the alignment systems for the optical cavities to the point of malfunctioning. They can also lower the observed squeezing value and create a coupling path for environmental and acoustic noise into the gravitational wave measurement. These challenges are expected to become more severe with the planned increase of the circulating laser power in GEO 600.

This work focuses on directly reducing the amount of HOMs in GEO 600, which is done in a number of ways. The existing ring heater behind one of the folding mirrors of GEO 600 is identified to cause a large astigmatism in this mirror, thus being the single largest source of HOMs. In order to independently change the curvature of the mirror in two degrees of freedom and to cancel the astigmatism, additional heaters are designed and installed to this mirror. Moreover, a feedback system for the aforementioned heaters is developed, which minimizes the HOM content in the darkport of GEO 600. Another heating based approach is realized by a thermal projection system which projects an array of 9x12 heaters to the beam splitter's surface, which can provide even more degrees of freedom in correcting HOMs.

An improved output mode cleaner (OMC) is designed to optically filter out HOMs before they reach the main photo diode. Further improvements to the output optics are done to allow in situ mode matching of the output beam to the OMC. An additional seismic isolation for the OMC reduces the coupling of environmental noise to the gravitational wave measurement.

Large baffles are installed to absorb spatially extended HOMs. The baffles are suspended as a pendulum with eddy-current damping, along with sensors and actuators to allow for investigation of a possible noise contribution.

Moreover, simulations of a new geometry for electrostatic mirror actuators (ESDs) are presented. These, unlike conventional ESDs, have no first order coupling of actuator motion to actuation force and do not reduce the free aperture of the optics. The latter is beneficial for reducing thermal noise by using large beams, and mitigating possible issues of light being scattered off the ESD. The analysis however yielded, that due to its lower actuation force, the new geometry would be better suited for smaller scale prototypes than for kilometer-scale gravitational wave detectors.

Keywords: GEO 600, gravitational wave detector, high order modes, thermal compensation, astigmatism

Kurzzusammenfassung

Der interferometrische Gravitationswellendetektor (GWD) GEO 600 machte viele Erfahrungen mit den Auswirkungen von Laserlicht, dass in Moden höherer Ordnung (HOMs) gestreut wird. HOMs können Rauschen in der Gravitationswellenmessung verursachen und Alignmentsysteme für die optischen Resonatoren negativ beeinflussen, bis hin zum Versagen. Außerdem können HOMs die beobachtbare Empfindlichkeitsverbesserung durch Squeezing verringern und bieten einen Pfad für die Einkopplung von Umgebungseinflüssen, wie etwa die von Akustik in die Gravitationswellenmessung. Es wird erwartet, dass diese Herausforderungen mit der geplanten Erhöhung der umlaufenden Laserleistung noch größere Bedeutung bekommen.

Diese Arbeit befasst sich mit der direkten Reduzierung von HOMs in GEO 600 auf verschiedenen Wegen. Der bereits existierende Ringheizer hinter einem der Faltspiegel produziert einen straken Astigmatismus und wird als größte Einzelquelle von HOMs identifiziert. Zusätzliche Heizer werden entworfen und installiert, welche es erlauben den Krümmungsradius des Faltspiegels in zwei Freiheitsgraden unabhängig voneinander einzustellen. Weiterhin wird ein Regelkreis für die o.g. Heizer entwickelt, der den Anteil der HOMs im darkport von GEO 600 minimiert. Ein weiterer auf Heizern basierter Ansatz ist die Realisierung eines thermischen Projektors, der eine Matrix aus 9x12 Heizelementen auf den Strahlteiler projeziert. Dies ermöglicht deutlich mehr Freiheitsgrade in der Korrektur der HOMs.

Ein verbesserter output mode cleaner (OMC) wird entwickelt, um HOMs optisch herauszufiltern, bevor sie die Photodiode erreichen. Weitere Verbesserungen der Ausgangsoptik ermöglichen eine in situ Modenanpassung des Laserstrahls an den OMC und eine verbesserte seismische Isolation, welche die Anfälligkeit gegenüber Umgebungsgeräuschen reduziert.

Zusätzliche Blenden werden mit einer Pendelaufhängung und Wirbelstromdämpfung installiert um räumlich ausgedehnte HOMs zu absorbieren. Außerdem werden Sensoren und Aktuatoren zur Messung möglicher Rauscheinkopplungen eingefügt.

Desweiteren werden Simulationen zu einer neuen Geometrie für elektrostatische Aktuatoren (ESDs) vorgestellt. Anders als konventionelle ESDs zeigt die neue Geometrie in erster Ordnung keine Kopplung von Bewegung des ESD zur Aktuationskraft und verkleinert nicht die benutzbare Apertur der Optik. Letzteres ermöglicht die Reduzierung thermischen Rauschens durch Verwendung größerer Laserstrahlen, und kann potentielle Probleme mit Streulicht von den ESDs vermeiden. Die Simulationen zeigen jedoch, dass die neue Geometrie aufgrund niedrigerer Aktuationskraft besser für kleinere Prototypen geeignet ist, als für GWDs im Kilometermaßstab.

Stichworte: GEO 600, Gravitationswellendetektor, Moden höherer Ordnung, thermische Kompensation, Astigmatismus

Contents

List of Figures

CHAPTER 1

Introduction

1.1. Gravitational waves

Gravitational waves (GWs) are perturbations in space time, caused by accelerated masses. Predicted in 1916 by Albert Einstein's general theory of relativity [Ein16], the existence of GWs was confirmed via the observation of the orbital period of the Hulse-Taylor pulsar system B1916+13 [HT75] [TW82].

The effect GWs is such, that they periodically change distances, perpendicular to their direction of travel. The effect that a passing GW would have on freely falling test masses is pictured in figure 1.1. However, their length change caused by them is tiny. Even the strongest sources of GWs, which are astrophysical events, such as supernovae or coalescing black holes or neutron stars, are expected to only cause relative length changes ('strain') of less than around one part in 10^{21} on Earth [SS09].

The goal of GW research is to eventually use them to complement traditional astronomy which is mainly based on observations of the electromagnetic (EM) spectrum. GWs have, compared to EM waves, a very low absorption cross section [Bla05], which makes them attractive tools for providing information on astrophysical questions. They can help to determine the equations of state of neutron stars [RMS+09], or be used as standard 'sirens', analog to standard candles [HH05]. Furthermore they can be used to examine the cosmic GW background, which carries information about the early phase of the universe, just like the cosmic microwave background. The cosmic GW background does however reach far closer to the big bang than its EM counterpart [AAA+09a]. For more information on GW and the astronomy enabled by them, the reader is referred to the excellent introduction in [Sch99].

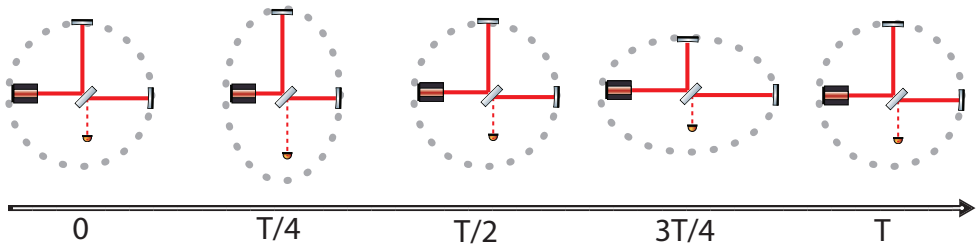

Figure 1.1.: The effect of a gravitational wave with a period T on freely falling test masses (depicted as gray dots) is shown here, for one of the two possible linear polarizations of the GW (the '+' polarization is shown, while the '×' polarization is omitted here). The direction in which the GW travels would be perpendicular to the image plane. The image also depicts a Michelson interferometer, and how its arms would change in length due to the GW.

1.2. Gravitational wave detectors

The expected scientific payoff of GW astronomy is very exciting, and attempts to build gravitational wave detectors (GWDs) have been made for half a century now, starting with the first bar detectors constructed in the 1960s by Joseph Weber [Web63].

The idea behind bar detectors is to measure the vibrational modes of a large metal piece, usually shaped as a sphere or a cylinder, hence the name 'bar detector'. A passing GW can excite an internal resonance of the metal bar, which is read out by SQUIDS[1] or interferometrically [CBC+97]. To reach a reasonable sensitivity with this method, the bar needs to be decoupled from environmental noise, which is usually done by seismically isolating it and by placing it in a vacuum system. Furthermore, the thermal noise, one of the main limiting noise sources in this measurement [Web66] can be reduced by cooling the bar.

The reliance of internal modes of the bar makes this method of GW detection inherently narrow-band, with a bandwidth of typically some Hertz for the first detectors, and about 100 Hz for modern ones [ABB+02] [BBB+08]. Bar detectors are operated until this day, reaching a strain sensitivity of about $10^{-21}/\sqrt{\text{Hz}}$ at frequencies of typically around a kHz [BBB+08]. More information on bar detectors can be found in [Ast02].

It is noteworthy that Weber claimed to have detected GW with his pair of bar detectors [Web68] [Web69], which at that time reached a strain sensitivity of 'parts in 10^{16}' [Web69]. However, the general consensus is that this was most likely the result of a measurement error, since none of the later detectors have (yet) detected signs of GW [LG73] [GL73] [LG74], even though modern detectors are orders of magnitude more sensitive, especially the interferometric GW detectors, which provide a very good broadband sensitivity.

The most sensitive GWDs to date are kilometer-scale, laser based Michelson interferometers. The mirrors of these interferometers are suspended in such a way that

[1] superconducting quantum interference device, a device to measure a changing magnetic field

they can be considered as freely falling in the direction of the measurement. This way, a passing GW would cause a differential length change of the interferometer arms, to which the Michelson interferometer is inherently sensitive. This is depicted in figure 1.1. And since GW cause relative length changes, longer interferometer arms will see a larger *absolute* length change and therefore cause a larger signal.

The first generation of long baseline interferometric GWDs reached a peak strain sensitivity of $3 \times 10^{-22}/\sqrt{\text{Hz}}$, and provided a useful measurement bandwidth from tens of Hertz to several kHz [AAA+09b]. This sensitivity is typically limited by photon shot noise at high frequencies, by mirror thermal noise at the peak sensitivity, and by seismic noise at low frequencies. With this level of sensitivity, there is a chance of detecting a close astrophysical event, like a supernova or a coalescence of two neutron stars or black holes, via their GW. The expected event rates that can be detected at this sensitivity are low though, in the order of 0.02 events per year for compact binary coalescence signals [AAA+10a] and less than 10^{-5} per year for burst like events (coincident with gamma ray burst observations) [LSF+09].

The first generation of large scale interferometric GWDs was represented by GEO 600 located in Germany, the two LIGO detectors in the US, TAMA300 in Japan and Virgo in Italy. TAMA300 was the first of these detectors to start taking astrophysically relevant data (in a so-called 'science run') in the year 1999, with GEO 600 and the LIGO detectors following in 2002 and Virgo in 2006.

In 2009, further upgrades took place, with the common aim to improve the sensitivity, increase the laser power and to prototype technologies for second generation GWDs, that resulted in Enhanced LIGO, Virgo+ and the GEO-HF upgrade program. After another data-taking run (two for Virgo+), Enhanced LIGO and Virgo+ were taken offline to allow for the commissioning of the 'advanced' (or second generation) GWDs in the same infrastructure. Those detectors, namely Advanced LIGO and advanced Virgo, are expected to be ten times more sensitive than their predecessors once they reach their design sensitivity [AAA+15a]. Another second generation detector currently in construction is the Japanese KAGRA detector. More information on the history of interferometric GWDs can be found in [PRRH11].

The GEO-HF upgrade program (more on this later in this chapter) is designed to be a less invasive upgrade, which will allow to keep GEO 600 running as the only active GWD for several years, until the advanced LIGO detectors start taking astrophysical data; their first science run (albeit not at their final sensitivity) is just starting in late 2015.

Any Earth-bound GWD will be limited by seismic, gravity gradient[2] or thermal noise at *some* low frequency [HAA+11]. The eLISA mission plans to overcome this limit and measure GW in a frequency band of 0.1 mHz to 1 Hz [ASAB+12] by moving the interferometer into space and using 1 million kilometer long arms [HD14]. The currently expected launch date of eLISA is 2034 [eC+15].

Another method of detecting GWs is pulsar timing. The working principle is to compare the arrival time of radio pulses from several pulsars. The long effective arm length and the need for long time averaging make this method suited to measure GWs

[2] Which is caused by density fluctuations in the surrounding of the detector.

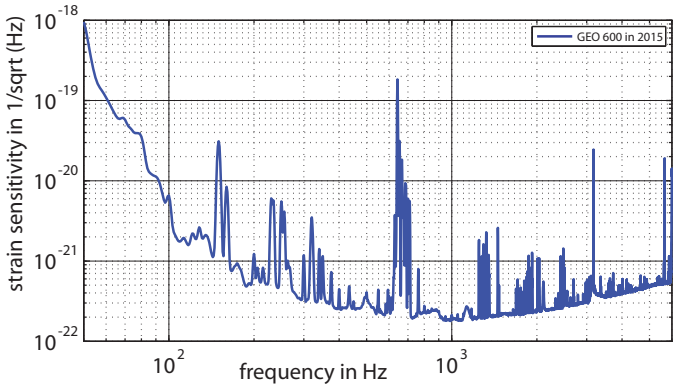

Figure 1.2.: Typical strain sensitivity of GEO 600.

in a frequency band from 10^{-9} to 10^{-6} Hz [MTG15].

GWs have not been directly measured so far. However, the expected detectable event rates for the second generation ground based interferometric detectors are much higher than for the first generation detectors. Binary neutron star inspiral signals for example, are expected to be audible to the advanced detectors[3] at a rate of 40 per year [SPF+14].

The possible scientific gains of GW astronomy are very exciting, and the same goes for the instruments that are designed to measure them. The most sensitive GWDs to date are the kilometer-scale, laser based Michelson interferometers. This work focuses on GEO 600 which, as mentioned previously, is the only interferometric GWD regularly taking GW data at the time of writing.

1.3. GEO 600

GEO 600 is one of the large-scale interferometric GWDs. As such, it is built as a dual-recycled Michelson interferometer [HFG+02] with 600 meter long, folded arms. At the time of writing this work, the peak sensitivity for GW strain of GEO 600 was in the order of $10^{-22}/\sqrt{\text{Hz}}$ at frequencies of about 1 kHz. A typical sensitivity curve of GEO 600 at the time of writing is presented in figure 1.2.

Large efforts are made to reach this level of sensitivity. Among them are placing all of the main optics in an ultra-high vacuum system with a residual pressure in the order of 10^{-8} mbar. Furthermore, multi-stage pendulums are used to seismically isolate the optics from the ground motion. As a result, the sensitivity of GEO 600 is limited by the fundamental photon shot noise at frequencies above 1 kHz. This is remarkable, in the sense that seismic and technical noises are suppressed even below the shot noise level, especially when considering the large circulating power of 2 - 2.5 kW of laser light, which defines the shot noise limited sensitivity. A simplified layout of GEO 600

[3] at their design sensitivity

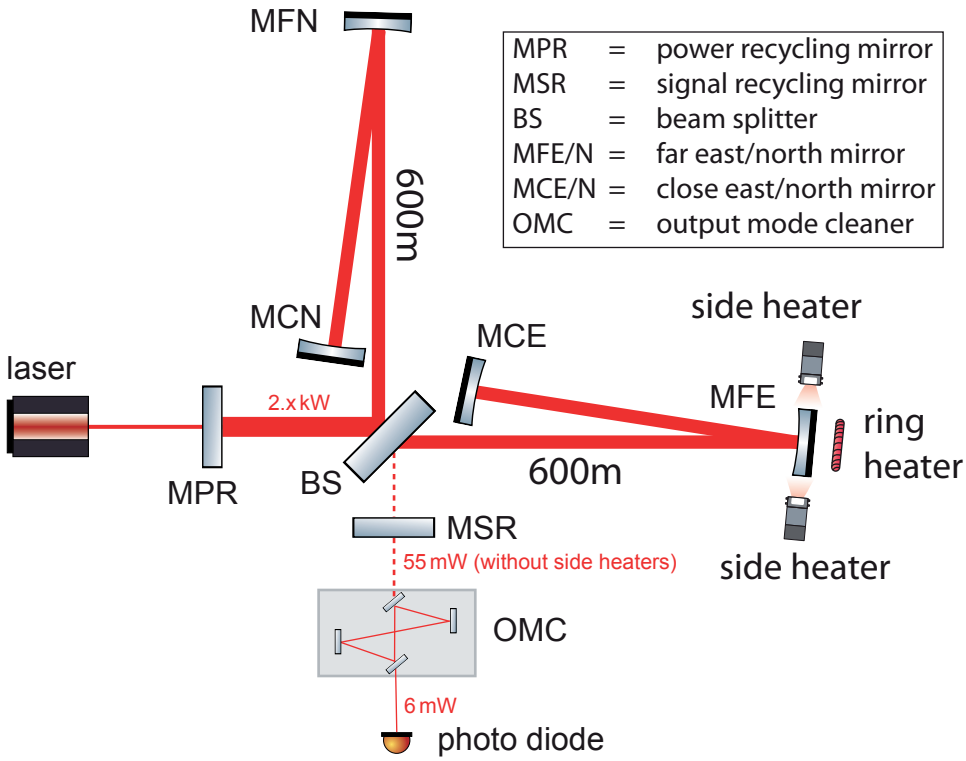

Figure 1.3.: A simplified layout of GEO 600. The power of the laser field at different points in the interferometer is given in red numbers.

is shown in fig. 1.3. The optical layout of GEO 600 is slightly different from other GWD in the fact that it has folded arms, which double the effective arm length. LIGO and Virgo do not use folded arms, but they use Fabry Perot cavities in the arms.

One notable feature of GEO 600 is that it has been the first to implement and demonstrate new technologies for GWDs, many of which will only now be implemented into the second generation of interferometer-based GWDs. For example, the main mirrors are suspended with monolithic fused silica fibers instead of metal wires. Also, GEO 600 makes use of electrostatic actuators for the main mirrors instead of coil-magnet based actuators, and the quantum shot noise is reduced by the injection of squeezed states of light. GEO 600 has also pioneered the use of a ring heater to adjust the curvature of a mirror [ADD+14].

At the time of writing, GEO 600 is the only interferometric GWD that still regularly takes astrophysical data, while the second generation detectors are being built. GEO is operated in 'Astrowatch' mode, which refers to scientific data taking at night and on the weekends, while the working hours are spend with implementing less invasive upgrades[4].

Much more information on GEO 600 and its history can be found in [DCN+92], [WAA+02], [WAA+06] and [ADD+14].

1.4. GEO-HF upgrade

The GEO-HF upgrade program, which has started in 2009, aims at improving the high frequency sensitivity of GEO 600, and this without extended downtime of GEO 600. It includes several improvements to GEO 600, which are enumerated here. A more detailed description can be found in [LC+12], [ADD+14] and [Pri12, p.13ff].

The improvements include the implementation of a new readout method ('DC readout') [DGP+10], along with the installation of an output mode cleaner [PDG+12].

Furthermore, the existing 12 W Nd:YAG laser has been replaced with a 35 W laser system, along with changes in the input optics [Aff14, p.27ff].

The bandwidth of the signal recycling cavity has been increased by installing a new signal recycling mirror with a reflectivity of 90%, while the old one had 98% [Pri12, p.35]. This mirror change has been carried out in conjunction with a shift of the tuning of the signal recycling cavity. It has been moved from a narrowband sensitive ('detuned') configuration to a broadband sensitive one ('tuned').

The implementation of squeezing, i.e. using squeezed vacuum states of light to reduce quantum shot noise was another part of the GEO-HF upgrade project [Col11], as well as the implementation of thermal actuators, described in this work.

At the time of writing, the ongoing work on improving the detector mainly focuses on further improvements of the shot noise limited sensitivity at high frequencies by lowering the losses for the injected squeezed vacuum field, and by increasing the circulating laser power.

[4] This work usually disturbs the detector too much to produce reliable GW data - hence it is flagged as maintenance time, instead of 'science time'.

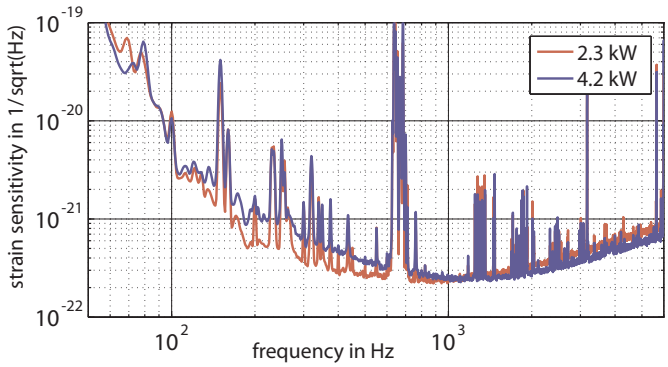

Figure 1.4.: Example of the unknown noise at increased circulating power, the sensitivity of GEO 600 is plotted with standard (red) and high (blue) circulating power. Note that for the sensitivity curves in this plot, no squeezing was applied.

Especially the latter has proven to be challenging. While the circulating power of GEO 600 can be increased over the currently used 2 - 2.5 kW, an unknown noise spoils the sensitivity of GEO 600 when running with larger power levels.

Figure 1.4 shows an example of this effect. Two sensitivity spectra of GEO 600 are plotted, one with the standard operating power, and one with an increased circulating laser power. It can be seen that the improvement in the shot noise limited region at above 1 kHz is roughly[5] as expected, i.e. scales with the square root of the power. At lower frequencies, the sensitivity gets worse though, and overall the integrated sensitivity is worse at high power operation.

The source of this effect is remains unknown, despite best efforts of the whole GEO 600 team. A good summary about the noise hunting and performed experiments regarding this noise can be found in [Aff14, p.145ff].

1.5. Gaussian beams and high order modes

All interferometric GWD of the first and second generation are and will be using laser light with a wavelength λ of 1064 nm. The understanding of the properties of laser beams and optical cavities played a crucial role in reaching the impressive sensitivity of today's GWD, and this work will refer to several of those properties. A very small introduction into the topic is provided below, while more details can be found in the excellent overview [KL66], which this section loosely follows.

Laser beams are usually described as Gaussian beams, which are a solution of the par-axial wave equation. In their simplest form, Gaussian beams have a Gaussian-shaped amplitude profile, and can be described by the parameters as illustrated in figure 1.5. It shows a Gaussian beam propagating along the z-axis, going through a

[5] In this case the improvement is slightly worse than the square root of the power, most likely due to the influence of a not increased the dark fringe offset, as explained in chapter 3.

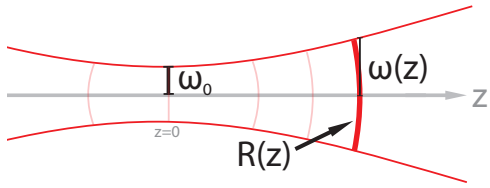

Figure 1.5.: Illustration of Gaussian beam parameters.

focus ('waist'), which is assumed to be at $z = 0$, where the beam has a radius[6] of ω_0. The beam radius at a position z on the axis of propagation is referred to as $\omega(z)$, and the radius of curvature of the wavefront is described as $R(z)$. Due to diffraction, the beam will diverge and its size will increase as

$$\omega^2(z) = \omega_0^2 \left[1 + \left(\frac{\lambda z}{\pi \omega_0^2}\right)^2\right]. \tag{1.1}$$

Furthermore, a wavefront with radius of curvature $R(z)$ can be assigned to the beam, with

$$R(z) = z \left[1 + \left(\frac{\pi \omega_0^2}{\lambda z}\right)^2\right]. \tag{1.2}$$

Consider a laser beam propagating in z-direction. In the most simple case, the amplitude E_{00} of this laser beam in the x-y plane (perpendicular to its direction of propagation) is

$$E_{00} = \frac{\omega_0}{\omega(z)} \exp\left(-i(kz - \Phi) - r^2\left[\frac{1}{\omega^2(z)} + \frac{ik}{2R(z)}\right]\right), \tag{1.3}$$

with

$$\begin{aligned} r &= \sqrt{(x^2 + y^2)}, \\ k &= 2\pi/\lambda, \\ \Phi &= \arctan(\lambda z/\pi\omega_0^2). \end{aligned}$$

The above represents the so-called fundamental mode. More complex beam shapes are possible as well. They can be represented as a linear combination of Hermite-Gauss (HG) modes, which form a complete basis system. Sometimes these modes are more generally referred to as transversal electromagnetic modes (TEMs). The complex transversal field amplitude E_{HG} of a HG mode is given by

$$E_{HG} = H_m\left(\sqrt{2}\frac{x}{\omega}\right) H_n\left(\sqrt{2}\frac{y}{\omega}\right) \times \frac{\omega_0}{\omega(z)} \exp\left(-i(kz - \Phi_{mn}) - r^2\left[\frac{1}{\omega^2(z)} + \frac{ik}{2R(z)}\right]\right), \tag{1.4}$$

[6] The beam size is defined as the radius where the amplitude has dropped to $1/e$ of its (maximal) value on the optical axis.

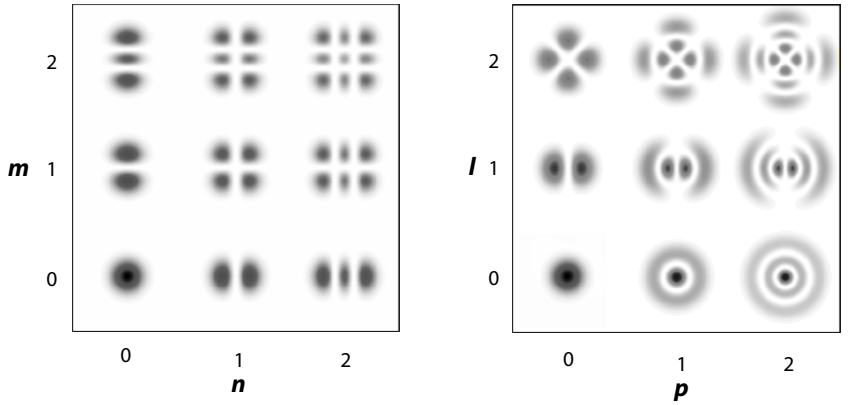

Figure 1.6.: Intensity distribution of the first few Hermite-Gauss (left) and Laguerre-Gauss (right) modes. Modified from [FS10].

with the Gouy phase Φ_{mn} depending on the so-called mode order $m+n$ as

$$\Phi_{mn} = (m+n+1)\arctan(\lambda z/\pi\omega_0^2) \tag{1.5}$$

and the Hermite polynomial $H_m(x)$ of order m. The first Hermite polynomials are:

$$H_0(x) = 1 \qquad H_2(x) = 4x^2 - 2 \tag{1.6}$$

$$H_1(x) = x \qquad H_3(x) = 8x^3 - 12x. \tag{1.7}$$

Another basis system that uses Laguerre polynomials is represented by Laguerre-Gauss (LG) modes. It is commonly used for systems with rotational symmetry around the beam axis. The amplitude E_{LG} of an LG mode is given by:

$$E_{LG} = \left(\sqrt{2}\frac{r}{\omega}\right)^l L_p^l\left(\sqrt{2}\frac{r^2}{\omega^2}\right) \times \frac{\omega_0}{\omega(z)} \exp\left(-i(kz - \Phi_{pl}) - r^2\left[\frac{1}{\omega^2(z)} + \frac{ik}{2R(z)}\right]\right), \tag{1.8}$$

with a phase shift of

$$\Phi_{pl} = (2p + l + 1)\arctan(\lambda z/\pi\omega_0^2) \tag{1.9}$$

and the Laguerre polynomial $L_p^l(x)$. The first few Laguerre polynomials are:

$$L_0^l(x) = 1 \tag{1.10}$$

$$L_1^l(x) = l + 1 - x \tag{1.11}$$

$$L_2^l(x) = \frac{1}{2}(l+1)(l+2) - (l+2)x + \frac{1}{2}x^2 \tag{1.12}$$

Figure 1.6 shows the transversal intensity distribution of the first nine HG and LG modes. Notice that the fundamental mode, i.e. the HG_{00} and the LG_{00} is the same in both basis systems. All of the GWDs use this mode, though the usage of other modes is being researched [Ful14].

In this work, all modes other than the fundamental HG_{00}/LG_{00} mode will be called high order modes (HOMs). HOMs can arise due to misalignment of optics, bad matching of a laser beam to the TEM_{00} eigenmode of an optical cavity, or due to imperfect optical surfaces and thermal effects.

Typically these HOMs are considered as 'junk light' [HHP14], since they can cause a multitude of issues and noise in the GW measurement, which will be detailed in the next chapter.

CHAPTER 2

Thermal lensing in the beam splitter of GEO 600

High laser power operation is one of the goals of the GEO-HF upgrade program. It is planned to increase the circulating light power from about 2 - 2.5 kW to about 20 kW. At this power level, thermal effects are expected to play a large role, and their effect on the interferometer has to be considered. Especially the thermal lens in the beam splitter may limit the power build up in the power recycling cavity (PRC) of GEO 600. This chapter gives an analysis of the thermal lens in the beam splitter and how it affects GEO 600 when operated at high laser power.

2.1. Introduction

Thermal lensing is often an issue when working with high power lasers. A high power laser beam can increase the temperature in an optic, and change its optical and physical properties, similar to the introduction of a lens.

Even though the optics in GEO 600 have a very low absorption at the laser wavelength of 1064 nm, the laser beam still deposits heat into the optics. It will introduce a temperature gradient in and axial of the optics. Several properties of the beam splitter depend on its temperature, such as the thermal expansion and the index of refraction Both of which will introduce a phase delay of the laser beam wavefront in the presence of a thermal gradient. In the following we are going to quantify this phase delay as the optical path difference (OPD). It describes the difference in path length as a function of the distance from the beam axis.

The beam splitter and its thermal lens are of particular interest for several reasons:

1. A high powered laser beam is transmitted though the beam splitter.
   Since GEO 600 has no arm cavities (other than Advanced LIGO and Virgo), the

PRC is designed to have a high power build up. All of the circulating power is incident on the beam splitter, and about half is transmitted.

2. The laser beam passes the beam splitter at an angle, see fig. 2.1 for an illustration. This leads to different beam sizes in the horizontal and vertical axis. This in turn will produce a thermal lens with different strength in the horizontal and vertical axis. This situation is different from the thermal lensing and thermal compensation systems in LIGO and Virgo, which worked on the input test masses of the arm cavities ([Wil09], [AAA+09c]). The angle can be computed via Snell's law:
$$n_1 \times sin(\gamma_1) = n_2 \times sin(\gamma_2), \tag{2.1}$$
where $n_1 = 1$ is the index of refraction in vacuum, $n_2 \approx 1.45$ the index of refraction in the beam splitter, and $\gamma_1 \approx 45°$ and γ_2 are the angles of the laser beam outside and inside of the beam splitter, respectively. The angles are measured to the surface normal. When applying Snell's law for the case of the GEO 600 beam splitter, we get an angle of approximately 29° inside the beam splitter.

3. In the PRC, the beam has the smallest diameter on the power recycling mirror MPR. It has a waist there, with a radius of about 1 cm. And because of the close proximity of MPR and the beam splitter, the beam size on the beam splitter is similar. This leads to a stronger thermal gradient compared to places where the beam is larger, for example on the folding mirrors.

4. The thermal lens in the beam splitter affects mostly the beam parameters in the east arm, and therefore has a common mode and a differential mode effect. This will result in a reduced interferometer contrast, by worsening the destructive interference at the darkport, and lower the power build up in the interferometer (see 2.3.2).

This work focuses on the thermal lens in the beam splitter, since the other optics in the high power path are used only in reflection and have only a common mode effect. The common mode effects will be strongly suppressed by the destructive interference at the beam splitter.

The beam splitter of GEO 600 is a cylindrically shaped fused silica substrate with a very low OH-content (Suprasil 311 SV). It has a diameter of 26 cm and is 8 cm thick. Both faces have a dielectric coating (see 3.3.3); on one face it is anti-reflective, while the other face has a coating with a power transmission of 51.4% [Fre03, p.31].

2.2. Thermal effects

The absorption of the bulk material beam splitter of GEO 600 has been measured several times, for example in [Deg08], [HLW+06] and [LB03], with varying results. The result of the most recent measurement [Deg08] yielded an absorption of 0.45 ppm (±10%) per centimeter for the whole beam splitter, i.e. substrate and coating, for the laser wavelength of 1064 nm. This value shall be used in this work.

Parameter	symbol	value	unit
ambient temperature	T_0	300	K
beam waist radius	ω	1	cm
beam waist radius x	ω_x	1.2	cm
beam waist radius y	ω_y	1	cm
path length in the BS	L_x	9.1	cm
path length in the BS	L_y	8	cm
laser wavelength	λ	1064	nm
Fused silica			
refractive index (at 1064 nm)	n	1.44963	–
thermo refractive coeff.	β	$10 \cdot 10^{-6}$	K^{-1}
thermal conductivity	κ	1.38	W/mK
thermal expansion coefficient	α	$0.55 \cdot 10^{-6}$	K^{-1}
photoelastic coeff.	Γ	0.27	–

Table 2.1.: Table of used parameters in this chapter.

The temperature profile in the beam splitter can be determined analytically, using a model from [SDM+94], which gives the temperature profile of an optic transmitting and partly absorbing a laser beam:

$$T(r) = T_0 + \frac{P p_{\text{abs}}}{4\pi\kappa} \sum_{k=1}^{\infty} \left(\frac{2r^2}{\omega^2}\right)^k \frac{(-1)^k}{kk!}, \tag{2.2}$$

with the temperature $T(r)$ at radius r from the beam axis, the absorption of the beam splitter p_{abs} per unit length and the power in the substrate P. Further variables are the thermal conductivity κ, the beam radius ω and maximum temperature T_0 (and for $r = \omega$, the sum gives a value of 1.32). With the parameters in table 2.1, it is possible to estimate a radial temperature gradient of about 4 mK between the beam axis and the beam radius ω for a circulating laser power of 2.5 kW in the beam splitter of GEO 600.

Additionally, a numerical model (using the software ANSYS [ANS]) was examined to verify the model described by equation 2.2. The temperature distribution of this model is shown in figure 2.1, and it agrees well with the analytical model. It shall be mentioned however that in reality the absorption is likely not uniform, but may be stronger at the dielectric coatings, and weaker (to keep the same total absorption) in the substrate. An indication for this may be the thermal image of the beam splitter face in [ADD+14].

With the temperature profile covered, it is possible to include the optical properties of the beam splitter into the analysis. Several of these optical properties are temperature dependent, and therefore influenced by the thermal gradient caused by the laser beam. Specifically, the temperature dependent properties of the optics are the refractive index n ('thermo-refractive effect'), and the shape, because the volume of the substrate material depends on its temperature ('thermal expansion'). Additionally, the refractive index may also change due to stress in the material ('thermoelastic

effect'), for example caused by thermal expansion.

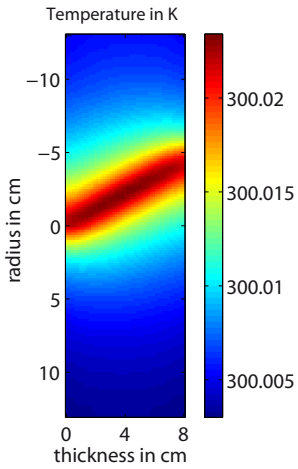

Figure 2.1.: Thermal cross-section view of the beam splitter, produced via a numerical model (with an ambient temperature of 300 K).

The radial thermal gradient in the beam splitter (ΔT) from the optical axis ($r = 0$) to the edge of the beam ($r = 1\omega$) and resulting optical path differences (ΔOPD) due to the different effects mentioned above can be analytically estimated. For this we use the previously determined absorption value of the beam splitter and formula 2.2.

The thermo-refractive effect is especially relevant when optics are used in transmission (see table 2.2). The index of refraction shows a temperature dependence, hence an optic used in transmission will be *optically* thicker on the beam axis (the $\mathrm{d}n/\mathrm{d}T$ coefficient of the GEO 600 main optics is positive), and therefore act as thermal lens. The OPD caused by the thermo-refractive effect is determined by the temperature gradient ΔT, the change of the refractive index $\beta = \mathrm{d}n/\mathrm{d}T$, and the physical path length L in the medium. It can be computed via:

$$\Delta\mathrm{OPD}_{\mathrm{thermo-refractive}} = \beta \times L \times \Delta T \tag{2.3}$$

As most materials, the beam splitter of GEO 600 expands when heated. It will be *physically* thicker on the beam axis than on the rim. The resulting OPD can be calculated with the coefficient of linear thermal expansion $\alpha = dL/dT$ and the beam radius ω:

$$\Delta\mathrm{OPD}_{\mathrm{thermal-expansion}} = 2 \times \alpha \times n \times \omega \times \Delta T \tag{2.4}$$

The elasto-optic effect affects the refractive index, which depends on stress in the optics's substrate material. It is defined by the photo-elastic coefficient Γ:

$$\Delta\mathrm{OPD}_{\mathrm{thermo-elastic}} = -\frac{n^3}{2} \times \Gamma \times \alpha \times L \times \Delta T \tag{2.5}$$

However, these thermal effects are different in strength. Table 2.2 shows the OPD per temperature gradient for each thermal effect, and compares their relative strengths for the case of the GEO 600 beam splitter (using the values from table 2.1). The main outcome of this comparison is that the thermo-refractive effect is the dominating one; from here on we will neglect the thermal expansion and the elasto-optic effects.

2.3. Characterization of thermal lenses

Thermal lenses are frequently treated as classical thin lenses, and thus characterized by their focal length f. It should be kept in mind however, that the radial OPD

Effect	$\Delta\mathrm{OPD}/\Delta T$ (m/K)	relative strength
thermo-refractive	$7.7 \cdot 10^{-7}$	1
thermal expansion	$1.6 \cdot 10^{-8}$	0.021
elasto-optic	$-2 \cdot 10^{-8}$	-0.026

Table 2.2.: Comparison of the relative strengths of thermal effects in the beam splitter of GEO 600. Only the values in the vertical (y) direction are compared here, updated from [Wit09].

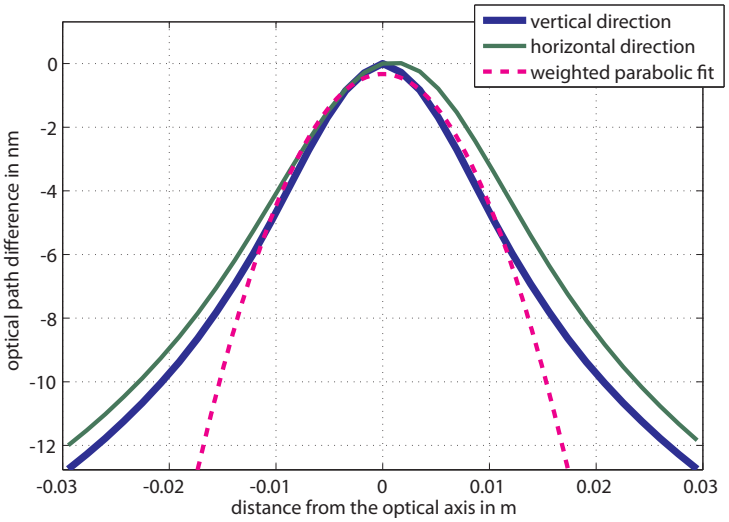

Figure 2.2.: The OPD caused by the thermal lens in the beam splitter (blue and green graphs) and a parabolic (thin lens) fit are shown. The fit has been weighted by the laser beam intensity profile; it is evident that it is a good representation of the OPD caused by the thermal lens, at least within the laser beam radius of about 1 cm. Another result is that the OPD curve in the horizontal direction is both asymmetric and wider than in the vertical direction. This is due to the fact that the laser passes the beam splitter at an angle (in the horizontal plane) of about 29°.

profile differs from the one for an ideal thin lens, especially far from the optical axis ($r > \omega$). For this work though, the simplification as thin lens is not critical, as we are interested only in the region within one beam waist ($r \leq \omega$). Fig. 2.2 shows the OPD profile of the thermal lens in the beam splitter, which we obtained via a the aforementioned numerical model, in comparison to a parabolic OPD-fit for a thin lens. Generally, the OPD of an ideal thin lens is given by a parabolic curve [Deg06, p.52]:

$$f = \omega^2/(2 \times \Delta\mathrm{OPD}), \tag{2.6}$$

and with eq. 2.3 and 2.2, this can be formulated as

$$f = \frac{4\pi}{2.6} \frac{\omega^2 \kappa}{\beta L P p_{\mathrm{abs}}}. \tag{2.7}$$

For the parameters of GEO 600 (given in table 2.1) this equation predicts focal lengths of about 10 km in the vertical direction at the standard operating power of 2.5 kW.

Another way to describe the strength of a thermal lens is by using the error function Θ_{SL} proposed by Lawrence [Law03, p.53]:

$$\Theta_{SL} = 1 - A^* A \tag{2.8}$$

with

$$A = \frac{< \Psi | e^{-i\Phi(x,y)} | \Psi >}{< \Psi | \Psi >} \tag{2.9}$$

Where $|\Psi >$ denotes the light field in the cavity in terms of transversal electromagnetic modes (TEM) as defined in [Sie86]. Furthermore $\Phi(x, y)$ describes a phase delay depending on the coordinates x and y perpendicular to the beam propagation direction.

It can be understood as the amount of light scattered into high order modes (HOMs) from a TEM_{00} beam when passing the thermal lens. Θ_{SL} is frequently used as figure of merit in simulations, but it is not practical to measure in an interferometer like GEO 600[1]. Instead, we will resort to quantities that can be directly measured and are related to the scattering loss, such as the power of HOMs at the darkport and the gain of the PRC. Both quantities are influenced by the thermal lens in the beam splitter, but mode healing (see section 2.4.4) and deformations of other main optics (for example intentional deformation as described in chapters 3 and 4) can impact those measures as well. To estimate the influence of the thermal lens in the beam splitter on the power at the darkport and the PRC gain we performed both simulations and measurements, which are presented in 2.3.2. First however, we do a comparison of GEO and Advanced LIGO with respect to the thermal lens in the beam splitter.

[1] It would require to pick off beams before and after the beam splitter, in the high power path. This is not desirable for a number of reasons: additional thermal lenses, additional losses, and the pickoff mirrors would have to be seismically isolated, and the comparison of both picked off beams is non-trivial either.

2.3.1. Comparison to Advanced LIGO

The unique challenge of thermal lensing in the beam splitter was already discussed earlier, but the gravity of this issue becomes clear when compared to the design values of Advanced LIGO, which is being commissioned at the time of writing this work. Table 2.3 compares the parameters relevant to the strength of the thermal lens in the beam splitter (see equations 2.6, 2.3 and 2.2). All of those parameters, mainly the beam size (which impacts the strength of the thermal lens quadratically) and the power in the PRC, lead to a stronger thermal lensing effect in the GEO 600 beam splitter. In total, the thermal lens in the GEO beam splitter can be expected to be more than 300 times stronger than the one in Advanced LIGO. Due to the arm cavities and the large power stored in them, Advanced LIGO will face strong thermal lenses in the input test masses of the arm cavities though.

	GEO 600 (GEO-HF final)	**aLIGO** (final)	rel. impact factor on thermal lens
power in PRC	20 kW	5.2 kW	3.8
beam width on BS	10 mm	53 mm	28.1
absorption in BS	0.45 ppm/cm	0.2 ppm/cm	2.25
BS thickness	80 mm	60 mm	1.3
			total: 312

Table 2.3.: Relative strength difference between the thermal lenses in the beam splitter substrates in GEO 600 and Advanced LIGO in their final design (the values for Advanced LIGO are taken from [AAA+15a]). The thermal lens in the beam splitter of GEO 600 will be about 312 times stronger than the one in Advanced LIGO.

2.3.2. Effect of the beam splitter thermal lens on the interferometer

For this work, we are interested in how the thermal lens affects the interferometer performance. Therefore we will be using the power build up in the PRC and the power at the darkport as measures for the thermal lens. Both can be obtained from the interferometer and are important for the operation of GEO 600. The gain of the PRC determines the amount of circulating light power, and circulating power will result in an improved signal-to-noise ratio in the gravitational wave measurement[2]. HOMs at the darkport can introduce multiple issues, which will be detailed in section 2.4.

Theory

The power recycling cavity of GEO 600 is formed by the power recycling mirror MPR and the close mirrors MCE and MCN. The thermal lens mainly affects the east arm of the PRC, a schematic unfolded drawing of which is shown in figure 2.3. In this

[2] The measurement benefits from increased laser power only when it is limited by photon shot noise, which is the case in GEO 600 for frequencies above 1 kHz.

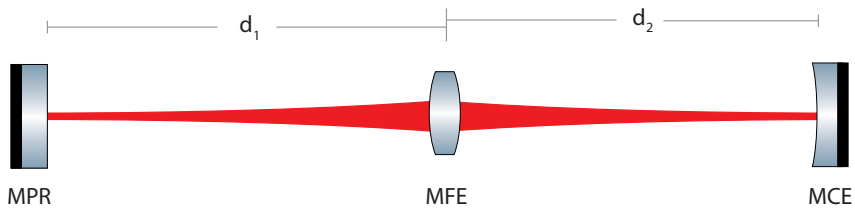

Figure 2.3.: Schematic drawing of the unfolded east arm in the PRC of GEO 600 (not to scale).

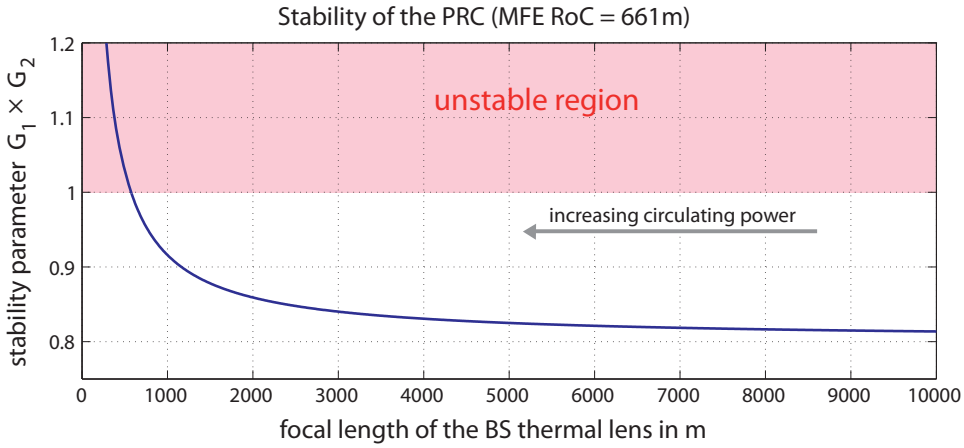

Figure 2.4.: Stability diagram for the east arm of the PRC in GEO 600 in dependence of the focal length of the thermal lens in the beam splitter. The stability parameter $G_1 \times G_2$ of the PRC of GEO 600 is presented as blue curve. Its value changes as the thermal focal length of the BS changes. The red region in the plot indicates where the PRC is optically unstable.

representation, the curved mirror MFE is treated as a simple convex lens. This simplification now allows us to perform a similar analysis as [WDG+07] to understand the effect of the thermal lens.

Typically, the stability of a two mirror cavity is characterized by the well known stability parameters g_1 and g_2, which are derived by the RoCs of the mirrors and their distance [Sie86, p.746ff]. According to [Kog65][3], analogue stability parameters G_1 and G_2 can be defined for each arm of the PRC, in the case of the east arm it would be:

$$G_1 = 1 - 2d_2/R_{\mathrm{MFE}} - d_0/R_{\mathrm{MPR}} \quad (2.10)$$

$$G_2 = 1 - 2d_1/R_{\mathrm{MFE}} - d_0/R_{\mathrm{MCE}}, \quad (2.11)$$

[3] [Kog65] uses an internal lens with focal length f in a resonator, just as shown in fig. 2.3, but since MFE is actually a mirror, we substituted f with $R_{\mathrm{MFE}}/2$.

where

$$d_0 = d_1 + d_2 - 2d_1d_2/R_{\mathrm{MFE}}. \tag{2.12}$$

The distances $d_1 = 598.45\,\mathrm{m}$ and $d_2 = 597.06\,\mathrm{m}$ are defined as shown in figure 2.3, while R denotes the radius of curvature of the corresponding mirror: a flat power recycling mirror, $R_{\mathrm{MFE}} = 661\,\mathrm{m}$ and $R_{\mathrm{MCE}} = 622\,\mathrm{m}$. The simulation of the thermal lens in the beam splitter can be performed by assigning its focal length to the RoC of MPR (R_{MPR}). This is justified by their proximity, the distance between MPR and the beam splitter is about 1.1 m, compared to the armlength of about 600 m. Now the stability of the east arm of the PRC can be assessed by checking the stability condition, which is analogue to the case of a simple two-mirror cavity:

$$0 \geq G_1 \cdot G_2 \geq 1 \tag{2.13}$$

Figure 2.4 plots the parameter $G_1 \cdot G_2$ in dependence of the BS thermal focal length. We see that when the focal length reaches the arm length of 600 m the PRC gets unstable, this would be the case at a circulating power of roughly 50 kW.

Furthermore we investigated the effect of the thermal lens on the beam size on the optics. Using formulae from [Kog65] we can compute the beam sizes ω on the mirrors:

$$\omega_{\mathrm{MPR}} = \sqrt{\frac{d_0\lambda}{\pi}\sqrt{\frac{G_2}{G_1 - G_1G_2}}}, \tag{2.14}$$

$$\omega_{\mathrm{MFE}} = \omega_{\mathrm{MPR}}\sqrt{1 + \left(\frac{\lambda d_1}{\pi\omega_{\mathrm{MPR}}^2}\right)}, \tag{2.15}$$

$$\omega_{\mathrm{MCE}} = \sqrt{\frac{d_0\lambda}{\pi}\sqrt{\frac{G_1}{G_2 - G_1G_2}}}. \tag{2.16}$$

Where λ denotes the laser wavelength of 1064 nm. We used the above to project the influence of the thermal lens on the beam sizes in the east arm of the PRC. The results are plotted in figure 2.5. The beam size changes significantly close to the point of instability. But even small changes in the beam size at the beam splitter[4] will lead to a reduced interferometer contrast and worse power build up in the interferometer, because the beam in the north arm of the PRC will not be changed as much by the thermal lens. The interference of the beams from both arms will be worse if the beams have a different size, more simulations and measurements about this are presented in the next sections and figure 2.6.

We found that the thermal lens in the beam splitter changes the beam sizes mainly in the east arm of the PRC, and as a result the beams from east and west arm do not interfere perfectly anymore. One way to improve this situation, is to change the beam size in the east arm back again. In GEO 600 this can be done via the already existing ring heater behind MFE. As is shown in chapter 3, the ring heater can be used to improve the contrast when a thermal lens in the beam splitter is present. A

[4] for which the size on the power recycling mirror is a good approximation, due to the close proximity of MPR and beam splitter

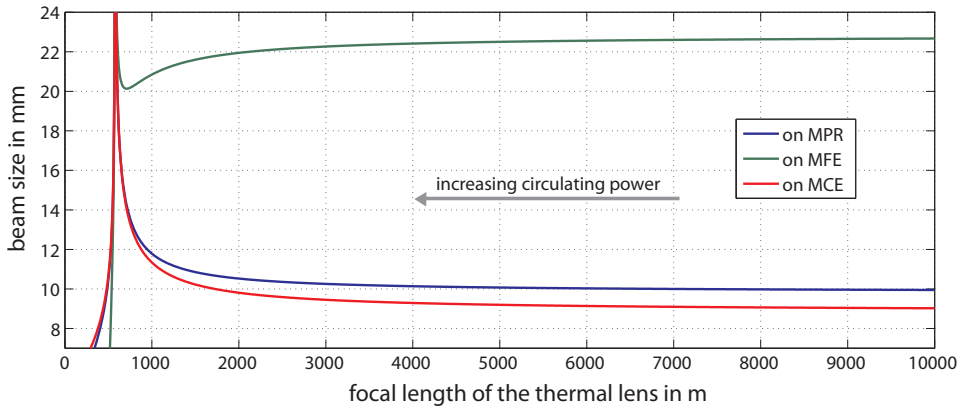

Figure 2.5.: This graphs show how the beam size on MPR, MFE and MCE changes due to a stronger thermal lens in the beam splitter. Up until a thermal focal length of 3000 m, there is little change in the beam sizes. Below that value, the beam size changes significantly, the apparent peak at approximately 600 m focal length of the beam splitter coincides with the PRC becoming unstable, as shown in figure 2.4.

more detailed analysis on the usage of the ring heater for the compensation of the thermal lens in GEO 600 is given in chapter 3 of this work.

Simulation

A simulation was performed about how the PRC gain and the power at the darkport would develop due to the thermal lens in the beam splitter, if the circulating power in GEO was increased. This was done using the software FINESSE [FHL+04] and the latest knowledge of GEO 600 [WG+14] at the time of writing. A FINESSE sample file for the simulations in this work is given as appendix A.5. The only power dependent parameter that was considered in this simulation was the thermal lens in the beam splitter. Other power dependent effects may arise which are not covered here, such as thermal lenses in other optics, for example the crystals of electro-optic modulators. However, we would argue that these are purely common-mode effects, which will affect the north and the east arm of the PRC, unlike the beam splitter thermal lens. Another effect that was not modeled was the effect of imperfections in the optics, for example micro-scratches on the mirror surfaces.

The figures 2.6a and 2.6b show the results of the aforementioned simulations. The PRC gain starts to drop when more than 5 W of laser light are directed to the input mode cleaners. At the same time, the power at the darkport starts to increase significantly. Note the maximum in the PRC gain at about 3 W input laser power, which is no coincidence. It is merely the result of two optimizations which were done to maximize the gain close to the current operating power (i.e. 2.85 W output of the laser is injected into the input optics of GEO 600). The first optimization was the change of a lens in front of the PRC [Aff14, p.111], while the second optimization

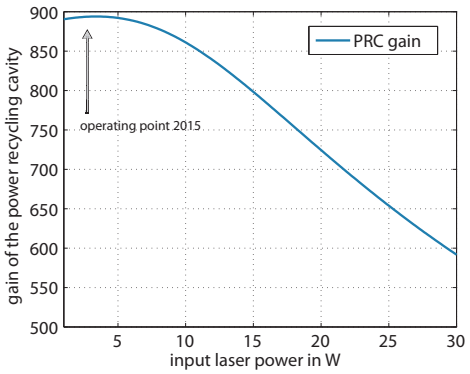

(a) Simulated gain of the PRC.

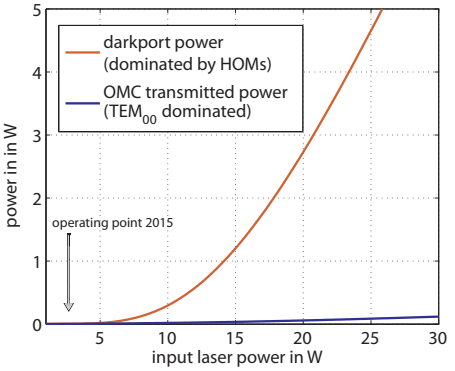

(b) Simulated power at the darkport before the OMC (red) and after the OMC (blue).

Figure 2.6.: Simulations of the thermal lens and its effect on the PRC. At higher laser powers than the current 2.85 W injected into the input mode cleaners, the thermal lens in the beam splitter lowers the power build up in the PRC and raises the power at the darkport. Note that the amount of HOMs at the darkport of GEO 600 in figure 2.6b goes to zero when no thermal effects are present (at low input laser power). This is due to the simulation, which assumes optics without imperfections apart from the beam splitter thermal lens.

is the curvature of the far east folding mirror, which we can dynamically change to compensate the thermal lens in the beam splitter (see chapter 3 for more information about the ring heater). Both changes affect the mode matching into the PRC, with the result that the mode matching is optimized for the current operating power.

Measurements

The simulations above predict a significant influence of the thermal lens in the beam splitter on the darkport power at only slightly increased circulating power. And this is what we observe in experiments as well. For measurements of the effect of the thermal lens, we prefer to use the power at the darkport as a measure for the thermal lensing. The reason being that it exhibits a larger relative change than the PRC gain, and because it can be directly measured, unlike the PRC gain. A measurement was performed, in which we increased the circulating light power in GEO, waited for thermal equilibrium, and recorded the power at the darkport. The results are plotted in figure 2.7, and confirm the simulations. The power at the darkport increases strongly when the circulating light power is increased. The increase is even stronger than predicted by the simulation in figure 2.6b, which can partly be explained by mirror imperfections that produce HOMs even without thermal lens, and scale linearly with power. Those imperfections are not modeled in the simulation, and account for about 30 mW of HOMs at the output port at the current operating power. We then used the output mode cleaner (OMC) to further analyze the HOM content in the output beam (see also in chapter 7), by scanning its length. Due to their Gouy phase

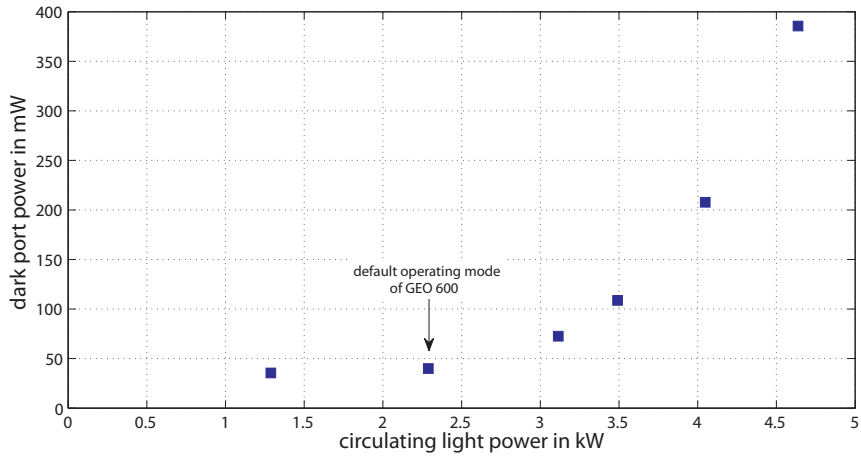

Figure 2.7.: This plot shows a measurement of the power at the darkport vs circulating light power in the PRC.

shift (see eq. 3.1 and accompanying text), the HOMs of different order will resonate at a different cavity length.

OMC scans at different circulating power levels were performed, and the result is plotted in figure 2.8. It shows that HOMs of order two are the ones showing most increase.

It is important to point out that there are two differences to the normal science operation to the presented plot: the sidebands to the TEM_{00} carrier ('Michelson Sidebands') are reduced to less than a tenth of the shown values, and the TEM_{00} carrier is increased by changing the dark fringe offset. The plot was done without any dark fringe offset, only some residual power of the TEM_{00} carrier showing in the plot.

2.4. HOM induced issues in GEO 600

High order modes at the output port of GEO 600 can act as a loss-channel and limit the power build up in the PRC, as shown above. Furthermore, a high amount of HOMs can have other implications, in the past they have led to multiple challenges in the commissioning and operation of GEO 600. A large amount of work has been assigned to cure the symptoms that HOMs cause in GEO 600, which are described below.

2.4.1. Direct noise coupling

HOMs can directly introduce noise to the gravitational wave (GW) measurement of GEO 600 when they reach the main photo diode. They are not resonant in the

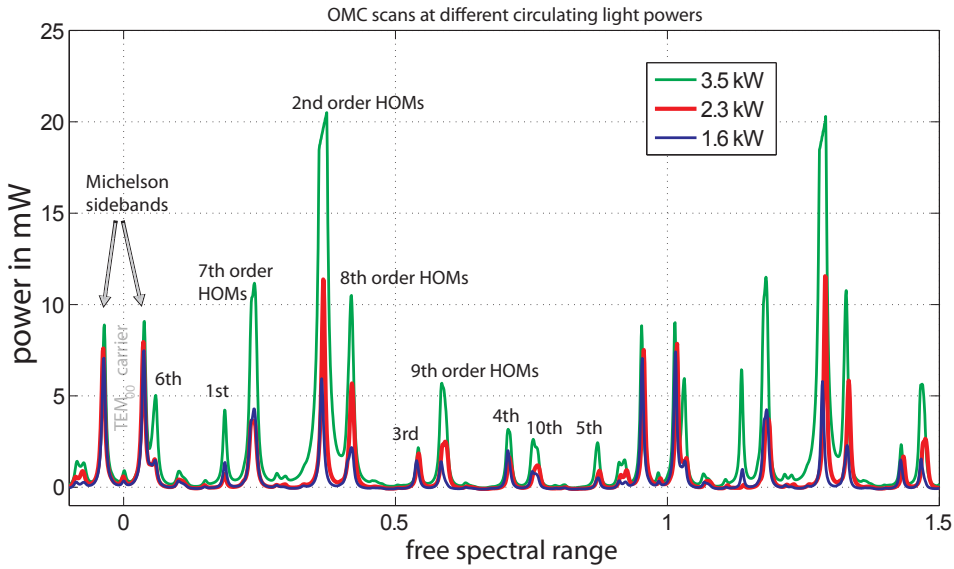

Figure 2.8.: OMC mode scans at three different power levels. Clearly, the power in HOMs is increased, with HOMs of order two seeing the most increase. Note that the second order HOM peaks height not is fully captured, it appears that its signal was too large, the data acquisition system was saturated. This mode scan was performed with the new OMC (see chapter 7), and without dark fringe offset, i.e. the TEM_{00} GW carrier is not present in this measurement, its position in the mode scan between the two Michelson sidebands is still marked in the plot. More information on the OMC and OMC mode scans can be found in chapter 7

recycling cavities of GEO 600, and carry no significant amount of GW signal. They would contribute shot noise on the photo diode though. To counteract this, an output mode cleaner (OMC) has been installed in front of the photo diode. HOMs will be reflected off the OMC, while the potentially GW carrying fundamental mode carrier light will still reach the photo diode. The OMC only provides a finite attenuation of HOMs though, they will still affect the GW measurement to a small degree[5].

The 6th order modes are expected to have the lowest attenuation by the OMC according to chapter 7. Therefore, the amount of noise caused by 6th order in GEO was measured, by setting the OMC length such, that the 6th order modes become resonant, reach the photo diode and are not attenuated. The resulting spectrum is scaled with the correct OMC attenuation factor that the 6th order modes would have in normal operation. We call this procedure 'pseudo noise projection', since unlike a traditional noise projection as presented in [Smi06], due to its procedure, the pseudo noise projection is not recorded at the same time as the GW signal. Figure 2.9 shows the resulting pseudo noise projection, along with a typical sensitivity curve of GEO 600. We find that the noise added by 6th order modes is a factor of ten or more below the current GEO 600 sensitivity for most frequencies, and therefore not limiting the sensitivity of GEO 600. At and above 2 kHz the noise contribution comes closest to the current strain sensitivity.

The attentive reader may have noticed that the noise projection curve in fig. 2.9 has some gaps. This is due to the specific way this noise projection was performed. It uses the output signal of the main photo diode, which is calibrated to strain sensitivity via a transfer function. The transfer function has been measured during a reference time, and only the frequency regions with high (>0.9) coherence are considered, hence the gaps. The online-generated strain sensitivity curve uses the output of the main photo diode as well, but uses a more complex, frequency dependent calibration at low frequencies (below about 150 Hz, the unity gain frequency of the differential arm length control loop). More information on the calibration of GEO 600 can be found in [Hil07, p.18ff] and [Hew04].

Given the over-proportional increase in power of the HOMs when increasing the circulating light power in GEO 600, as shown in figure 2.7, the noise contribution of HOMs may become more relevant when GEO reaches the design goal of the GEO-HF upgrade of increasing the circulating power by a factor of seven.

2.4.2. Photo diode saturation

GEO uses photo diodes to sense various auxiliary beams for the purpose of alignment among others. One example is a photo diode which senses the beam at the darkport, which is used during lock acquisition. A large amount of HOMs can lead to saturation of the photo diodes, and saturated photo diodes were a candidate for an unexplained noise process in GEO 600. As a result, all suspected photo diodes were attenuated (some of them permanently) with neutral density filters. This lowers the risk of

[5] More information on the power of HOMs in GEO 600 and the OMC and its attenuation of HOMs is given in this work in table 4.1 and chapter 7.

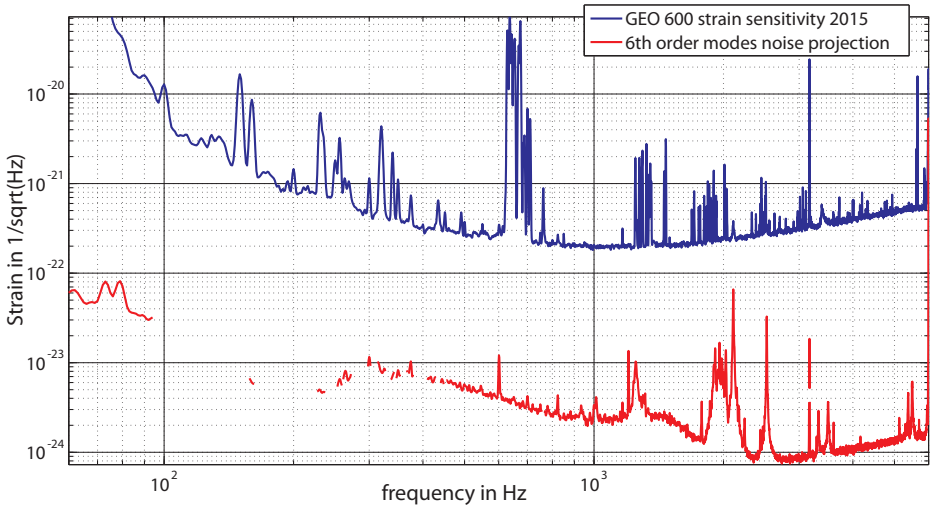

Figure 2.9.: Pseudo noise projection of the 6th order modes, i.e. how much noise from the 6th order HOMs is coupled into the GW measurement, and typical GEO 600 sensitivity. Compared to HOMs of other orders, the noise contribution of the 6th order HOMs is larger, due to the weaker attenuation of 6th order modes by the OMC.

saturation and serves as future-proofing for when the circulating power in the PRC is increased.

Unfortunately the unknown noise appears to be not affected by this modification, more details on the unknown noise and attenuation of the photo diodes can be found in [Aff14, p.146].

2.4.3. Output mode cleaner alignment

An issue with HOMs arose with the automatic alignment (AA) system of the output mode cleaner (OMC), after the signal recycling mirror (MSR) had been changed from 98% reflectivity to a mirror with 90% reflectivity [Pri12]. With the new MSR installed, the power of HOMs at the darkport increased, due to less mode healing (see also section 2.4.4). This caused the AA system of the OMC to malfunction. It would *mis*align the darkport beam with respect to the OMC, leading eventually to instability and lock losses.

The reason for the problems with HOMs are connected with how the OMC would be aligned by the AA system; it worked by maximizing the power behind the OMC. In principle, the AA system would align the OMC in such a way, that the overlap between the TEM_{00} carrier beam in the Eigenbasis of the dual-recycled Michelson interferometer and the TEM_{00} Eigenmode of the OMC is maximized. But when the beam incident on the OMC has a large content of HOMs, as is the case since changing MSR, just maximizing the power in transmission of the OMC is problematic. When misaligned, the $TEM_{01,10}$ modes leaving GEO, can overlap with the TEM_{00}

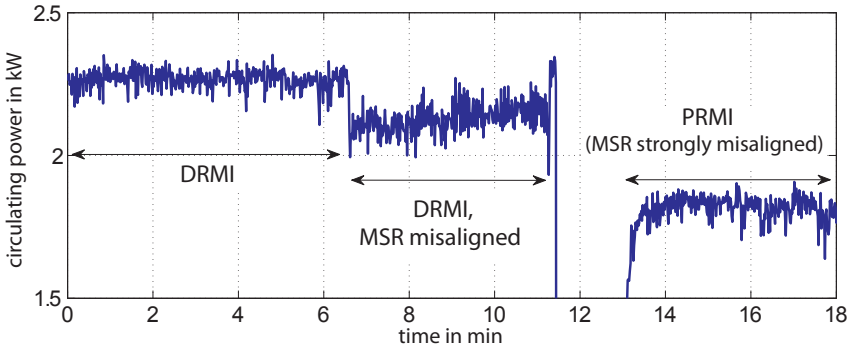

Figure 2.10.: This plot shows the circulating power in GEO 600 for three different alignment settings of MSR. the first case is normal operation as dual recycled Michelson interferometer (DRMI) with MSR aligned, then with MSR misaligned slightly, and finally with MSR misaligned strongly. In the latter case, the misalignment is strong enough to effectively cancel out the signal recycling cavity. Therefore this case is called PRMI (power recycled Michelson interferometer). The misalignment of MSR has a direct effect on the circulating laser power due to the effect of mode healing. Not only the total circulating power level is affected by MSR alignment, but it shows noticeably more fluctuations for the case of a misaligned MSR.

Eigenmode of the OMC. Indeed this is what happened, and the OMC would be misaligned by the AA system.

Eventually a new AA system, which is less susceptible to HOMs, had to be implemented [Pri12, p.82ff].

2.4.4. Alignment of the signal recycling mirror

Together with the end mirrors MCE and MCN, the signal recycling mirror (MSR) of GEO 600 forms the signal recycling cavity, which can resonantly enhance gravitational wave signals, and improve the sensitivity of GEO 600. The signal recycling cavity does have another big impact on the interferometer, it causes mode healing (see [Pri12, p.41]). In short, HOMs can be converted back to TEM_{00} light in the signal recycling cavity, increasing the circulating power and decreasing the amount of HOMs at the darkport. The mode healing depends on the alignment of MSR, meaning that misalignment of MSR will cause power fluctuations in the PRC and at the darkport.

An experiment has been performed that shows the influence of the signal recycling cavity on the circulating power in the PRC. For this, the circulating power in the PRC was recorded for different alignment states of the signal recycling mirror MSR. The result is shown in figure 2.10, the power in the PRC drops noticeably for a slightly misaligned MSR. A strong misalignment of MSR, such that such that it does not form the signal recycling cavity anymore, leads to strong power drop in the PRC. This experiment confirms that in the presence of HOMs, the alignment of the signal recycling cavity does influence the power in the PRC. Due to this mechanism, alignment noise in MSR (in the presence of HOMs) can lead to noise in the GW

measurement, and it was observed that a higher amount of HOMs can result in a worse sensitivity of GEO 600 [Wit13].

2.4.5. Squeezer phase control

The usage of squeezed (vacuum-) states of light is currently viewed as a key technology for further improvement of the sensitivity of GWD, and is being considered as a potential upgrade for the advanced detectors. GEO 600, was the first GWD to employ squeezing [Col11], and has collected several years of experience with integrating squeezed vacuum states of light into a GWD to improve its sensitivity. Among other effects, mainly optical losses, HOMs have shown to be limiting the amount of observed squeezing in GEO 600 [DSV+15].

The improvement in sensitivity is limited by optical losses and the phase mismatch between the injected squeezed field and the circulating light in GEO 600. The aforementioned phase is continuously optimized by a control loop. One way of generating an error signal for this is to use the darkport beam in front of the OMC. However This error signal provides only a low signal-to-noise ratio, due to the presence of many HOMs in the darkport beam, which contribute to shot noise, but not to the signal. As a consequence, the improvement by the injected squeezed light is lower than it potentially could be. Even worse, it has been observed that when using this error signal, HOMs will lead to wrong information on the squeezer phase error signal at certain frequencies and thus worsen the GW measurement in the presence of HOMs.

Alternative error signals for the phase of the squeezed beam are currently being investigated to mitigate the influence of HOMs [ADD+14].

2.4.6. Scattered light

The radius of a gaussian beam is commonly defined as the radius, at which the intensity has dropped to $1/e^2$ of its value on the beam axis. We will use the same definition throughout this work. One important aspect of HOMs is that they are larger, i.e. have a larger beam radius than the corresponding TEM_{00} beam. According to [Sie86, p.691], the radius r_n of a HOM with index n is

$$r_n \approx \sqrt{n} \times \omega, \tag{2.17}$$

where ω is the radius of the corresponding TEM_{00} beam. In fact, some HOMs that are produced in GEO 600 extend further than the mirror radius, and illuminate the inside of the vacuum tank. Light scattered from the mirrors surfaces (via its microroughness or dust particles) have the same effect and can be treated as very high order modes. Figure 2.11 shows an example of both, HOMs extending beyond the mirror radius and scattered light from the mirror's surface. Combined, both effects are called 'stray light', and are the cause of multiple issues in the past of GEO 600, especially if a part of it reaches the main photo diode. In [Hil07, p.31] it is calculated that a stray light level of 10^{-20} W reaching the main photo diode can already spoil the sensitivity of GEO 600. Furthermore, stray light bouncing of the inner walls of the vacuum

chambers may lead to acoustic and seismic noise coupling into the gravitational wave measurement.

Stray light was another candidate for the unknown noise mentioned in section 2.4.2, therefore big black glass baffles were installed in several of the vacuum chambers to absorb the stray light (more details in 6). This decreased the stray light level in those vacuum chambers by a factor of two to three [Aff14, p.44], but the unknown power dependent noise was still present after the installation.

An additional issue with stray light lies in the method of sensing the local mirror positions. The mirrors in GEO 600 are suspended as multi-stage pendulums. The suspensions feature sensors and actuators, which are used for alignment and for damping of the pendulum modes. The sensors are implemented as 'shadow sensors' (details in chapter 6). Simplified, they consist of an LED, which shines light on a small pin, and a photo diode, that senses the light from the LED. Depending on the position of the pin, it will more or less shadow the photo diode. The current of the diode is read out and used as position signal. Unfortunately, the photo diodes in the shadow sensors are not only sensitive to the LED's light, but to stray light from the interferometer as well. This led to mirror misalignments, instability and lock losses when performing high power experiments with GEO 600. A solution to this problem was implemented by modulating the LEDs and then demodulating the signal of the shadow sensor photo diodes [Aff14, p.44]). However, this modulation scheme has not been implemented to all suspended optics, and it was shown to lead to a higher level of feedback noise in the controlling of the local mirror position [Aff14, p.56]. Therefore reducing the amount of HOMs is still beneficial.

2.5. Methods of compensating the thermal lens

After having established the challenge of thermal lensing in optics of gravitational wave detectors, and in the beam splitter of GEO 600 in particular, possibilities of compensating the thermal lenses are presented.

2.5.1. Interferometer design and materials

The first way to deal with the issue of thermal lenses happens already in the design phase of the interferometer. The size of the laser beams on and in the optics has a large influence on the strength of the thermal lensing, because the thermal gradient generally scales with the square of the beam size (see eq. 2.2). The layout of the interferometer plays a role as well, especially optics in transmission of a high powered laser beam are more challenging in term of thermals than an optic in reflection. In the latter case, only one coating of the optic would 'see' the high powered laser beam. An optic in transmission though will absorb the high powered beam in coatings on both sides and in the substrate material.

Another design decision is the selection of materials for coatings and substrates of the optics. The absorption of both directly affect how much the optics are heated. At the time of writing, all large detectors use fused silica as substrate for their main op-

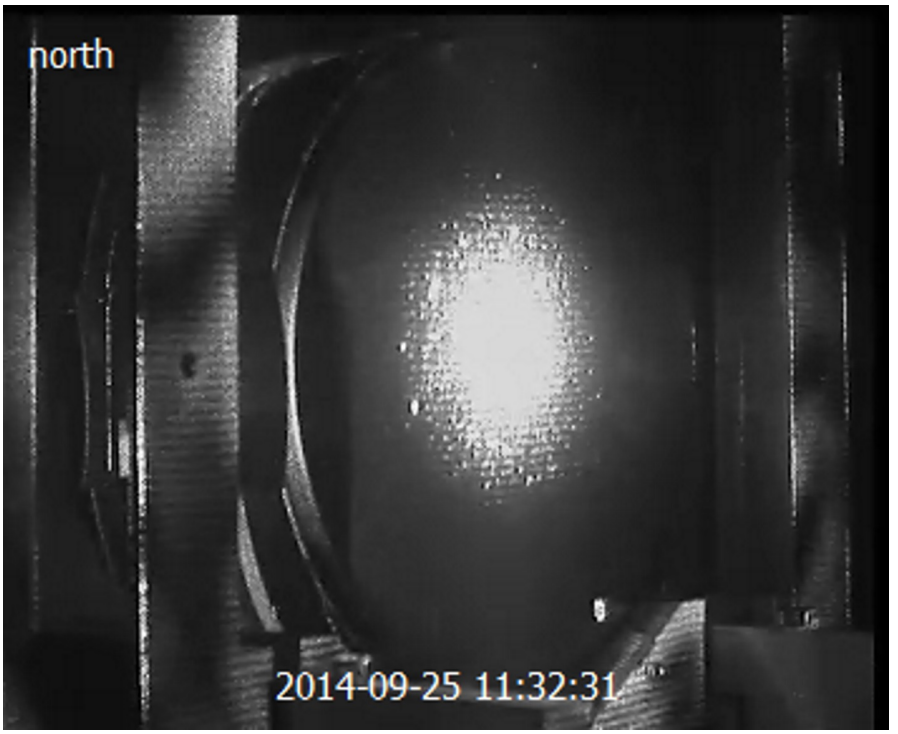

Figure 2.11.: This image (taken with camera that is sensitive to the laser wavelength of 1064 nm) shows the highly reflective front surface of the north folding mirror. The bright spot on the mirror is caused by the laser beam. Laser light is scattered from the mirror surface into the camera. High order modes extending beyond the mirror edge can be seen as well. They illuminate spots on the metal bars left and right of the mirror, as well as the catcher underneath the mirror. Furthermore, the 'illuminated' parts in the image show a pattern of horizontal stripes, with a spacial period of 2-3 mm, compared to the mirror diameter of 180 mm. The stripes are produced by the interference of two beams hitting the mirror at an angle, which is discussed in detail in [HCG+14].

tics. As the manufacturing processes improve, other materials may be used. Sapphire is one candidate ([TSM+02]). It has low absorption[6] at 1064 nm, and its thermal conductivity is over 30 times higher than the one of fused silica (at room temperature), which also makes it suitable for use as cooled optics. KAGRA [AMS+13], which is currently in an early phase of its construction, will be using sapphire optics.

2.5.2. Additional lenses and pre-curving

Introducing additional optical elements, such as lenses or curved mirrors, to counteract thermal lenses is also possible. A positive focal length thermal lens could be compensated by the addition of a lens with a negative focal length. But adding optics into the high power path is generally not desirable, as they would introduce additional absorption and thermal issues. Pre-curved optics, i.e. optics with a curvature that takes thermal effects into account, such that the curvature is correct when heated by the laser beam, may be an alternative. Both solutions would not scale with the laser power though, and may cause issues when the heat entry to the optics is different than anticipated. This can also be the case when the interferometer is not locked, and thus not heated by the laser. To regain lock, it may be necessary to (pre-)heat the optics.

It would be possible to partly realize the solution of pre-curved optics in GEO 600 by swapping the mirrors MFN and MFE, since the radii of the far mirrors differ[7]. In chapters 2.3.2 and 3.2 we show the benefits of a stronger curved MFE compared to MFN.

A similar, yet not power dependent solution was discussed, but not realized for GEO 600 and the thermal lens in the beam splitter [Fre03]. A compensation plate was to be installed into the north arm. The sole purpose of the compensation plate is to introduce the same thermal properties as the beam splitter has into the north arm. This way, the beams going to the north and to the east will be affected in the same way, and can destructively interfere in the beam splitter again.

2.5.3. Cooling

Since the thermal lens is the result of optics being heated by the laser beam, an obvious solution to the issue of thermal lensing is cooling the optics. If one wants to counteract the thermal lens, the cooling should be applied on the beam axis[8]. One way of selectively cooling the surface of a mirror while minimizing seismic coupling, is via radiation. A cold target would be imaged on to the optics, thus extracting

[6] [HBB+14] has measured an absorption of about 43 ppm/cm, which is still more than two orders of magnitude higher than the best currently available fused silica though.

[7] This is true in the cold state, i.e. without using the ring heater behind MFE. The cold radii of curvature are [WDG+07] 686.7 m for MFE and 666 m for MFN.

[8] Cooling via the pendulum wires/fibers, as it would be used to operate a cryogenic interferometer (for example planned in KAGRA [SAC+14]), is counter-productive for thermal lensing. It would increase the thermal gradient from the center of the mirror to its circumference. On the other hand, the materials chosen for a cryogenic interferometer, i.e. sapphire or silicon would have a better conductivity than fuse silica, and thus show less thermal lensing.

heat from it. Radiative cooling has been proposed by [JKKPD09] as a method to compensate thermal lenses. However, it is not a viable solution for the case of the beam splitter of GEO 600, as described in [Wit09]. The main reason is the relatively low cooling power, which is mostly restricted by the amount of heat radiated by the close-to room temperature optics.

The maximum amount of cooling power P_{cool} can be easily estimated with an assumed temperature T of 300 K of the beam splitter and an area A of the laser beam spots on each side of the beam splitter. For simplicity, the area is assumed to be an elliptic spot with semi-major- and semi-minor axis of 1.5 cm and 1 cm for each face of the beam splitter. The maximum possible cooling power is then

$$P_{\mathrm{cool}} = \sigma \times 2A \times T^4 \approx 0.45\,\mathrm{W}. \tag{2.18}$$

Realistically, this will be further reduced by practical issues, such as that the cool target will not be at absolute zero temperature, and that the useful solid angle in which the thermal power is radiated will be restricted.

2.5.4. Heating

Another way of compensating thermal lenses in optics, is to create a flat OPD profile by additional heating of the optic. This could be done via heating an annular area around the beam axis. This method has been demonstrated in LIGO and Virgo ([BFL+04], [ANDF+09]) with CO_2 lasers on the input test masses to the arm cavities. Further development of this technique is being done for the application in advanced detectors and beyond. The main areas of development are the stabilization of the CO_2 lasers, the use of thermal radiation, and variability and optimization of the spatial heating profile (see chapter 5).

2.6. Summary

The magnitude, cause and effect of the thermal lensing in the beam splitter of GEO 600 has been discussed. Along with these, the a direct measurement of the thermal lensing in the beam splitter has been performed with a thermal imaging camera. The resulting thermal images have been used to obtain a model independent measure of the absorption in the beam splitter of GEO 600.

Simulations and measurements of the effect of thermal lensing in the beam splitter and the resulting increase of HOMs have been presented. The result being that the thermal lens in the beam splitter will ultimately limit the circulating light power in the PRC, which will directly affect the sensitivity at high frequencies.

Reducing the effect of the thermal lens in the beam splitter is not only beneficial for the power build up in GEO 600, but can prevent multiple potential issues, that arise by an increased amount of HOMs in the PRC. Even at the currently used circulating light power of 2 - 2.5 kW, HOMs have posed many challenges in the operation of GEO 600.

A new method of estimating the noise contribution of HOMs to the GW measurement in GEO 600 is presented and performed. But HOMs can affect the operation of GW detectors in many ways, other than via direct noise contribution.

These issues are noise produced by scattered light, stronger coupling of MSR motion to sensitivity in the presence of HOMs (via mode healing) and issues with phase control for the injection of squeezed light. All of those are expected to become much more challenging when the circulating light power will be increased to the planned 20 kW.

This work focuses on mitigating the challenges related with HOMs and the thermal lens in the beam splitter. One mitigation strategy is to change the curvature of optics in the interferometer to counteract the thermal lens in the beam splitter. This is detailed in the next chapter, which shows how a change in the curvature in the far east mirror can improve the thermal-lens-limited interferometer contrast of GEO 600.

CHAPTER 3

Ring heater as thermal lensing compensation

This section describes the work done in characterizing and improving the performance of the existing ring heater at GEO 600, which is located behind the far east folding mirror. The characterization brought insights on how the thermal lens in the beam splitter can be partly compensated by running the ring heater at higher power, as well as the surprising finding that the heater itself is responsible for a large amount of higher order modes (HOMs) in GEO 600. Within this work, the ring heater has been improved by installing a reflector, which increases the heating efficiency and makes stronger heating of the far east folding mirror (MFE) possible without the risk of decreasing its lifetime by increasing the current. Another improvement that was implemented was a Labview controller which optimizes the heater power faster than the thermal timescale of the ring heater-mirror system.

3.1. History

All large interferometric gravitational wave detectors (GWDs) use very high quality custom-made optics for their main mirrors with very demanding specifications. In the case of GEO 600, the radius of curvature (RoC) of the far east folding mirror (MFE) was found to be 687 m, and thus off from the originally specified 640 m [WDG+07]. The mismatch of the RoCs of the folding mirrros posed significant challenges in locking the power recycling cavity (PRC) of GEO 600. Eventually, in 2004, a ring heater was installed behind MFE (figure 3.1 shows a photograph) to correct the RoC of MFE. The ring heater is comprised of a ring shaped glass rod, and a thin stainless steel foil wrapped around it. The metal foil is heated up by an electrical current, and heats the rear side of MFE via thermal radiation. The resulting temperature gradient in MFE from back to front causes it to deform and shorten

the RoC. The implementation of the ring heater finally allowed locking the PRC of GEO 600. Even today we cannot lock the PRC of GEO 600 without using the ring heater to correct the RoC of MFE[1]. Originally, the ring heater was planned to be a temporary solution to the locking problems related to the RoC of MFE, until the mirror could be exchanged. But since it has solved those problems and generally worked well, it was decided to keep the mirror MFE in combination with the ring heater. More details on the installation of the ring heater can be found in [LFG+04].

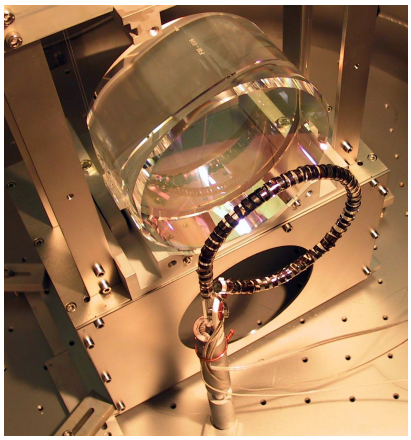

Figure 3.1.: Image of the ring heater behind the far east folding mirror [LFG+04].

While GEO 600 was the first of the GW observatories to implement the ring heater as a mirror RoC correction system based on black body radiation, similar systems have recently been developed both at Virgo [AAA+13] and for Advanced LIGO, where ring heaters are part of the baseline design [HC+10].

3.2. Ideal curvatures of the far mirrors

What would be the best combination of radii of curvatures of the far mirrors[2]? In order to answer this question, we performed a FINESSE simulation. In the simulation, we can change the RoC of both far mirrors (MFE and the far north folding mirror (MFN)), and observe the effect on the interferometer. We use the power recycling cavity gain factor (proportional to the circulating power in the interferometer) as well as the power leaking out of the dark port as a figure of merit for the ideal mirror RoCs. The simulation is performed twice, once for 3 W injected into the PRC, and once for the envisaged 20 W injected into the PRC. In the simulation, the power states differ only in the thermal lens in the beam splitter. The results of the simulations are plotted in figure 3.2. One obvious feature is that for the high power state, the ideal combination of RoCs is different than for the current (low-) power state. For both power states, there is a clearly preferable region in terms of PRC gain and power at the darkport. Please note that GEO has no facilities to tune the RoC of MFN at the moment of writing this thesis, nor are there plans to install thermal actuators at MFN.

[1] GEO 600 was locked the first time as dual-recycled Michelson-interferometer in 2003 [GFM+04], using a preliminary, lower reflectivity power recycling mirror MPR. Those mirrors were then swapped for the final high grade versions. Before the swap, it was possible to lock the PRC without the ring heater

[2] It was already briefly mentioned in [WDG+07] and chapter 2 that changing the RoC of MFE may help to counteract issues due to thermal effects.

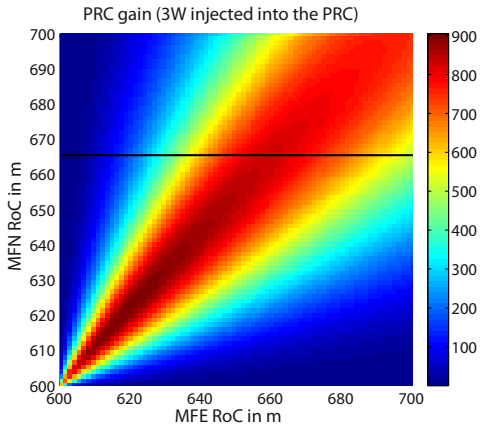

(a) PRC gain - current power

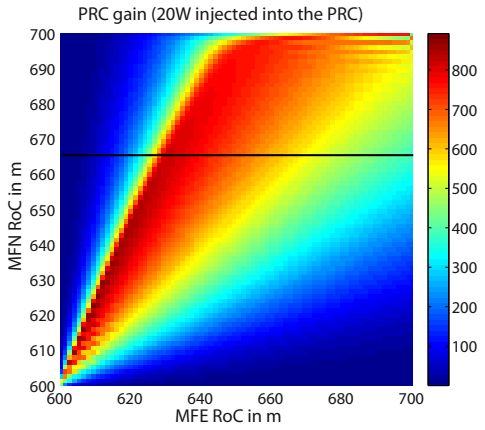

(b) PRC gain with high power

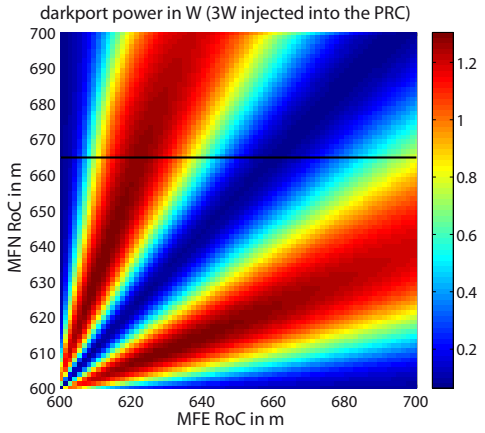

(c) Power at the darkport - current power

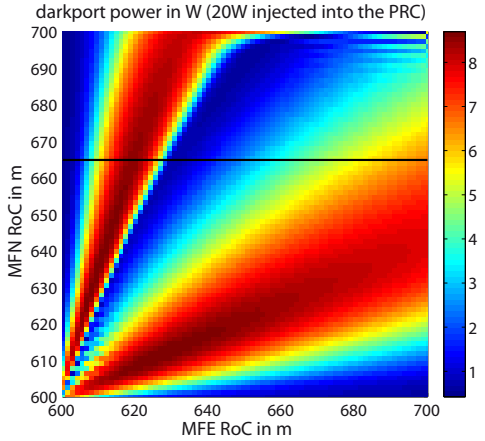

(d) Power at the darkport - high power

Figure 3.2.: Gain of the power recycling cavity (**a** and **b**) and power at the dark port (**c** and **d**) for different curvatures of the far mirrors, simulated with FINESSE. The RoC of the mirror MFN, which unlike for MFE cannot be changed, is shown as black line.

If we now consider that MFN has a curvature of 666 m [WDG+07], figure 3.2 predicts the optimum RoC for MFE to be about 660 m for the current power state, while 620-630 m are ideal for the high power state. Therefore we should try to decrease the RoC of MFE (i.e. heat MFE more) if we increase the circulating power in GEO.

We have verified the simulations shown above by increasing the circulating power in GEO, and then minimizing the power at the darkport[3] by adjusting the ring heater power. In fact, with high power operation, we can lower the power of HOMs at the darkport significantly. Figure 3.3 shows the results from the experiments. It plots

[3] The relative change in darkport power is far larger than that of the gain of the PRC, therefore we look at the darkport power.

the power at the darkport over the circulating light power for three different settings of the ring heater, along with a straight line, which represents a linear increase of darkport power (which would represent an ideal compensation of the thermal lens in the beam splitter in terms of darkport power). Note that in this experiments only the ring heater power was varied, and not the power of the side heaters (see next chapter). When adjusting the side heaters as well, the outcome likely matches the simulations even better.

The figure shows that we can compensate the thermal lens in the beam splitter with the ring heater behind MFE in terms of gain of the PRC and power at the darkport. Furthermore, it shows that for each circulating power level, the heating power has to be optimized individually.

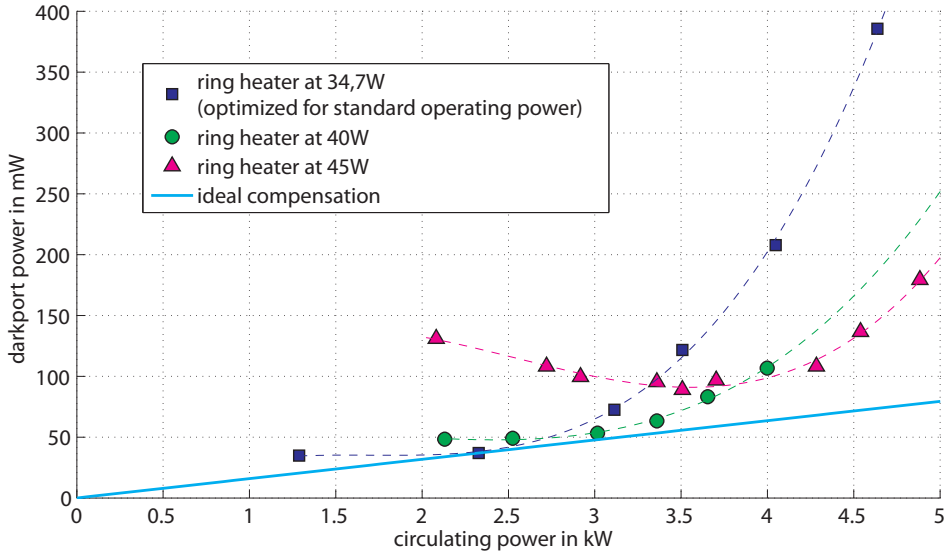

Figure 3.3.: Experimental verification of the simulations. When the circulating light power is increased without changing the ring heater settings, the darkport power increases strongly. When the power of the ring heater is adjusted as well, the power at the darkport, which mainly consists of HOMs, can be significantly lowered. The circles, triangles and squares represent measured data points, while the dashed lines are cubic fits to the measured values. Only the ring heater power was varied in this experiment, the side heaters remained at a constant power.

3.2.1. Limit for the ring heater

It has been established that the thermal lens in the beam splitter of GEO 600 can be compensated by changing the RoC of the mirror MFE in terms of power build up in the PRC and HOMs at the output port of GEO 600.

This section investigates the principal limitations in the usage of the ring heater for thermal compensation, while practical considerations, such as the heating power,

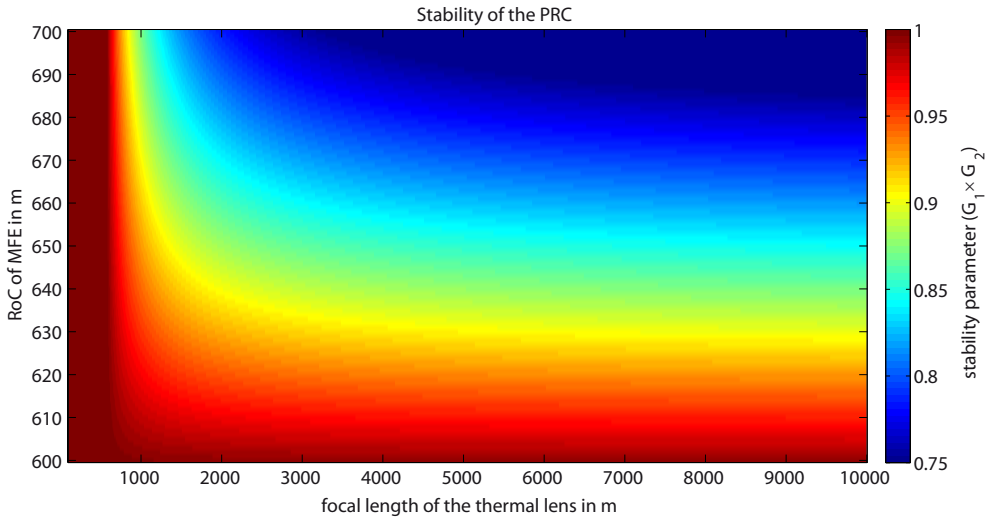

Figure 3.4.: Stability diagram of the PRC, showing the effect of the thermal lens in the beam splitter and of the RoC of the mirror MFE on the stability parameter $G_1 \times G_2$.

the thermal time constant and thermal noise are addressed later in this chapter.

The first principal limitation is that changing the RoC of the mirror MFE changes the stability parameters G_1 and G_2 (as defined in equation 2.10) of the east arm of the PRC, which may lead to the PRC being optically instable. To investigate this, the stability diagram from figure 2.4 is expanded to include the RoC of the mirror MFE as a second dimension, using the equations 2.10. The resulting stability diagram is shown in figure 3.4. From this figure it becomes apparent that by increasing the heater power, thus decreasing the RoC of MFE, the stability factor of the PRC changes closer to instability, i.e. $G_1 \times G_2 = 1$. Another finding is, that the point of the optical instability of the PRC will be reached at a thermal focal length of the beam splitter of 600 m, which translates to a circulating power of roughly 50 kW, regardless of the ring heater setting.

In conclusion, the deterioration of the power build up in the PRC and the increase of HOMs at the output port of GEO 600 can be minimized by adjusting the RoC of the mirror MFE. However, the ring heater cannot be used to prevent the optical instability of the PRC, which arises due to the thermal lens in the beam splitter. Instead, when using the ring heater to 'compensate' for the thermal lens in the beam splitter, it will bring the PRC closer to optical instability.

The change in the cavity G-factor of the PRC by the ring heater will also change the Gouy phase of the PRC in the east arm, which will influence the resonance condition of the optical modes in the PRC. The Gouy phase describes an additional phase that a gaussian beam acquires when passing though a focus (see [Sie86, p.682ff]). According to [WDG+07], the Gouy phase Θ for a round trip of the fundamental mode in the

case of the GEO 600 PRC is defined by

$$\Theta = 2 \arccos(\sqrt{G_1 G_2}), \tag{3.1}$$

while higher order transverse modes TEM_{mn} experience a Gouy phase shift relative to the fundamental mode of $(m + n) \times \Theta$ (analogue to the case of a two-mirror cavity). The PRC of GEO 600 is operated at resonance to the fundamental mode (TEM_{00}). HOMs will resonate along with the fundamental mode when their Gouy shift between them approaches multiples of 2π, which is to be avoided, since GEO 600 uses the fundamental TEM_{00} mode for the gravitational wave measurement. A co-resonance with another mode may decrease the power in the fundamental mode, and thus lower the shot noise limited sensitivity or cause other issues. We use the same criterion as [WDG+07] to set a boundary for how close a HOM can be to resonance, namely $1/F$, with the finesse F of the PRC of about 2350. Figure 3.5 shows for which values of the thermal lens and for which RoC of MFE certain HOMs become resonant in the PRC. The analysis shown in this figure includes HOMs up to an order of $(m + n) = 11$, since this is the highest order which we have measured to appear in GEO 600 (for example see table 4.1 on p.68 in this work). Furthermore, modes of order 11 and higher are expected to experience significant losses in the PRC and SRC of GEO 600. The reason is that the radius of HOMs increases with the square root of the HOM order in that direction (see equation 2.17). $\mathrm{TEM}_{n,m}$ modes with n or m larger than 11 will not fit anymore onto the folding mirrors[4]. Additionally, the PRC of GEO 600 is mode degenerate, i.e. all TEMn, m modes with the same order $n + m$ will have the same resonance conditions. And may couple into each other via mirror imperfections.

Practical issues might emerge when the HOMs are co-resonant with the fundamental mode in the PRC, for example both may show a coupling of power between them, which may affect the stability of the interferometer. Therefore figure 3.5 sets further practical boundaries on the strength of the thermal lens and the RoC of MFE at which GEO can operate. Especially for a thermal focal length of about 1 km and the current RoC of MFE, several HOMs show co-resonance with the fundamental mode in the PRC.

At the currently used RoC of MFE (661 m), the first co-resonance condition for a HOM (for the 8th order modes), when increasing the circulating power, will be reached at a thermal focal length of 2.2 km. Using equations 2.2 and 2.6, this can be translated to a circulating light power level of about 15 kW. This should not be seen as a 'hard' limit tough, unlike the optical instability shown in figure 2.4. It may e a practical limit though. The exact practical consequences of crossing the co-resonances as shown in figure 3.5 are unknown. It should be added, that when the PRC lock is acquired, the beam splitter is still cold and therefore possesses a thermal lens with

[4] The folding mirrors have a free aperture with a radius of 85 mm, while the TEM_{00} beam radius is 25 mm on those mirrors. The largest order TEM that the folding mirror can support is then $(85\,\mathrm{mm}/25\,\mathrm{mm})^2 = 11.6$, according to equation 2.17. Note that this again uses the common definition of beam size via the $1/e^2$ drop of intensity. Because of that, HOMs of smaller order will already face significant losses. The interested reader is pointed to table 6.1 in chapter 6 for TEM_{00} beam sizes and clear apertures at various locations in GEO 600.

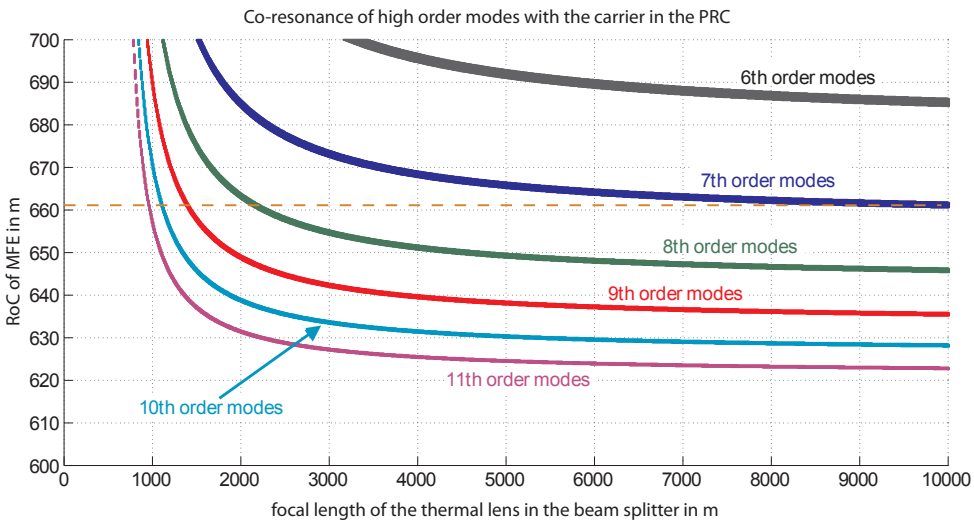

Figure 3.5.: This plot shows for which parameters of the PRC, HOMs are co-resonant with the TEM_{00} carrier beam (up to mode order 11). The typical operating condition for GEO 600 in 2015 is with a RoC of MFE of 661 m shown as a dashed line in the plot.

a very long focal length. And according to figure 3.5, the seventh order HOMs are co-resonant with the fundamental mode during this stage. However, no investigation specifically tailored for this effect was carried out.

A change in the stability parameters G_1 and G_2 will also result in a changed Gouy phase, as predicted by equation 3.1. This means that both the thermal lensing in the beam splitter and changing the RoC of the mirror MFE will introduce an additional phase to the east arm of the PRC, and slightly change the dark fringe condition of the PRC[5]. This has resulted in the observation, that the effective offset from the darkfringe slightly changes, according to the thermal state of the beam splitter and the curvature of MFE, even without changing the physical differential arm length of the PRC. It is reported in [Aff14, p.141f] that the power of the TEM_{00} carrier beam on the main photo diode can change due to this effect, but it should be noted that in normal operation, the power on the main photo diode is controlled, and therefore does not change (but the differential arm length in the PRC will change instead).

While the simple analytic model from above can provide an explanation of the findings, the real situation is more complex; hence a full optical simulation with the software FINESSE is employed. Figure 3.6 shows the result of the simulation, in which the microscopic difference in the arm length of the PRC is varied. The arm

[5] Typically the PRC of GEO 600 is operated at close to the dark fringe, i.e. the microscopic differential length of the two arms of the PRC is chose in such a way, that the most of the laser light at the output port of the beam splitter recombines destructively, and constructively at the input port.

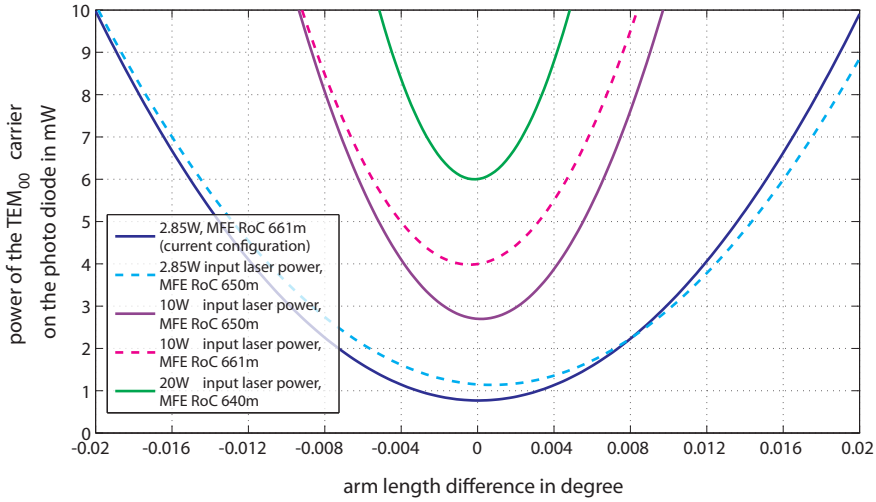

Figure 3.6.: This plot shows the power of the TEM_{00} carrier at the output port of GEO 600 for varying the arm length difference of the PRC of GEO 600. Several curves are simulated for different thermal lens values in the beam splitter and RoCs of the mirror MFE. One can see that the dark fringe condition, i.e. a minimum of light at the output, gets slightly shifted for not matching RoCs of MFE and input power (dashed lines).

length difference is defined as the microscopic[6] length difference of both arms of the PRC, which will affect the resonance condition of the PRC. This value is given in degree, with 1 degree equal to $\lambda/360$ meters, and λ being the wavelength of the laser light of 1064 nm. It is possible to reproduce the effect of the shift in the dark fringe condition when the thermal lens in the beam splitter and the RoC of MFE do not match, whereas 'matching' means good power build up in the PRC. This situation is represented by the dashed lines in figure 3.6. Indeed this effect can be recreated via simulation, now it is interesting to see if this will have an influence on the sensitivity of GEO 600. The ideal value for the dark fringe offset has been determined in [Hil07, p. 128ff] already, however many parameter of GEO 600 have changed since then, among those are: higher circulating power, a changed RoC of the mirror MFE, a different signal recycling mirror , a different tuning of the signal recycling cavity (tuned instead of detuned), and the influence of different parameters on the ideal dark fringe offset has not been examined either.

The investigation is performed in a similar way as in [Hil07], by plotting the shot noise limited sensitivity of GEO 600 for varying dark fringe offset values. For this, a shot noise model is created, and shown in figure 3.7. GEO 600 is shot noise limited for frequencies of 800 Hz and above, while other (not simulated) noise sources dominate at lower frequencies. The shot noise model as shown above is plotted in dependence of the dark fringe offset as a 2D plot for the following cases:

[6] as opposed to the macroscopic arm length difference of several centimeters for the using the so-called Schnupp modulation technique

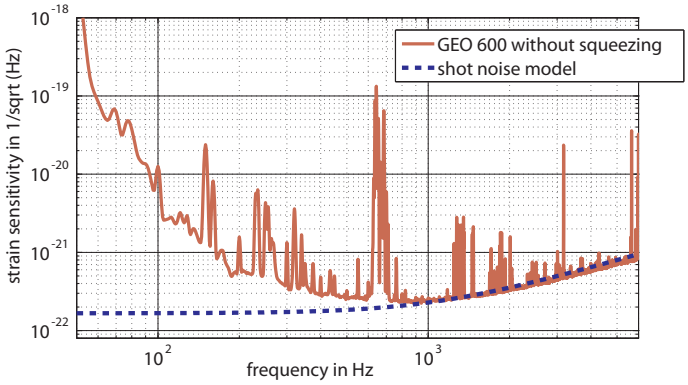

Figure 3.7.: GEO 600 sensitivity (without the injection of squeezed vacuum states of light) and a simulated shot noise model. It can be seen that GEO 600 is shot noise limited at frequencies above 800 Hz. The simulated shot noise model fits the real sensitivity of GEO 600 well.

1. the current (2015) operating parameters of GEO 600, i.e. 2.85 W of laser input power to the input optics and a MFE RoC of 661 m,
2. 2.85 W of laser input power to the input optics and a MFE RoC of 650 m,
3. 10 W of laser input power to the input optics and a MFE RoC of 661 m,
4. 10 W of laser input power to the input optics and a MFE RoC of 650 m,

and are plotted in figure 3.8. Note that this are the same parameters as used in the four bottom traces in figure 3.6. It is apparent that while the ideal offset from the dark fringe in terms of best shot noise limited sensitivity is larger in the cases (2) and (3), where the combination of MFE RoC and thermal lens in the beam splitter are not ideally matching in terms of power build up in the PRC.

Another consideration is that in practice, choosing the dark fringe offset is a trade-off, and typically it is chosen to be as small as possible without sacrificing too much sensitivity, as a large amount of carrier light at the darkport may cause more noise coupling, for example of laser amplitude noise, into the gravitational wave measurement. However, some parameter combinations, lead to a large drop in shot noise limited sensitivity at very small dark fringe offsets, and this needs to be considered when choosing the operating point.

3.3. Ring heater characterization

3.3.1. Temperatures

Since the installation of the ring heater in 2004, it has been found that for ideal performance, its power had to be increased. This was done several times. The power

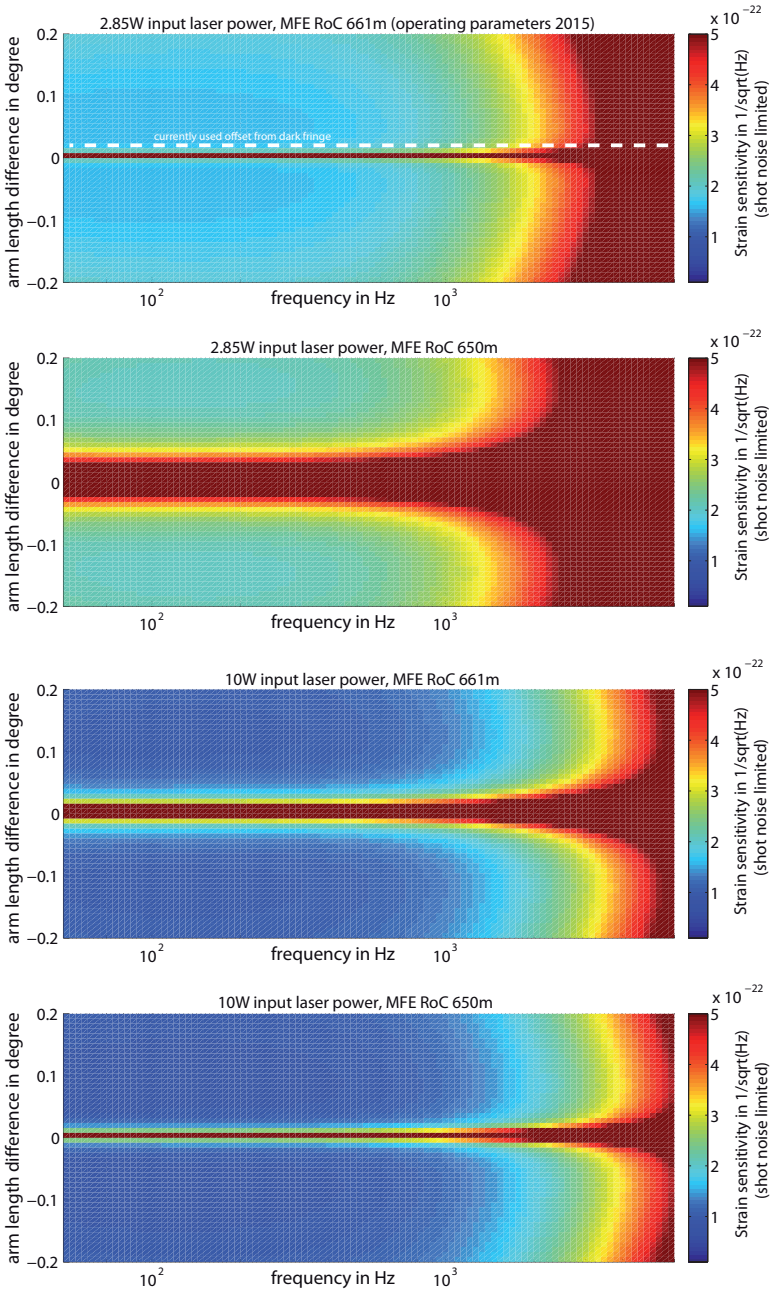

Figure 3.8.: Influence of the dark fringe offset on the shot noise limited sensitivity, for different circulating power levels and curvatures of the mirror MFE. The generally better sensitivity in the bottom two plots can be attributed to a larger circulating power. It can be seen that the ideal setting of the dark fringe offset can also depend on the thermal state of the beam splitter and the mirror MFE.

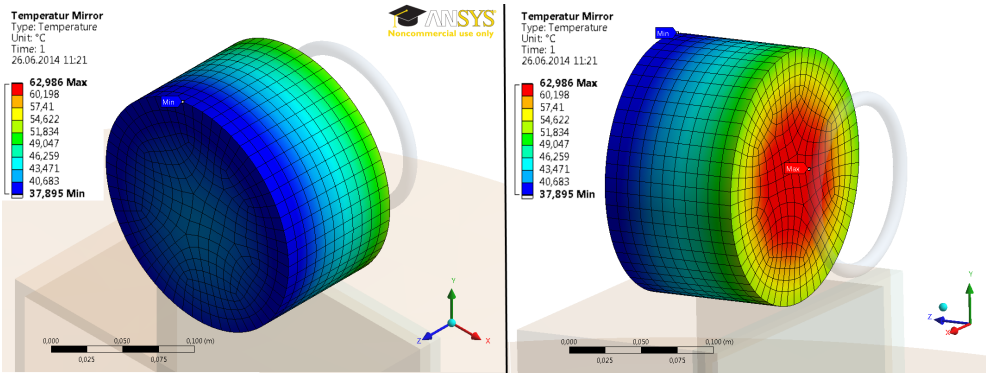

Figure 3.9.: This figure shows the outcome of the FEM model for the expected temperature distribution in the mirror for the default ring heater setting. The hexahedral meshing of the mirror in the FE model can be seen as well.

was raised from 70 W when it was installed to finally 90 W in 2012. The simulations above explain the need for higher heating power; the circulating laser power in GEO had been increased over the years. For ideal performance of the ring heater, its power had to be increased as well. In order to reach a RoC suited for the current (2015) amount of circulating laser power of 2-2.5 kW, a thermal gradient of about 25 K from back to the front of the mirror is required. For the current amount of heating power, our FEM model (see section 3.4) predicts temperatures of 63°C for the AR-coated side and 38°C for the HR-coated side of the mirror. To reach a curvature of 620-630 m, the heating power of the ring heater has to be increased by a factor of two, such that the temperatures in MFE reach 110°C on the AR and above 50°C in the HR coated side, according to the FEM model (more on the FEM model in 3.4).

3.3.2. Thermal noise

We installed a reflector (see section 3.5), which makes the heating of the mirror MFE more efficient and enables us to heat (and curve) MFE more. Large RoC changes in MFE, however require a large temperature gradient in MFE (and using the ring heater for this will result in large absolute temperatures). This may lead to an increased level of thermal noise in the coating and in the substrate of MFE, and may thus lower the signal-to-noise ratio in the gravitational wave measurement of GEO 600. In order to make sure the increased temperature in MFE does not noticeably degrade the sensitivity of GEO, we use the latest thermal noise model from [HCG+14], which specifically estimates the thermal noise contribution of the folding mirrors and the interference pattern on it. Furthermore we used the material parameters from table 3.1. We estimated the thermal noise contribution of Brownian-, thermo-elastic-, and thermo-refractive thermal noise, for two hypothetical cases. Case one assumes that MFE has room temperature (assumed as 300 K), the second case assumes a uniform temperature of 400 K. This model is relatively basic, it does not take temperature

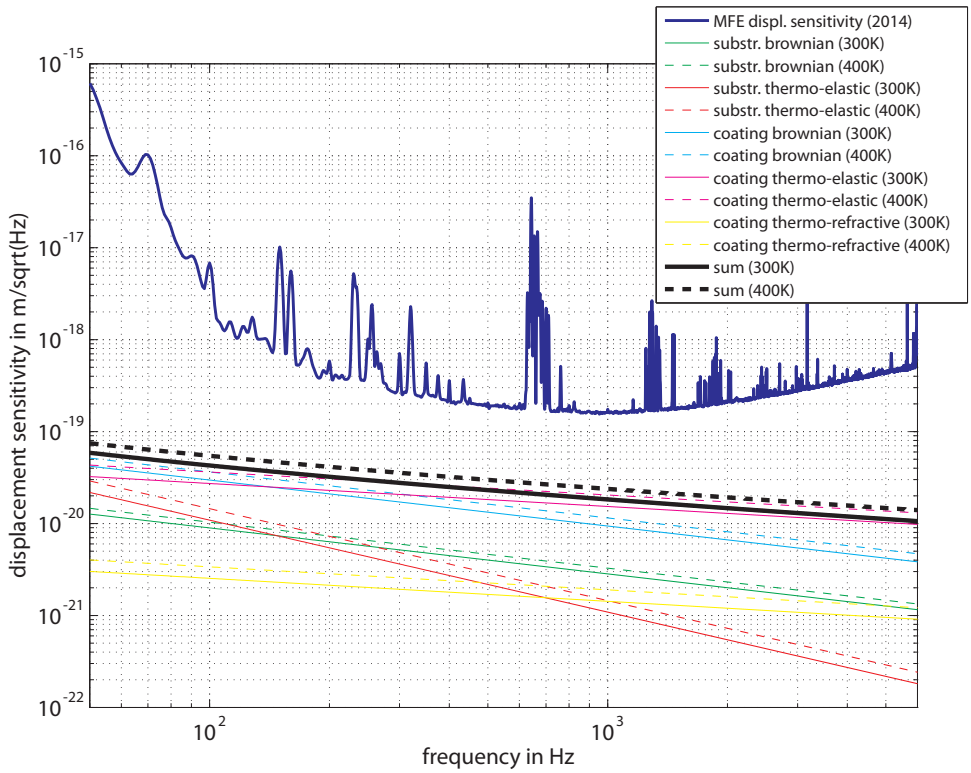

Figure 3.10.: This figure shows an estimation of the thermal noise induced by the folding mirror MFE. The solid lines represent different thermal noise contributions when MFE is at room temperature, while the dashed lines show the same noise contributions assuming a uniform temperature of 400 K in MFE. For comparison, the sensitivity of GEO 600 to displacement of MFE is shown as well (blue curve).

dependent material parameters into account, and neglects the thermal expansion of the coating (the effect of which will be considered in 3.3.3 though). Any influence of the thermal gradient in the mirror MFE on the thermal noise is neglected as well. Still we think that this model is accurate enough to determine if the increased temperature will have a noticeable effect on the observed thermal noise in GEO 600.

Figure 3.10 shows the results of the thermal noise model. The black curves represent the incoherent sum of the different thermal noise processes at 300 K (solid line) and at 400 K (dashed). Compared to the sensitivity to MFE displacement (blue line) the increase in thermal noise when going from 300 K to 400 K is small. We do not expect to observe the additional thermal noise of MFE (due to heating it) in the sensitivity of GEO 600.

3.3.3. Coating properties at higher temperatures

Modern laser interferometers rely on thin dielectric coatings on transmissive substrates (usually glass, fused silica in the case of GEO 600) for their high quality optics. The coatings consist of pairs of a low- and a high refractive index material. An incoming light wave will be partly reflected at each refractive index change. The thickness of the coating layers is chosen such that the reflected waves interfere, either constructively (for a highly reflective (HR) coating) or destructively (for an anti-reflective (AR) coating).

One concern when increasing the temperature of the ring heater is how the coating properties of the adjacent mirror might change at high temperatures. MFE has dielectric coatings on both faces, one highly reflective, and one anti-reflective for 1064 nm laser light.

Modeling the coating behavior in terms of optical properties and their temperature dependent change is straight forward. We use a freely available MATLAB library [Orf04], which computes the reflectivity of a dielectric coating when given the properties (i.e. thickness, refractive index and number of layers) of the single coating layers. The coating of MFE consists of layers of silica (SiO_2) and tantala (Ta_2O_5). The physical properties we assumed for the model are given in table 3.1. With in-

Property		
material	SiO_2	Ta_2O_5
nb of layers (estimate, based on transmission)	19 (HR)	19 (HR)
layer thickness (room temperature) ($L_{T\mathrm{room}}$)	1064 nm/4	1064 nm/4
refractive index (room temperature) ($n_{T\mathrm{room}}$)	1.44963	2.035
$\beta = \mathrm{d}n/\mathrm{d}T$	$8.5 \cdot 10^{-6}$ /K	$1.4 \cdot 10^{-5}$ /K
$\alpha = \mathrm{d}V/\mathrm{d}T$	$5.1 \cdot 10^{-7}$ /K	$3.6 \cdot 10^{-6}$ /K
Young's Modulus	72 GPa	140 GPa
Poisson ratio	0.17	0.23

Table 3.1.: This table gives an overview over the physical properties that were assumed for modeling the coating of MFE.

creased temperature, both the optical (via dn/dT) and the physical (via dL/dT)[7] thickness of the coating layers change. We computed the refractive index n when heated to temperature T and the physical thickness L when heated as follows:

$$n = n_{T\text{room}} + \beta \times T \times n_{T\text{room}} \tag{3.2}$$

$$L = L_{T\text{room}} + \alpha \times T \times L_{T\text{room}} \tag{3.3}$$

Our model predicts a transmission of the HR coated side of 7.2 ppm at room temperature, which changes to 7.05 ppm at 100 K above room temperature. Therefore we do not expect to notice any difference in the optical properties of the coating at the temperatures that we can reach with the ring heater.

3.4. Thermal radius of curvature change and astigmatism due to MFE ring heater

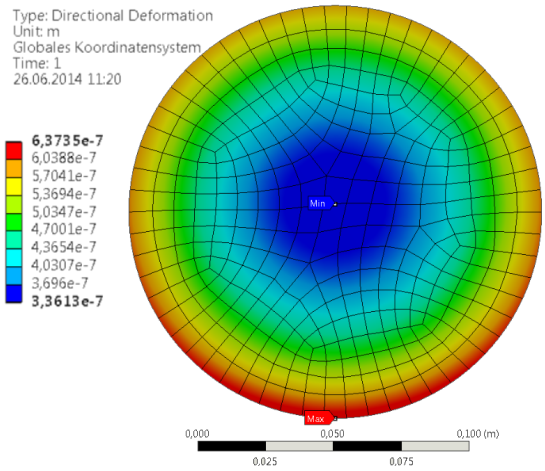

Figure 3.11.: Deformation of the HR-coated side of MFE in beam direction due to heating, as predicted by the improved FEM model that was developed in this work. Because of a slightly higher temperature at the bottom, the deformation is stronger there. The black lines in the mirror surface indicate the boundaries of the finite elements.

During this work, a detailed FEM model of MFE and the ring heater was created to simulate the performance of the ring heater. Using this FEM model, we found that the ring heater itself was causing a large fraction of the observed astigmatism in GEO 600. This is a surprising find, since the earlier, more simple FEM model used in [LFG+04] shows a uniform heat distribution in the far east mirror (MFE), and therefore no astigmatism.

The new FEM model *does* show an astigmatism in the far east mirror arising from the ring heater. It differs from the previous model in the fact that it includes not only the mirror and the ring heater, but also the surrounding area, i.e. the bottom plate of the vacuum tank and the catcher[8]. The geometry of the new FEM model is shown in fig. 3.12. This enables it to simulate the

[7] Which in this case we assume to be identical to the dV/dT coefficient - this may overestimate the expansion.

[8] in GEO, the catcher is a metal box underneath the mirror. It is supposed to prevent damage of the mirror, in case one of the fibers break which suspend the mirror.

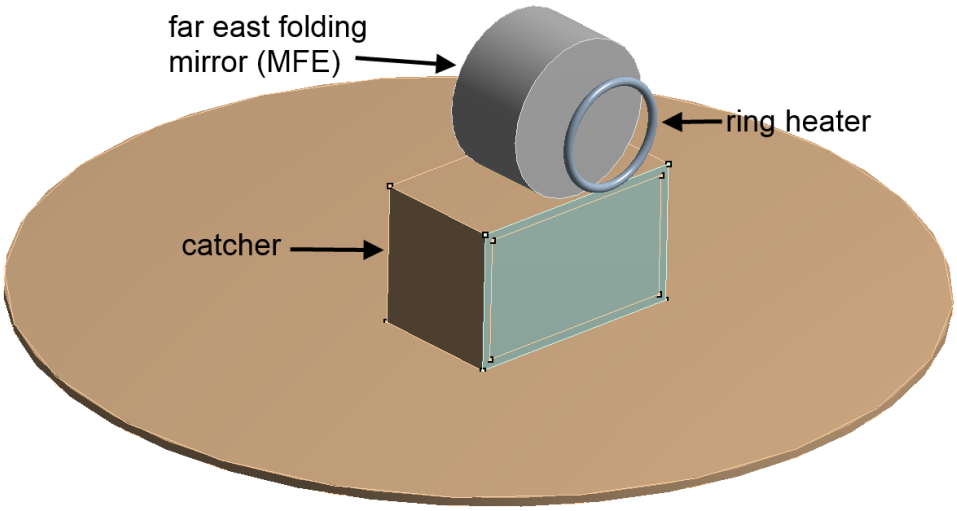

Figure 3.12.: This figure shows the geometry of the new FEM model of the far east folding mirror and the ring heater behind it. This new model includes the catcher and the baseplate of the vacuum tank.

main reason of the astigmatism; some of the heat radiation from the ring heater is reflected from catcher and tank baseplate to the bottom of the mirror. Thus the mirror gets heated unevenly and deforms astigmatically.

The FEM model confirms that this mechanism does create an astigmatism, such that the RoC in vertical direction is smaller than the RoC in horizontal direction. Explicitly, the FEM model predicts RoCs of 657.4 m (horiz.) and 655.7 m (vert.) for the currently ideal heating power. The deformation in beam direction of the HR surface due to the ring heater is presented in fig. 3.11. As mentioned before though, small omissions in the model can have implications in the results, therefore the RoC of MFE was determined by measurement as well.

We measured the RoC of MFE by comparing the observed output beam shape with simulated output beam shapes. This was done in PRMI mode, to exclude the effect of mode healing.

First we simulated what the darkport beam shape for different RoCs of MFE would look like. For easier orientation we arranged the output beam shapes in a grid according to the RoC of MFE in x (horizontal) and y (vertical) direction, as shown in fig. 3.13. From the simulated plots it is clear that a wrong RoC of MFE would result in low order Hermite-Gauss and Laguerre-Gauss modes, which is what we see in the real word as well. We then record the actual output beam shape of GEO 600 via a CCD camera (see fig. 3.13) and match it to the simulated shapes. We do this process for ring heater powers of 33.1, 34.7 and 36.5 W[9] and observe clearly different beam

[9] These measurements were performed after a reflector for the ring heater had been installed, which increased the heating efficiency by a factor of 2.5 (see 3.5).

shapes. When matching the observed shapes with the simulated, we take the FEM model into account, which predicts a stronger curvature in the vertical axis. The matching gives us the RoC of MFE in dependence of the ring heater power, which we approximate as linear in the observed region. We get the following relation for the observed range (with ring heater power P_{ring}):

$$\mathsf{RoC}_x = -1.3\,\mathrm{m/W} * P_{\mathsf{ring}} + 625\,\mathrm{m} \tag{3.4}$$

$$\mathsf{RoC}_y = -1.5\,\mathrm{m/W} * P_{\mathsf{ring}} + 610.4\,\mathrm{m} \tag{3.5}$$

We estimate the error in this measurement to be about $\pm 2\,\mathrm{m}$, mostly due to uncertainties in how the interferometer is represented in the simulation, and to the accuracy of matching the beam shapes. The possible range of RoCs that are accessible by the ring heater are shown as red arrow in fig. 3.13. According to the simulations, the ideal RoC in terms of darkport power is (horiz./vert.) 661 m/661 m. This RoC however is not achievable with the ring heater, which led to the development and installation of additional heaters, as described in chapter 4.

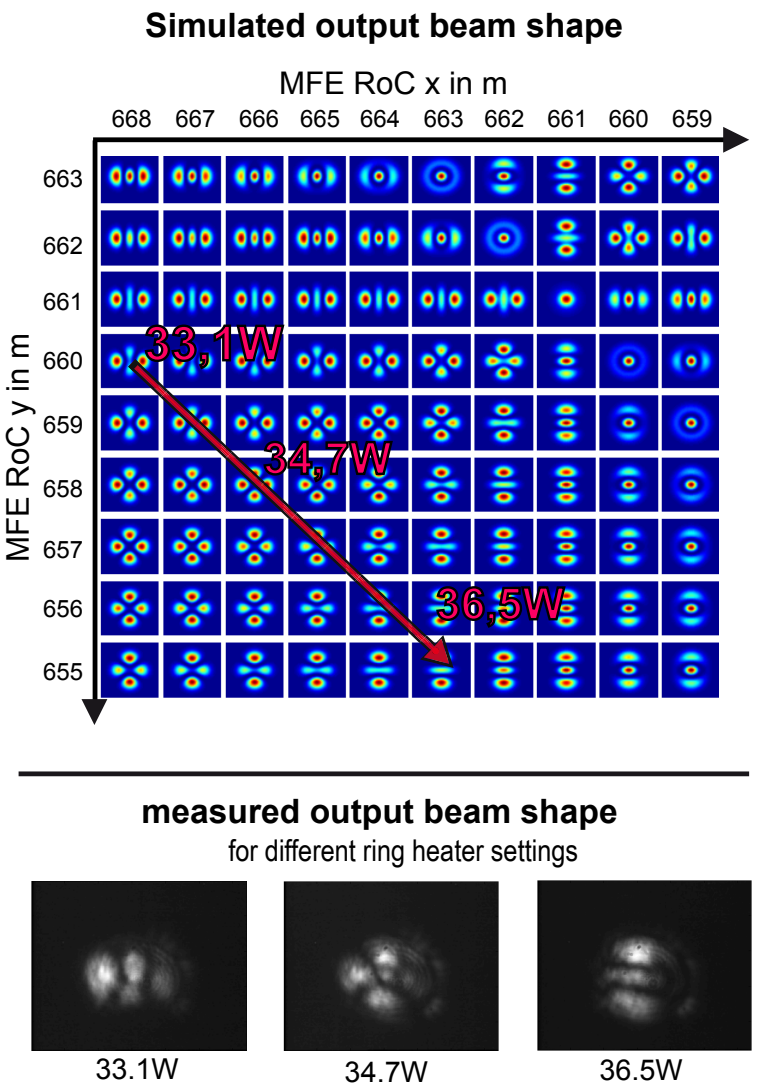

Figure 3.13.: This figure shows how the observed dark port beam shapes can be compared to the simulated output beam shapes (via FINESSE), in order to measure the RoC of the far east mirror. The CCD images of the output beam on the bottom are matched to the matrix of simulated output beam shapes (the difference in simulated shapes is due to different RoCs). The arrow indicates how changing the ring heater power affects the RoC. The ideal RoC in terms of HOMs at the darkport of 661 m/661 m cannot be reached with the ring heater alone ([WLA+14]). Note that the simulation and the measurements are done with GEO used as power recycled Michelson interferometer (without signal recycling).

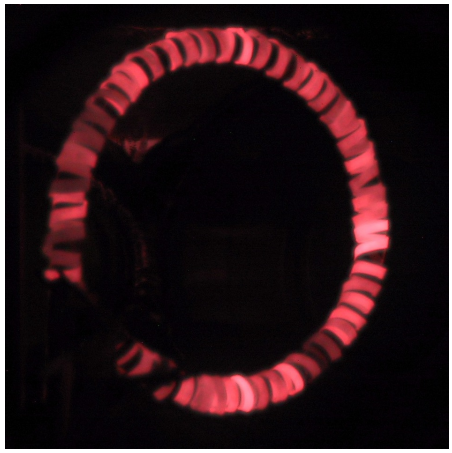

(a) Photograph of the ring heater at default operating power (90 W) before the installation of the reflector. It is visibly (but faintly) glowing. The glowing appears stronger in the photograph due to a long exposure time.

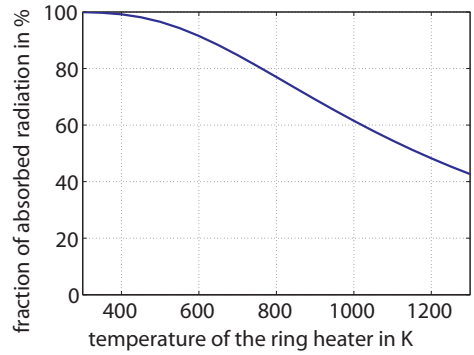

(b) Percentage of radiation absorbed in MFE at different ring heater temperatures, due to the transparancy of the mirror for shorter ($\leq 3.5\,\mu$m) wavelengths.

Figure 3.14.: Photograph of the ring heater and projection of the transmitted power at different temperatures.

3.5. Reflector for the ring heater

3.5.1. More power

From section 3.2 it is clear that we want to have the possibility to increase the heating power deposited in MFE. This way we could use the ring heater to partially compensate the thermal lens in the beam splitter. Moreover it would allow to change the RoC of MFE faster than the thermal timescale by first overshooting the power of the ring heater. In 3.3.3 we have already established that the optical properties of the dielectric coatings of MFE are no reason of concern for the envisioned temperatures. Furthermore, the bulk material of MFE, fused silica, should be sufficiently pure and void of defects to not having to worry about thermal stress induced damage to the mirror. However, there were concerns about the lifetime of the ring heater itself, of both, quartz ring and the metal foil, since at normal operation it was already visibly glowing (figure 3.14a shows a photo of the heater in operation).

Apart from concerns about its life time, a further increase in temperature of the ring heater would potentially introduce additional issues. At even higher temperatures, more thermal radiation is emitted at shorter wavelengths, while the long wavelength output changes comparably little. A higher fraction of the radiation would be just transmitted through the mirror, and a lower fraction would be absorbed, as plotted in figure 3.14b. Furthermore, the increased short wavelength part may interfere with

the OSEMs (see chapter 6.5 for more information on the OSEMs in GEO 600), which use near infrared LEDs. Therefore, instead of further increasing the ring heater temperature, it was decided to design and install a reflector to increase the efficiency of the MFE ring heater.

3.5.2. Design and installation of the reflector for the MFE ring heater

The reflector was designed with several requirements in mind:

- It should increase the efficiency of the heating by at least a factor of two. This would be necessary to reach the RoC of 620-630 m mentioned in 3.2.
- It should not obstruct the center of the mirror.
  Even though MFE is highly reflective for the 1064 nm laser, it still has a transmission of 8.3 ppm for the main laser beam. The transmitted beam is used for alignment purposes and should not be blocked.
- It should not introduce backscattering problems.
  We have observed before that backscattering can be a severe problem in GEO 600 [Gro03, p.33ff], especially if parts (such as the reflector) are brought close to the beam.

Based on these requirements, the reflector was built in such a way that when viewed from the front, it has an annular shape, with the outer dimensions slightly smaller than the mirror MFE (170 mm diameter), and an inner free aperture with the same inner radius as the existing ring heater (120 mm). These dimensions are chosen to minimize backscattering. Furthermore, the reflective surface has been designed to have no surfaces which are perpendicular to the laser beam axis. The reflecting surface does not have a single radius of curvature, instead it is a free-form curve which, compared to a spherical or parabolic shape, has a higher gain with the given size constraints. The exact spatial distribution of heat on the backside of the mirror is only a very minor concern. We carried out further FEM simulations that confirm that mostly the total power deposited on the back of the mirror will determine the shape of the HR-coated front. The distribution of the heat on the AR-coated backside, on the other hand, has only a negligible influence.

The reflector was milled from a single piece of aluminum and subsequently polished for good reflectivity (for infrared light). Even with the inevitable (thin) layer of oxide that will form on the surface, polished aluminum has more than 90% reflectivity from 0.9 μm to 12 μm according to [M+76].

Figure 3.15 shows a CAD drawing of the reflector assembly.

Seismic isolation with Fluorel feet

We build an adjustable height stage for the reflector and put it on four 4x4x4 mm Fluorel feet for seismic isolation. Fluorel is a fluoroelastomer, a rubber-like material, which can be made UHV-compatible when treated according to [BCF09]. The

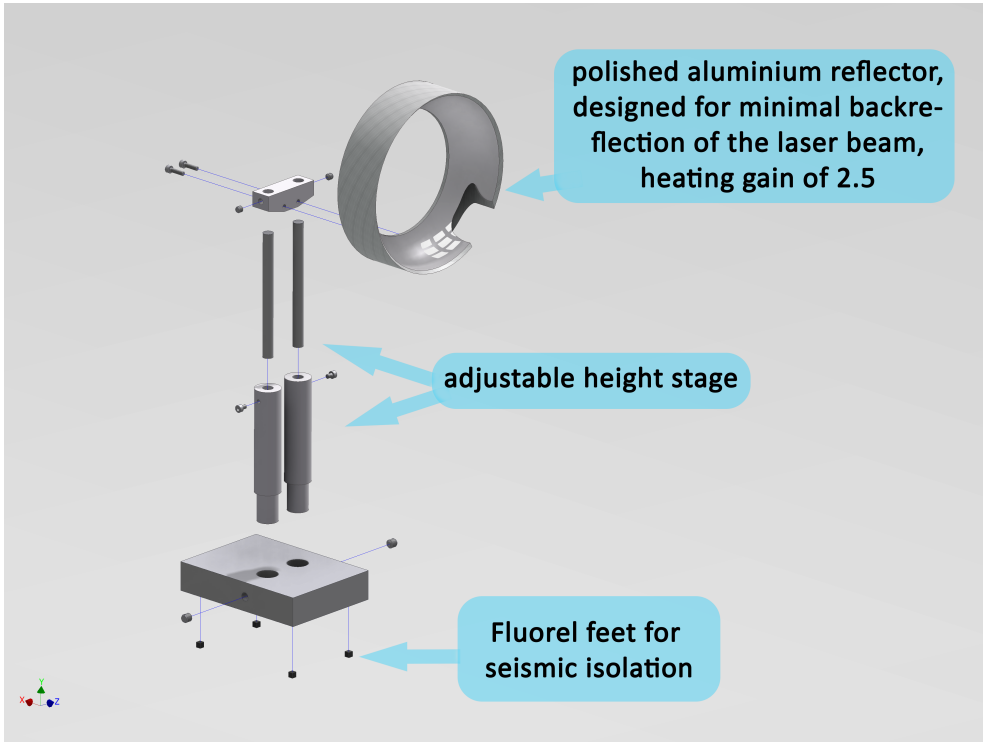

Figure 3.15.: This figure shows the CAD model of the reflector which has been installed to increase the efficiency of the MFE ring heater. A cross section drawing of the reflector can be found in D.1 on page 184.

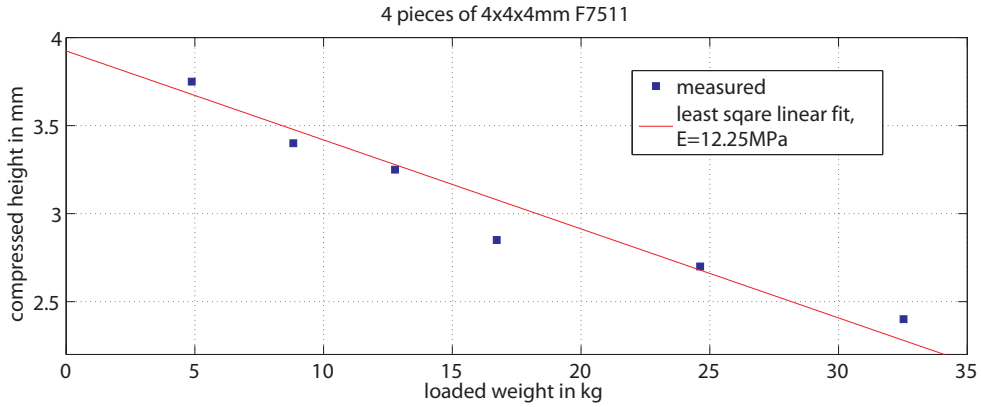

Figure 3.16.: Measurement of the Young's modulus of the Fluorel which was used to seismically isolate the reflector for the MFE ring heater.

treatment involves cleaning the Fluorel in an ultrasonic bath, repeatedly boiling it in deionized water and baking it.

In order to estimate the isolation performance of the Fluorel pads, the system of reflector and Fluorel pads can be regarded as a harmonic oscillator, which will provide seismic isolation above its resonance frequency (though typically Fluorel provides less isolation at high frequencies than the expected $1/\text{frequency}^2$ for a pure harmonic oscillator [GSSS96]). In this picture we can treat the Fluorel pieces as loaded spring, with a resonance frequency f_{res} of

$$f_{\text{res}} = \frac{1}{2\pi} \times \sqrt{k/m}, \tag{3.6}$$

where m is the mass of the reflector and k the spring constant. Further we can assume a force equilibrium with the earths acceleration $g = 9.81\,\text{m/s}^2$ and the spring deflection x:

$$m \times g = k \times x \tag{3.7}$$

Inserted into eq. 3.6, we get the resonance frequency of a loaded spring, depending on the steady-state compression of the spring.

$$f_{\text{res}} = \frac{1}{2\pi} \times \sqrt{g/x} \tag{3.8}$$

The relation of compression to loading of the Fluorel is given by the Young's modulus, which has been measured by observing the compression of the Fluorel when loaded with different weights. We did this using four 4x4x4 mm Fluorel pads, and computing the Young's modulus E with

$$E = \frac{m \times g \times L}{A \times x}. \tag{3.9}$$

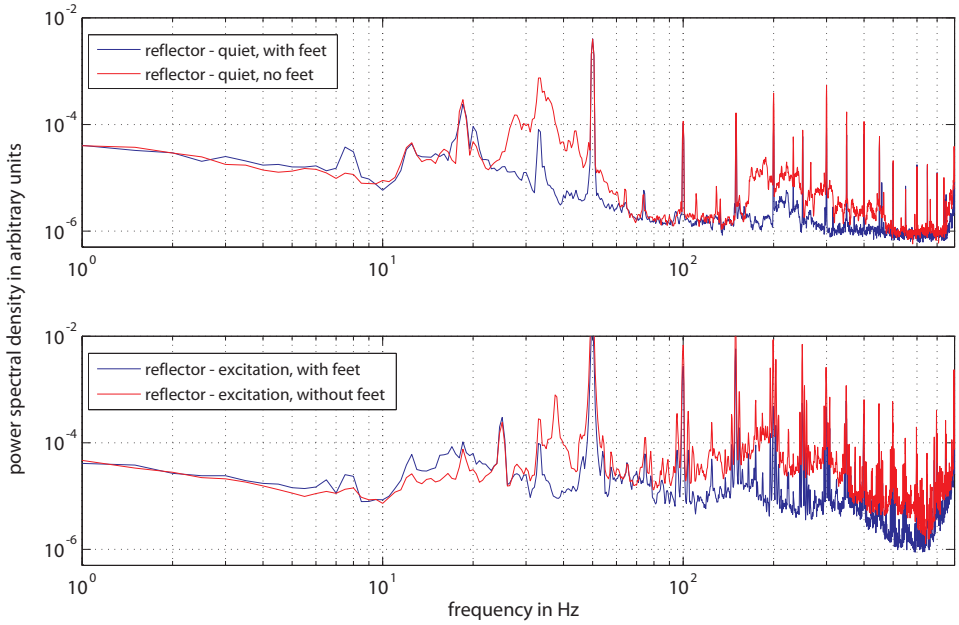

Figure 3.17.: Measurement of the seismic isolation of the flourel feet. The measurements was performed in a quiet environment (top) and with external seismic excitation (bottom).

Where A is the area of the of the Fluorel in the compressed direction ($4\times$ 16 mm^2), L is the uncompressed height (4 mm), m is the mass of the suspended object, x is the compression of the Fluorel and g is the Earth's acceleration of 9.81 m/s^2. figure 3.16 depicts the results of the measurements. We find the Young's modulus to be about 12 MPa. With this result we expect a resonance frequency of 38 Hz for the reflector, which weighs 3.5 kg.

Furthermore, the seismic isolation has been measured by attaching an accelerometer (B&K model 4381) to the top of the reflector (pointing in beam direction) and measuring the signal of the accelerometer, once with and once without Flourel feet. This has been performed twice, once in a quiet environment, and once with additional seismic excitation. The excitation was generated by running a grinder, which was mounted to the same table on which the reflector sat for the aforementioned measurements. Figure 3.17 plots the spectra of this measurements. It is evident that the Fluorel feet provide seismic isolation starting about 25 Hz - 35 Hz (measured with- and without excitation, respectively). This fits reasonably with the prediction by equation 3.8.

3.5.3. Results of the reflector installation

We find that the reflector increases the efficiency of the ring heater. Before installing the reflector, the ideal heating power in terms of HOMs at the darkport was 90 W,

when GEO 600 was operated with its standard circulating light power. With the reflector, we reach the same curvature with 34 W of heating power. This corresponds to an increase in efficiency of a factor of 2.5. Moreover we compared the strain sensitivity of GEO 600 before and after the installation[10] and found no sign of scattering.

3.6. Feedback control of the mirror shape of MFE

After the temperature of the ring heater could be lowered due to the increased efficiency, the concerns mentioned earlier in 3.5.1 about its life time were no longer valid. Earlier we showed that the ideal RoC of MFE (and therefore ideal heating power as well) depends on the circulating laser power.

3.6.1. Labview interface

A Labview interface for the ring heater was developed, which ties into the existing Labview infrastructure, such that the heating power is monitored and recorded in our data acquisition system. Additionally this makes it possible to programmatically set the power. Those new capabilities were used to implement a control loop that automatically puts the ring heater to the ideal setting. A screenshot of the Labview interface is provided as figure 3.18.

3.6.2. Modulation technique and loop shape

A control loop was implemented to optimize the power of the ring heater. Every control loop needs an error signal, which can be minimized by the loop. In the case of the ring heater, we generate the error signal from the amount of power in the beam at the darkport, before the OMC. There, the output beam is completely dominated by HOMs. The power of those HOMs is strongly influenced by the ring heater (as show in figure 3.3). However, in *steady state* it is not possible to get directional information (i.e. if the ring heater power should be increased or decreased) from just the power at the output. When the power is changed though, we obtain information if the change increased or decreased the power of the HOMs. Therefore, we introduced a modulation/demodulation technique to get directional information. It works by adding a small sine-shaped modulation with a period of 10 min to the DC ring heater power. Now we create the error signal by demodulating the power at the darkport with the same 10 min period and a fixed phase, and apply a lowpass filter to it. This error signal is then inverted and fed back to the DC offset of the ring heater power. The whole control loop is implemented entirely in Labview. A schematic view of this feedback loop is presented in figure 3.19.

The loop shape (or 'open-loop transfer function') defines the behavior of feedback loops. Of special relevance is the unity gain point where the gain reaches one. the loop affects the system mainly where the gain is above unity. The stability of the

[10] The reflector was installed at the same time as the side heaters (see 4) and the baffle (see 6.4) in the far east vacuum tank.

Figure 3.18.: The VI to control the ring and side heaters.

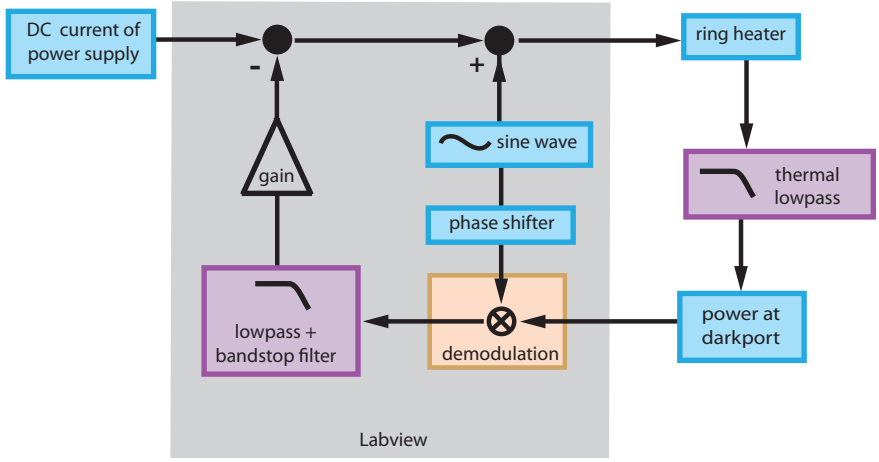

Figure 3.19.: A schematic drawing of the control system for the ring heater.

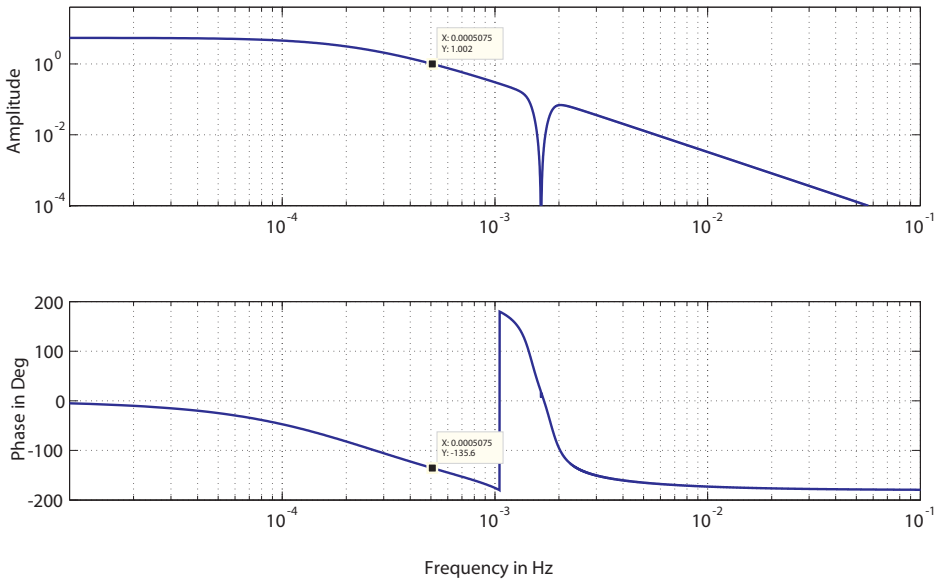

Figure 3.20.: Loop shape of ring heater control system

loop can be determined by the phase margin at the unity gain point. More details on control theory can be found in [Fre03].

The loop shape of this control system will be defined by the transfer function of ring heater power to optical power in the dark port beam and by additional filters introduced in Labview. The former has been measured to be a single pole lowpass filter with a cutoff frequency of 2×10^{-4} Hz (which is equivalent to a time period of about 1.4 h). The final shape of the loop is presented in figure 3.20. It is stable, with a phase margin of about 45 ° and a unity gain frequency of approximately 5×10^{-4} (this is equivalent to a period of roughly 0.6 h) - which is shorter than the thermal time scale. Effectively, the control loop can 'over-' and then 'undershoot' in order to reach the ideal RoC faster than the thermal timescale.

3.6.3. Result

Figure 3.21 demonstrates how the loop performs. Initially (t=0 hours), the feedback loop is off and the DC level of the ring heater is not at the ideal setting in terms of dark port power. One side effect of this is that the modulation of the ring heater is clearly visible in the dark port power, while at the minimum of the darkport power, the modulation should (to first order) not influence the darkport. The modulation in the darkport does indeed disappear at the right side of the plot. At the time marked as one hour on the x-axis we activated the feedback loop. Subsequently the DC level power of the ring heater is increased by the loop, minimizing the darkport signal. A lock loss of the PRC, occurred at about 2 hours on the time-axis. As long as the PRC

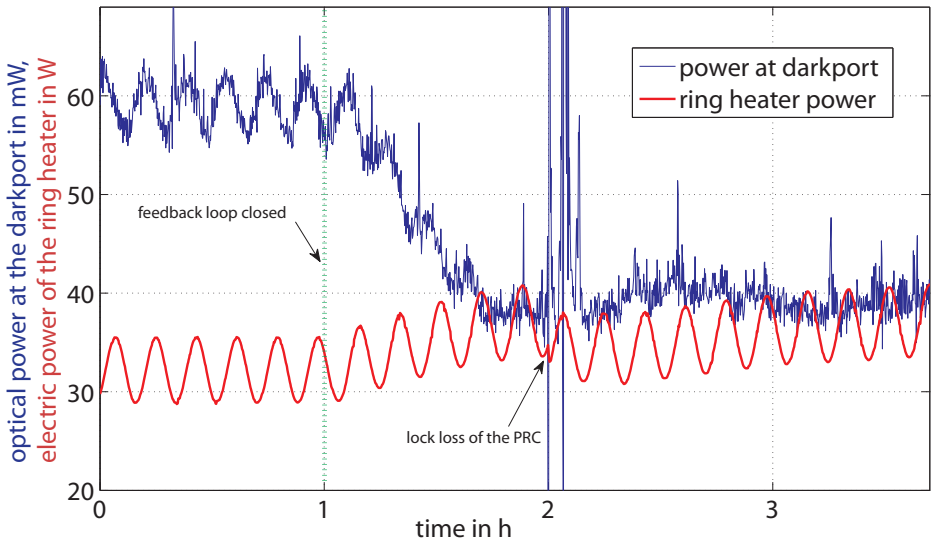

Figure 3.21.: This plot shows the performance of the ring heater loop, plotted are the power at the dark port of GEO 600 and the heating power of the ring heater. After the loop was turned on at 1 hour, the loop adjusts the ring heater to minimize the darkport power.

is unlocked, it is in an undefined state, and the error signal is not useful. The loop is programmed in such a way, that in the case of an unlocked PRC it sets the ring heater DC power level to a default state and disables the loop until lock is regained. The lock loss was unrelated to the heater loop. Typically, the duration of PRC locks are in the order of several hours, therefore it is not unlikely to see a lock loss in the timescale of this experiment.

With the installed reflector and the control system, the ring heater can be used to compensate the thermal lens in the beam splitter.

3.7. Summary

This chapter discussed the possibility of using the existing ring heater behind the far east end mirror MFE in GEO 600 for the compensation of the thermal lens in the beam splitter. The result is, that with an ideal curvature of the mirror MFE, a linear increase of HOMs with increasing circulating light power can be achieved. The validity of this method of compensating the thermal lens in the beam splitter has been shown through experiments for obtainable light powers at the time of writing, and through simulations for the final GEO-HF circulating light power.

Potential issues of this approach, such as increased thermal noise due to temperature increase, or a change of coating properties due to thermal expansion have been examined, and not found to be limiting. Another issue is the changing of the PRC

stability parameter by changing the RoC of MFE, which may lead to co-resonances in the PRC, which ultimately has unknown consequences.

Due to power constraints of the ring heater however, this usage of the ring heater was not feasible with the existing ring heater setup. Therefore, a reflector was developed, characterized and installed, to increase the effective heating power by a factor of 2.5.

A feedback system for the ring heater has been implemented, using the power of the (HOM dominated-) darkport as error signal. It keeps the RoC of the mirror MFE at its ideal (thermal lens dependent) value in terms of HOM generation. Additionally, using this loop, the ideal RoC of MFE can be reached significantly faster than the thermal time constant of the mirror MFE. This feedback system represents the very first demonstration of a control loop which optimizes the mirror shape in any GW detector.

Future work may include more optimization of the control loop to increase its unity gain frequency, i.e. to make it faster, as the current implementation does not use all of the possible dynamic range of the ring heater.

Furthermore, the ring heater and its effect on the mirror curvature have been thoroughly characterized via FEM simulations, as well as the comparison of observed beam shape and simulated beam shape in GEO 600. A new finding of this work is, that the ring heater introduces a significant astigmatism, and therefore HOMs in GEO 600.

The next chapter describes the installation of additional heaters, that make it possible to curve the mirror in two degrees of freedom to reduce this astigmatism.

CHAPTER 4

Side heaters for astigmatism correction

The design, installation and results of two additional heaters to the far east folding mirror (MFE) are presented in this chapter. These side heaters are installed laterally to the mirror, and use an improved design compared to the existing ring heater. The new heaters are the first demonstration of a segmented heating system in a gravitational wave detector. They make it possible to change the mirror's radius of curvature (RoC) in two degrees of freedom (DoFs), and can greatly reduce the amount of higher order modes (HOMs) at the output of GEO 600.

Parts of this work have been published as [WLA+14].

4.1. Motivation for additional heaters at the far east mirror

As shown in the last chapter, the (cold) RoC of MFE deviates from the specified value of 640 m[1]. GEO 600 uses a ring heater to sufficiently change the RoC of MFE to function (i.e. to make it possible to lock the PRC). However, using the ring heater causes a large fraction of the high order modes present in GEO 600. As shown in chapter 2.4, HOMs can and have caused issues in the operation of GEO 600, therefore we decided to correct the astigmatism. One option of correcting the astigmatism in the existing mirror was to modify the ring heater setup, either by installing a different ring heater or an additional heat shield. However, it seemed difficult to design the correct geometry, which takes the surrounding in the vacuum tank into account. Instead, we settled on the more flexible solution of installing additional

[1] The RoCs of other optics deviate from their specifications as well [WDG+07], but MFE showed the largest difference.

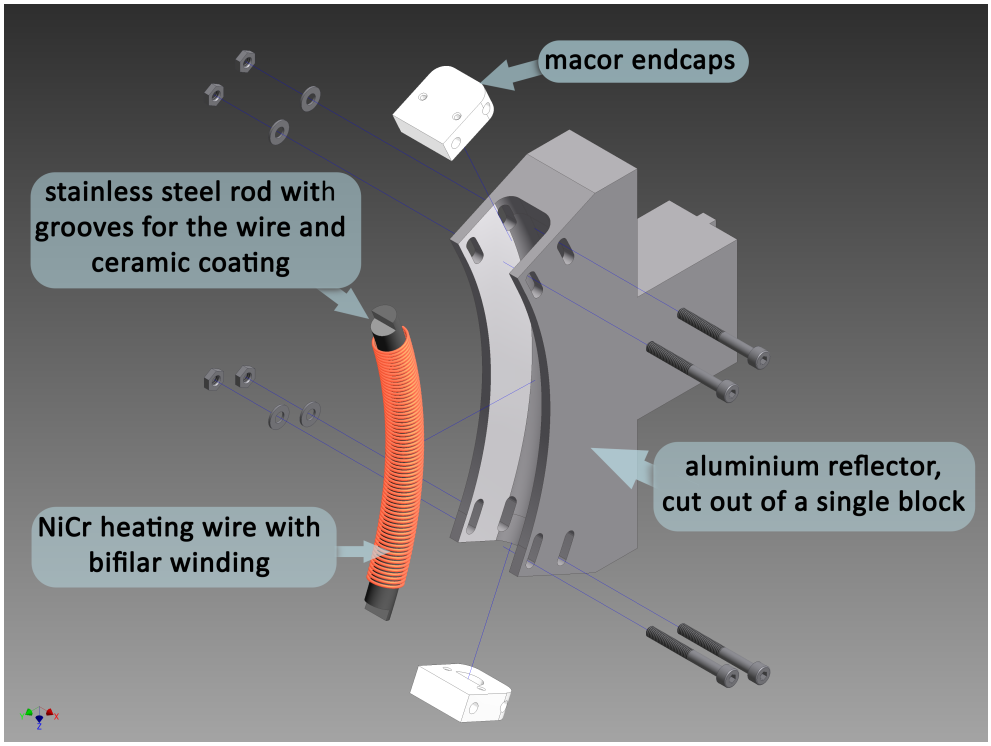

Figure 4.1.: CAD drawing of one of the side heaters [WLA+14].

heaters. Those heaters would be directed towards the sides of the mirror, since they should produce a curvature in the horizontal direction (while the ring heater causes a stronger curvature in the vertical direction, see 3.4). We carried out FEM simulations which confirmed that *side heaters* with a power of several Watts can produce the desired curvature in the mirror.

4.2. Design and construction

The side heaters should use the same fundamental design as the ring heater, which has been running reliably at GEO 600 for over 10 years at the time of writing. While the new heaters still rely on a current-heated metal wire, its design is more advanced in some key aspects. Each of the two side heaters consists of a curved, ceramic-coated, stainless steel rod with grooves for a nichrome (NiCr6015) heating wire with a diameter of 0.5 mm and total length of about 2 m, the resistance has been measured to be 10.8 Ohm. The rod is curved in such a way that when installed, it is concentric with the rim of the mirror. This assures heating the sides of the mirror evenly. Further measures to produce a more uniform heating are grooves which help producing even windings, and the usage of a stainless steel rod. Due to the thermal conductivity of

steel, the whole steel rod acts as heater. The uniformity of the temperature distribution can be judged from figure 4.4; 4.4b shows a thermal image of one of the side heaters (in air), the temperature distribution is much more uniform than in the ring heater (figure 3.14a on p.50).

The NiCr wire is wound onto the rod with a bifilar[2] winding, minimizing the magnetic field that it produces (see figure 4.2a). This is important, because the main mirrors of GEO 600 are suspended as triple pendulums and the upper stage uses coil magnet actuators for damping and alignment [Goß04]. The bifilar winding greatly reduces the magnetic field produced by the heaters, thus reducing the risk of magnetically coupling noise into those actuators.

The coated steel rods are installed into polished aluminum reflectors, which increase the heating efficiency and restrict the thermal radiation to one direction, such that similar problems as with the ring heater are avoided. Small ceramic (Macor) housings provide thermal and electric insulation between the reflector and the steel rods.

The finished assemblies of NiCr wire, coated rod and reflector are then mounted to posts made out of an ITEM ([iIG14]) $30 \times 30\,\mathrm{mm}^2$ aluminum profile, for rigidness and easy adjustment of the height. Figure 4.1 shows a CAD drawing of one of the heaters. The side heaters have been installed at a distance of about 10 cm from the mirror.

4.2.1. Ceramic coating

The stainless steel rod is electrically conducting, therefore it was coated with a $200\,\mu\mathrm{m}$ thick ceramic coating (97% Al_2O_3, 3% TiO_2) for electrical insulation.

Since this is the first time this kind of coating is introduced into the UHV (ultra high vacuum) system of GEO 600, it was necessary to make sure not to contaminate the vacuum system; materials with high out-gassing rates will degrade the high quality optics. We tested the UHV compatibility of the coated rod with our residual gas analyzer (RGA). The RGA is a mass spectrometer (Dycor model LC-D, [AME]) attached to a vacuum chamber under UHV. The UHV still contains traces of gas and the RGA can be used to analyze the residual gas. The (RGA-) mass spectrum of the coated heater rods is shown as orange graph in figure 4.3, while a reference with empty and clean vacuum chamber is shown in green. The amount of long-chain (and therefore high mass) carbohydrates, which are of special concern, is at or below the reference level. The spectrum is only increased (with respect to the reference) at low atomic masses, which indicates water molecules and fragments thereof. We found the coating to be UHV compatible.

4.3. Side heater performance

From the experiments, we find that the side heaters are a good tool to reduce the HOM content at the dark port of GEO 600. For a circulating light power of about 2.5 kW in the PRC and a ring heater power giving the lowest power at the output,

[2] A closely spaced parallel winding, see figure 4.2a for a graphical explanation.

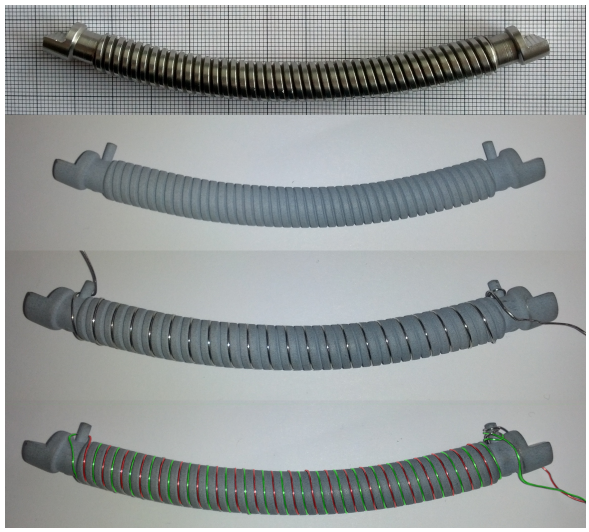

(a) Stainless steel rod

(b) Reflector

Figure 4.2.: Photographs of the reflector (4.2b) and the stainless steel rod for the side heaters at different stages of the construction (4.2a). From top to bottom:
- stainless steel rod, bend and with grooves
- with ceramic coating
- NiCr wire wound halfway
- finished heater rod - the different winding directions have been colored in green and red in the image above.

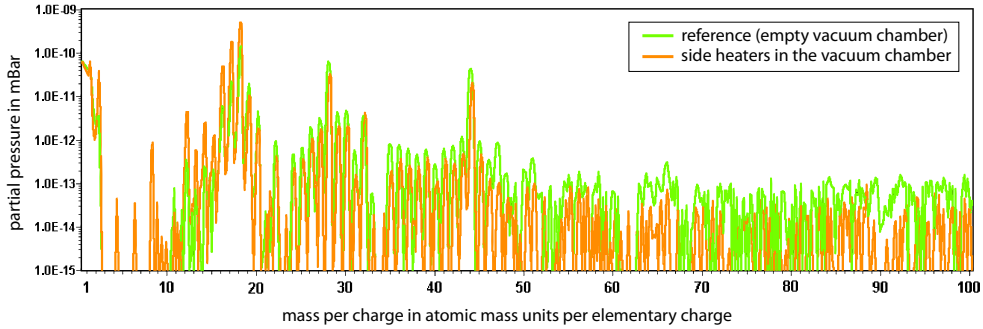

Figure 4.3.: This figure shows the mass spectrum of the residual gas analysis of the ceramic coating for the side heaters. It shows the partial pressures for different atomic masses. The green curve is a reference taken with an empty vacuum tank, while the orange curve shows the spectrum with a coated side heater rod.

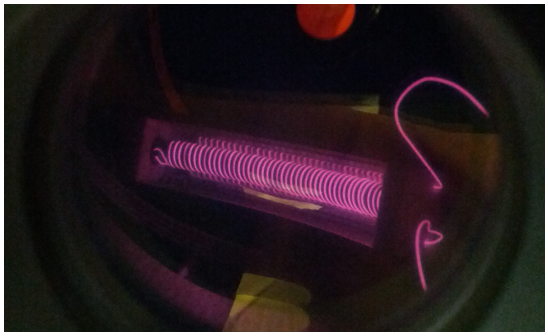

(a) Vacuum bake of one of the side heaters.

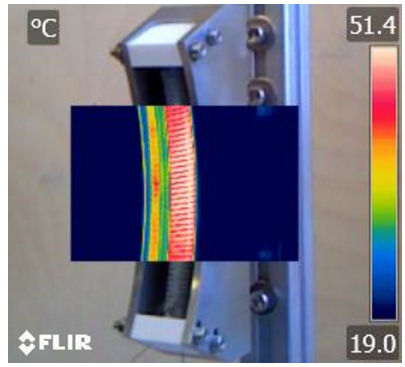

(b) Thermal image (taken with a FLIR E60 thermal imaging camera)

Figure 4.4.: This figure shows the temperatures which the side heaters can reach. The highest temperature was reached during the vacuum bake, the NiCr wire was operated at 70 W and visibly glowing in bright orange. **(a)** shows a photograph. The color reproduction is wrong due to a weak IR filter in the camera. **(b)** shows a thermal image after 2 hours of operation at 2.5 W in air, the hottest point reaches 51.4 °C.

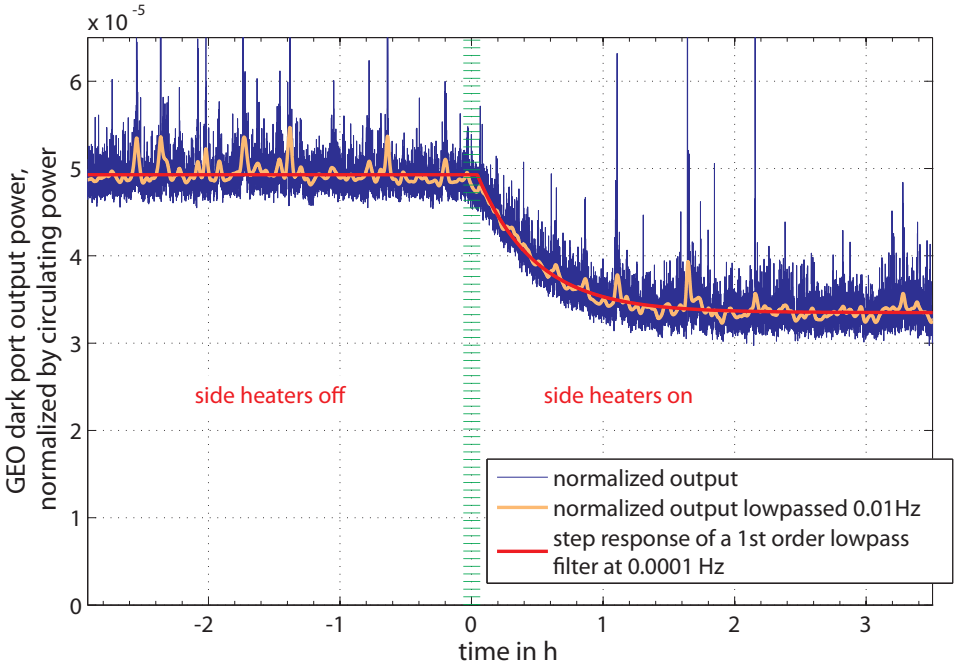

Figure 4.5.: Time series of the normalized power leaving the dark port of GEO 600. At the start of the experiment the side heaters are off, and the ring heater at its default setting. The side heaters are turned on at the time marked as zero hours on the time axis [WLA+14].

the optimal power of the side heaters is 2.5 W each. Subsequent optimization of the ring heater power shows that this is the optimum setting. At this power, the maximal temperature of the side heaters has been measured (in air, see figure 4.4b) to be above 51 °C. While it is hard to predict the life time of the NiCr wire at this temperature, probably it will be not an issue, seeing that the vacuum bake happened at orange glowing (i.e. 900 - 1000 °C) temperatures (see fig.4.4a).

An experiment was performed, in which we let GEO run without the side heaters engaged, then switched the side heaters to the previously determined optimal heating power level. The effect on the normalized power at the dark port is shown as figure 4.5. Moreover, this experiment helps us to determine the time constant of the side heaters. The response of the dark port power can be fitted with a first order lowpass filter with a cutoff frequency of $f = 10^{-4}$ Hz, which gives the time constant of $t = 1/f \approx 2.8$ hours.

Using the side heaters, we can reduce the total power at the output of GEO 600, which is dominated by HOMs, from 55 mW to 37 mW. Since the TEM_{00} light has a power of 6 mW at the dark port of GEO 600, the side heaters reduce the total power of HOMs in GEO 600 by about 37%. We neglect the sidebands of the TEM_{00} mode, which are used to control the interferometer, since their power is negligible, they carry significant power only during lock acquisition (this state is shown in figure 4.7). Another measure of the improvement is the total power at the output *normalized* by the circulating light power in the PRC. By this measure, the *normalized* output power is reduced by 30%.

The improvement from the side heaters is well visible in the beam shape at the output of the interferometer. Figure 4.6 shows CCD camera images of the output beam without and with side heaters, respectively, for both operating modes: PRMI [3] and DRMI[4]. A direct comparison of measured beam shape to simulated beam shapes, as done for the ring heater in fig. 3.13 does not work well for the side heaters. The reason is, that in the case of ring heater only, the order two modes, caused by the ring heater, completely dominated the output beam, whereas the side heaters reduce those modes. The output beam is no longer dominated by modes of order two, but is equally comprised of several HOMs of different orders. Their origin is most likely higher order distortions of the optics of GEO 600, for which we do not have a good model yet, although there have been earlier efforts to simulate the effect of higher order mirror distortions [Pri12, p. 35-40].

When using GEO 600 as power recycled Michelson interferometer (PRMI), the effect of the side heaters is even more pronounced, because there is no mode healing effect of the signal recycling cavity. In PRMI mode, the side heaters reduce the power at the dark port from 54 mW to 30 mW. After normalizing to the circulating light power, this corresponds to a reduction of 50 percent.

In fact, when using the side heaters, the normalized output power of GEO 600 in PRMI mode is the same as in the normal, dual-recycled, operating mode. In other words, using the side heaters, we can match both arms of GEO 600 well enough to each other, that the mode healing effect of the signal recycling cavity becomes negligible,

[3] power recycled Michelson interferometer
[4] dual recycled Michelson interferometer, the normal operating mode of GEO 600.

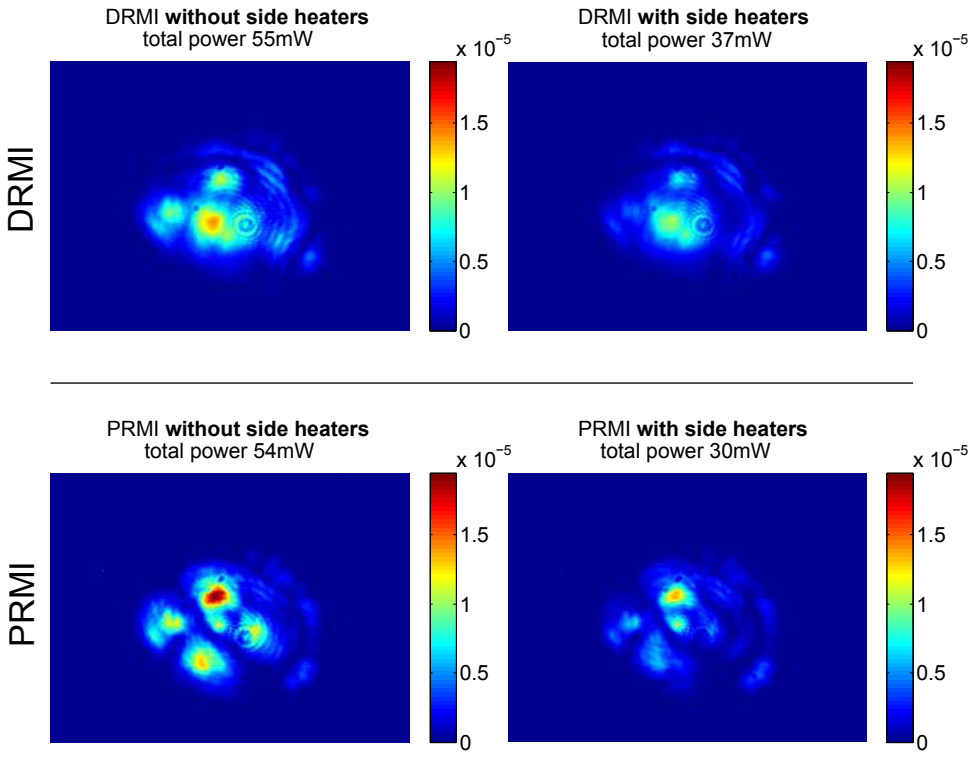

Figure 4.6.: This figure shows calibrated (to Watt per pixel) CCD camera images of the dark port output of GEO 600. In the top row shows the dark port image in normal (DRMI) operation, with and without the side heaters. The bottom row shows the situation in PRMI mode. Especially in PRMI mode, but also in DRMI mode, the lower power in HOMs is apparent [WLA+14].

as there is nothing to 'heal' (in terms of darkport power). This demonstrates that we can ideally match the east mirror to the north mirror in two degrees of freedom.

The output mode cleaner (OMC, see also chapter 7), a small cavity at the output of GEO designed to suppress HOMs, was used to analyze and further quantify the amount of HOMs in the output beam. By scanning the length of the OMC, we can distinguish HOMs of different order (in the Eigenbase of the OMC) from each other; they will be resonant in the OMC at different times (and therefore different OMC lengths) during the OMC scan. Figure 4.7 shows two such OMC scans, one with and one without utilizing the side heaters. It shows that the side heaters reduce mainly the order two HOMs by more than threefold, and order one modes by a factor of 2.5. Table 4.1 gives a more detailed overview.

HOM order	**1**	**2**	**3**	**4**	**5**	**6**	**7**	**8**	**9**	**10**	**11**
power w/o SH (mW)	7.8	16.5	3.3	4.2	1.4	3.7	3.4	1.3	2.2	0.6	0.6
power with SH (mW)	3.1	4.9	1.4	2.5	1.5	2.8	2.6	1.3	1.8	0.6	0.5
ratio	2.5	3.4	2.4	1.7	0.9	1.3	1.3	1	1.3	1	1.2

Table 4.1.: This table shows how the power in HOMs at the output port is influenced by the side heaters. The power in the 6th order modes, which overlap with one of the modulation sidebands was estimated by subtracting the other sideband and assuming both sidebands have the same power.

4.4. Summary

Additional heaters have been installed at the far east mirror MFE, to correct the astigmatism caused by the ring heater.

The design, installation and characterization of those side heaters was discussed in this chapter. They feature a new design, based on a ceramic coated steel rod, with a bifilar wound nickel-chrome wire. The setup of ring and side heaters in GEO 600 is the first realization of a segmented heating system in any gravitational wave detector, and allows to independently change the RoC of the mirror MFE in the horizontal and the vertical direction, and therefore to optimize the contrast of GEO 600.

It is shown, that with the side heaters it is possible to reduce the total power at the darkport, which is dominated by HOMs, by 37%.

The logical extension to this work, i.e. the heating in even more degrees of freedom, is presented in the next chapter. It covers the installation of a matrix of 108 small heaters, which are projected to the beam splitter of GEO 600.

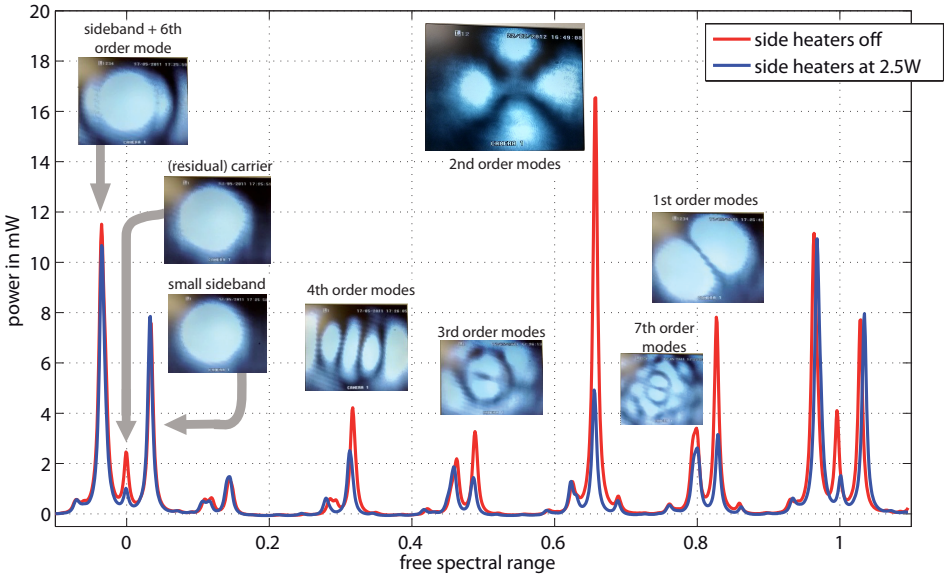

Figure 4.7.: This image shows the signal of the main photodiode during an OMC scan over one free spectral range, once with and once without using the side heaters. Additionally CCD-camera images of the mode shape are shown. Note that the height of carrier and sidebands is not representative for normal science operation of GEO 600; in normal operation, the carrier is kept at a constant height of 6 mW via adjusting the darkfringe offset, and its sidebands are turned down to below one tenth of the plotted values.

CHAPTER 5

Thermal projector for spatial heating of the beam splitter in GEO 600

This chapter provides the logical extension of the work in the previous chapters. As shown before, high order modes (HOMs), especially those created by the thermal lens in the beam splitter (thermal HOMs) can be suppressed by appropriate heating of the mirror MFE. However, it has also been shown that this may introduce practical challenges, for example with co-resonances of HOMs with the $TEM_0 0$ beam at large heating powers. Furthermore, to compensate HOMs that are caused by mirror imperfections, one requires more than the two degrees of freedom than the heater setup of MFE can supply.

The solution to this is presented in this chapter, which details the design and implementation of a spatial heating system at the beam splitter of GEO 600. It consists of an array of 108 small heaters which are projected to the surface of the beam splitter. Furthermore, this thermal projection system can be used for compensating the beam splitter thermal lens at its source, and thus provides a means of mitigating issues when using the MFE heating setup.

5.1. Motivation

It has been shown experimentally and via optical simulations (see chapter 3) that thermally induced HOMs in the power recycling cavity (PRC) of GEO 600 can be compensated via the heaters at MFE. However, this may not work as well for large powers anymore. Also, the darkport of GEO 600 does show HOMs even if there is no thermal lens present, for example right after locking the PRC when the mirrors are still cold, or when using low circulating light power. These 'cold' HOMs are caused

by imperfect mirror surfaces, and scale linearly with the circulating light power in GEO 600. That means that for the final envisaged power increase of a factor of seven for GEO-HF, even with ideal compensation thermal HOMs, we can expect cold HOMs in the order of several hundred milliwatts (around 30 mW of HOMs at the darkport are measured in chapter 4.3, with the currently used light power and ideal compensation of the thermal lens by the MFE heaters), accompanied with all the challenges associated by them (see chapter 2.4).

Due to their nature, the cold HOMs require more degrees of freedom in manipulating the phase of the wavefront than the heater setup at MFE can supply. Therefore, a thermal projection system, consisting of 108 small heaters was developed and installed at the beam splitter of GEO 600 in the course of this work.

Naturally, as the thermal projection system is aimed at the beam splitter, the usage of it for compensating the beam splitter thermal lens and the connected thermal HOMs is investigated as well. While it has been shown in the previous chapters that thermal HOMs can be effectively compensated by the heater setup at the mirror MFE, the thermal projection may be a good alternative and can avoid the potential issues described in 3.

5.2. Cold HOMs in GEO 600

Since the thermal projector can be used for compensating both thermal and cold HOMs, it is useful to determine their relative amount in the darkport of GEO 600.

The amount of HOMs caused by mirror imperfections (cold HOMs) can be measured when the interferometer optics are still cold, i.e. right after bringing the power recycling cavity (PRC) to resonance (this is also called locking the PRC). For this, the PRC was kept off-resonance to allow the optics to cool down, and then locked, once with high, and once with the standard operating power. It takes several minutes until the optics are heated, and the total amount of HOMs at the output of the PRC increases over this time frame. The value of HOMs right after locking the PRC though is assumed to be representative of the cold HOMs[1]. One could think that some of these HOMs are created already on earlier stages of the input optics chain or in the laser itself (which is nearly always running, also during the 'cool down time' in this experiment). However, it can be argued that the two input mode cleaners in front of the PRC will reject a large amount of those HOMs, and furthermore the PRC itself is a high finesse cavity, which by itself will reject most of the HOMs at its input. Therefore it is concluded that the HOMs which leave GEO 600 at the output port are generated in the PRC.

The aforementioned measurement has been performed at GEO 600 to determine the ratio of cold and thermal HOMs at the standard power level. Note that for this experiment the heaters at MFE have been set to a fixed power, to exclude their influence on this measurement (it has been shown in chapter 3 and 4 that the thermal

[1] On very short timescales, HOMs may arise due to misalignment of optics, on average however (and on timescales which are still very short compared to the thermal timescale), the automatic alignment systems keep all optics well aligned.

	circulating laser power	cold HOMs (mW)	total HOMs (mW)	ratio
	2.3 kW	32	36	1.1
	3.5 kW	51	144	2.8
ratio	1.5	1.6	4	

Table 5.1.: Amount of cold and total HOMs at the darkport of GEO 600, measured with a cold interferometer (directly after locking the dual-recycled Michelson interferometer), and a hot interferometer (after reaching thermal equilibrium), respectively. Note that the heaters at the mirror MFE have been set to a fixed setting (which is optimized for the standard operating power of 2.x kW) throughout this experiment.

HOMs can be well compensated by those heaters.). The result is given in table 5.1. From this one can see, that the amount of cold HOMs increases proportionally with the input light power, as expected. This is not true for the total amount of HOMs, where thermal HOMs play a large role. Furthermore, it is apparent that the HOMs at the darkport of GEO 600 are dominated by cold HOMs at the current standard power level, as they make up 90% of the total HOMs at the output port (this is due to the setting of the MFE heaters, which are set to compensate the thermal HOMs at this circulating power level). In contrast to this, the cold HOMs cause only about a third of all HOMs at the darkport at the high power level used here, (when the MFE heaters are not adjusted). The ratio will become even smaller with higher circulating power levels, as indicated in chapter 2.3.2 of this work.

5.3. Spatial heating of optics elsewhere

The challenges associated with mirror imperfections and thermal effects are not unique to GEO 600, they have been experienced at other GWDs [AAA+07], [AAA+09b]. Not only that, but many design aspects which are considered for future GWDs require exceptionally smooth mirror surfaces. Examples of those are the usage of LG_{33} modes [HMY+11], or the usage of marginally stable cavities [GBF+10]. The idea to 'heat away' mirror imperfections, or more precisely to correct distortions in the laser wavefront has been proposed before [LZF+02], but prior to this work only been realized as heating that acts on one degree of freedom (DoF) in GWDs. Examples of this are the ring heater in GEO 600 (see chapter 3) or the CHRoCC system that was used in Virgo [AAA+13], which effectively functions as a ring heater and curves the mirror in one DoF. The difference is that its heat source is a single button heater and that it is directed to the front face of the mirror.

Both LIGO and Virgo [BFL+04] [AAA+11] used CO_2 laser based heating systems for thermal lenses in their input test masses (ITMs) for their Fabry Perot arm cavities. The CO_2 lasers were used to project a static annular heating pattern, which was produced by using masks (in initial LIGO and in advanced LIGO [BCH+15]) or axicons (in enhanced LIGO, [Bro07]).

Spatial heating systems with more degrees of freedom are being developed in the context of advanced Virgo though. Most notably a scanning CO_2 laser sys-

tem [AAA+15b], and one based on an array of small heaters ('CHRACC'), similar to the system presented in this work [DVKM13]. It is possible though that none of those systems with an on-the-fly adjustable heating pattern will be needed and thus may not be used in advanced Virgo [Los15].

Spatial heating of optics outside the field of GWD

Not only the field of GWD benefits from spatial heating of optics; other fields of research are currently investigating spatial heating systems with many DoF. One example of such a spatial heating system can be its use for overcoming challenges in extreme ultraviolet (EUV) lithography which is considered a key technology for further miniaturization of integrated circuits (ICs) [WH10], and therefore making more potent and energy-efficient ICs available. EUV lithography faces the issue, that the projection optics of the lithography system exhibit significant absorption for the used short wavelengths, and cooling them may not suffice to suppress thermal aberrations to the desired level in it. Saathof [SSSMS15] has developed a spatial heating system to counteract those thermal aberrations in EUV lithography. This system is based on an off-the-shelf video projector with an incandescent light bulb, which will project light on a mirror. For this to work, the mirror has to have a special absorptive coating though, which is not a feasible option for the beam splitter of GEO 600.

Another application of thermal projection systems is in the testing of military hardware. 'Thermal scene projectors' (see for example in [SLO+09] or [HGW+07]) are used to project thermal videos of vehicles for the testing of infrared seeking equipment. While these systems seem interesting for use in GWDs on first look, their limited availability, high cost are practical issues. Furthermore, many of these systems focus on producing high temperatures on a chip of small area, which is not suited to the absorption properties of fused silica, which is used in all current GWD[2].

5.4. Spatial heating of the beam splitter

5.4.1. On CO_2 laser based heating

A number of possible ways to realize thermal projection systems have been considered for the installation in GEO 600.

A CO_2 laser based heating projector, similar to the ones used in LIGO/Virgo was considered, however the case of the thermal lens in the beam splitter of GEO 600 is different from how the CO_2 laser systems were used in LIGO and Virgo. Both used the CO_2 lasers to heat the ITMs of their arm cavities for an active wavefront correction. One potential challenge in this is noise introduced by the CO_2 laser. Generally, intensity noise of the CO_2 laser may couple into the GW measurement by changing the optical path length via a thermally-induced change of refractive index (thermo-optics), thermal expansion or thermal stress (as explained in chapter 2.2).

[2] KAGRA - which will use sapphire optics - is considered to be a future GWD in this work.

Additionally, when heating only one face of the optic, the whole optic will deform, which leads to so called 'flexure' noise.

The noise coupling via the thermo-optic effect is attenuated in the case of heating the ITMs of arm cavities, as there is no substrate inside of the comparatively high finesse cavity (but only in the lower-finesse PRC). The advanced versions of LIGO and Virgo will introduce additional compensation plates, which are glass substrates in front of the ITMs, upon which the CO_2 lasers will act. This will move the other ways of noise coupling, i.e. the thermal expansion and the flexure effect, out of the arm cavities and thus reduce their noise coupling into the GW-measurement.

This strategy of moving the thermal actuation out of the highly displacement sensitive cavity is not as straightforward in GEO 600, since it has no arm cavities, but uses a high finesse PRC. The heating of the mirror MFE from the backside (see chapters 3 and 4) is one way to do it, but it may cause practical issues as described in chapter 3.

The noise coupling of thermal actuation on the beam splitter in GEO 600 can be estimated in the same way as it has been done for the ITMs in LIGO in [Bal06, p.65]. It describes the noise coupling of relative intensity noise (RIN) of a thermal actuator to the displacement signal z. Here we will only consider the noise coupling of the $\frac{dn}{dT} = \beta$ effect, which is given as:

$$z = \frac{P_{\text{heat}}}{2\pi f C \rho} \times \frac{O}{\pi \omega^2} \times \beta \times \text{RIN}, \tag{5.1}$$

with the frequency of interest f, the beam size $\omega = 1\,\text{cm}$, the power of the thermal actuation P_{heat} and a spatial overlap factor[3] of the heating pattern and the interferometer beam $O = 1/30$. The other factors specify material parameters of fused silica, namely the specific heat $C = 740\,(\text{J/KgK})$, the density $\rho = 2202\,\text{Kg/m}^3$ and $\beta = 8.5 \cdot 10^{-6}\,1/\text{K}$. Equation 5.1 can also be written as

$$z = 8.8 \times 10^{-13}\,\text{m} \times \left(\frac{P_{\text{heat}}}{10\,\text{W}}\right) \times \left(\frac{1000\,\text{Hz}}{f}\right) \times \text{RIN}, \tag{5.2}$$

which sets an allowable upper limit on the RIN of a thermal actuator. Considering that the current displacement sensitivity of GEO 600 is in the order of $10^{-19}\ \text{m}/\sqrt{\text{Hz}}$ at 1 kHz, the RIN should not exceed a level of about $1\times10^{-7}/\sqrt{\text{Hz}}$ to not spoil the sensitivity of GEO 600. This is better than the RIN of about $10^{-5} - 10^{-6}/\sqrt{\text{Hz}}$ of the CO_2 projector in initial LIGO [Bal06, p.67], and also below the RIN requirement of $4 \times 10^{-7}/\sqrt{\text{Hz}}$ for the CO_2-laser based projector of advanced LIGO [Wil11]. Another point is that the above is based on the current (2015) sensitivity of GEO 600, and does not consider possible improvements, for example due to an increased circulating light power, which would make the requirements even more stringent.

An incoherent thermal source will exhibit a shot-noise-limited RIN [Boy82] at all relevant wavelengths. The RIN is approximated here by choosing the peak wavelength λ_{peak} and therefore peak photon energy of hc/λ_{peak} as representative for the whole

[3] The ideal heating pattern will be determined later in this chapter, for this first estimation we will use the same factor as [Bal06]

Planck spectrum. At a temperature of 800 K and a power P_{heat} of 10 W, the RIN is

$$\mathrm{RIN} = \sqrt{\frac{hc/\lambda_{\mathrm{peak}}}{P_{\mathrm{heat}}}} \approx 8 \times 10^{-11} / \sqrt{\mathrm{Hz}}. \tag{5.3}$$

The thermal source will be heated by a power supply, which may couple in additional noise though. However, the coupling of power fluctuations to temperature changes of the thermal source will exhibit a (single-pole) low pass behavior which will limit their influence at higher frequencies, furthermore it may be possible to use electrical filters to suppress noise from the power supply.

Because of this lower noise performance, it was decided to use an incoherent thermal source over a CO_2 laser for the heating of the beam splitter.

5.4.2. Methods for thermal projection

The commercially available thermal scene projectors have already been discussed above and found to be not suitable due to their high cost and small area.

Micro-mechanical digital mirror devices (DMDs), like the devices sold by Texas instruments [TI], are another possibility to produce a desired spatial light distribution. The available chips are designed for application with visible light though. This is reflected in the glass cover over the chip and the size of the individual mirrors. Any use of a DMD for GEO 600 would require the protective glass cover to be replaced by a far IR-transmitting material, with unknown impact on the micro-mechanical properties of the DMD. A further consideration is the size of the individual mirrors which is comparable to the wavelength of the desired heating radiation, which may produce issues with diffraction.

Another commercially available option would be an array of IR emitters, like the IRPA64 [ELE]. It was decided however, that an in house custom made option would be more customizable for the intended purpose. The design of which was part of this work and is described in the next section.

5.5. Design and characterization of the thermal projection system

The thermal projection system for the beam splitter of GEO 600 consists of three parts: the heater array, an optical system to project the latter onto the beam splitter and electronics to drive and address the individual heaters. Each part is described in detail below.

5.5.1. Heater array

Several prototypes of the heater array have been designed and built in the course of this work (for more information on the prototypes, see chapter A.1.1), before settling on a final design. The final heater array is realized as 108 thin-film platinum

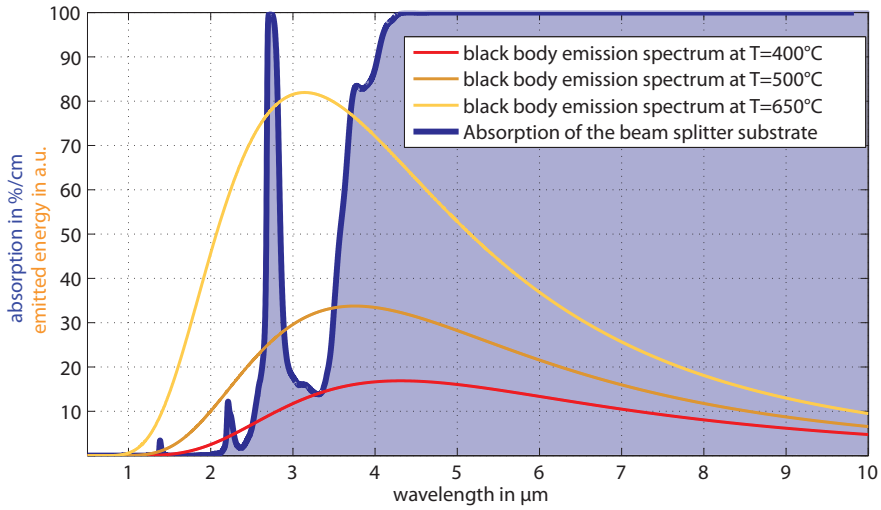

Figure 5.1.: This figure shows the absorption of the beam splitter substrate, and black body emission spectra for different temperatures. The data for the absorption curve is taken from [Herb]. This data reaches only up to the values up to 5 μm, beyond 5 μm data from [KPJ07] was used.

resistors, arranged in a 9x12 grid, which are soldered[4] to a custom circuit board (PCB), as shown in figure 5.2. Additionally, a polished aluminum reflector grill has been fitted around the resistors, which are installed to be standing upright. This way, the radiation from both faces of the resistors can be utilized.

Heaters

The individual heaters that are built into the heater array are commercially available thin-film platinum resistors, originally sold as temperature sensors (usually known as 'Pt100'). The specific model that is used in this work is the model HD421 made by Heraeus [Hera], which houses the platinum film between two ceramic layers.

While commercial micro-heaters were considered to be used for this project, the Pt100 elements do offer several advantages over them for the intended application. Among those are their availability, their cost, the available range of resistances and the easy temperature measurement.

One interesting property of the Pt100 elements is that their resistance changes in a very defined and (mostly) linear way in dependence of their temperature. The Pt100 elements used here show a resistance of 100 Ω at 0 °C, hence their name. Their resistance R at the temperature T (in degrees Celsius) can be approximated as a

[4] The solder joints were checked with the heater array in operation, and it was found that with the standard solder Sn60/Pb38/Cu2, the joints did not melt or soften due to the heaters.

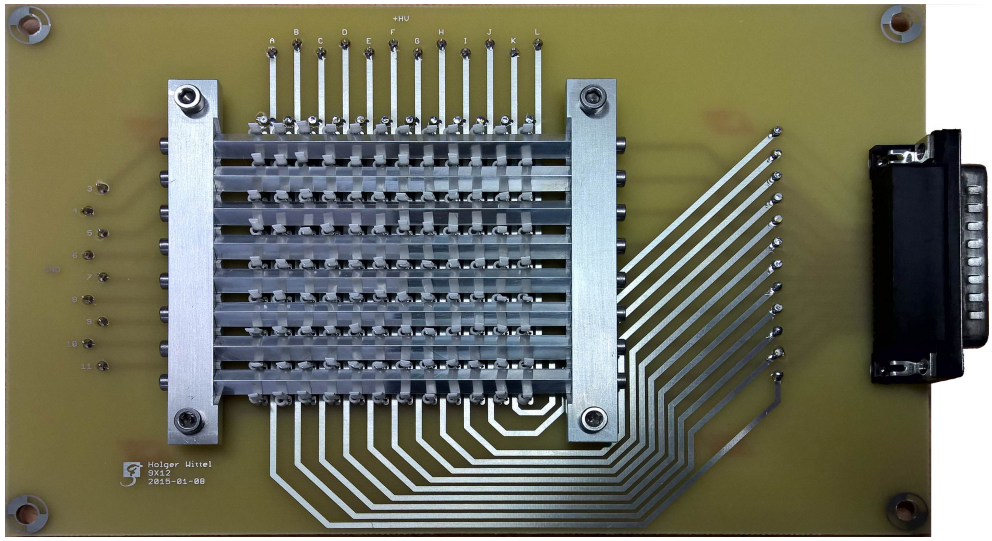

Figure 5.2.: Photograph of the heater array with 9x12 Pt100 elements for the thermal projector.

simple linear model with

$$R(T) = 0.3850\,\Omega/\mathrm{K} \times T + 100\,\Omega, \tag{5.4}$$

The data-sheet [Herc] gives resistance values for temperatures up to 850 °C. Both $R(T)$ curves, from the data-sheet and from the simple model for the Pt100 elements are shown in figure 5.3a. Both curves show a good agreement below temperatures of 400 °C, but even at 800 °C, they only differ by about 10%. Therefore, for simplicity, we will use the simple linear model of the resistance change with temperature for this work. Furthermore, the electrical power to reach a certain temperature has been measured, with the results presented in figure 5.3b. The temperature depends on the electrical power with the fourth power, according to the Stefan-Boltzmann law. Another find is that an electrical power in the order of 2 W is required to reach 650 °C (the relevance of this temperature is shown below).

One concern in the usage of Pt100 elements was their lifetime, while the ones used in this work are rated for temperatures up to 850 °C, this is only valid for use as sensor. When used as heater, their maximum tolerable temperature may be lower. This was tested in two ways.

The first way was to heat several samples for one minute by applying a DC current, then let them cool down to room temperature, and perform an electrical inspection by measuring the resistance at room temperature. Then this procedure would be repeated and the sample would be heated again for one minute, but to a higher temperature, until the Pt100 samples would fail. Figure 5.4 shows a graphical representation of this measurement, which was done with three different types of Pt100

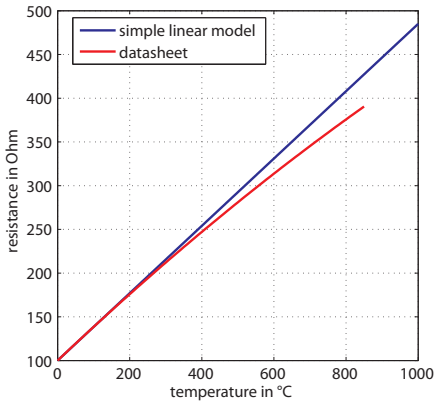

(a) Resistance of the Pt100 elements in dependence of temperature, according to the data-sheet and via a simple linear model.

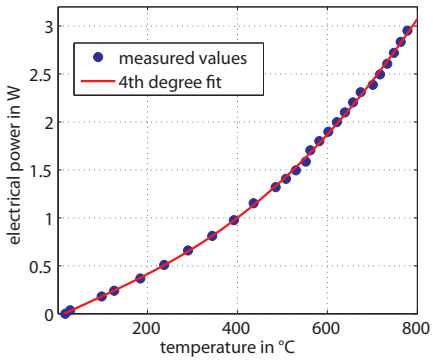

(b) Temperature versus electrical power. As can be seen, the measured values can be well described by a 4th order fit, as predicted by the Stefan-Boltzmann law.

Figure 5.3.: Electrical properties of the Pt100 elements.

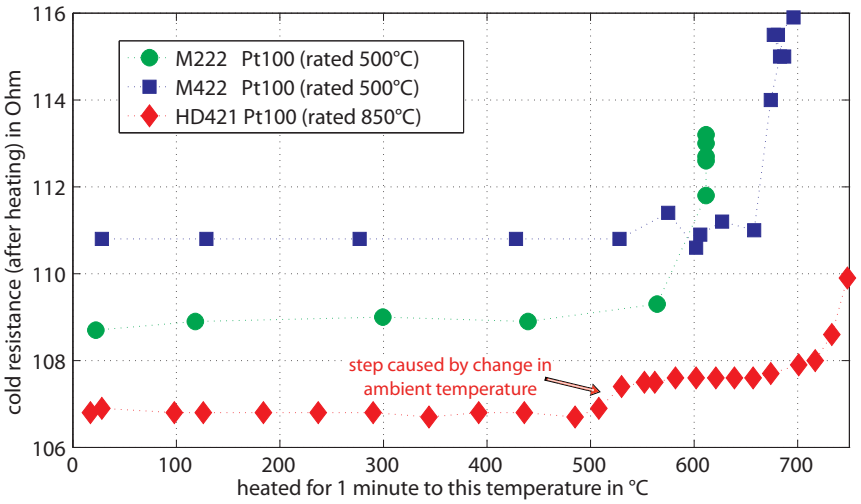

Figure 5.4.: This shows the temperature test of three different types of Pt100 elements. The temperature was determined by the resistance of the Pt100 elements. The slight increase in cold resistance after heating the HD421 above 500 °C was caused by a delay between the measurements, after which the room temperature had changed, which resulted in a different cold resistance (the Pt100 are temperature sensors after all). This is also the explanation of the different starting levels of the cold resistances of the three elements, as each one was tested on a different day with different ambient temperature.

elements. It can be seen, that all three different Pt100 elements show the same behavior, albeit at different temperatures. At lower temperatures, the resistance at room temperature (in the following 'cold resistance') shows no change, but it would rise sharply just before the Pt100 elements failed. And while the failure mechanism is not exactly clear, the change in the cold resistance of the Pt100 elements points to a chemical/mechanical change, and can be used to determine the 'health' of the Pt100s. Furthermore, this measurement points to a maximum safe temperature for using the Pt100 as heaters, namely the highest temperature $T_{\max}$ for which no change in the cold resistance appears. The following $T_{\max}$ values can be determined from the figure above:
- about 550 °C for M222,
- about 600 °C for M422,
- about 650 °C for HD421.

Based on this result, it was decided to use the model HD421 in the heater matrix. Of course, the values for $T_{\max}$ are only valid for the conditions in the experiment, i.e. time scales on the order of minutes of heating.

The second experiment was facilitated to see if there is a long(er) term drift in the cold resistance when the Pt100s are heated for a longer time at a temperature below $T_{\max}$. For this, two HD421 were heated to 500 °C for about 5 hours. And after letting them cool down, their cold resistance was compared with another Pt100 element that has not been heated and no significant difference was found. And while no other long-running specific tests regarding the life time of the Pt100 elements were done, all failures of Pt100 elements during this work could be attributed to intentional overheating or a faulty power supply.

The last property that was investigated was the uniformity of the cold resistance of the heaters that were installed into the heater array. This was done by measuring the resistance of each heater in the array at room temperature with a multimeter, the accuracy of which is assumed to be $\pm 0.05\,\Omega$, which is half of the display accuracy. The result of this measurement is plotted in figure 5.5. Apparently, there is a range of $0.4\,\Omega$ in the measured resistances. Also there is a strong gradient in the measured resistance along the rows of the array, which incidentally was the order in which the Pt100s were measured. It can partly be explained as systematic error, due to a temperature change during the measurements. The room temperature was measured using a Testo 615 thermometer to be 21.4 °C before and 21.7 °C after the measurement, which accounts for a shift in resistance of $(0.385\,\Omega/\mathrm{K}) \times 0.3\,K = 0.12\,\Omega$. That leaves a range of $0.28\,\Omega$ in the Pt100, which could be explained by temperature gradients in the array in the order of 0.7K. The outcome of this measurement is that the individual Pt100 in the heater array are very similar in terms of the cold resistance, and will be considered equal in the course of this work.

Reflector grill

The heater array features an aluminum reflector grill, as can be seen in figure 5.2. Its purpose is to direct the infrared radiation from both sides of the heater into the

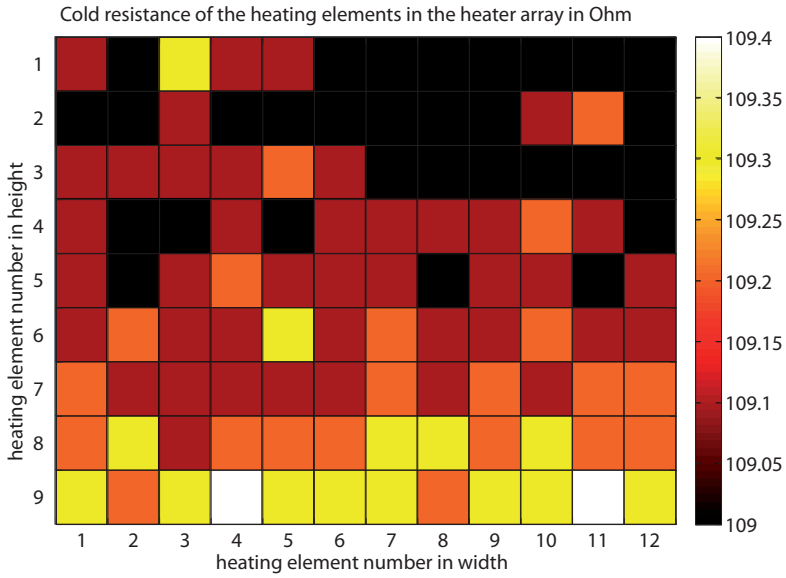

Figure 5.5.: Measurement of the homogeneity of the Pt100 elements in the heater array.

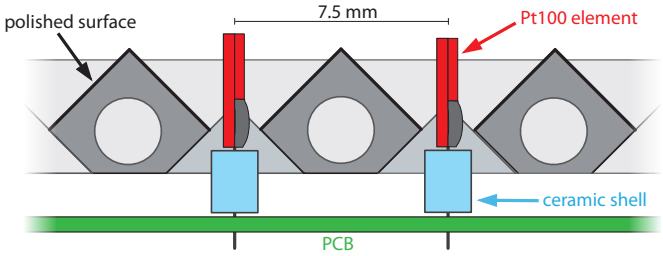

Figure 5.6.: Schematic cross section of the heater array.

optical imaging system, which projects it to the beam splitter.

The hand-polished surfaces of the reflector grill are simply V-shaped, which greatly simplified the manufacturing over a curved reflector design (prototypes with parabolic shapes have been tested, but no clear benefit was apparent[5], see also appendix A.1.1). Furthermore, they can be unbolted separately, which has proven to greatly simplify the assembly process, because of the small opening through which the heaters go. The schematic cross section of the assembled heater array in figure 5.6 makes this clear. Since the reflector grill is electrically conductive, it was decided to fit a ceramic shell over one leg of each heater to avoid short circuits.

[5] The reason for this may be that the reflector is not larger than the heaters, and that the reflector grill is only used to direct infrared light into the actual imaging system.

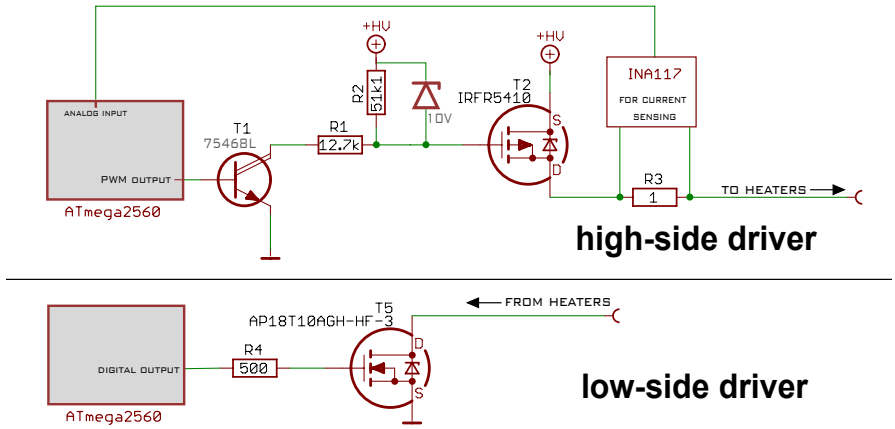

Figure 5.7.: Simplified schematic representation of the high- and low-side driver circuits.

5.5.2. Electronics

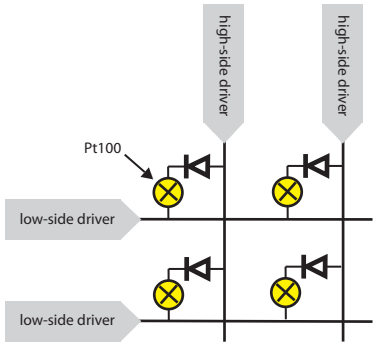

Figure 5.8.: Schematic circuit of a part of the heater array. Diodes on the PCB of the heater array are necessary to suppress cross-coupling between the heaters.

This section describes electronics which have been designed as a part of this work to drive a current through the heaters in the array. Some design goals are that the Pt100 can be independently heated with several different power levels (i.e. more finely than just on/off). This can be achieved with a number of different designs. In the end it was decided to use a multiplexing scheme with field-effect transistors (MOSFETs) as high- and low-side drivers, arranged as pictured in figure 5.7 and 5.8. The high- and the low-side drivers act as switches. The low-side driver is simply an n-channel MOSFET connected to ground. The high-side driver is a bit more complex, due to the usage of a p-channel MOSFET, which requires additional circuitry to shift the micro-controller output (max 5V) to the required gate voltage (80-100 V). Additionally, the high side driver includes a sensing resistor of 1 Ω, the voltage drop on this resistor is read by a micro-controller. This way, the current through each heater can be determined via Ohms law. The current and the applied voltage are known, therefore the resistance of each hot Pt100 element[6] can be deduced, which gives the temperature of each Pt100 via the linear relationship from equation 5.4.

In the multiplexing scheme used here, only one row is connected to ground at a time

[6] Their resistance depends on their temperature, as explained before.

via the low side driver, while the other rows are not connected. The Pt100 elements in this row can now be individually driven by the high side driver. While the high side driver represents a simple switch, it can still be used to adjust the power of the individual heaters via pulse width modulation (PWM)[7].

This usage of multiplexing also means that only one row can be heated at a time. Therefore, in order to reach a certain heating pattern that spans over the whole array, one has to heat one row, then quickly heat the next row and so on. Ideally the switching of rows happens very quickly, at least fast enough such that two heating cycles of the same heater happen in a shorter time span than the thermal time scale (the data sheet [Herc] gives a thermal half-time in moving air (with 2 m/s) of 3.3 seconds). With the current design, the line frequency is limited by the high-side driver, where the gate capacitance of the p-channel transistor and the 12.7K resistor build an RC-lowpass with a cutoff frequency of $f = 1/(2\pi RC) \approx 16\,\mathrm{kHz}$. In principle, this switching could be made faster by using a dedicated MOSFET driver IC.

Furthermore, due to the low duty cycle, each of the heaters needs to be driven stronger than if it were operated at DC to reach the same temperature. All electronic components have been dimensioned to withstand at least 100 V to allow for this overdriving.

Electrical coupling to the GW strain sensitivity is always a concern for electronics in GWD, and especially in this case, since the multiplexing scheme is equivalent to quickly switching significant amounts of electric power. Several precautions have been done to mitigate this potential issue, like putting the high and low-side drivers into a shielded electronic box and using shielded cables. Moreover, the electrical cross-coupling has been checked at all stages of the development of the thermal projector, using the prototypes shown in appendix A.1.1. No electrical cross-coupling has been found.

An Arduino micro-controller board (Ardiuno Mega ADK [Ard]), which features an Atmel ATMega2560 micro-controller with external oscillator, is used to control the high- and low-side drivers and to generate a specific heating pattern in this way.

5.5.3. Optical system

This section describes the optical imaging system, which is used to project the heater array to the beam splitter face.

The imaging system is entirely situated outside of the vacuum system, shining IR radiation through a ZnSe viewport[8], which greatly simplifies its handling, but on the other hand restricts the possible power density on the beam splitter (as explained later).

The imaging system of the thermal projector has been designed to fit with both anticipated use cases of the thermal projector, i.e. for compensating cold HOMs and for compensating thermal HOMs.

[7] PWM uses a high frequency square wave (i.e. on/off) signal, the duty cycle of which is adjusted to change the heater temperature.

[8] ZnSe is transparent for a wide band of IR radiation, and the viewport used at GEO 600 has a broadband IR anti-reflective coating.

Requirements for compensating thermal HOMs are given by the simulations in [Wit09, p.39, p.67] already, which assumes a power of 7.5 W absorbed in the BS over an area[9] of about 140 cm^2, leading to a power density of 0.05 W/cm^2. Since the heater array has dimensions of 60×55 mm, the optical system has to provide a magnification factor of 2.5 for the projection to reach the aforementioned dimensions.

If one assumes a power of 1 W per heater[10] for the whole array, spread over an area with 2.5 times the size (in linear dimensions) of the heater array, one gets the achievable power density P_{dens} of

$$P_{\mathrm{dens}} = \frac{108\,\mathrm{W}}{2.5^2 \times (6 \times 5.5)\,\mathrm{cm}^2} \approx 0.5\,\mathrm{W/cm}^2, \tag{5.5}$$

which, together with simulated value from above, sets a limit for the required power transmission of the optical system in the order of 10%.

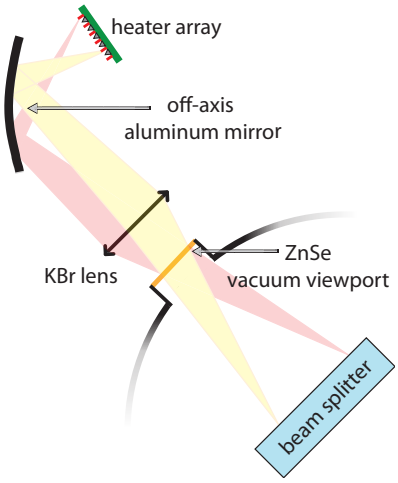

Figure 5.9.: Schematic illustration of the imaging system (not to scale).

The imaging system was designed to make it possible to adjust the magnification factor from 1.8 to 2.5 (depending on the position of the lens) using the well known ABCD matrix formalism [Sie86, p.581ff]. It is realized by two optical elements, an off-axis mirror and an IR transmissive lens, both are located outside of the vacuum system of GEO 600, and project an image of the heater array through an IR transmissive ZnSe vacuum window on the beam splitter. Both optical elements have been custom made, since they require large usable apertures (diameter >10 cm) which are not available as off-the-shelf components. The off-axis mirror was designed as an off-axis section of a paraboloid, such that it can be used to fold the imaging system (which is necessary due to space constraints). It was milled from an aluminum piece with a ball cutter by the company [Rum] to have an apparent focal length of 590 mm for an angle of 80 degree[11]. It was subsequently polished in the workshop of the AEI. The other part of the imaging system is a KBr[12] lens (KBr is IR transmissive) with a focal length of 450 mm at 4 μm.

[9] The source assumes an elliptical, annular heating pattern with a varying outer radius of 6.5-7.5 cm, (for the area calculation we assume a constant 7 cm) and an inner radius of about 2 cm

[10] Which will result in a heater temperature of 400°C according to figure 5.3b. The emission peak at this temperature is at 4.3 μm (predicted by Wien's law), therefore it will be assumed that all IR radiation will be absorbed by the beam splitter at this temperature (the reader is referred to figure 5.1, which plots black body emission curves and the absorption of the beam splitter). In principle it is possible to further increase the heater temperature. Even though this will lead to some power being transmitted through the beam splitter, the total absorbed power will increase as well.

[11] The parent paraboloid of which this mirror is a section has a focal length of 352 mm.

[12] The lens was made by [Kor].

Figure 5.9 shows a schematic illustration of the optical system.

It is apparent that the opening angle, and therefore the power transmission, of the optical system is limited by the opening angle defined by the vacuum viewport and the beam splitter.

The following presents an estimation of the power transmission through the optical system, using the entendue. The etendue (sometimes called acceptance or throughput) of an ideal optical system is preserved, and can only ever increase for any non-ideal optical system. It is defined as the product of opening angle of the ray bundles and the area of the source (or the image of it).

As mentioned before, the etendue of the imaging system is restricted by the vacuum window. The two dimensional opening half-angle α_{output} of the ray bundle on the beam splitter is defined by the radius r_V of the vacuum viewport and the distance d_{BS-V} between the beam splitter and the viewport:

$$\alpha_{\text{output}} = \arctan\left(\frac{r_V}{d_{BS-V}}\right) = \arctan\left(\frac{45\,\text{mm}}{600\,\text{mm}}\right) \approx 4.3°. \tag{5.6}$$

The etendue e_{output} of the imaging system is constrained by this angle and the magnification factor M_{output}:

$$e_{\text{output}} = M_{\text{output}} \times \alpha_{\text{output}}. \tag{5.7}$$

With this, one can easily compute the opening half-angle on the input (at the heater array) side:

$$e_{\text{output}} = M_{\text{output}} \times \alpha_{\text{output}} = e_{\text{input}} = 1 \times \alpha_{\text{input}}. \tag{5.8}$$

Which leads to an input acceptance half-angle of $\alpha_{\text{input}} = 10.75°$ for a magnification factor of 2.5, and an $\alpha_{\text{input}} = 8.6°$ for a magnification of 2. This can be used to compute the fraction of power that is radiated by the Pt100 elements within this acceptance angle, using Lambert's cosine law (and going to a solid angle):

$$\left(\frac{\int_0^{\alpha_{\text{input}}} \cos(\alpha)\,\mathrm{d}\alpha}{\int_0^{90°} \cos(\alpha)\,\mathrm{d}\alpha}\right)^2. \tag{5.9}$$

Which gives only about 3.6% for an angle $\alpha_{\text{input}} = 10.75°$, about three times less than the requirement set above by equation 5.5. A way to greatly improve the power transmission of the optical system is presented in section 5.8, but would require to open the vacuum system and install optics in there. As this is the first installation of this kind of system in any of the GWDs, it is useful though to test the system even with a lower power transmission. With all optics outside of the vacuum system, some flexibility in the choosing the magnification factor is retained for example.

Due to losses from the reflector grill, it may be needed to operate the heaters at a higher temperature than the 400 °C which were assumed for eq. 5.5. This should not pose an issue though, since it was shown in section 5.5.1 that Pt100 can be operated up to 650 °C when used as heaters.

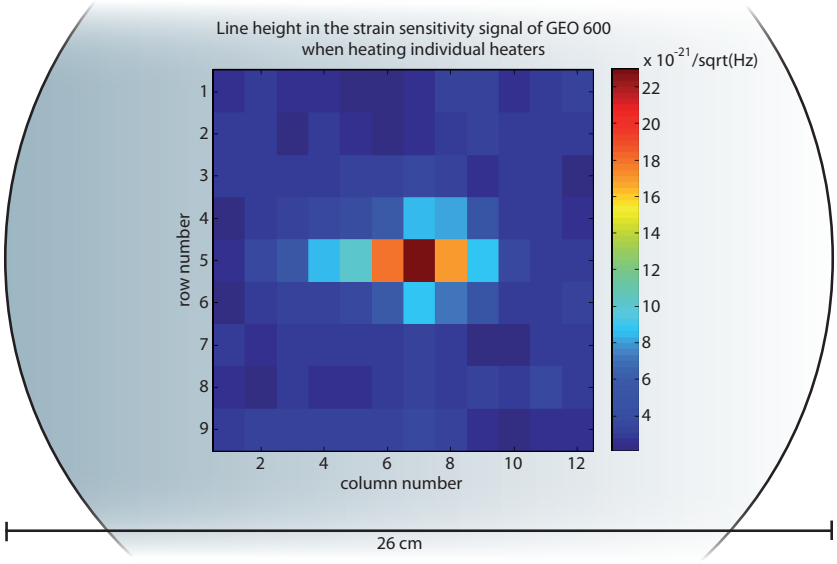

Figure 5.10.: Measurement of the interferometer response in terms of line height (at the heater array line frequency of 120 Hz) in the strain sensitivity, when heating the Pt100 individually. For scale, the outline of the beam splitter is included in the background. The heater matrix was projected with a magnification factor of two in this measurement.

In practice it was shown, that a magnification factor of two is preferable, in which case one gets a transmission of 2.25% of the optical system. Still the power density, i.e. power per area, will be similar in this case, since the power is distributed on an area which is smaller by a factor of $2.5^2/2^2 = 1.6$.

5.6. Measurement, modeling and results

5.6.1. Alignment

The heater array is aligned to the laser beam in the beam splitter in two steps. First, if necessary, a coarse alignment is done via one of the prototype heater arrays, which has two laser diodes on it. The array is aligned such that the beams of the laser diodes hit the vacuum viewport through the optical system. Once the coarse alignment is complete, the final heater array is swapped in place.

The second step is the fine-alignment. It works by modulating individual heaters and observing the response of the interferometer differential arm length (strain sensitivity) signal. For this work, the heater at the (x,y)-position (7,5) of the 12x9 array is picked as central heater[13]. Its naturally modulated by the way of its multiplexed

[13] The reason for picking this heater over the one at position (6,5) is the angle of the beam in the beam splitter.

driving with one ninth of the line frequency of the heater array. With proper coarse alignment, this modulation signal will be visible in the strain sensitivity signal of GEO 600. The heater array can then be aligned in such a way that this signal is maximized - at this position the image of the central heater on the beam splitter will have the maximal overlap with the main laser beam in GEO 600.

To further refine the alignment, the resulting modulation responses of the strain sensitivity signal of GEO 600 can be recorded for further pixels as well, which allows a mapping of the main laser beam of GEO 600. Figure 5.10 shows the result of such a measurement. The main uncertainty in this measurement is originated from the slightly varying level of the strain sensitivity measurement, which is always present. We estimate this uncertainty by the standard deviation of the out-most 'pixels', i.e. along the edges, in fig. 5.10. In this measurement points, we expect no or only very little direct influence of the heating on the main beam. By doing this, a standard deviation of 0.36×10^{-21} /sqrt(Hz) is found and assumed to be the uncertainty in this measurement.

Furthermore this measurement shows that the resulting line in the strain sensitivity of GEO 600 is caused by the dn/dT effect, and not by electrical coupling or radiation pressure, because if that were the case the mapping of the beam would not be possible in this way.

5.6.2. Model of the projection

As in previous chapters, modeling plays a crucial role in the understanding of the underlying system.

A simple model of the projection on the beam splitter was created with Matlab [Mat], with the goal of recreating the measurement from figure 5.10, to check if the projection of the beaters to the beam splitter works as expected. The model is rather simple, the complete code is provided in listing 5.1. It uses only the physical dimensions of the heater matrix, the beam size at the beam splitter and the magnification factor of the optical system, the latter has been slightly adjusted to match the measurement.

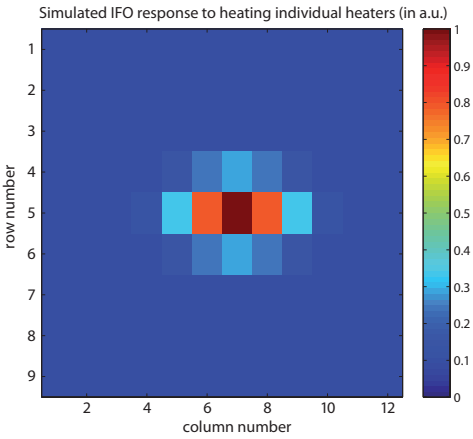

Figure 5.11.: Simulation of heater alignment

The output of this model is given as figure 5.11, and it can be compared to the measurement in figure 5.10. While the reproduction via the model is not perfect, it is still in good agreement with the measurement.

Listing 5.1: Matlab model of the matrix heater projection

```
%% Simulate mapping of TEM_00 beam to the heater matrix
%% March 2015 - Holger Wittel

%% parameters
wy=10;          %beam size in mm (vertical)
wx=10/cosd(45); %beam size in mm (horizontal)

magnification=1.7; %magnification of the imaging system
%-------------------------------------------------------
%% create a grid of the 9x12 heaters
heater_pitch_x=5;   %distance between the heaters in mm (horizontal)
heater_pitch_y=7.5; %distance between the heaters in mm (vertical)

x=-6:5;     %define the 12 heaters in x-axis (horizontal)
y=-4:4;     %define the 9  heaters in y-axis (vertical)
x=x*heater_pitch_x*magnification;   %scale to mm on the BS
y=y*heater_pitch_y*magnification;   %scale to mm on the BS

[X,Y]=meshgrid(x,y);    %produce a grid of the images of the heaters on
    the BS
%-------------------------------------------------------
%% make TEM00 amplitude projection
TEM00=exp(-((X.^2)/wx.^2) -((Y.^2)/wy.^2)); %TEM00 beam [a.u.]
imagesc(TEM00 +0.1)   %display the result, add background of 10% of the
    maximum value
caxis([0 1])
colorbar
xlabel('column number')
ylabel('row number')
title('Simulated IFO response to heating individual heaters (in a.u.)')
```

5.6.3. Heating pattern optimization & results

While the many DoFs offered by the thermal projection system offer many possibilities to fine tune the heating pattern, they also pose the challenge of simultaneously optimizing them. An approach of optimizing the thermal projection is done in this work, which does not require any a priori knowledge of either the mirror surfaces or the thermal state of the interferometer. This method was applied in two cases. In the first at the standard operating power of about 2 kW in the PRC, to which the ring- and side heaters have been optimized, and therefore the heating should only affect the cold HOMs. In the second case, the thermal projection was applied to a higher power state, with 3.2 kW circulating in the PRC, but with leaving the ring- and side heater settings unchanged. This way, the hot HOMs dominate the darkport and the influence of the thermal projection on them can be estimated.

Guessing

Before any systematic optimization takes place, it is worthwhile to try guessing the right compensation pattern. And while this method is not expected to result in the ideal projection pattern, succeeding to reduce HOMs by guessing an actuation pattern can signal a basic understanding of the system, and lay a foundation for

further optimization. The best guesses achieve a reduction in the order of 10% of the HOMs in the standard power state, by projecting a heating pattern that is derived from a Hermite-Gauss$_{02}$ (HG_{02}) mode onto the beam splitter. This heating pattern consists only of the side lobes of a HG_{02} mode, and its size and the positioning are matched to the beam parameters of the main laser beam of GEO 600. Figure 5.12 shows the spatial distribution of this pattern. A more exact representation of a HG_{02} shaped heating pattern with positive and negative heating via the introduction of a bias was also tried, but yielded worse results.

At the higher power state, the HG_{02}-shaped best guess mentioned above leads to a reduction of only about 5% of total HOMs at the darkport, which is only a quarter of the performance at low power. Incidentally, in the higher power state, the cold, i.e. not-thermally induced HOMs, make up about one quarter of the total darkport power, as seen in table 5.1. Therefore it may be concluded that this heating pattern affects mostly the cold HOMs. The best guess for the a heating pattern for the higher power state is an annulus shaped heating pattern, which can reduce the total power of HOMs at the darkport by 10%. The exact spatial profile of this heating pattern is shown in figure 5.12.

Actuation matrix

A standard technique that is used to relate an actuator basis to a different sensing basis is the usage of an actuation matrix. While there is no 'right' basis system for the thermal actuation, some basis systems are preferred for practical reasons. Due to the large number of DoFs and the long timescale of thermal experiments, compared to most other measurements at GWDs, it is beneficial to use a basis system which will deliver good results with a limited set of basis vectors, thus effectively reducing the number of DoFs.

A natural basis system for sensing the HOMs at the output port are the HG modes. For this, the beam at the darkport is considered as a linear superposition of HG modes, which can be expressed as a vector $\vec{dp}$.

However, for practical reasons, the sensing basis is modified to contain not the individual HG modes as elements. Instead each element represents the power of all modes of a particular order, starting from order two. The vector $\vec{dp}$ will have the elements $\vec{dp} = (x_2, x_3, ...x_n)$, where x_n denotes the power of all HOMs of order n. This particular choice of $\vec{dp}$ is motivated by the fact that the individual elements x_n can be easily measured by scanning the length of the output mode cleaner (OMC, see chapter 7) of GEO 600. Furthermore, the power of the fundamental mode and the first order mode HOMs in the output beam of GEO 600 are actively controlled in GEO 600, and therefore not useful as sensor for use with the thermal projector.

One weakness of this approach is that the individual modes of a certain order could be influenced differently by the same heating pattern, and thus their combined power may give misleading information of the effectiveness of the thermal projection. However, the HOM orders with the largest power are usually of orders 2,6,7, and sometimes[14] 8 (see for example figure 7.7 on page 126). Of those, the modes 2,6, and

[14] This has been observed to vary, it may be connected to thermal state of various components and

8 are dominated by a single HG-mode. This is verified by investigation of camera images of the beam profile in transmission of the OMC, when its length is set to be resonant for modes of this certain order.

For the actuation basis it is beneficial to select a basis which has a large overlap with the sensing basis. This may allow to get a good compensation without having to utilize all of the DoFs. One obvious choice are HG-shaped heating patterns. Since the HG polynomials have both positive and negative values, it was attempted to introduce a bias in the heating pattern to allow for negative heating. This did not prove to be fruitful however, a uniform bias heating with the thermal projector proved to increase the power of HOMs at the darkport of GEO 600. The ultimate reason for this is not clear, it may be due to a gap between the individual heaters, which leads to a not completely uniform heating distribution on the beam splitter. Instead, the positive parts and the negative parts of each HG mode are heated separately.

Any heating pattern is expressed as a vector $\vec{h}$ with the aforementioned basis vectors.

The actuation matrix $\hat{M}$ is then measured by heating in the individual basis vectors of $\vec{h}$. For this, the vector $\vec{\mathrm{dp}}$ containing the HOMs at the darkport is separated into a vector $\vec{\mathrm{dp}}_0$ that contains the HOMs when no heating is present and a vector $\vec{\mathrm{dp}}_{\mathrm{heat}}$ that is measured when heating the beam splitter:

$$\vec{\mathrm{dp}}_{\mathrm{heat}} = \hat{M} \cdot \vec{h} + \vec{\mathrm{dp}}_0. \tag{5.10}$$

The desired heating pattern to achieve a certain HOM distribution at the dark port can be obtained via inverting $\hat{M}$:

$$\vec{h} = \hat{M}^{-1} \cdot (\vec{\mathrm{dp}}_{\mathrm{heat}} - \vec{\mathrm{dp}}_0). \tag{5.11}$$

A graphical representation of $\hat{M}$ is given in A.1.2. Due to the choice of the basis, the matrix $\hat{M}$ is not square, the system of linear equations that it represents is overdetermined. Together with its nature of being derived from measurements, it is not exactly solvable, i.e. invertible. Therefore a least squares approximation of the inverse is used, which has been obtained with the MATLAB *pinv()* command.

The actuation matrix formalism from above is used to create spatial heating profiles to counteract HOMs in the darkport of GEO 600, several heating profiles have been tested. Among them a spatial heating profile to reduce second order modes at the darkport of GEO 600, one to reduce HOMs of the orders 2,7 and 8, and a heating profile to reduce all HOMs from orders two to nine. The reason for this arrangement is that HOMs of second order are the most prominent in the darkport of GEO 600. Furthermore the output of GEO 600 in the modes of orders seven and eight is dominated by a single HG mode in each case, according to camera images of the beam in transmission of the OMC.

A measurement of the power at the dakport of GEO 600 while those heating profiles are applied via the thermal projector is given in figure 5.13. One finding from the displayed measurement is that the heating profile to minimize all HOMs at the darkport

alignment of optics.

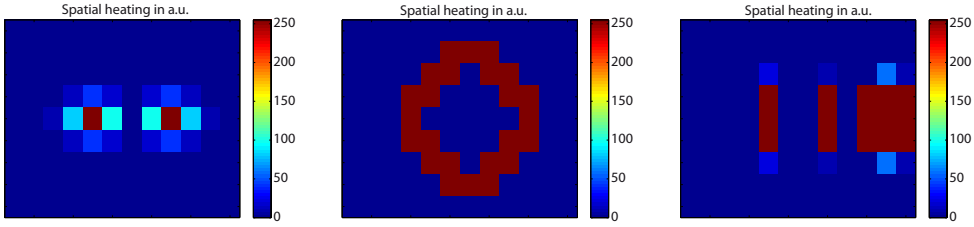

Figure 5.12.: Spatial heating profiles used for the thermal projector. A HG_{02}-inspired heating profile is shown on the left. The center image represents the best obtained annular heating profile, and the right hand image was obtained via the actuation matrix formalism.

of GEO 600 (cyan, at slightly before 1.5 hours in fig 5.13) does not work well. This is expected, when considering that in this case the actuation matrix method will only work when the HOMs of the to-be-reduced order are dominated by a single mode, as explained above. This is however not the case for HOMs of all orders from two to nine, hence the small impact of this heating profile.

The best reduction of HOMs at the darkport of GEO 600, at both the standard and the higher circulating laser power state, was achieved by a combination of the annular pattern and the spatial heating profile obtained by the actuation matrix formalism to reduce second order modes. With this, a reduction of the HOMs at the darkport of 31% in the standard power state, and 24% in the high power state is obtained.

5.7. Sensitivity

The impact of using the thermal projection system on the strain sensitivity of GEO 600 has been measured by simply comparing a stretch of data with heating of the beam splitter to a reference time without heating of the beam splitter. It is expected that the choice of heating pattern will have an influence on the noise coupling. A larger overlap of heating pattern with the laser beam would lead to a higher coupling, as can be seen by the overlap factor in equation 5.1. Figure 5.14 shows the resulting strain sensitivity spectra of GEO 600 for an annular heating pattern (top) and for the heating pattern with the largest reduction in HOMs (a combination of annular pattern and the result from the actuation matrix, at the bottom of fig. 5.14). Both spectra are plotted on a reference sensitivity spectrum without heating. It can be seen that neither affects the sensitivity above 250 Hz, but both have narrow band influence, resulting in peaks in the spectra, most likely due to the multiplexed driving. While we see some peaks in the sensitivity due to the heating, it should be kept in mind that the multiplexing frequency can be shifted up or down and this will move the resulting peaks as well. The multiplexing frequency has not been optimized (for example for best sensitivity) for this measurement.

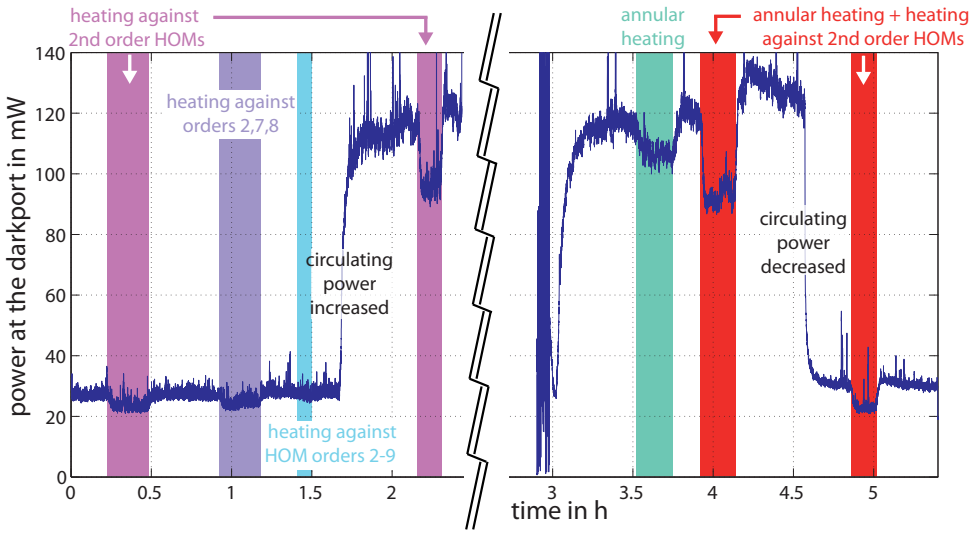

Figure 5.13.: Measurement of the power at the darkport of GEO 600 while projecting different heating patterns with the thermal projector onto the beam splitter. The time during which the thermal projection was active are colored. Note that this measurement was performed without the usual offset from the dark fringe and with the TEM_{00} control sidebands greatly reduced. This way the power in the fundamental mode at the darkport of GEO 600 is reduced as much as possible and HOMs dominate the darkport power. Also note that the plot shows two separate measurement times, as indicated by the zig-zag line. For simplicity however the data is treated as a continuous time series here.
The circulating laser power in GEO 600 is raised to the high power state from 1.6 to 4.5 hours, which explains the increased power at the darkport.

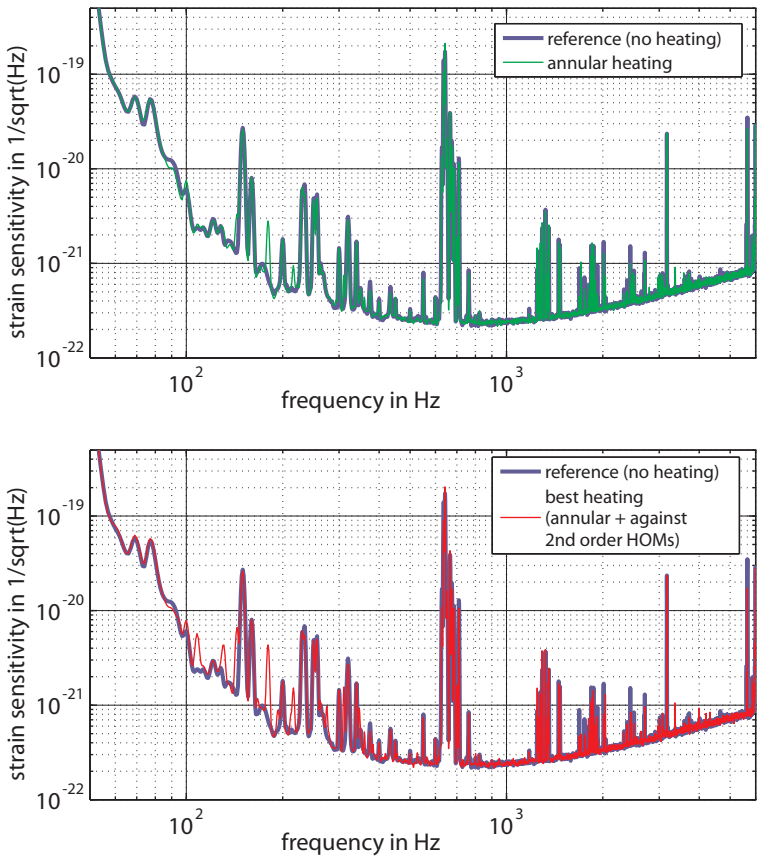

Figure 5.14.: Strain sensitivity of GEO 600 with thermal projection on the beam splitter, for an annular heating (top), and the best obtained heating profile (bottom).

5.8. Outlook

The thermal projection system would benefit from an increased heating power, as it is shown by the estimation in 5.5.3. Another indication for the need for more heating power are the measurements in the previous section. One would assume that it should be possible to 'overheat', i.e. when the heating power of the thermal projector is increased it should be possible to find an optimum power, at which the HOMs at the darkport are at a minimum, and the HOMs at the darkport would get worse by any further increase of the heating power. With the presented setup though, the thermal projector operates only on one side of the optimum. Thus the measurements above show the are taken with the full power of the thermal projector.

The heating power of the thermal projection system can be increased in three ways. Namely by operating the heaters at a higher temperature, increasing the area of the heaters or using more of them, or by changing the optical system. The latter is the clearly preferred solution.

An increase in heater temperature would be limited to the maximal tolerable temperature of the heaters, as determined in section 5.5.1. Even if this was not an issue, once the maximum of the radiated black body spectrum of the heaters passes the lower absorption edge of the beam splitter (at about 500° C - 600° C, see figure 5.1), any further temperature increases will only deliver a diminishing additional heating of the beam splitter.

It may be possible to use more heaters, packed more densely. However, more than a factor of 1.5 to 2 increase in heater density per area is not deemed realistic. A change in the imaging system will return in a larger improvement.

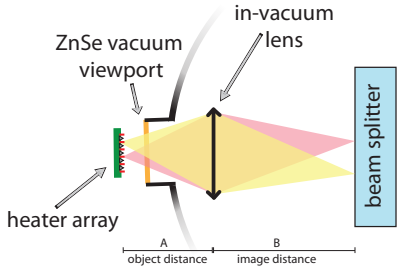

Figure 5.15.: Illustration (not to scale) of the proposed in-vacuum lens setup for an increased power transmission of the thermal projector.

As shown above, the imaging system, and more precisely the angle spanned by viewport and beam splitter surface, is severely limiting the power transfer from heater array to the beam splitter. One easy way to overcome this limitation is to place optical components into the vacuum chamber with the beam splitter.

One possible way would be a projection system consisting of a single IR transmissive lens (for example made of ZnSe) in the vacuum chamber, while the heater array would be still situated outside of the vacuum chamber, but in close to the vacuum viewport. A possible realization of this setup is outlined in the following, figure 5.15 shows a schematic illustration of the proposed setup.

Since the magnification factor M of the current system has been proven to be useful, the new setup should keep approximately the same magnification. This defines the posi-

tion of the lens through the ratio of image distance B and object distance A:

$$M = B/A. \tag{5.12}$$

For a total distance between the beams splitter's surface and the heater array of $A + B = 700\,\text{mm}$, and a desired M of 1.8, the resulting image distance B is 450 mm and the object distance A is 250 mm.

The needed focal length f of the lens can be determined by the thin lens formula:

$$\frac{1}{A} + \frac{1}{B} = \frac{1}{f}, \tag{5.13}$$

which returns a desired focal length of about 160 mm. The power transmission of the proposed setup can be compared to the current system, for example by comparing the etendue of both systems, defined by the solid angle at the output side of the system. The magnification of both systems is approximately the same and can therefore be discarded in this comparison.

The current system is limited by the solid angle on the image-side, defined by the viewport and the beam splitter. The two dimensional half-angle has been determined to be 4.3°, or a solid angle[15] of 18.5 $(°)^2$. The output angle (on the image side) of the proposed system will depend on the diameter of the lens which is used. With a diameter of 150 mm[16], the result is an image-sided two dimensional angle of $\arctan(75\,\text{mm}/450\,\text{mm}) \approx 9.5°$, or a solid angle of 90 $(°)^2$ which is nearly a factor of five more, and would fulfill the requirement set in equation 5.5.

Another measure that could be taken is to use as zero-length flange adapter to mount the vacuum viewport onto the vacuum chamber, instead of the currently used tubular flange adapter. This could further reduce the distance, and thus increase the angle between the viewport and the beam splitter.

5.9. Summary

Thermal effects and imperfections in the optics are major sources of HOMs in GWDs. To correct for this, a thermal projection system is developed for use on the beam splitter of GEO 600. It consists of an array of 9x12 thin film platinum resistors, which are projected on the beam splitter's partly reflective face through an IR transmissive viewport in the vacuum chamber.

The thermal projector is characterized in a number of ways, among them the maximum temperature of the resistors, the uniformity of the resistance and the properties of the projection system. As this is the first installation of such a system in any GWD, a method of aligning the projector is developed, based on modulating the heaters.

[15] With $1\,(°)^2 = \left(\frac{2\pi}{360°}\right)^2$

[16] A lens with a focal length in the order of its diameter may seem very unwieldy, however, typical materials used in the far IR region, such as ZnSe, Germanium or Silicon have a larger refractive index than glass or fused silica, which allows to manufacture lenses with focal lengths in the order of the diameter of the lens or shorter.

The heating pattern was optimized to reduce the amount of HOMs at the darkport of GEO 600 by using the actuation matrix formalism. A reduction in the HOMs at the current operating power of 31% could be achieved. Furthermore the possibility of using the thermal projection system for the reduction of thermally induced HOMs is explored as well. A reduction of 24% of HOMs is achieved at when running GEO 600 in a state with increased circulating laser power.

Further improvements of the performance of the thermal projection system are possible, as it is currently limited by the low power transmission of the optical system. The delivered power is restricted by the solid angle defined by the aperture of the vacuum viewport and beam splitter surface, and could be improved by moving the optical system into the vacuum chamber. In this case, the optical system could likely be reduced to a single lens in the vacuum chamber, and the heater array would be located directly in front of the viewport, outside of the vacuum chamber.

A further development may be the design of a vacuum-compatible version of the thermal projector which can than be used to reduce mirror imperfections, scattered light and losses at other optics.

CHAPTER 6

Baffles

The previous chapters have shown approaches to reduce high order modes (HOMs) by heating the optics in an appropriate way. This chapter shows another approach in dealing with HOMs and scattered light, which works by spatially filtering them out.

Scattered light and filtering it out via seismically isolated baffles has been an important topic of research since the early days in the field of interferometric gravitational wave (GW) detectors ([VBB96], [Coy96]), and will be even more important as the advanced detectors will reach a light power in the order of 800 kW circulating in their cavities [HC+10].

In GEO 600, baffles, large black glass plates, were installed into the ultra-high vacuum (UHV) system of GEO 600 in the course of this work. They have an aperture through which the main laser beam of GEO 600 passes without significant clipping loss. All light which extends beyond the free aperture of the baffles, such as HOMs and scattered light, will be absorbed by the baffles.

However, the baffles still have a small residual reflectivity. It is possible that this small amount of reflected unwanted light can cause issues, such as seismic and acoustic noise coupling, in the detector and contaminate the gravitational wave measurement.

Several attempts of estimating the noise contribution of baffles have been made, based on optical simulations and measurements of mirror surface figures ([AAA+15b], [Chi12]).

In the course of this work, an in situ projection of baffle motion to the GW measurement of a GW detector is created. An advanced design of the baffle suspension including sensors and actuators is necessary to enable this measurement, the design and installation of which was part of this work and is presented here as well.

6.1. Motivation for additional baffles

In this work, we will refer to all light that leaves the intended path set by the optical system of GEO 600 as scattered light. This can cause issues when the scattered light hits the inner wall of the vacuum chambers, and after another scattering process recombines with the circulating laser beam in GEO 600 and disturbs the GW measurement.

Several mechanisms can lead to scattered light. Dust particles, defects on the mirror surfaces, micro-roughness and surface deviations of the optics can cause scattering. This can lead to HOMs that are larger than the mirrors[1] (A photograph of this is presented in figure 2.11 on page 29, it shows scattered light in the inside of one of the vacuum chambers of GEO 600).

Scattered light has been a challenge in all GW detectors ([TAKS04], [AAA+10b], [OFW12], [HGS+06]). The issue becomes clear when one considers the great sensitivity of the GW detectors. As [Hil07, p.31] shows, the maximum tolerable power of stray light on the photo diode of GEO 600 is in the order of 10^{-20} W. This is challenging to reach, especially when considering the large amount of light stored in the optical cavities of the GW detectors of several kilowatts.

In GEO 600, scattered light has manifested itself in a number of different ways. For one, it has been shown to degrade the GW measurement sensitivity in several instances ([HAA+03], [GC+08]). Moreover, it has been observed that scattered light couples into the OSEMs (optical sensing electro magnetic actuators), which are used for sensing and damping the motion of the suspended optics[2]. The OSEMs produce an optically measured DC position signal, which can be affected by scattered light from the interferometer. Any stray light on the photo diode of the OSEM will contaminate the error signal measured by the OSEMs and cause the corresponding feedback servo to erroneously move the suspended optic. Exactly this has been observed in GEO 600 [ADD+14]. This was especially severe when experimenting with high circulating light power in GEO. As a measure against the coupling of stray light into the OSEMS, a modulation/demodulation scheme has been introduced to the OSEMs, which allows them to discriminate the scattered light. This comes not without its own issues though, the modulation scheme has been shown to introduce additional noise to the pendulums and to be influenced by fluctuations in the 50 Hz power line frequency [Aff14, p.53].

A lot of work has been done already to reduce the amount of scattered light in GEO 600. The inner walls of the corrugated 600 meter long vacuum tube in the arms of GEO 600 are a large potential surface that potentially could reflect scattered light back into the interferometer. This is prevented by conical, blackened stainless steel baffles in the arms, such that the laser beam does not 'see' the shiny inner side of the vacuum tubes [WAA+02].

Another measure is the optical layout, especially on optical benches for auxiliary beams, where it is usually avoided to place optics in the beam waist. This avoids the cat's eye effect [Hil07, p.49ff]. A third measure is the installation of anti-reflective

[1] Their radius scales with square root of the mode order, as described in equation 2.17 on page 27
[2] See section 6.5 for more information on the OSEMs.

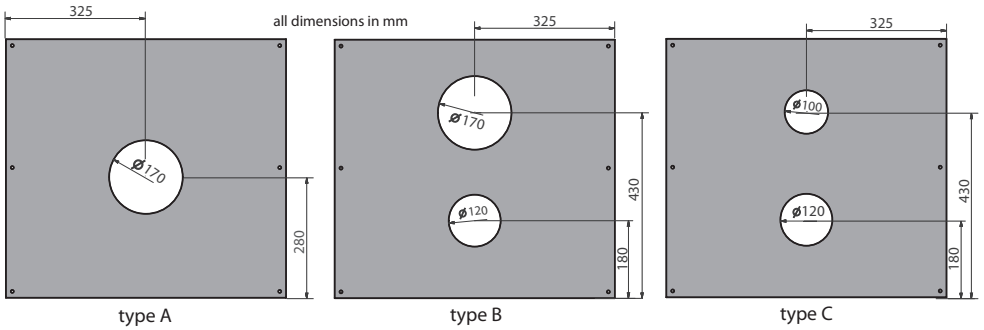

Figure 6.1.: An illustration of the three different types of rectangular baffles, including dimensions and positions of the cutouts in millimeters.

(AR) coated viewports in the vacuum system, and avoiding to hit those windows under normal incidence with the laser beam. This way, the residual back-reflex from the AR-coated windows cannot directly enter the interferometer again. Instead it is directed to a beam dump.

GEO 600 has shown unexplained noise at frequencies below 1 kHz (see chapter 1.4 in this work and [Aff14, p.145ff]), and it has been established that the strength of this noise depends on the amount of circulating light power in GEO 600. Therefore, scattering has been a strongly suspected candidate for the unexplained noise.

Challenges with scattered light were already anticipated before this work, and large black glass baffles had been ordered and delivered (but not installed) in 2007 already. The challenges associated with scattered light have become more severe since then, especially since the GEO-HF upgrade program started, which aims to increase the circulating light power in GEO 600. The final push for the installation of those baffles, aside from the multiple issues with scattering mentioned before, was the unknown power dependent noise. The baffles should suppress scattering in the interferometer, and if the unexplained noise would change after the installation of the baffles, this would be a strong indication of its origin.

6.2. Prerequisites

6.2.1. Description of the new baffles

The baffles are large black glass plates, manufactured by SCHOTT [Sch]. They measure 650 mm x 600 mm x 3.6 mm (HxWxD), have an anti-reflective (AR) coating on one side, six through holes with a diameter of 7 mm and round cutouts through which the laser beam can pass. The cutouts vary in size and position, according to where the intended location of the baffle is. In total, there are four different types of baffles available at GEO 600, three of which are shown and named in figure 6.1.

Type A is designed to be placed in front of the far folding mirrors MFE and MFN,

the single circular aperture has the same size as the mirror[3].

The baffles of type B and C are intended to be used in the vacuum tanks TCN and TCE that accompany the close folding mirrors of GEO 600, MCN and MCE (see p. 5 for a simplified layout of GEO 600). Type B would be installed in front of each mirror MCN and MCE (i.e. between mirror and 600 meter long beam tube), while type C would be installed behind those mirrors (i.e. between the reactions masses for those mirrors and the beam splitter). Due to the folded arms of GEO, the baffles of type B and C need two apertures, the lower one for the 'outgoing' beam from the beam splitter, and the top one for the beam incident on the end mirror MCE or MCN. The difference between type B and C is the size of the upper aperture. For type B it has 170 mm in diameter, the same size as the usable aperture of the end mirror. In contrast, type C, which will be used in transmission of the end mirror[4] has a smaller aperture for the beam transmitted by the end mirrors. The reason for this lies in the electrodes for the electrostatic drives (ESDs) on the reaction masses of those mirrors, as they reduce the free aperture in transmission of the end mirrors. More information on the layout and function of the ESDs in GEO 600 is given in chapter 8 of this work.

The fourth type of baffle, which is not shown here, is round with a circular cutout. It was supposed to be installed between the beam splitter and the signal recycling vacuum tank.

Installation plan

Installing the baffles into the vacuum system of GEO 600 bears some risk, as opening of the vacuum tanks and working close to the main optics of GEO 600 can potentially damage the interferometer is several ways. For one, the main optics or their suspension could be damaged. As shown in figure 6.2, the main optics of GEO 600 are suspended as multiple stage pendulums, and the lowest stage features 250 μm thin fused silica fibers [Goß04, p.107], which can be easily damaged when touched. Another risk is the accidental venting of the 600 meter long corrugated vacuum tubes. If vented, their large surface would store a large amount of water molecules from the air, and subsequently deteriorate the pressure in the vacuum system after the installation. Therefore, the arm tubes are kept under vacuum at all times.

When necessary, for example when working on the main optics, the arm tubes can be sealed off the connected vacuum chambers by large, double-walled gate valves. Those gate valves are leaky however, unless their center-space is constantly pumped. A pump failure or a power outage can therefore lead to the unintentional venting of the arm tubes, when working on the main vacuum chambers. When GEO 600 was built, the water vapor stored in the inner walls of the arm tubes was baked out by sending a large current thought the arm tubes [ADD+14]. This method would be very work-intensive though, as there are a large number of electronic components

[3] The main mirrors of GEO 600 are made of substrates with a diameter of 180 mm, they have chamfered edges though, such that the useful surface has a diameter of 170 mm.

[4] The mirrors MCE and MCN are coated with a highly reflective (HR) coating on the side facing the interferometer arm. It has a residual transmission of 12 ppm. The transmitted beam is used for alignment sensing.

location	aperture radius (mm)	beam radius (mm)	aperture defined by
MPR reaction mass	37.5	10	free aperture of MPR reaction mass
TCE/N outgoing beam	50	10	baffle
MFE	85	22.6	aperture defined by mirror size
MFE	85	22.6	baffle
MCE/N reaction mass	22	9.1	free aperture in ESD electrodes
MCE/N	60	9.1	baffle

Table 6.1.: This table shows beam sizes and apertures at various points in GEO 600. It also shows the free aperture at those points or close to them as defined by the baffles. The values for the beam sizes are taken from figure 2.5 on page 20 for a thermal focal length of 10 km and rounded to a tenth of a millimeter. The values for the free apertures are taken from [Goß04, p.48] and [Gro03, p.167].

connected to the vacuum system that would need to be disconnected. Of course, measures to mitigate those risks are taken, such as the use of multiple pumps for the gate valves, an emergency power generator and having personel 24 hours per day on site during work on the vacuum system.

In order to minimize the loss of science time and the risks associated with venting the ultra high vacuum system and working close to the main interferometer optics, it was decided to install only a subset of the available baffles during the course of this work. This should already show an improvement in the amount of scattered light in the interferometer, and allow to make a statement on the influence of scattering on the laser power dependent noise.

The remaining baffles can be installed as the need arises. Three baffles were installed in total. One of type A was installed in front of the far east folding mirror (MFE). This work was carried out together with the installation of the reflector for the ring heater and the installation of the side heaters as explained in chapters 3 and 4.

Additionally, a baffle was placed in front of each of the mirrors MCN and MCE. For this, baffles of type C were used *upside down*[5]. This gives the benefit of partly shading both the ESD electrodes and the aluminum reaction mass of the power recycling mirror with using only one baffle per vacuum chamber. Both apertures are still sufficiently large that clipping of the laser beam is not an issue, as all the beams passing though those type C baffles have radius of about 1 cm. Table 6.1 gives a more detailed overview of the beam sizes and the free apertures of the corresponding baffles in the configuration they have been installed in GEO 600.

[5] This refers to the originally intended orientation, which is shown in figure 6.1.

6.2.2. New detailed CAD model of a vacuum chamber and the triple pendulum suspension

It quickly became clear, that due to their large size, it would be challenging to fit the baffles into the vacuum chambers without damaging the suspended optics, since the clearances are less than a centimeter. For this it was deemed desirable to check with a CAD model how the baffles could be fitted into the vacuum chambers. Unfortunately the existing model of the main vacuum chambers and the suspensions, as shown for example in [Goß04, p.60,69], [Gro03, p.22] and [Aff14, p.24] was too simplified to make precise statements on the fitting of the baffles. Therefore it was necessary to build a new, more detailed CAD model of the inside of a main vacuum chamber for this work. The new CAD model is based on a mixture of data from the existing simple CAD model, a test suspension setup, spare parts and photographs. Figure 6.2 shows this new CAD model of the vacuum chamber TFE, with the triple pendulum suspension for the mirror MFE, and the ring- and side heaters.

Because of that model, it was obvious that the baffles would not physically fit though the hexagonal structure at the top of the suspension, as shown in figure 6.2, but must instead be rotated and carefully maneuvered with its shorter side through the gap between the hexagon and the lower part of the vacuum chamber and then be rotated back again inside the vacuum chamber. The new CAD model has proven to be very helpful in the design and fitting of not only the baffles, but for the installation of the reflector for the ring heater and the side heaters in TFE as well.

6.3. Suspending, damping and installing the baffles

When installing the baffles, great care must be taken to not *introduce* additional scattering. Even tough the baffles are AR coated on one side, they still have some residual reflectivity. This reflectivity of the AR coating has been measured to be about one percent, using a Nd:YAG laser and a power-meter at close to normal incidence [WL12]. Moreover, scattered light is expected to hit the baffles, which is the reason for their installation after all.

To make sure that the baffles would work as expected and to mitigate possible issues arising from the residual reflection from the baffles, several measures were taken. For one, the baffles are installed into a frame, which dampens the internal modes of the baffles. Furthermore, they are seismically isolated by either rubber feet (in TFE) or by suspending them as a pendulum (in TCE and TCN). All baffles were installed with their AR coated side towards the 600 meter long arms, and are tilted downwards by 2 degrees, such that any direct reflection of scattered light is not send back into the interferometer, but towards the existing baffles in the arm tubes.

Using simple trigonometry and the simplified drawing in figure 6.3, it can be computed where the residual reflex of the baffle will hit the corrugated 600 m long arm tube or the existing baffles ('arm-baffles' in the following) in it[6]. It can be assumed

[6] As mentioned before, the baffles in the arm tube have been designed that the mirrors do not 'see' the inner walls of the corrugated arm tube.

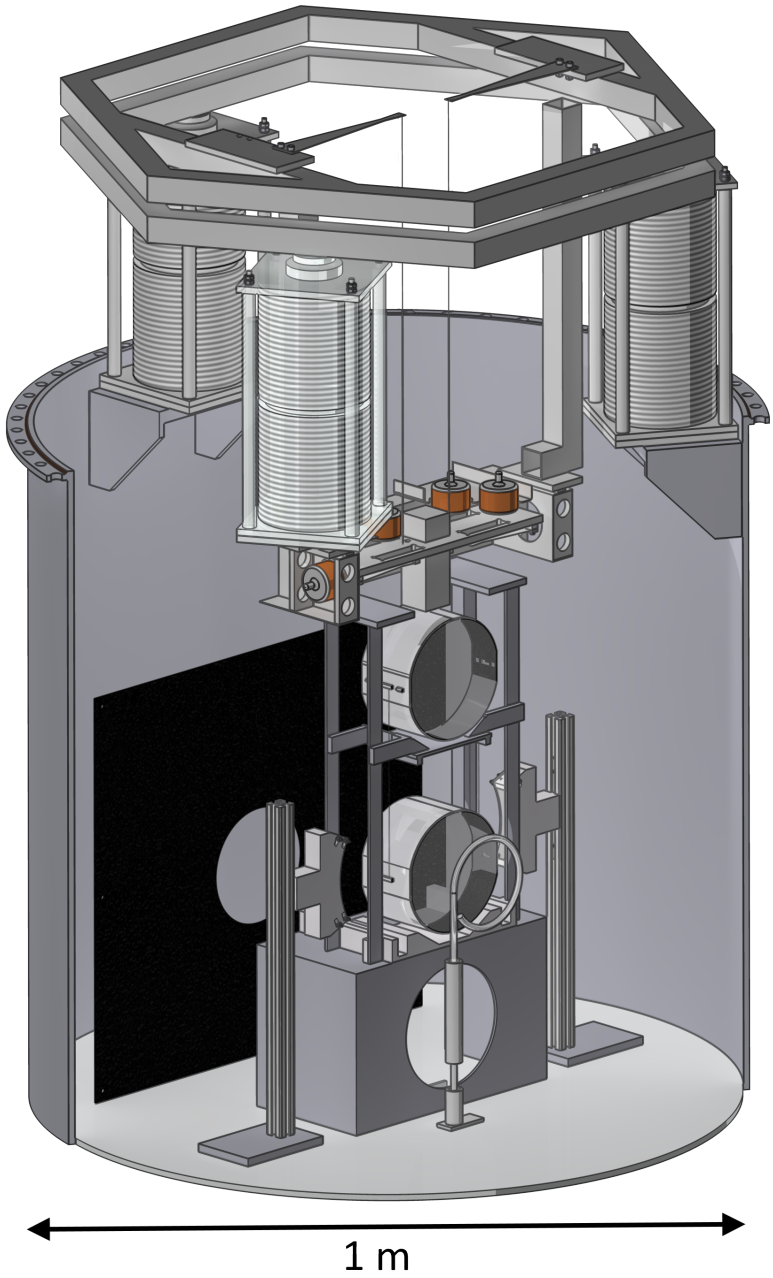

Figure 6.2.: New CAD model of the main suspension in the vacuum chamber TFE. For scale, a baffle of type A is placed into the vacuum chamber, without any frame or suspension. The side heaters are included as well, the reflector for the ring heater has been omitted in this image for clarity.

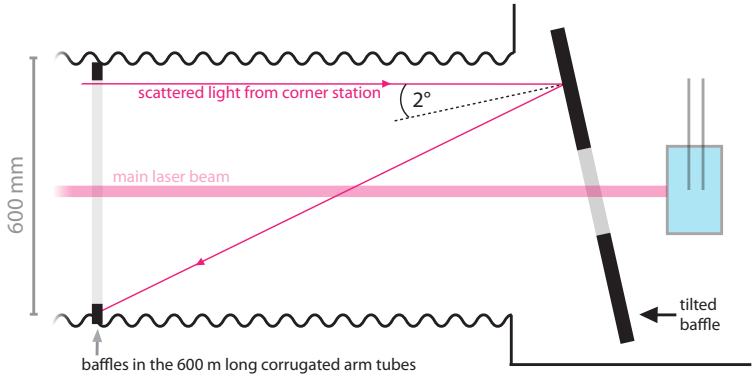

Figure 6.3.: Schematic illustration (not to scale) of the tilted baffle, and the residual reflex of its anti-reflective coating. The tilting angle of the baffle is exaggerated in this figure.

that the scattered light from the 600 m distant corner station will enter the vacuum chamber with the tilted baffle horizontally. And as another assumption, we assume that the incoming scattered light will be located at the top of the arm tube, as shown in figure 6.3, this would be equal to a worst case scenario. With this, the distance x can be computed, which tells where the residual reflex of the scattered light beam will hit either the tube wall or the arm-baffles, measured from the tilted baffle. This distance is

$$x = \frac{600\,\text{mm}}{\tan(2 \times 2°)} \approx 86\,\text{m}. \tag{6.1}$$

The design, construction and installation of the baffle suspensions was done as a part of this work, as detailed in the next sections.

6.4. Baffle suspension in TFE

The baffle in TFE was installed in November 2012, along with the reflector for the ring heater (see chapter 3.5) and the side heaters (see chapter 4). As mentioned before, we did not install the bare baffle, but built a frame around it to suppress the mechanical eigenmodes of the baffle. For the baffle in TFE, this frame consists of two aluminum pieces, between which the baffle is clamped. To actually dampen the resonances of the baffle, a soft, lossy material is used between the aluminum pieces and the baffle. In this case, an insulated, vacuum compatible ribbon cable[7] [Gor] is used to dampen the mechanical baffle resonances. Furthermore, additional aluminum profiles (ITEM [iIG14]) are used to stiffen this frame, and to build a stand for it, such that it can stand upright, tilted by a defined angle of two degrees. Figure 6.4 pictures this construction.

The damping of the internal resonances of the baffle in the frame has been measured in a test setup. For this measurement, the baffle was replaced by a glass plate to

[7] which is used throughout the vacuum system of GEO 600

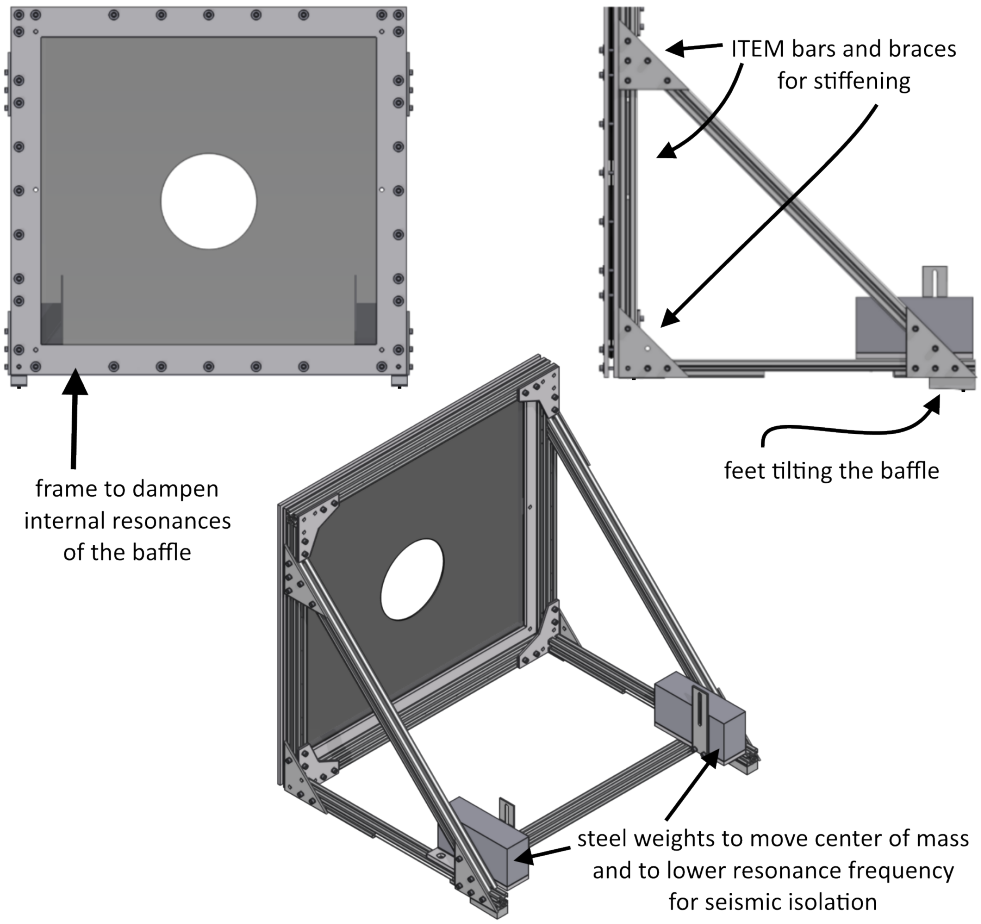

Figure 6.4.: CAD model for the baffle setup in TFE. The baffle is clamped in between two aluminum frame pieces, the piece on the back is further stiffened by ITEM bars and braces. The whole construction is put on rubber (Fluorel) feet in the vacuum chamber.

mitigate the risk of damaging the baffle. The glass plate was custom made, with a shape mimicking a baffle of type B. The damping of the internal resonances was measured using an accelerometer (Brüel & Kjær model 4381) at the center of the glass plate, once in the frame and once without the frame. The top graph in figure 6.5 shows the resulting data from the accelerometer as spectra. Comparing the red graph for the bare glass plate and the blue curve for the damped glass plate, the effect of the damping becomes clear. Several resonance peaks between 10 and 25 Hz are damped well, and some more above 100 Hz. In the measurement with the frame a sharp peak appears at 75 Hz, the origin of which is not clear. The lines at multiples of 50 Hz are most likely related to electrical pickup from the electricity grid, and can be ignored in this measurement. Overall, the internal modes of the baffle are damped enough, such that they are not distinguishable from the background signal in the accelerometer measurement. The effect of the damping is especially apparent for the mechanical modes at low frequencies, which potentially could be excited easily by seismic activity.

Another design feature of the baffle suspension in TFE is its seismic isolation, which is realized by putting the complete baffle-frame-assembly on four 4x4x4 mm^3 Fluorel feet (F7511[8] obtained from [Gum]), similar to the reflector for the ring heater (see chapter 3.5). The Fluorel feet will act as springs with a resonance frequency f_{res}, above which seismic movement will be reduced by a factor of $1/f^2$, with f being the frequency of interest.[9]

With equations 3.6 through 3.9, the weight of the baffle assembly of about 31 kg and the Young's modulus of Fluorel as determined in chapter 3, the resonance frequency can be computed to $f_{res} = 13$ Hz.

The seismic attenuation via the Fluorel feet has been measured in a laboratory setup with a glass plate replacing the baffle in the frame. For this, we placed an accelerometer close to the center of the glass plate and measured its signal once with Fluorel feet and once without. To increase the signal to noise ratio of this measurement, we applied additional vibrational excitation to both setups, by running a grinder in the same room. The bottom plot of figure 6.5 shows the accelerometer spectra. The seismic attenuation is clearly visible for frequencies above 4 Hz. This is even lower than the computed value, and may point to the Fluorel slightly changing its elastic properties under the load of the baffle assembly. This is however not evident from the measurement in figure 3.16 on page 53. Figure 6.6 shows a photograph of the installations in the vacuum chamber TFE. The baffle in the frame is visible on the right, and the mirror MFE on the left hand side.

[8] Which was treated according to [BCF09] and positively tested for ultra-high vacuum compatibility in a vacuum test chamber with connected residual gas analyzer. A second batch that was ordered, treated and tested turned out to be not vacuum compatible however.

[9] $1/f^2$ is true for a harmonic oscillator, for rubber suspensions, such as the Fluorel suspension in this case, the exponent is between one and two [GSSS96].

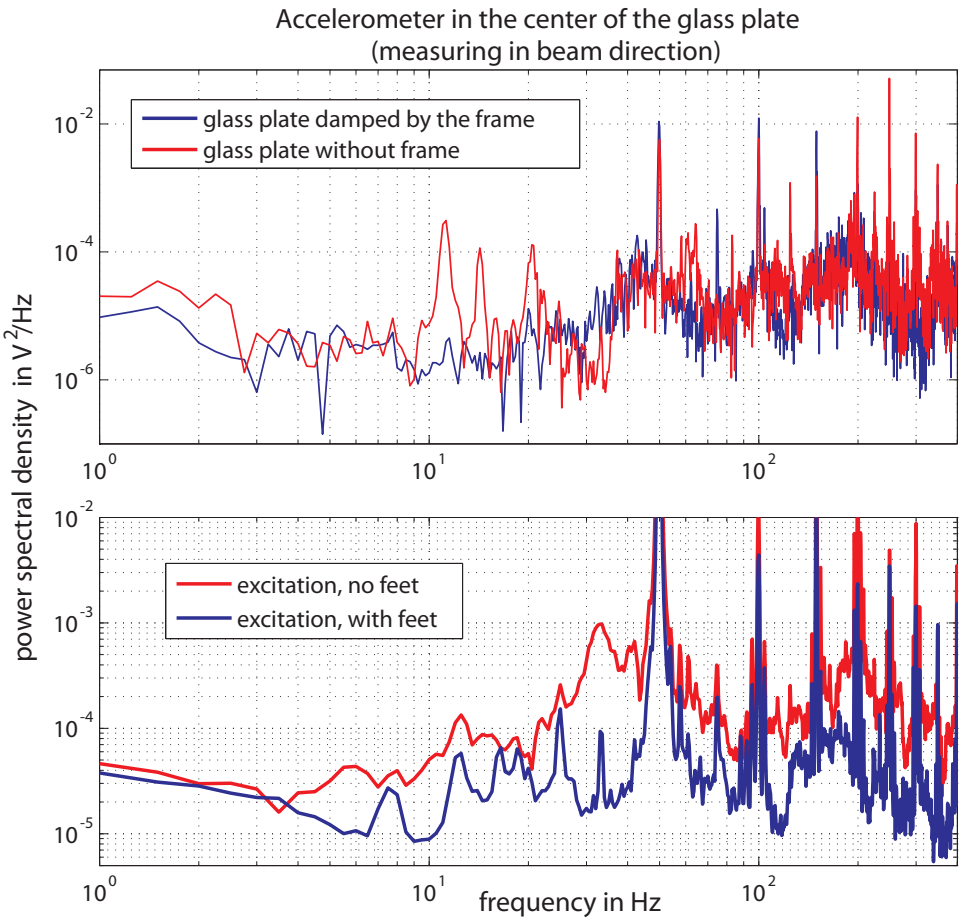

Figure 6.5.: Accelerometer measurements on the TFE baffle construction.
Top: Measurement of the damping of the internal resonances of the baffle (which was replaced by a glass plate for the measurement). The two graphs show the signal of an accelerometer, which was attached to the center of the glass plate. This measurement was performed once with the glass plate in the frame to dampen its resonances, and once without the frame. The damping works well for the first few modes of the baffle at around 10 Hz, and for some at higher frequencies as well. Lines at multiples of 50 Hz are likely electrical pickup from the power line.
Bottom: Measurement of the seismic isolation by Flourel feet. An accelerometer was attached to the center of the glass plate, and its signal was measured, once with the Fluorel feet and once without. To increase the signal-to-noise ratio of the accelerometer measurement, the ground vibrations were increased by turning on a grinder located in the same room (for both measurements). Apparently the Fluorel feet provide seismic isolation at frequencies above 4 Hz. The isolation appears to be constant at high frequencies, this could possibly be explained by acoustic coupling.

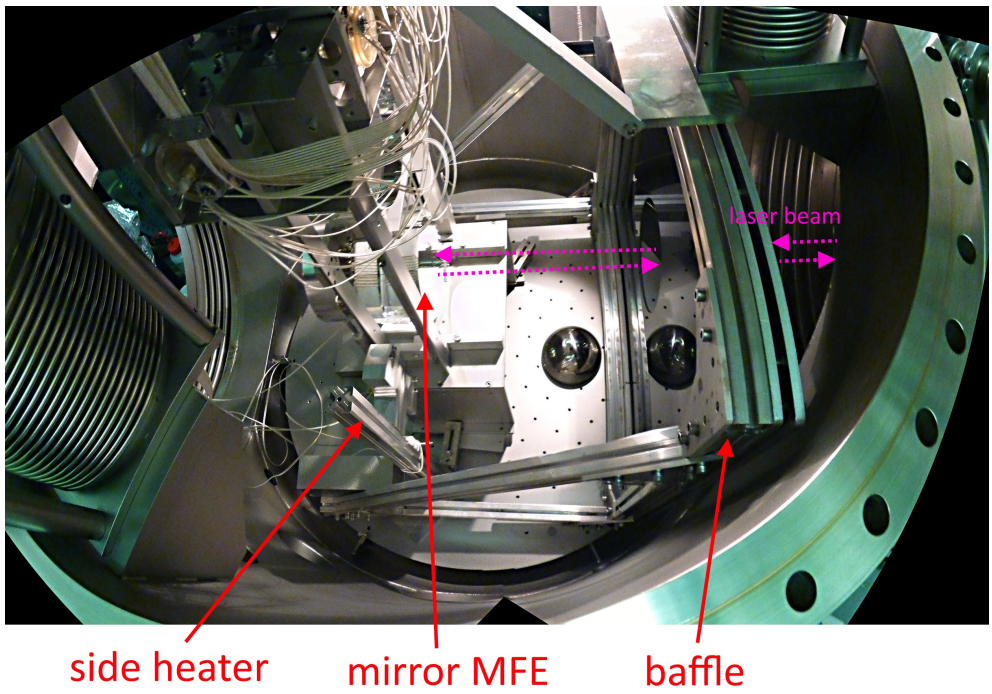

Figure 6.6.: Photograph of the baffle and side heaters in TFE. This image was produced by stitching multiple images together, to get a wider field of view. On this image, the path of the laser beam is shown as dashed purple line, it would enter the vacuum chamber from the right though the aperture in the baffle be reflected of the mirror MFE and leave the vacuum chamber again through the aperture in the baffle. The small reflective steel half-sphere left to the baffle was supposed to be used for a manual pre-alignment of the laser beam, by providing a reflected image of the mirror's front face to a camera located behind the mirror MFE.[10] It turned out that the manual alignment of the laser beam is well possible without using the reflected image of the half-sphere, it remains unused.

[10] The large baffle partly obstructs a vacuum viewport, which is located on the left hand side of the image above.

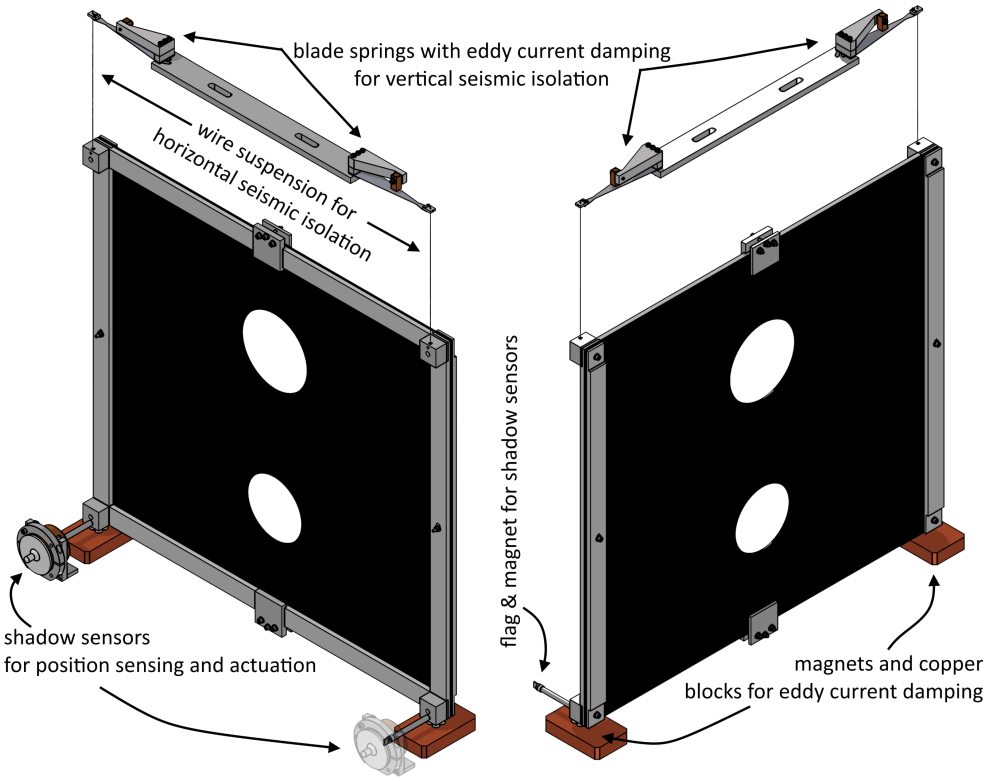

Figure 6.7.: Illustration of baffle suspensions in TCE and TCN. The bar at the top would be bolted to a standoff inside the vacuum chamber.

6.5. Baffle suspension in TCE and TCN

The baffles in the vacuum chambers TCE and TCN were installed in August 2013, about nine months later than the baffle in TFE. This allowed further development of the suspensions of the baffles. Changes to adapt the baffle frame were necessary, as there is less available space in the vacuum chambers TCE and TCN for the baffles. The reason for this is that those chambers do not only house one mirror on a triple pendulum suspension chain, but two. In those vacuum chambers, a second triple-pendulum suspension carries a reaction mass with the electrostatic comb drive (for more information about the electrostatic drives, see chapter 8 in this work). Furthermore, unlike in the vacuum chamber TFE, the weak beam that is transmitted through the mirror is directed out of the vacuum chamber by additional optics in the vacuum chamber.

All this led to the development of a more compact frame for the baffles, and a seismic isolation that relies on a pendulum suspension with steel wires, instead of Fluorel feet.

Figure 6.7 shows an illustration of the baffle suspension in the vacuum chambers TCN and TCE. As for the baffle in TFE, Gore wire is used as lossy material between frame and baffle to dampen its internal resonances.

The horizontal seismic isolation is achieved by suspending the baffle as a pendulum with steel wires. Eddy current damping (ECD) is used to further improve the seismic isolation, and is realized by magnets with alternating polarity glued to the bottom of the frame, and putting large copper blocks directly underneath it in the vacuum chamber. To not contaminate the ultra high vacuum system, very pure, oxygen-free copper has been chosen for this application.

Even more magnets are attached to structures around the frame for additional ECD, as can be seen in the photograph in figure 6.9.

Just as the baffle in the vacuum chamber TFE, the baffles described in this section are suspended with a slight angle, such that any residual reflection of its surface will not be directed back into the interferometer. This angle is realized by clamping the suspension wires on the baffle frame not directly above the center of mass (CoM) of the baffle assembly. This way, the baffle will experience a restoring torque due to gravity, until the CoM and the suspension point are aligned in vertical direction. The schematic drawing in figure 6.8 illustrates this effect.

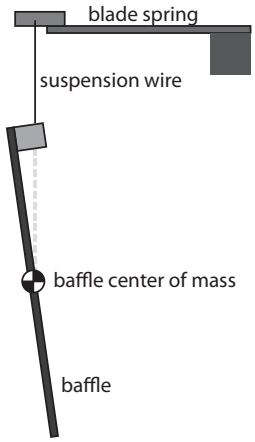

Figure 6.8.: The tilt angle of the baffles is in-built into the suspension, by attaching the wires horizontally offset from the center of mass. This way, gravity will introduce a torque which tilts the baffle until the CoM is below the suspension point again.

The CoM of the baffle assembly can be approximated to be in the center of the baffle with good accuracy, as indicated by the CAD model (presented in figure 6.7). When not tilted, the horizontal distance between the suspension point of the baffle frame and its CoM is 21 mm. With some trigonometry it follows that the suspended baffles will be tilted by two degrees, just as the baffle in TFE. This introduces tilting of the baffles and has the additional benefit that it serves as a safety measure as well. In case the suspension wires break, the angle makes it more likely that the baffles will fall away from the main optics in the vacuum chamber.

The vertical seismic isolation is realized by attaching the steel wires not to a rigid structure, but to blade springs instead, with a vertical resonance frequency of 2.2 Hz (with the baffle attached). These blade springs, sometimes called cantilever springs, act as harmonic oscillator in the vertical direction, and thus provide a vertical seismic isolation. Additionally, magnets are attached to the blade springs along with copper pieces for ECD.

The blade springs are of the same type that is used throughout the suspension systems of the main optics in GEO 600. They are pre-bent, such that they are flat when the baffles are attached. More information on the blade springs can be found in [Goß04, p65ff].

Another design feature of the suspended baffles in TCN and TCE is that their longitudinal position can be read

out and actuated upon. As sensors and actuators we use OSEMs, which are used for the main optics of GEO 600 as well. Small poles with magnets on top are attached at the bottom edges of the baffles' frames, as can be seen in figure 6.7. A coil attached to the bottom of the vacuum chamber can now act on the those magnets. The position sensing is done via an LED that shines light on one side of the aforementioned pole, and a photo diode on the other side of the pole detects the incoming amount of light from the LED, which depends on the longitudinal relative position of the pole and the OSEM. Effectively this measures the shadow that is cast by the rod, hence the sensor in the OSEMs is sometimes called 'shadowsensor'. More information on the OSEMs and their usage in the suspensions of the main optics in GEO 600 can be found in [Goß04] and [PTH+00].

The sensing and actuation scheme with the shadow sensors allows us to estimate the amount of noise added by the baffles by the method of noise projection.[11] For this, we excite the motion of the baffles with the actuators and measure a transfer function of this motion to the gravitational wave (GW) measurement[12]. After having measured the transfer function, we can use it to estimate the effect of the baffle motion during normal, quiet times on the GW measurements. This is done by multiplying the measured motion of the baffles (via shadow sensors) with the aforementioned transfer function. More information on the method of noise projections can be found in [Smi06]. If the noise added by baffle motion is found to be too high[13], they can be used to actively dampen the motion of the baffles, this however was found not to be necessary.

One potentially limiting factor in the noise analysis is the fact that in this case, only two shadow sensors are used for each baffle. Therefore, they cannot actuate and sense on all degrees of freedom of the baffles. We would argue however, that the ones that are installed can excite the 'swing' pendulum mode, which causes a large displacement in the beam direction. Especially baffle movement in beam direction can have a large impact on the GW measurement, as a residual reflection of stray light off the baffle will carry a time varying phase shift, similar to the expected GW measurement signal.

Another possible mechanism of how the baffles could introduce noise into the GW measurement is by horizontal or vertical movement (both perpendicular to the laser beam), such that the laser beam gets clipped on the apertures of the baffles. We would argue that this effect is negligible for two reasons. First, all apertures of the baffles are at least more than three times larger than the beam radius (see table 6.1). Furthermore, table 6.1 also shows that the existing apertures in GEO 600 (i.e. defined by the ESD pattern, the reaction mass of the power recycling mirror and the mirror size of MFE) are all smaller or of the same size as the free aperture of the closest baffle.

[11] Given the sensitivity of the GW measurement of GEO 600 and its sensitivity to scattered light, some amount of measurable noise coupling can be expected. Ideally the influence of this is insignificant compared to the GW sensitivity.

[12] The transfer function measurement works in the regime of small amplitude baffle movement (smaller than the wavelength of the laser beam). In case of large amplitudes, a nonlinear effect called 'fringe wrapping' will emerge [Hil07, p.34].

[13] Typically the limit is set to one tenth of the GW sensitivity, which we will use here as well.

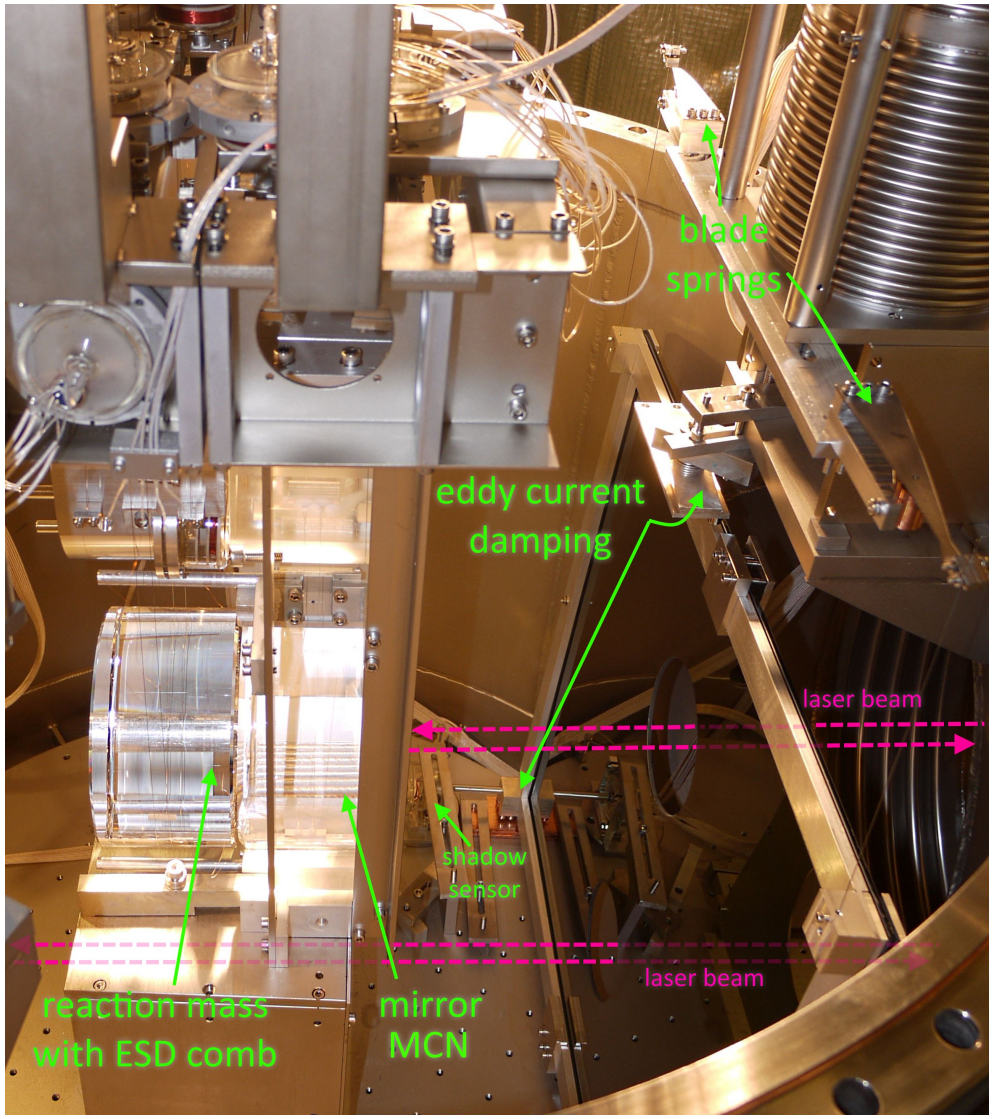

Figure 6.9.: Photograph of the baffle installation in TCN. The baffle is located on the right, while the mirror MCN and its reaction mass are visible on the left hand side. The paths of the laser beam through the apertures in the baffle is drawn as a purple dashed line.

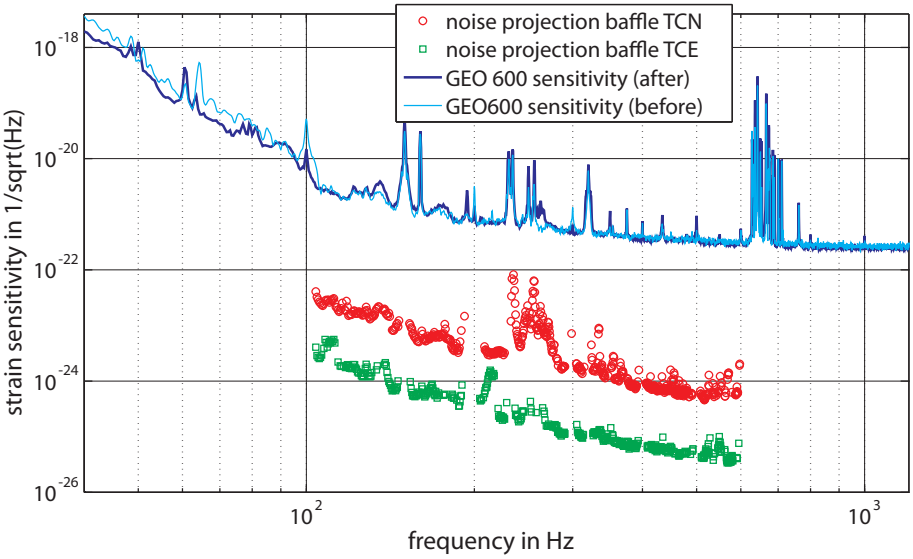

Figure 6.10.: Noise projections for the baffles installed in TCN and TCE, as measured by the OSEMS in the baffle assembly. For comparison, a spectrum of the GEO 600 strain sensitivity from a time before the installation of those baffles is shown as well.

The noise projections have been carried out as described above, and figure 6.10 plots the results. It shows a spectrum of the GW strain sensitivity of GEO 600. Furthermore it shows the noise contribution of each baffle, determined by the noise projections. The noise introduced by the baffle in TCN is larger than the one added by the baffle in TCE, but it is still about a factor of 100 lower then the measured sensitivity of GEO 600 for most of the measurement band. Between 200 Hz and 300 Hz however, the added noise is more than that. The exact reason for this is not clear, a resonance in the baffle assembly could be the cause. The transfer function measurement of baffle motion to GW strain sensitivity proved challenging since the coupling was very low, especially at high frequencies. This is most likely due to the strong ECD. The ordinary method would be to inject white noise at all frequencies to measure the transfer function. In this case we injected band-limited white noise over a small bandwidth of 100 Hz to increase the signal-to-noise ratio of the measurement. By this, the transfer function was measured piecewise over the desired frequency range. This was repeated until all relevant frequencies were covered. The transfer functions which were obtained like this were then stitched together to create a single transfer function. The transfer functions have a $1/f^2$ drop-off at high frequencies, as expected from a single pendulum suspension. Graphs of the transfer functions are supplied as figure A.7 in appendix A.2.

6.6. Summary and outlook

We have developed suspensions and frames for baffles, which were installed into the ultra-high-vacuum system of GEO 600. The main reasons for this work were issues with scattered light in GEO 600 and the suspicion that an observed increasing noise at high laser power operation may be influenced by the baffles. We observed no effect on the unknown noise at high powers, but we did observe a reduction of stray light in the vacuum chambers with the baffles installed. The stray light was measured by the shadow sensors in the main mirror suspensions, and showed a reduction of a factor of about two [Aff13].

To help with the installation of the baffles, a new, more detailed CAD model of the inside of one of the vacuum chambers of GEO 600 was built. This model is available for future installations into the vacuum system of GEO 600 as well.

A notable feature of the baffle suspensions in TCN and TCE is the integrated sensing and actuation scheme, which is based on shadow sensors and magnet coil actuators. This construction allowed us to make an in situ noise projection of baffle motion to strain sensitivity of the GW measurement. The noise projection for the baffles is highly relevant for the advanced detectors, where stray light issues are expected due to the large circulating light power.

While the baffles are used to spatially filter unwanted light, the next chapter will explain an optical filtering method of unwanted light by an optical cavity, the output mode cleaner.

CHAPTER 7

A new output mode cleaner for GEO 600

This chapter describes the output mode cleaner (OMC), which has the purpose of optically filtering high order modes out of the output beam of GEO 600, thus preventing them from reaching the main photo diode.

In the course of this work, a new OMC was designed for GEO 600, based on the design of the existing one. This chapter details measurements and reduction of the acoustic coupling of the OMC, improvements in the mode matching of the GEO 600 output beam to the OMC, and finally the design and results from the new and improved OMC.

7.1. The output mode cleaner

The output mode cleaner of GEO 600 is a small optical cavity located at the output of GEO, directly in front of the main photo diode. Its purpose is to transmit only the fundamental TEM_{00} mode of the gravitational wave (GW) carrier beam (and potentially GW induced sidebands) contained in the output beam of GEO 600. All other components of the output beam, such as higher order modes (HOMs) and radio-frequency (RF) modulation sidebands, used for controlling the interferometer, are mostly reflected off the OMC and strongly attenuated on the photo diode (PD). This is beneficial to the signal to shot-noise ratio, since only the fundamental TEM mode potentially carries a significant amount of detectable gravitational wave signal. The HOMs do not, since the recycling cavities are kept resonant at the fundamental TEM_{00} mode[1], which results in a much better signal to noise ratio for the TEM_{00}

[1] This is the case in all currently operating gravitational wave observatories. Other modes could be used in principle though, particularly the use of the LG_{33} mode is currently being researched, as it may be advantageous in terms of thermal effects. The usage of the fundamental mode

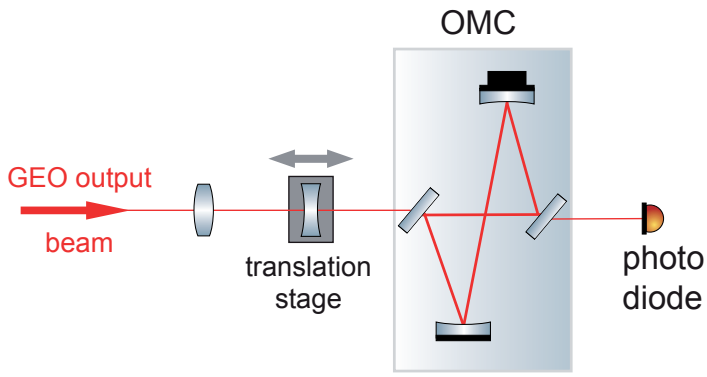

Figure 7.1.: Schematic layout of the OMC and the mode matching telescope, consisting of two lenses in front of it.

mode.

The OMC is build as a four-mirror bow-tie cavity, with two flat mirrors with a power transmission of 2% and two highly reflective mirrors[2] with a RoC of 2.35 m [Pri12, p.49]. One of the curved mirrors is placed on a piezo actuator, such that the length of the OMC can be actuated upon and locked to resonance of the TEM_{00} carrier in the GEO output beam. All mirrors of the OMC are glued to a rectangular fused silica breadboard.

Figure 7.1 shows a schematic drawing of the OMC setup. Good mode matching of the output beam of GEO 600 to the OMC is ensured by a mode matching telescope consisting of two lenses in front of the OMC. All components shown in figure 7.1 are located in a vacuum chamber (TCOc) that is separated from the ultra high vacuum (UHV) system of the main interferometer, to allow for easy access and quick turnaround times when TCOc should be opened. Furthermore, all optics in TCOc are placed on three seismic isolation platforms (M-30 isolators by Minus-K Technology Inc. [Pri12, p.60]). This seismic isolation acts as a very soft spring, on which the optical table in TCOc 'floats'. The table needs to be carefully balanced by shifting weights on the table, ideally after each opening of the vacuum chamber.

7.2. Additional seismic isolation of the OMC to reduce acoustic coupling

In the course of this work, it was discovered that GEO 600 showed a larger than expected coupling of acoustic noise into the main gravitational wave signal. Since all main optics of GEO 600 are located in vacuum, acoustic coupling usually points to an

has technical reasons, mostly mirror polishing and surface figures. Surface imperfections could convert the wanted LG_{33} into an unwanted HOM of the same order [BFC+12].

[2] One of them has a transmission of about 100 ppm.

insufficient seismic isolation, in combination with either scattered light, or alignment sensitive systems, such as the OMC. In the end, this coupling could be traced to the OMC and the seismic isolation in which the OMC is located (TCOc). When misaligned, HOMs can overlap with the TEM_{00} eigenmode of the OMC, get transmitted to the photodiode and thus increase the measured shot noise.

Another layer of seismic isolation was added to the OMC by putting the OMC breadboard on four rubber (Viton) feet, and tested the acoustic coupling before and after. More specifically, we performed acoustic injections with a speaker, in which we used a swept sine signal (i.e. a mono-frequent signal which changes the frequency with time), which allowed us to maximize the injected noise power per bandwidth. We then judged the strength of the acoustic coupling[3] by creating spectrograms[4] of the measured GW strain signal at the time of each injection (one before and one after putting in the rubber feet). To simplify the comparison, we produced figure 7.2, which shows the ratio of the spectrograms of both injections (bottom of figure A.8). It shows the injected signal as spectrogram as well (top). The spectrograms during the time of both injections are attached as appendix A.8 on page 153.

Looking at the top spectrogram in figure 7.2, the injected signal appears as a diagonal line, and for the case of direct coupling, we would expect to find a similar line in a spectrogram of the strain sensitivity at the time of the injection. The ratio plot at the bottom of figure 7.2 shows the *ratio* of the interferometer response to identical acoustic injections with and without rubber feet, where stronger coupling appears in reddish, and lower coupling in blueish colors. Among the visible changes is what appears to be a glitch in the interferometer signal at about 160 s, it shows as a vertical line which is ignored here. Furthermore, the constant lines at 600 - 700 Hz have increased in height. These lines are the violin modes of the main suspension fibers, which are constantly visible in the GW measurement [SSHK10], and their height is known to vary according to the seismic conditions and lock duration. We see no connection between the violin modes of the main suspensions and any work done in TCOc. The red spot at approximately 90 seconds shows stronger down-conversion of acoustic signals of 90 Hz to 45 Hz in the GW strain measurement. This is not intended, but given that the measurement band of GEO 600 targets signals above 50 Hz [GHF+04], this is still acceptable.

We do see an improvement in the direct linear coupling of acoustic noise for frequencies above 400 Hz, and a great reduction in the non-linear coupling, where higher harmonics for injections of 200 - 800 Hz appear. Those harmonics are reduced by up to a factor of 100 by the installation of the Viton feet. While the reduction of acoustic noise coupling was a great success, it also raised concerns about the previously existing seismic isolation in TCOc, and ultimately led to the installation of an additional layer of seismic isolation, a second steel plate on rubber feet, as shown in [Pri12, p.60ff].

[3] Typically noise coupling is treated via the well known method of linear transfer functions. In this case however, we observed strong nonlinear coupling, which cannot be represented by a linear transfer function.

[4] A spectrogram is a time-frequency plot, and shows the evolution of a frequency plot (spectrum) over time.

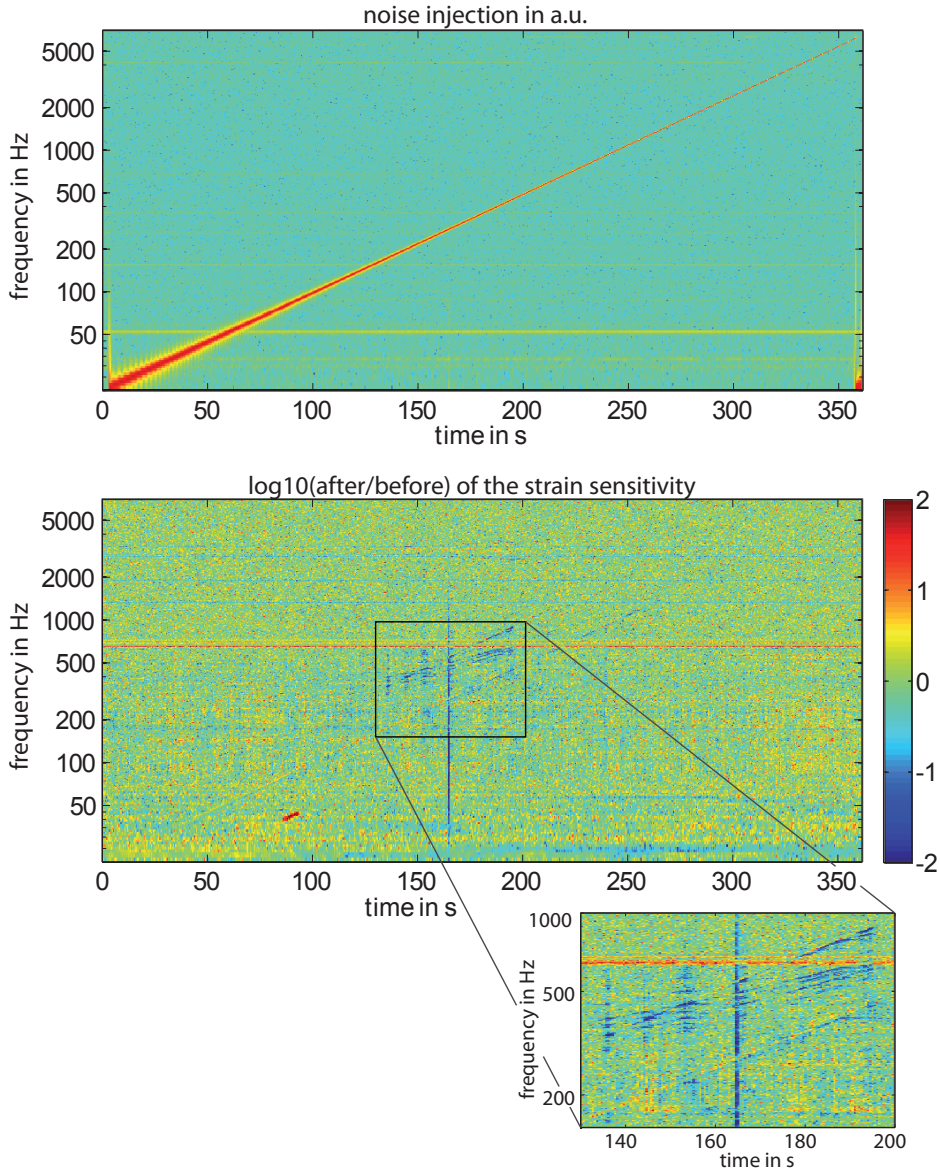

Figure 7.2.:
Top: Spectrogram of the injected acoustic swept sine signal. This signal was injected twice, before and after the installation of rubber feet underneath the OMC.
Center: Logarithm of the ratio of spectrograms during the injections. This plot was produced via building the pixelwise ratio of the strain sensitivity during both acoustic injections, and plotting the logarithm.
Bottom: Magnified view of the region with reduced nonlinear coupling from the ratio plot.

7.3. A movable lens stage for in situ mode matching

In August 2012, another improvement of the output optics was implemented on the two mode matching lenses. The lenses are used to match the beam coming from the output of GEO 600 to the TEM_{00} eigenmode of the OMC. Bad mode matching to the OMC will cause signal carrying light to be reflected off the OMC. This has implications for the sensitivity of GEO 600: less light leads to less power on the main photo diode and an increased relative shot noise level. Losses have a direct impact on the application of squeezed light in GEO 600 as well, they lower the amount of observable squeezing. Previously, mode matching to the OMC had to be done by hand, with the vacuum chamber vented (i.e. in air). While evacuating the chamber again, the position of the lenses or the balancing weights may slightly shift. Therefore it is desirable to be able to adjust the mode matching without opening the vacuum chamber, under vacuum condition.

In order to improve this situation, we mounted one of the mode matching lenses on a movable lens stage (Newport AG-LS25, vacuum version) such that we can change the mode matching in vacuum. Additionally, the stage allows much more precise positioning of the lens; it is moved in steps, with a minimal step size of 50 nm (the individual steps are however not entirely repeatable). The cables that were supplied with the stage were replaced with vacuum-compatible Gore-wire[5] and soldered using flux-free solder. Furthermore, it was necessary to design and fabricate custom vacuum compatible parts to bolt the translation stage to the table, the lens holder to the translation stage and to get it to the correct height. Figure 7.3 shows the assembly before the installation, without the lens.

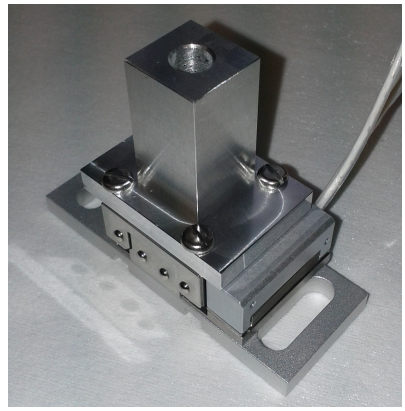

Figure 7.3.: A photograph of the translation stage with mounted custom parts before the installation.

Results

With the translational stage, it was possible to for the first time to optimize the mode matching in situ, i.e. under vacuum[6]. This is the first demonstration of in situ OMC mode matching in any GW detector.

The method to judge the quality of the mode matching was as follows: We locked the dual recycled Michelson interferometer, while the length of the OMC was continuously scanned. We then examined the signal in transmission of the OMC (from the main photo diode), this mode scanning is the same method as explained in chapter 2.3.2 and

[5] which is used in many parts of GEO 600

[6] It was however not possible to keep the OMC length locked to the GEO 600 output beam and quickly (i.e. performing many steps in a short amount of time) move the stage at the same time, hence the length of the OMC was scanned for this measurement.

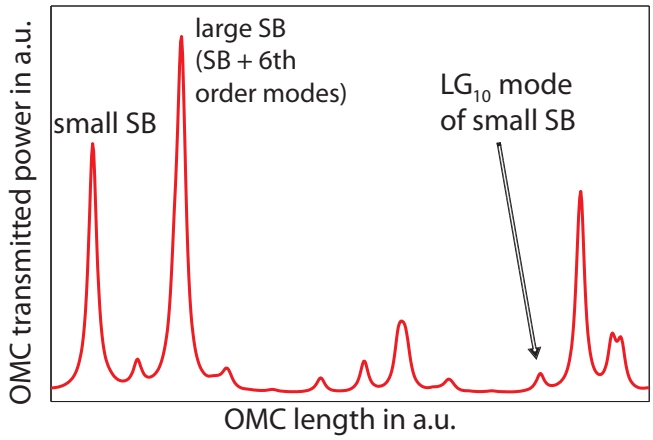

Figure 7.4.: Illustration of the measurement of the mode matching losses.

4.3. According to [And84], a mode mismatch between input beam and a cavity when coupling a TEM_{00} beam into said cavity will excite the first order radial mode of the cavity. This fact was used in determining the mode matching losses into the OMC. In the mode scan, we measured the light power of the small[7] sideband of the TEM_{00} carrier beam and the LG_{10} mode of it and compute their ratio. This measurement is illustrated in figure 7.4. In the case of GEO 600 we use the Michelson sideband for this measurement, since it is a TEM_{00} mode, and unlike the gravitational wave carrier, usually does not show a significant amount of HOMs.

Using the method mentioned above, we were able to improve the mode matching losses into the OMC from $(4.5 \pm 0.5)\%$ to better than $(3.4 \pm 0.4)\%$. These values are the mean values of five measurements each, and the error is assumed to be one standard deviation of those five measurements. The main limiting factor is the measurement of the amount of power in the LG_{10} mode of the Michelson sideband. In the mode scan it overlaps to some amount with the second order HOMs of the carrier, and after optimizing the mode matching via the translation stage, the power of the LG_{10} mode becomes very small and is hard to be distinguished from the background in the mode scan. Therefore the value of modematching losses after the optimization can be seen as upper limit.

[7] The RF modulation is intentionally added by an electro-optic modulator (EOM) to the TEM_{00} beam, before it enters the PRC. This produces two RF sidebands at 14.9 MHz ('Michelson sidebands'). When setting the OMC to transmit this sidebands, one appears to have larger power. The reason for this is that a HOM is resonant at the same time as one of the RF sidebands. Hence the naming 'small' and 'large' sideband. This flaw of the OMC was corrected by building a new one, as explained in the next section.

7.4. Replacing the OMC

In 2013, the decision was made to replace the existing OMC by a new one. The main driving force for this decision was that the observed squeezing value was lower than expected, and one possible explanation were losses from the OMC optics [C+11]. The frequent opening of TCOc may have led to dust or dirt on the OMC mirrors, therefore the OMC was to be removed from the vacuum tank and to be examined properly in the lab.

The old OMC has been performing as expected in terms of suppressing HOMs and the Michelson sidebands. However, one disadvantage was that 6th order modes co-resonate with one of the two Michelson sidebands. This has created the issue that one Michelson sideband appeared larger than the other in a mode scan of the OMC. In practice this had a minor effect on the usability of the OMC.

At this time we did not have an assembled spare OMC at hand, and did not want to reduce the Astrowatch duty cycle too much. As a consequence a new OMC was prepared with the objective to fix the issue with the 6th order modes, such that the OMC can separate the 6th order modes and the Michelson sidebands at 14.9 Mhz.

Later, the investigation of the original OMC revealed that it did not show the presumed losses. The cause for the observed low squeezing value [VM13] still remains to be found.

7.4.1. Simulations and Design

The existing OMC had performed well enough in terms of suppressing HOMs and the sidebands of the carrier beam. We decided to keep the same basic design of the OMC, using the same parts, but alter the length of the cavity to avoid overlapping sidebands and HOMs. This should keep the needed changes in the physical and control infrastructure small.

We applied the following criteria in determining the length of the new OMC:

1. The power of the Michelson control sidebands at 14.9 Mhz should be attenuated by a factor of at least 100 in transmission of the OMC (when locked to be on resonance for the TEM_{00} carrier).

2. The power of all HOMs which appear in GEO 600 should be attenuated by a factor of at least 100 in transmission of the OMC (when locked to be on resonance for the TEM_{00} carrier).

3. HOMs should neither overlap with each other (when they are of different order) nor with the Michelson control sidebands.

4. A similar length as the existing OMC is preferred.

Points 1 and 2 have been requirements for the construction of the first OMC [Pri12, p.47], point 3 aims to fix to avoid the current issue of the existing OMC, while point 4 ensures easy integration into the current infrastructure.

Using an analytic model, as explained below, and a numerical simulation in the software FINESSE [FHL+04], we determine that a new output mode cleaner in the same basic design as the original one, but with a cavity round trip length of 687.3 mm (old OMC: 66 cm [Pri12, p.49]) would fulfill all conditions mentioned above. The new OMC shares the same basic design with the old one, using identical parts, which are assembled in such a way, that the cavity is slightly longer. The change in length is achieved by scaling all lengths accordingly (compared to the old OMC), while keeping the angles the same. Keeping the basic design had the advantage of making the swap very easy, and should not change the mechanical resonances by much, keeping the first mechanical modes in frequency regions of multiples of the violin modes of the main suspensions of GEO 600.

FEM simulations

Before looking at the optical properties of the new OMC, we will investigate some mechanical properties. When changing the mirror positions on the fused silica baseplate compared to the old OMC, the frequencies of the mechanical eigenmodes of the OMC may shift in frequency. We compared the frequencies of the first ten mechanical modes of the new and the old OMC via an FEM (finite element method) model. As a simplification, the model treats the OMC as a monolithic fused silica structure. Not modeled are properties of the piezo actuator on the curved north mirror of the OMC (it is treated as part of the monolithic structure), nor the influence of the glue and the optical coatings. Still the model should be a good representation of the mechanical properties of the OMC, as indicated by the measurements below.

Table 7.1 shows the simulated frequencies of mechanical modes from the FEM model and actual measured frequencies. The resonance frequencies were measured by offsetting the OMC longitudinal lock point from the point of maximum transmission. This way, we introduce a strong linear coupling of noise in the OMC length to the transmitted power. Consequently, the mechanical resonances of the OMC show as peaks in a spectrum of the transmitted power. Figure 7.5 shows a spectrum of this measurement. The mechanical modes are identified by matching lines in the aforementioned measurement to the expected resonance frequencies.

Generally, the frequencies of mechanical modes of the old and the new OMC differ by less than one percent, with the exception of the 4th and 5th order mode. Therefore we do not expect complications due to mechanical modes of the new OMC. Moreover, the frequencies of the simulated and the measured mechanical modes agree well with each other[8], unlike for the case of the old OMC [Pri12, p.102].

High order mode and sideband suppression

One of the most important design aspects of the new OMC was to achieve the desired suppression of HOMs and the Michelson control sidebands. An analytical model of the OMC ensures that the requirements for the HOM suppression and spacing are met. The model that is used here is the one of a Fabry-Pérot cavity used in chapter

[8] except for mechanical modes of order 6 and 10, which could not be identified in the measurement

Mode order	old OMC (FEM, [Pri12])	new OMC (FEM)	new OMC measured
1st	1260 Hz	1250 Hz	1250 Hz
2nd	1906 Hz	1902 Hz	1899 Hz
3rd	2274 Hz	2291 Hz	2240 Hz
4th	2327 Hz	2440 Hz	2436 Hz
5th	2353 Hz	2445 Hz	2522 Hz
6th	2785 Hz	2782 Hz	?
7th	3558 Hz	3520 Hz	3506 Hz
8th	3767 Hz	3762 Hz	3609 Hz
9th	4170 Hz	4164 Hz	4164 Hz
10th	4733 Hz	4734 Hz	?
11th	5516 Hz	5578 Hz	5504 Hz

Table 7.1.: Comparison of the frequencies of the first ten mechanical modes of the old and the new OMC (obtained via FEM). The 6th and 10th mechanical resonances could not be identified, as there are no strong lines at or close to the expected frequency.

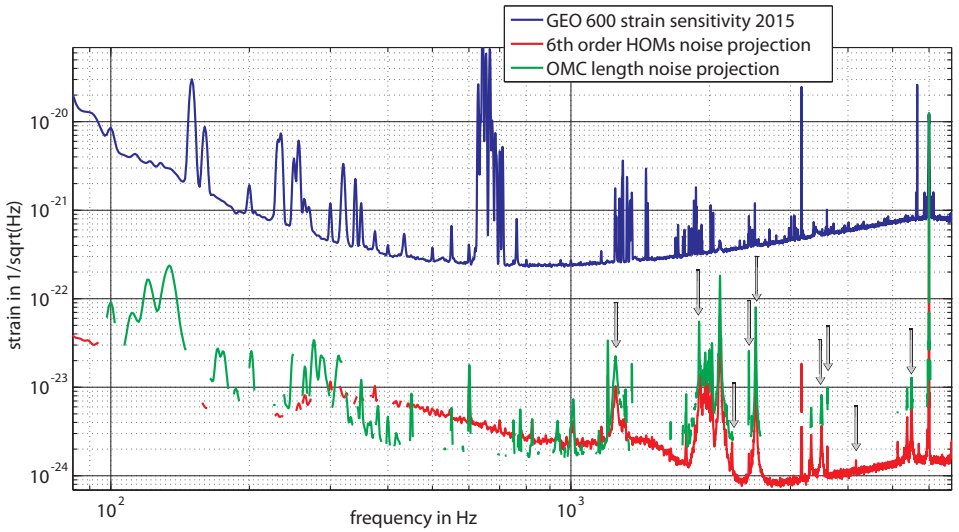

Figure 7.5.: This figure shows the typical sensitivity of GEO 600 in 2015 (blue), the 6th order HOM noise contribution (red, from figure 2.9), and the coupling for length noise in the OMC (green). Both the OMC length coupling noise and the noise due to the 6th order HOM are well below the measured sensitivity of GEO 600. The large lines at 3.2 and 6 kHz are added intentionally via the piezo in the OMC. The mechanical resonances of the OMC are indicated via gray arrows.

2.3.2. We view the OMC as a half symmetric, folded Fabry-Pérot resonator, with a half length $L_{1/2}$, and two curved mirrors with a radius of curvature R_c. All properties are now computed as in the literature [Sie86], the free spectral range (FSR) of the OMC (c being the speed of light in vacuum)

$$\mathrm{FSR} = c/(2L_{1/2}) \approx 436\,\mathrm{MHz}, \tag{7.1}$$

the cavity g-factor

$$g_1 \cdot g_2 = (1 - L_{1/2}/R_c)^2 = 0.729, \tag{7.2}$$

and the round trip Gouy phase shift Θ of

$$\Theta = 2\arccos(\sqrt{(g_1 g_2)}). \tag{7.3}$$

A high order mode will experience a phase shift proportional to its mode order, a TEM_{mn} mode for example will have an additional Gouy phase of $\Theta_{mn} = (m+n)\Theta$ over the fundamental TEM_{00} mode. This allows us to compute where a HOM of a specific order will appear in the mode scan. The power transmission factor T of those HOMs in the OMC can be calculated by the Airy function:

$$T = \frac{1}{1 + 4(F/\pi)^2 \sin^2(\pi\nu/\mathrm{FSR})}, \tag{7.4}$$

for which we assumed the OMC to be lossless, ν represents the desired frequency and $F = 155$ represents the cavity finesse. Figure 7.6 shows the results of this model, by plotting one FSR of the new OMC, along with the frequencies and transmission factors of HOMs up to an order of 11 and the Michelson sidebands at 14.9 MHz. It can be seen that all of the considered HOMs and the sidebands do not overlap and comply with the requirement of an attenuation of at least a factor of 100. Note that we typically do not see modes of orders higher than 11 in the output beam of GEO. Nevertheless, the attenuation of HOMs up to an order of 20 was checked, and all are attenuated by the required factor of at least 100.

7.4.2. Results

The new OMC was finally installed in May 2013, and has been in use since then. We find that it works as expected, with the desired suppression of HOMs and sidebands. Moreover, the 6th order modes are now clearly separated from the former 'large' sideband. Figure 7.7 compares a mode scan of the old and the new OMC, showing that the separation of the 6th order mode and the Michelson control sidebands is now possible. Furthermore, the peaks in the modescan, caused by HOMs appear as predicted by the analytical model above.

7.5. Summary

Several improvements to the OMC were achieved in the course of this work. The installation of additional seismic isolation to the OMC significantly lowered the coupling of acoustic noise to the GW measurement.

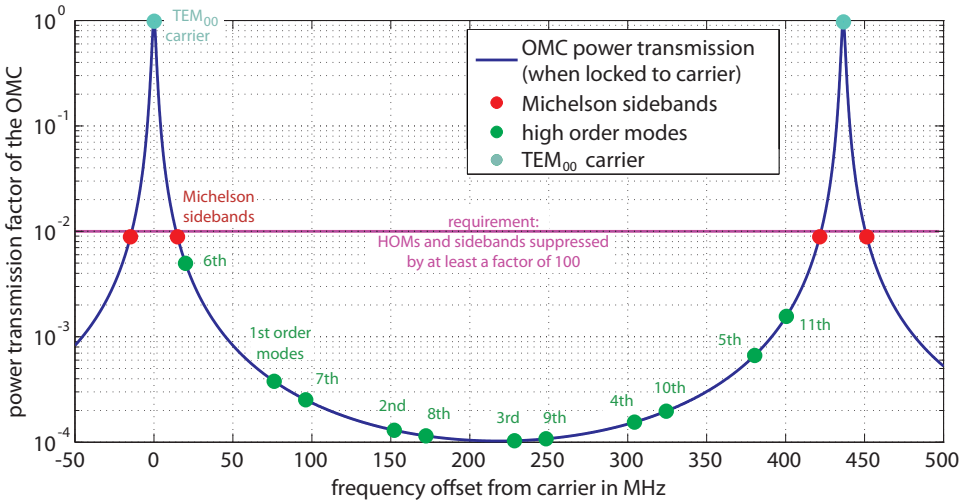

Figure 7.6.: This figure shows the simulated frequencies of HOMs and their transmission factor in the new OMC. With this representation it is easy to identify HOMs in a modescan of the OMC, furthermore it shows that none of the first 11 HOMs overlap with the sidebands.

Furthermore, this work demonstrated the first in situ mode matching under vacuum of the interferometer beam into the OMC in any of the GW detectors. This ensures the best possible mode matching, as opposed to the conventional way of mode matching by hand under atmosphere, where the optics may slightly move when the vacuum chamber is evacuated again. Also, the planned power increase in GEO 600 may change the mode matching condition between the GEO 600 output beam and the OMC.

A new OMC was designed for GEO 600, with a different length, such that a high order mode is no longer resonant for the same OMC length together with one of the Michelson control sidebands. Further characterization of the new OMC was done, and unlike for the old OMC, the mechanical modes of the new OMC are in good agreement with FEM simulations.

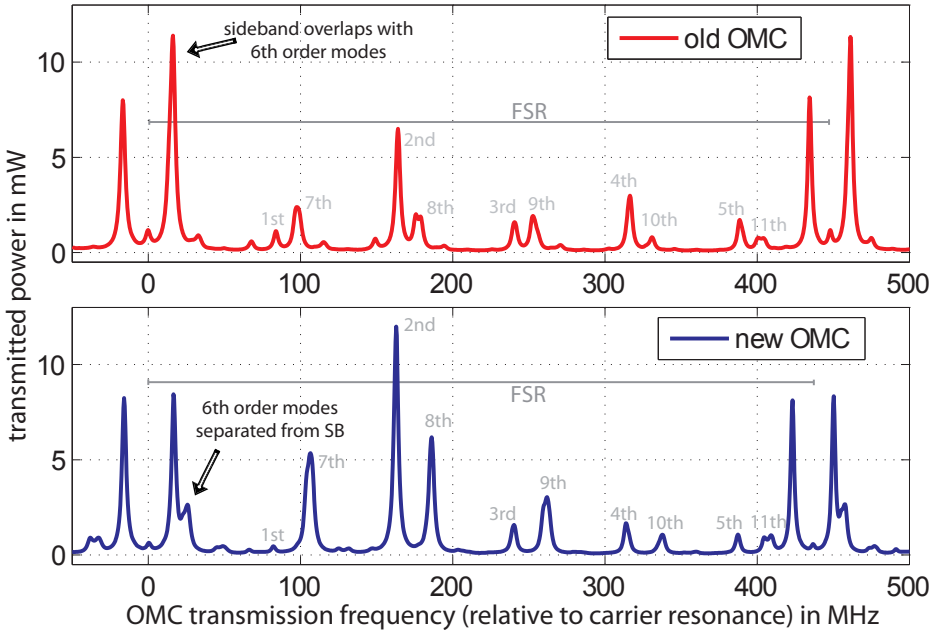

Figure 7.7.: This figure shows mode scans done with the old and the new OMC. Both cases plot slightly more than one free spectral range, the x-axis is scaled to show the resonance frequency of the OMC in MHz, relative to one resonance of the carrier beam. Due to different lengths of the OMCs, HOMs will be resonant at slightly different frequencies, which leads to the intended separation of the 6th order mode and the Michelson control sideband at 14.9 MHz. Note that this figure should only be used to compare the position of HOMs, but not their strength. The reason is that the amount of HOMs depends on the exact interferometer state (thermal state, alignment, etc.) and both measurements shown above were not performed at the same time. Note that due to a hysteresis in the piezo actuator in the OMC (which has been observed before [Pri12, p.65], not all positions of HOMs match exactly with figure 7.6.)

CHAPTER 8

New design for electrostatic actuators

The previous chapters of this work have shown methods of mitigating issues with high order modes (HOMs) and unwanted light in gravitational wave detectors (GWDs). Several solutions of dealing with HOMs and scattered light have been presented in earlier chapters of this work. They work either by different methods of deforming the optics (chapter 3 and 4) or the wavefront directly (5), and by filtering the HOMs out (in chapters 6 and 7).

Thermally induced HOMs and scattered light can be addressed in the design phase of an experiment already. Ideally, no objects that would restrict the beam size and/or possibly cause backscattering should be installed close to the laser beam. In reality however, the optics of GWDs need to be actuated upon, such that they can be brought to and kept at their operating position and the optical cavities in the interferometer are on resonance. Traditionally, all GWDs employ a hierarchical system of actuators on different levels of the multi-stage pendulums that suspend their optics. Mirror level actuators will by definition be located close to the optics, and thus are prone to the issues stated above. Electrostatic drives (ESDs) perform the role of mirror-level actuators in GEO 600 and in advanced LIGO [HDG+07], [HC+10].

This chapter presents an alternative geometry for ESDs, which provides the maximal clear aperture of the optics, unlike the conventional design that is used in GEO 600 and advanced LIGO. Furthermore, this setup is much simpler and shows less coupling of seismic noise to length noise.

The presented geometry has been considered for GEO 600 [ADD+14], but due to a larger obtainable force, the conventional design was chosen for GEO 600 in the end.

It will be shown that the obtainable force of the new geometry is too small to be feasible for GWDs with their large optics. However, it is well suited for many of the smaller (with optics of $\leq$100 g) experiments in the field of GWDs, which often have

similar requirements as their kilometer-scale cousins. As a consequence, this chapter will focus on the application of the new ESD geometry in the context of the AEI-10 m prototype interferometer.

Parts of this chapter have been published as [WHB+15].

8.1. The AEI 10 m Prototype facility

A prototyping facility for advanced technologies related to interferometric GWDs is being set up in the Albert Einstein Institute in Hanover, Germany. The AEI-10 m Prototype interferometer facility (AEI-10 m) features an L-shaped ultra high vacuum (UHV) system, with 10 meter long arms and seismically isolated optical tables. It will house a power-recycled Michelson interferometer with Fabry Perot cavities in the arms. In addition to the seismically isolated tables, triple stage pendulum suspensions are used for the main optics. The interested reader can find more information on the AEI-10 m in [GBB+10] and [GHL+12].

One of the goals for this interferometer is to reach a sensitivity better than the standard quantum limit. For this, large beams are used in the AEI-10 m, that will make use of the full aperture of the 100 g heavy main mirrors to keep the coating thermal noise small. One consequence of this is that the conventional mirror level actuators cannot be used.

8.2. Conventional mirror level actuators in GWD and GWD prototypes

All of the GWDs and smaller scale prototype experiments like the AEI-10 m take great care of seismically isolating their optics. Therefore, all direct actuation on the optics must happen contact-free, to not introduce a seismic shortcut. Two main technologies for mirror level actuation are used in the field of GWDs.

The first method is magnetic actuation. Usually this is realized by a combination of permanent magnets glued to the back of the mirror and coils that are used as electromagnets to actuate on the magnets. For displacement sensitive optics, the coils will have to be seismically isolated, for example by also suspending them as multi-stage pendulums, just like the optics.

This kind of actuation is provided in GEO 600 via the OSEMS (see chapter 6) for the upper- and intermediate pendulum stages and for mirror level actuation on some auxiliary optics, but not directly on the main mirrors. Initial LIGO, its enhanced version eLIGO and Virgo have used magnetic actuation on their main mirrors.

Magnetic actuation has the advantage of being able to exert large forces on the optic, as well as being a well understood technology. There are downsides as well though. The permanent magnets that are glued to the mirror lower the mechanical quality factor of the mirror, which may increase the thermal noise of the mirror substrate [SMYT11]. Another issue is the Barkhausen noise, which is caused by

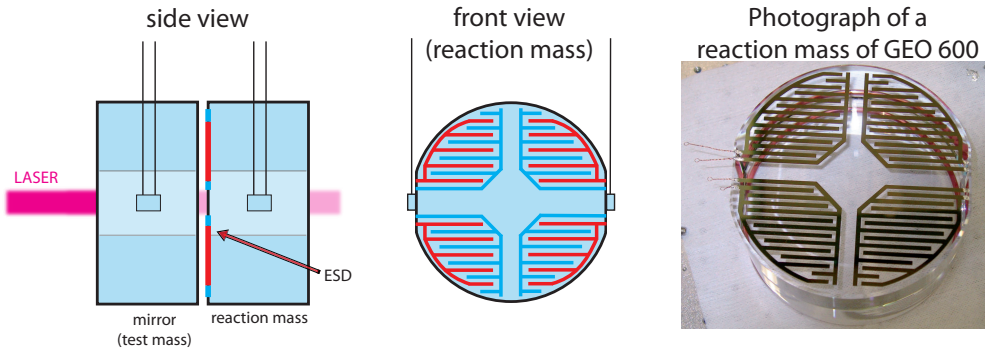

Figure 8.1.: Schematic view and photograph of the ESD comb drive in GEO 600 [WHB+15].
Left: Side view of the mirror that is actuated upon and the reaction mass with the ESD electrodes.
Center: Front view of the comb-shaped ESD electrodes on the reaction mass. The electrodes are colored in red and blue to show the different polarities.
Right: Photograph of the reaction mass with ESD comb drive from GEO 600.

magnetic domain flipping in permanent magnets and can possibly introduce noise in this way [SC+09].

The second method is the actuation via electrostatic forces. This kind of actuator has been pioneered by GEO 600 [ADD+14], and a similar design will be used in aLIGO as well [CAC+12]. The setup of ESDs used in GWDs is based on comb-shaped electrodes that are attached to the surface of a reactions mass behind the mirror. The reaction mass is seismically isolated in the same way as the mirror (sometimes called 'test mass'), i.e. via a multi stage pendulum. When a voltage is applied between the electrodes of the ESD-comb, inhomogeneous electric field will extend into the test mass. Being a dielectric[1], the test mass will experience a force that pulls it towards the reaction mass[2]. Figure 8.1 shows a photograph and schematic drawings of the ESD comb pattern in GEO 600.

The actuation via ESD has several advantages over using magnets, the main one being that no magnets need to be glued to the optics, which can lower the mechanical quality factor of the optic and therefore lead to increased thermal noise. Moreover, Barkhausen noise and noise coupling via spurious magnetic fields (which could be caused by ring- and side heaters or other electric components nearby) can be neglected when using ESD actuation.

Despite of having some advantages over the use of magnets, electrostatic comb drives can pose challenges for the use in GWDs. One of them is the reduced free aperture of the mirror in transmission, which can be intolerable for some experimental setups, like the AEI 10 m. Other challenges are the thin film damping [DHN+11], which can cause additional noise. It is associated with Brownian force noise due to

[1] fused silica in the case of GEO 600 and advanced LIGO
[2] The reaction mass will see the same force, pulling it towards the test mass according to Newton's third law of motion.

residual gas molecules[3], which is strongly amplified by the close distance between the reaction- and the test mass.

One of the largest challenges that are associated with electrostatic actuation is the matter of charges on the optics, which can change the total force of the actuator, or introduce cross coupling between different degrees of freedom in the case of distributed charges. The build up of charges on the optics can happen in a number of ways. For example, when the mirror comes in contact with an ESD electrode, by touching it, or due to friction with gas molecules if the vacuum system is vented. Another mechanism could be charging via UV radiation from ion getter vacuum pumps. Several mitigation strategies have been developed at GEO 600 and advanced LIGO for the issue of charges, for example by intentionally shining UV light onto the optics [HDG+07], or by using ionized nitrogen [UFRW14].

The next sections introduce and simulate an alternative geometry for ESDs which solves some of those issues of conventional ESD comb drives.

8.3. Geometry

The alternative geometry for ESDs consists of two parallel plates located either at the sides, or above and below the mirror, as illustrated in figure 8.2. If a voltage is applied to the ESD plates, the electrical field will result in a force on the dielectric mirror. An obvious benefit to this arrangement is that the full mirror aperture remains usable, which is a requirement for the AEI-10 m.

8.4. Basic principle & analytical model

The working principle of ESDs is that an inhomogeneous electric field is built up in a dielectric medium (i.e. the mirror). If the mirror is not centered longitudinally between the plates, it will be subject to a force that pulls it towards the center of the plates along the gradient of the electric field. In order to analyze our new ESD design, we first turn to a simplified analytic model, before using finite element (FE) simulations later. Our simplified model shall be the case of a dielectric slab inserted into a parallel-plate capacitor (as in [Mar84]), which is pictured in figure 8.3. Calculating the force for this simple model is a standard problem in electrodynamics. The force is given by [Mar84]:

$$F = (\epsilon_r - \epsilon_0) \cdot E_D \cdot U_{ESD}^2 / 2 d_{\text{plates}}, \tag{8.1}$$

where E_D is the plate depth, U_{ESD} is the voltage across the plates and d_{plates} is the plate separation. ϵ_0 and ϵ_r are dielectric constants (see also table 8.1 for the values and symbols used in this chapter). This formula is only valid under certain assumptions:

1. There is no gap between the dielectric and the plates.

[3] All GWD and smaller GWD prototype experiments that achieve a high displacement sensitivity are housed in a vacuum system.

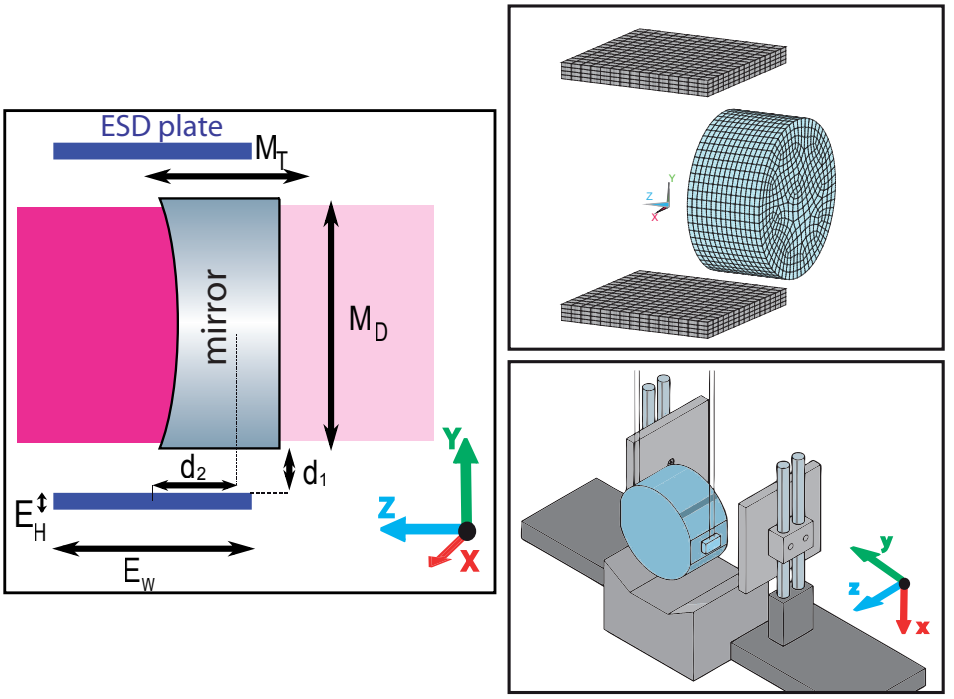

Figure 8.2.: Presentation of the alternative ESD geometry [WHB+15].
Left: Basic geometrical setup of the ESD plates with respect to the main test masses/mirror. Please note that this sketch can be either side-view or top-view, depending on the actual installation. The probing laser beam is shown in purple while the beam transmitted through the mirror is painted with a lighter color. The dimensions M_T, M_D, E_H, E_W, and $d_{1,2}$ are defined in table 8.1.
Top right: View of the FE model that was used in this article. The elements modeling the space around mirror and ESD plates are omitted here for clarity.
Bottom right: A mock up drawing of what a potential installation might look like.

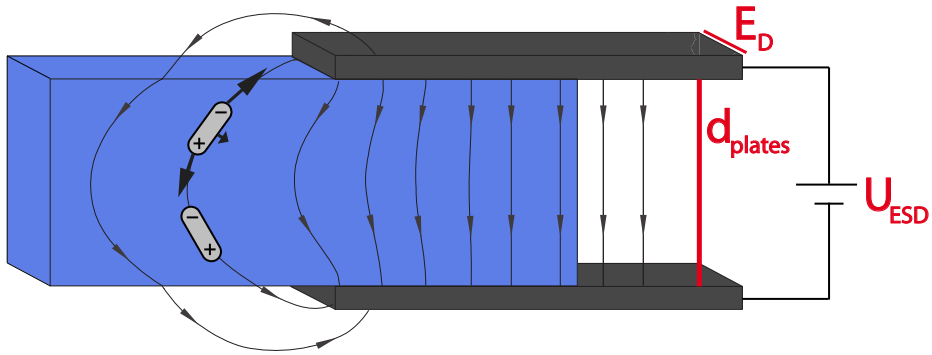

Figure 8.3.: Illustration of the simple model. A slab of a dielectric material between two parallel capacitor plates. The electric field is pictured with arrows (illustration modified from [Mar84]). Electrical dipoles on the left show the origin of the force in the inhomogeneous field.

2. One end of the dielectric material is in a homogeneous electric field between the plates.

3. The other end of the dielectric is far outside of the plates, it does not 'see' the electric field of the plates.

We can use the formula for the simplified case to approximate the order of magnitude of the force that the ESD will provide. The exact strength of the force must be determined by finite element methods, since none of the assumptions mentioned above is exactly fulfilled.

To estimate the force that the ESD can provide using the simplified formula, first we compute an effective dielectric constant $\epsilon_{r_{\text{eff}}}$ for a mirror between the two plates, since it does not fill the space between the ESD plates completely. We determine a 'fill factor' of $A_{\text{mirror}}/A_{\text{plates}} = \pi r^2_{\text{mirror}}/E_D \cdot d_{\text{plates}} = 0.54$. Now we can multiply the fill factor with ϵ_r and get an effective $\epsilon_{r_{\text{eff}}} = 2$. With the values given in table 8.1 and an $\epsilon_{r_{\text{eff}}}$=2, equation 8.1 gives a position independent force of the order of a few μN.

8.5. Quantitative analysis using FEM

To get a more precise estimate of the force than the order of magnitude estimation from the simple model above, we use an FEM model. The FEM simulations in this article were performed with the software ANSYS 13 [ANS], using the macro 'EMFT'. The parameters used throughout this analysis, unless noted otherwise, are given in table 8.1.

The origin of the coordinate system is located in the center between the ESD plates. The Z-axis points from the flat mirror surface to the center between the plates (sometimes called 'longitudinal direction' or 'beam direction'). The Y-axis

Mirror diameter	M_D	4.90 cm
Mirror thickness	M_T	2.45 cm
Mirror material	-	fused silica
Mirror dielectric constant	ϵ_r	$3.7\epsilon_0$
Mirror mass	m	102 g
Pendulum length	l	20 cm
Lateral distance mirror-ESD	d_1	1.05 cm
Long. relative position mirror-ESD	d_2	3.075 cm
Applied voltage	U_{ESD}	1000 V
ESD dimensions (one plate)	E_WxE_HxE_D	5 cm x 0.5 cm x 5 cm
ESD plate separation	d_{plates}	7 cm
Number of nodes	n_{nodes}	221944

Table 8.1.: Properties used for the FE simulations presented in this chapter.

points towards one of the plates and the X-axis is perpendicular to the Y and Z-axes. Figure 8.2 shows the geometry of the new ESD setup. The force that the ESD applies on the mirror in dependence of the relative longitudinal position between mirror and ESD is plotted in figure 8.4. From this dependency we also find the best operating distance between mirror and ESD: the maximum and to first order flat force of 1.4 μN appears when the mirror is shifted by 3.075 cm relative to the ESD plates. We choose this position as our potential operating point.

From the force the magnitude of the ESD range can be deduced. We assume that the mirror is suspended as a pendulum of the length l. The full (DC) actuation range z_{DC} is reached when the pendulum back action force cancels the ESD-force:

$$z_{\text{DC}} = -F_{\text{operating}} \cdot l/mg \approx 0.28\,\mu\text{m (at 1 kV)}. \tag{8.2}$$

From the equations 8.2 and 8.1 it also follows that the range is inversely proportional to mirror mass and plate separation:

$$z_{\text{DC}} \propto 1/(m \cdot d_{\text{plates}}) \tag{8.3}$$

This is the reason why this new kind of ESDs is only suited for the case of small mirrors.

Figure 8.5a shows that the force that can be obtained scales quadratically with the applied voltage, if the mirror is in the operating position. This agrees very well with the prediction from equation 8.1. The amount of force per voltage can be used to further characterize the ESD. If we write the quadratic relation as $F = \alpha U_{ESD}^2$, then we obtain $\alpha = 1.4 \times 10^{-12}\,\text{N/V}^2$. For comparison, the conventional ESDs in aLIGO and GEO 600 can deliver $2.9 \times 10^{-10}\,\text{N/V}^2$ and $4.9 \times 10^{-10}\,\text{N/V}^2$ respectively ([SMYT11], [Str06]).

Figure 8.5b shows how the force changes when the plate separation is varied. The simple analytic model predicts an inverse square law (note that $\epsilon_{r_{\text{eff}}}$ depends on the plate separation, as explained above), the FE model however returns a force inversely

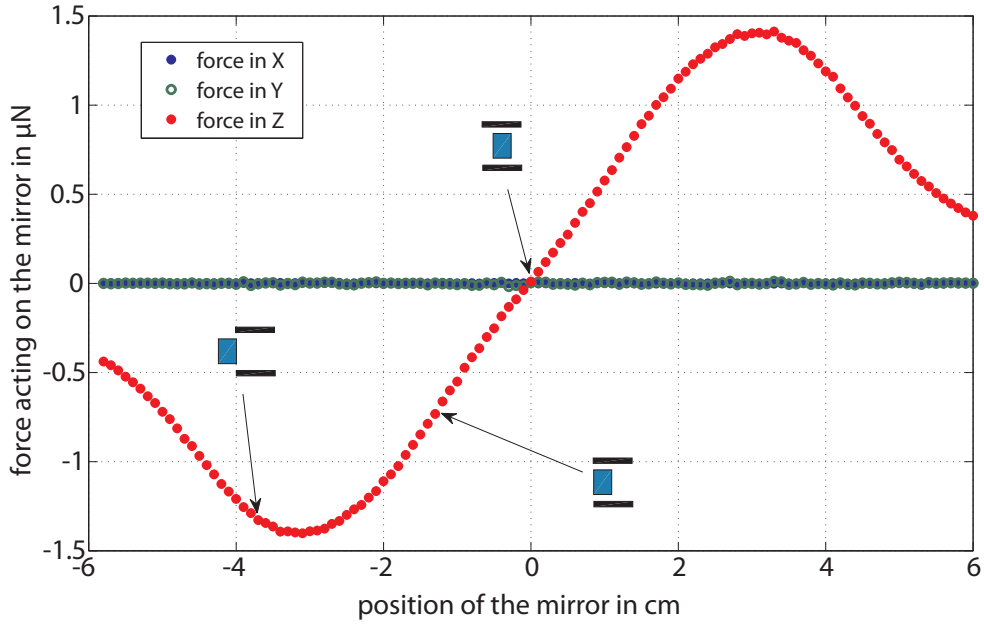

Figure 8.4.: Longitudinal force on the mirror, versus relative longitudinal position of mirror and ESD. The x-axis shows the relative distance between the mirror center and the center of the capacitor plates [WHB+15].

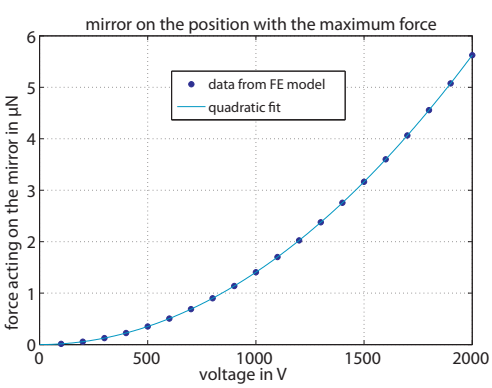

(a) Force versus voltage.

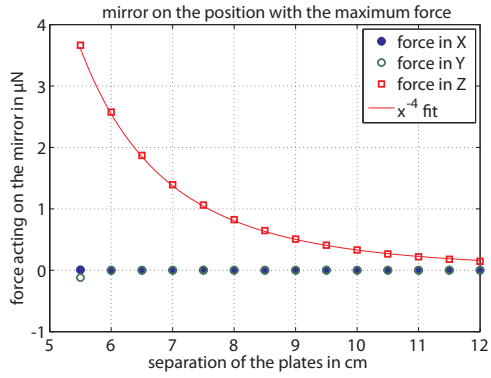

(b) Force in dependence of the plate separation.

Figure 8.5.: Figure (a) shows the force on the mirror for different voltages. (b) shows how the force depends on the plate separation (assuming that the mirror is at the ideal operating position). Both plots assume the relative position of mirror and ESD to be the position with the optimal force [WHB+15].

proportional to the fourth power of the plate separation. The stronger drop-off may be due to a decreased region with homogeneous electrical field for large plate separations.

It is important to point out that the AEI-10 m prototype will have a hierarchical system of several actuators, of which the ESDs will be the ones with the smallest range and the fastest actuation. Coil magnet actuators with larger range will be located at the upper pendulum stages and in the seismically isolated tables. These actuators are however less suited for fast actuation, because above the pendulum resonances in the order of 1 Hz, the mirror movement will be filtered by the pendulum transfer function of f^{-2} per pendulum stage. The exact frequency range and expected RMS actuation voltage of the ESDs will depend on the properties of the aforementioned other actuators (not all of which are installed at the time of writing the thesis at hand), as well as on the specific implementation of the longitudinal length control scheme.

8.6. Requirements & noise

Provided that the mirror and ESD are positioned ideally, the derivative of the force provided by the new ESD configuration, is zero. Together with the performance of the seismically isolated tables in the AEI-10 m prototype interferometer [WBB+12], it is possible to mount the new ESD directly to the table without additional seismic isolation. Figure 8.6 shows the expected coupling of seismic noise through the new ESDs for non-ideal positioning of the mirror with respect to the ESD plates. Even with the ESDs 3.75 mm off from the ideal longitudinal position, the noise contribution in the AEI-10 m interferometer would still be lower than the sum of all other classical

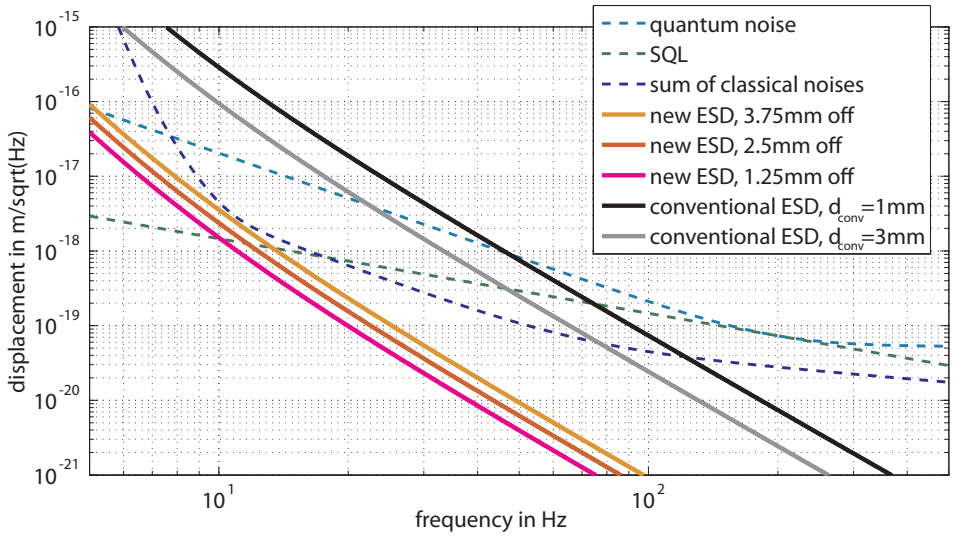

Figure 8.6.: Comparison of seismic noise coupling in the AEI-10 m prototype interferometer for ESDs with the conventional design and our novel ESD configuration. The reddish traces indicate projections of how much table movement would couple into the interferometer if the novel ESD configuration is used, but the plates are not located ideally. The dashed lines indicate the sum of all classical noise (for example laser-, thermal-, seismic noise etc.), quantum noise and the Standard Quantum Limit (SQL) of the planned AEI-10 m sub-SQL interferometer. We have also included a projection of the seismic noise coupling if conventional ESDs mounted on the tables would be used, where d_{conv} indicates the distance between the mirror and the ESDs (gray and black traces). As one can see, the seismic noise coupling of the novel ESD design is lower by about a factor 100 compared to a conventional ESD design [WHB+15].

noise sources at all frequencies.

In order to allow a direct comparison of the seismic coupling of a conventional ESD design and our new ESD design, we included the expected noise coupling from a conventional ESD design in figure 8.6 (see gray traces). For this analysis we assumed the force on the mirror for a conventional comb-shaped ESD design, which is given by [Gro03, p.13]:

$$F = a \cdot \epsilon \cdot \epsilon_r \cdot U_{ESD}^2 \cdot d_{\mathrm{conv}}^{1.5}, \tag{8.4}$$

where d_{conv} is the separation between the mirror and the ESD and a is a geometry factor that depends on the actual shape of the electrode pattern, and the dimensions of the mirror and the ESD. The strong scaling of the force with d_{conv}, explains the large coupling of seismic from the ESD to the test mass. For this analysis we assumed that both kinds of actuator provide the same longitudinal range and are bolted to the tables. The new ESD design provides a reduction in seismic noise coupling of about a factor of 100 compared to the conventional design.

Moreover, we also investigated how precisely the ESD plates (of the new design)

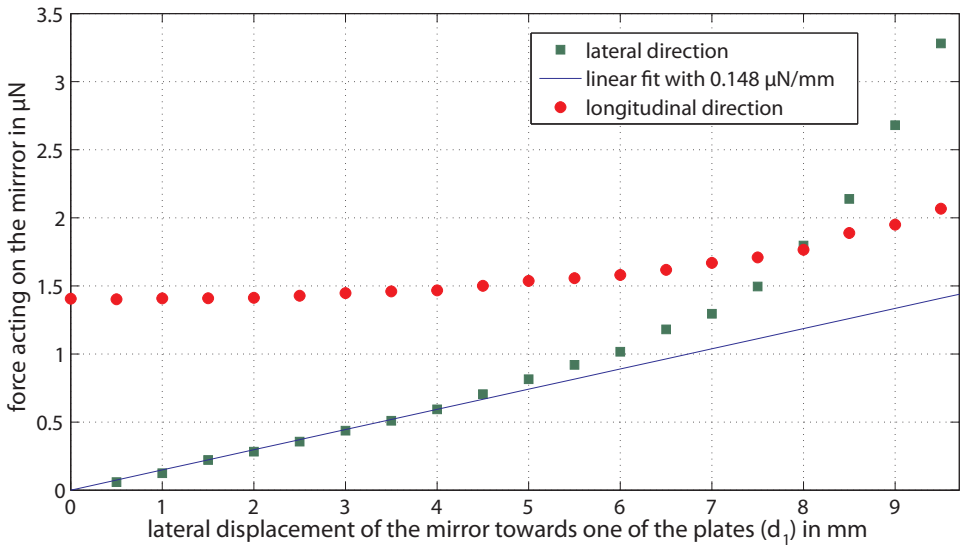

Figure 8.7.: Lateral force on the mirror, versus relative lateral position of mirror and ESD [WHB+15]. The lateral force is proportional to the lateral displacement (for small displacements).

have to be positioned in the direction along their surface normal. If the mirror is closer to one of the ESD plates, it will see a force towards the closer plate. This situation has been simulated using the FE model. The results can be seen in figure 8.7. If we arbitrarily set a limit for the force towards the closer plate to 1/10 of the force in beam direction, then the mirror must be centered between the plates within slightly less than 1 mm. For the case of small lateral displacements in the range of a few millimeters[4] we can approximate the force in lateral direction to scale linearly with the lateral displacement. In this case, the linear scaling factor is $0.148\,\mu\mathrm{N/mm}$.

All investigations in this work assume an uncharged mirror. Charges could be introduced to the mirror in several ways, for example by touching it, if the mirror touches the ESD plates, or through friction or migration of charges that may occur when evacuating or venting the vacuum system in which it sits.

We expect a significant change in the force provided by any kind of ESD for a charged mirror, and this is true for both the conventional type of ESD and for the presented geometry. It has been demonstrated in the past that UV light can be employed for reducing the total charge of a mirror [HDG+07]. However, the amount and distribution of charges that can be expected are not known, and will have to be determined experimentally.

[4] An experienced experimenter will be able to achieve this easily.

8.7. Asymmetries in the vicinity of the ESD

As mentioned earlier, the main optics of the AEI-10 m interferometer will be hung as a multi-stage pendulum, which is usually the case for gravitational wave detectors and their related, scaled-down prototyping facilities. In order to keep the mechanical losses low, the pendulum wires are typically dimensioned such that they are loaded to a significant amount of their breaking stress [TCH+12]. In the case of the AEI-10 m prototype, it is planned to use fused silica fibers with a diameter of 20 μm for the lowest pendulum stage. To protect the main optics if a fiber breaks, a 'catcher' will be placed underneath each suspended mirror.

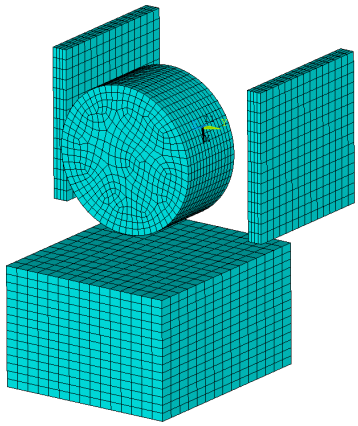

Figure 8.8.: Geometry of catcher, mirror and ESD plates for the FE model.

One could argue that such catchers may alter the performance of the ESDs proposed in this article, as they break the symmetry of the electrostatic environment close to the ESDs. Such asymmetries may introduce a (position-dependent) torque on the mirror, which would lead to coupling of longitudinal mirror motion to mirror alignment. We do not expect the same effect from symmetrically positioned parts around the ESDs. The goal of this section is to estimate upper limits due to this effect.

We simulated the effect of a sample configuration with catcher, which is modeled as a cuboid. In this simulation, the ESD plates are at the sides of the mirror. The catcher is positioned in such a way that it is centered below the mirror at the ideal operating point. It sits 1 cm below the mirror and is 4 cm tall. In the beam direction, the catcher projects from the mirror by 1 cm on each side. The catcher is 6.5 cm wide and is assumed to be at ground potential, while the ESD plates were set to +500 V and -500 V. The geometry of ESD plates, mirror and catcher, which was assumed for the FE model, is given in figure 8.8. The inclusion of a metal catcher in the simulation caused no significant change in the longitudinal force of the ESD. It did however produce a lateral force of about 20% of the longitudinal force towards the catcher (at the operating position). Also there will be a torque around the Y-axis. Fortunately, the torque around the Y-direction, which is the strongest, is flat to first order if the catcher is centered with respect to the mirror. It is important to note that this crude catcher geometry is used as a worst case scenario to set an upper limit. Still, this analysis showed that a metal catcher, as it is usually used, can introduce a coupling of longitudinal actuation to other degrees of freedom. This should be kept in mind when designing mechanical structures such as the catcher in close vicinity of the ESDs. To reduce the influence of mechanics around the mirror, one may, for example, use a different catcher geometry or material, such as Macor or polyether ether ketone (PEEK), a vacuum compatible polymer. Another way may be to increase the distance between catcher and the mirror. The

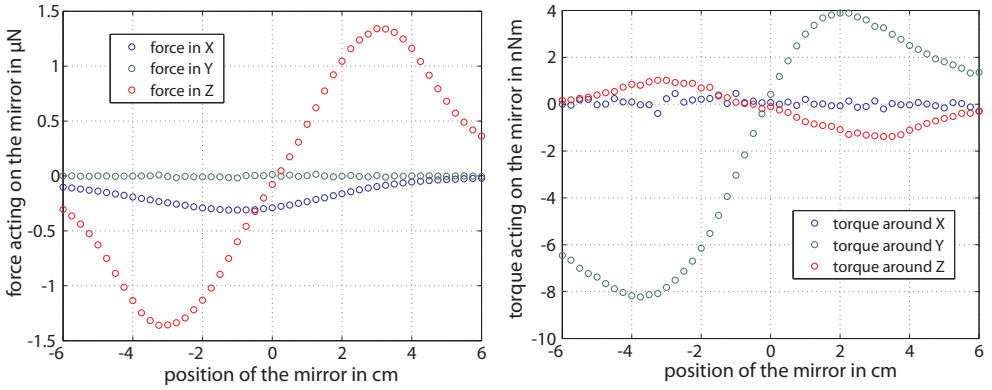

(a) Force on the mirror.

(b) Tourque on the mirror.

Figure 8.9.: Force and torque on the mirror with a metal catcher close to the mirror. The catcher's position was kept constant (with the z-coordinate of its center of mass at -3.075 cm), while the mirror was moved [WHB+15].

AEI-10 m interferometer suspension will feature 'fibre guards', an aluminum semi-enclosure around the fibres that suspend the mirror. Their presence will necessitate the ESDs to be installed at the top and bottom of the mirrors. A detailed description of the design of the AEI-10 m prototype suspensions can be found in [Ham].

8.8. Verification and accuracy of the FE model

As the work presented in this chapter relies heavily on the use of FEM simulations, it is crucial to validate them. Here we present three methods of validation. Additionally, an ANSYS sample code is attached as appendix A.4 on page 153 to make the analysis in this chapter reproducible.

A good method of validating the results obtained by the FE model is to compare it to an analytic model. In the case of this work, a simplified analytic model has been presented in section 8.4, with the result that the force obtained via the analytic model is in the same order of magnitude as predicted by the FE model.

A second way to validate the results of the FE model is to cross check if the same result can be obtained with a different method instead of using the macro 'EMFT'. For this a different approach of obtaining the results from figure 8.4 was chosen that relies on basic physics. This approach considers the ESD as a plate capacitor, the potential energy E_{pot} stored in its electric field is:

$$E_{\mathrm{pot}} = \frac{1}{2} C V^2, \tag{8.5}$$

where C is the capacitance and V the voltage. In the FE model it is possible to obtain the potential energy by summing over all elements. By doing this we can get

the relation between capacity and relative position between mirror and ESD plates, as shown in figure 8.10a.

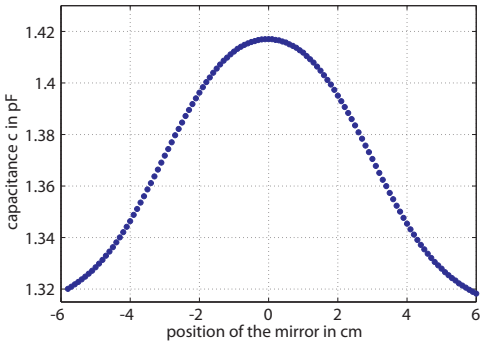

(a) Capacitance of the system.

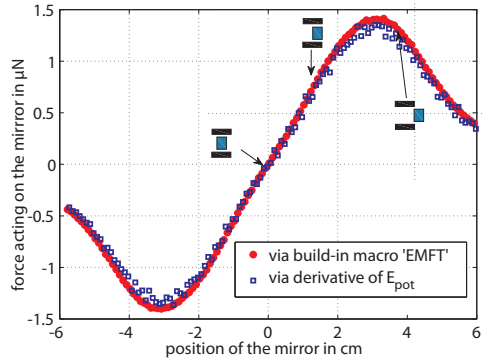

(b) Force on the mirror, computed with the macro 'EMFT' and with equation 8.6.

Figure 8.10.: Check of the macro 'EMFT', based on the total potential energy stored in the system, which is proportional to the capacitance.

The force on the mirror F can be obtained from the potential energy of the system as well. Analogue to the case of simple mechanics, we obtain the 'equation of motion' by taking the negative derivative of the potential energy. In this case however, we are not interested in the time evolution, but in what happens when the position of the mirror is varied:

$$F = -\frac{d}{dz} E_{\text{pot}} \tag{8.6}$$

The calculation of the force has been carried out according to 8.6 and figure 8.10b shows a comparison of the results of both methods. We find that both deliver nearly identical results. Therefore we conclude that the ANSYS macro 'EMFT' returns correct results.

Another important aspect of any FE model that needs to be evaluated is its meshing. In this work, we used a mesh of 3-dimensional hexahedral elements (SOLID122) for the ESD plates and the mirror, as can be seen in figure 8.2. The space around them was modeled using the same type of elements in tetrahedral shape.

The mesh size, i.e. the size of the finite elements, is a trade-off in most kinds of FE analysis. A finer mesh will yield more accurate results at the expense of time needed for the computation. To find a good compromise for the mesh size for this work, we performed a mesh convergence analysis. In this analysis we computed the force on the test mass in the FE model at the ideal operating point, and we repeat this computation for different mesh sizes. For this, we introduce a parameter M_{div}, which defines the number of finite elements along linear edges of the model, for example the long edges of the ESD plates. Furthermore, to reduce computational cost, we define that the ESD plates should have $M_{div}/4$ elements in height. This is justified by the

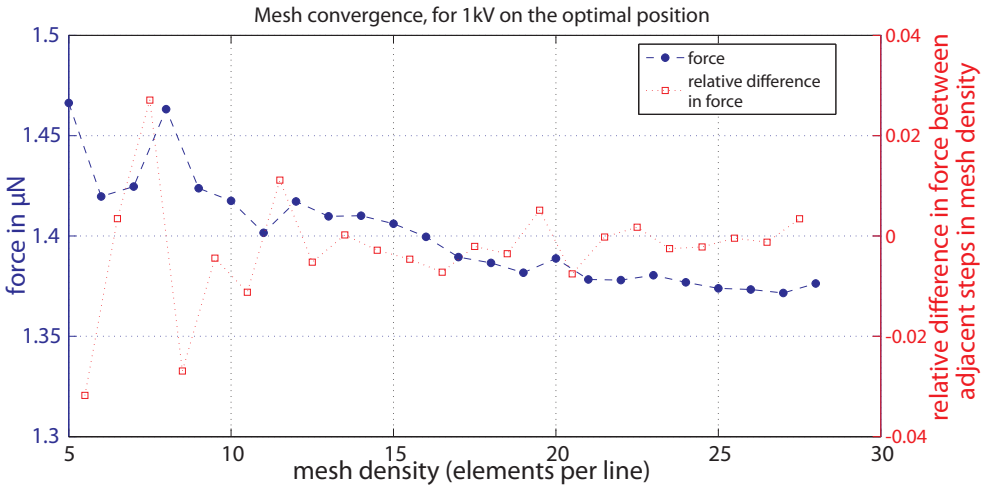

Figure 8.11.: This plot shows the resulting force on the mirror in the investigated scenario in dependence of the mesh size [WHB+15]. The resulting force converges for high mesh densities to what will be assumed as 'true' value at the highest mesh density.

geometry of the plates, and that as conductor, the electric field in them should be small.

Figure 8.11 shows the result of the mesh convergence analysis. As expected, the resulting force changes with the mesh size with stronger change for a more coarse meshing than for a finer one. Based on figure 8.11, a mesh density of 15 elements per line was chosen for the analysis presented in this work. Assuming that the finest mesh with 28 elements per line is accurate, the error introduced by picking the more coarse mesh with 15 elements per line can be estimated. This is done by comparing the force at both mesh densities. It differs by about 3%, which will be assumed is the accuracy of the presented analysis.

8.9. Summary and outlook

This chapter presents an alternative geometry for electrostatic mirror actuators (ESDs) that are currently used in GWD, based on two parallel plates. Furthermore, the very first characterization of this alternative geometry is done via an analytic model and FEM simulations for the example case of the AEI-10 m. This new geometry offers several advantages over the conventional comb-shaped design. Among them are that it offers the maximal free aperture of the optics, which prevents issues with beam clipping and scattering. Another advantage is the absence of first order noise coupling of position to force noise. Due to this, ESDs of the new geometry require a less sophisticated seismic isolation than the conventional ESD design. In the case of the AEI-10 m, they could be bolted directly onto the seismically isolated tables and still would not significantly affect the displacement sensitivity of the AEI-10 m.

This is a great practical benefit, as the conventional designs usually need multi stage pendulums with active damping and actuators for their seismic isolation.

The parallel plate ESD design does offer less force per applied voltage though. For the example case in this work, a force of 1.4×10^{-12} N/V^2 was determined, more than two orders of magnitude lower than for the conventional comb drives in full scale GWD. Therefore this new ESD geometry is mainly suited for smaller scale prototype and table top experiments with sensitive laser interferometers such as the AEI-10 m. These experiments have mirrors of ≤ 100 g, two orders lighter than the ones on full scale GWDs, which will offset the smaller force.

For these smaller scale experiments, the new geometry offers many advantages over the conventional design, and the presented simulations will help with its implementation into emerging projects. Both the AEI-10 m prototype interferometer [Grä13, p165ff] and the Glasgow speedmeter experiment [GBB+14] have chosen to implement the presented kind of actuator based on this work.

It may be useful to perform further experimental tests of the new geometry, especially investigating the effect of charged optics on the performance of the ESD. While mitigation strategies exist and are presented in this chapter, the amount and distribution of charges on the optics that can be realistically expected are unknown at this point.

CHAPTER 9

Summary and Outlook

High order modes (HOMs) can pose significant challenges for interferometric gravitational wave detectors (GWDs). In the case of GEO 600, they have been deteriorating the sensitivity of the gravitational wave (GW) measurement, worsening the performance of the alignment systems, and in this way causing power fluctuations and instability in locking the optical cavities. HOMs have also decreased the performance of the squeezed light injection in GEO 600.

This work focuses on reducing the source of the multitude of HOM related issues in GWDs, by suppressing and filtering HOMs. This is demonstrated in several ways in the example of GEO 600. The different approaches of HOM suppression are heating of optics and the optical and spatial filtering of HOMs.

The challenges involving HOMs are expected to become even more severe in future generations of GWDs, due to their increased sensitivity and their large circulating light power. HOMs created by thermal effects pose a challenge for the planned power increase in GEO 600 as well. HOMs saturating photo diodes used for alignment of the optical cavities have been identified as one practical limiting factor for the possible circulating light power in GEO 600 [Aff14, p. 141].

This work shows through simulations and experiments that the ring heater behind the far east folding mirror can be used to greatly reduce thermally induced HOMs in GEO 600. By selecting the appropriate heating power, the mirror is thermally deformed, and thus the thermal effects can be compensated in terms of the gain of the power recycling cavity and amount of HOMs. For this, the ideal curvature depends on the circulating laser power. Moreover, the installation of a reflector increases the heating efficiency by a factor of 2.5 and increases the possible dynamic range of the ring heater.

A control system for the aforementioned heater makes it possible to automatically

and continuously adjust the heating power to its ideal value in less than the thermal time scale. Similar techniques may prove useful for second generation GWDs, which have incorporated ring heaters into their design as well.

A further improvement provided by this work to the heater setup at the far east folding mirror is the installation of two additional heaters lateral to the mirror. Their design evolved from the first generation of ring heaters in GWD, which are used in GEO 600 and in advanced LIGO, and which both consist of a heating wire wrapped around a glass ring. Presently, as an outcome of this work, the side heaters are based on a stainless steel rod with a ceramic coating and grooves that allow for the bifilar winding of the heating wire. This construction minimizes the magnetic field from the electrical current in the wire and reduces the variance in winding and heating between both side heaters. With the inclusion of the side heaters, the heater setup at the folding mirror represents the first realization of a segmented heating approach in any GWD, and makes it possible to ideally adjust the mirror's radius of curvature in two degrees of freedom (DoFs).

GEO 600 greatly benefits from the side heaters in that they can cure an astigmatism caused by the ring heater, and reduce the HOMs at the darkport of GEO 600 by 37%.

The successful implementation of the two DoF heating at the far east folding mirror has inspired the development of a thermal projection system with even more degrees of freedom discussed in this work. The thermal projector is realized as a matrix of 9x12 thin film resistors, which are used as heaters, and projected through a viewport in the vacuum system onto the beam splitter's surface. Using the thermal projector, it is possible to alter the shape of the wavefront of the laser beam in GEO 600 and to directly influence HOMs, reducing the effects of imperfections of the optics and thermally induced aberrations alike. This will also be beneficial to counteract the thermal lens in the beam splitter of GEO 600. At the current circulating power level, the HOMs can be well suppressed by using the heater installation at the far east folding mirror to change its curvature. At significantly higher laser power levels though, this may cause side effects, as was shown by simulations. Compensating the beam splitter's thermal lens directly via thermal protection onto the beam splitter on the other hand is a possible strategy to counteract the effects of the thermal lens in the beam splitter, and will be needed once the circulating power in GEO 600 is raised.

The amount of tuning that is possible due to the large number of DoFs set the thermal projector apart from the CO_2 laser based spatial heating systems used in first generation GWDs, which were based on masks and axicons. Spatial heating systems with a similarly large number of DOF are currently being studied for use in second generation GWDs, however, the thermal projection system in GEO 600 is the first implementation of such a system in a GWD.

It is demonstrated that the thermal projector in GEO 600 can reduce HOMs caused by mirror imperfections, i.e. in the low power state by about 30%, and the mostly thermally induced HOMs a high power state by about 24%. Limiting factors in the performance are likely the available heating power and the sensing of the individual HOMs. The power is planned to be improved via moving the projection optics into the vacuum chamber, which then avoids the limiting small solid angle between viewport and beam splitter. The sensing of the HOMs could be improved with the installation

of a phase camera or a Hartman sensor at the darkport of GEO 600.

Another part of this work is the optical and spatial filtering of HOMs. The optical filtering of HOMs is done by a small optical cavity, called the output mode cleaner (OMC), placed directly in front of the main photo diode. The existing OMC in GEO 600 was swapped with a new one, which has a slightly different optical length. The length of the old OMC is such, that 6th order modes co-resonate with fundamental mode sidebands at 14.9 MHz which are used for control of the interferometer. The new design resolves this issue.

The design and characterization of the new OMC is part of this work, while the older OMC now serves a spare. Further improvements are done to the output mode cleaner in GEO 600 through this work. By installing additional seismic isolation of the OMC, a nonlinear coupling of acoustic noise to the gravitational wave measurement signal is strongly reduced.

Additionally, the mode matching of the darkport beam of GEO 600 into the OMC is improved by the implementation of a movable lens stage. The mode matching of the interferometer output beam to the OMC is an important factor in advanced GWD, especially when squeezed vacuum states are used to increase the sensitivity, as is done in GEO 600. This feature is considered as a possible upgrade for advanced LIGO and advanced Virgo. A non-ideal mode matching will not only negatively affect the GW measurement by increasing relative shot noise, it will negatively affect the squeezing performance as well by introducing losses. For this reason, adaptive mode matching schemes are in development for use in advanced LIGO. However, the implementation of in-situ mode matching in GEO 600 is the first in any GWD, and it makes it possible to change the mode-matching without opening the vacuum chamber.

The approach of spatially filtering of HOMs is realized by the installation of additional baffles. They consist of large black glass plates with a free aperture through which the laser beam, and lower order HOMs can pass The spatially more extended HOMs of very high orders and scattered light will be absorbed by the baffles. The installation of the large baffles is additionally motivated by the effort to find the source of an unexplained noise in the GW measurement, which arises when the circulating power in GEO 600 is increased. Scattered light has been one of the strongest candidates for this unexplained noise. The installation of baffles into several vacuum chambers of GEO 600 significantly reduces the amount of scattered light in that particular vacuum chambers, but ultimately had no effect on the unexplained power dependent noise. The baffles will help however to reduce other issues with strong stray light when the planned power increase in GEO 600 is done.

Furthermore, this work discusses an alternate design for electrostatic drives (ESDs) as mirror actuators. The new design is based on two parallel plates, which can be located either at the sides or at top and bottom of the mirror. When placed correctly, a voltage applied to the plates can introduce a force on the mirror. This type of actuator has already been considered when GEO 600 was constructed [ADD+14], but was dismissed quickly after first calculations.

The alternate design of the ESDs has many benefits over the conventional comb-shaped ESDs. They do not restrict the free aperture of the mirror, and have no first order coupling of actuator motion to its force. The latter can greatly simplify

the requirements for the seismic isolation of the ESD. The attainable force by the alternate ESD design is lower than the force by a conventional design though, therefore the alternate ESD geometry is only suited for the case of small mirrors ($<$100 g), as they are used in many smaller scale GWD prototype experiments. This work presents the first finite element simulations for the new ESD geometry, based on the case of the AEI-10m prototype experiment. Both the AEI-10m prototype and the Glasgow speedmeter proof of principle experiment have decided to use the alternate ESD geometry.

APPENDIX A

Appendix

A.1. Thermal projector

A.1.1. Prototypes of the heater array

The heater array is a crucial part in the thermal projector, which was detailed in chapter 5 of this work. The high temperatures posed challenges for the development of a suitable design of the heater array. Several prototypes have been designed and build in the course of this work, and are briefly presented below.

The first prototype heater array is pictured in figure A.1. It consists of a PCB with a grid of 2x2 Pt100 elements of different types[1]. A ceramic (Macor) spacer is placed between the heaters and the PCB to protect the glue and solder on the PCB from excessive heat. Two of the Pt100 elements are attached with high temperature thermal paste (Thermigrease TG 20033 [Mue]) to small copper blocks. The copper blocks would be heated directly and increase the thermally radiating area. Initially, the copper blocks in the image have a low emissivity for infrared wavelengths, but after being heated in air, they would form a dark oxide layer with a large emissivity. However, no clear benefit of using the copper blocks was found.

Figure A.2 shows an evolved version of the above, with a 12x12 array of Pt100 elements, ceramic spacer and individual reflector discs for each Pt100 element. It does not have diodes installed on the board though, thus shows a large cross coupling between the heaters.

Further development led to the 5x3 heater array, which is displayed in figure A.3.

[1] The elements visible in this picture are M422 and M222 from the company Heraeus. The blue color indicates a lower maximum temperature rating (up to 500°C) than the white HD421 (up to 850°C) which are used throughout this work

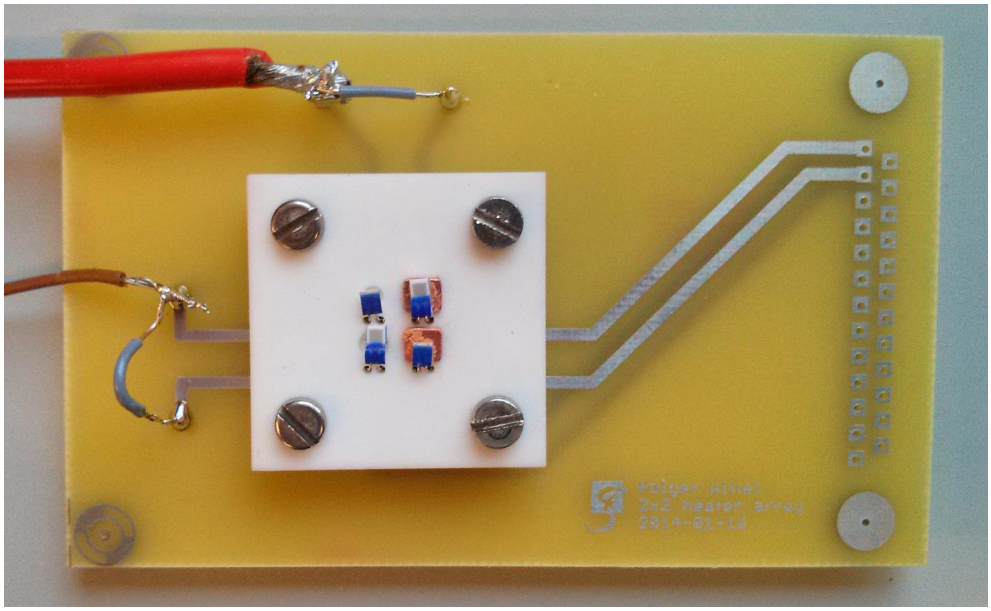

Figure A.1.: 2x2 prototype with ceramic (Macor) baseplate and copper block underneath the heaters.

This heater array differs to the previous prototypes in two ways. For one, instead of a ceramic spacer between Pt100 elements and PCB, it uses a polished aluminum reflector. And secondly, the Pt100 elements are standing upright, i.e. perpendicular to the PCB plane. This way, the radiation from both face of the Pt100 elements can be utilized for the thermal projection. Furthermore, since polished aluminum possesses a low emissivity for infrared radiation (other than Macor), even when hot, it will not significantly contribute to the infrared projection by itself, and thus not 'dilute' the projected heating pattern (of course the reflection from the Pt100 will).

Different geometries of the reflector have been explored. Figure A.4 shows two examples, one reflector with straight V-shaped surfaces (left), and one with parabolic reflector surfaces. It turned out that there is not significant advantage of the parabolic shape, therefore the V-shaped geometry has been chosen for the final design, due to easier manufacturing. Both reflectors pictured in figure A.4 have been 3D-printed with a ZCorporation ZPrinter 650 (at the Faculty of Architecture and Landscape Sciences at the University of Hanover)

The most used prototype of the heater array however did not have any heaters, instead it is a matrix of LEDs, as shown in figure A.5. This was used for developing the software of the projection system.

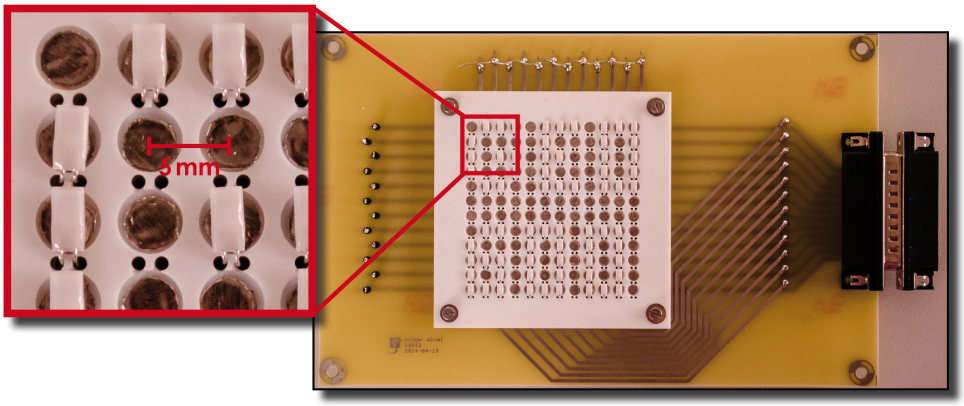

Figure A.2.: A photograph of the matrix heater PCB with ceramic (Macor) spacer, reflective disks and Pt100 resistors (not all are installed on the photo) [ADD+14].

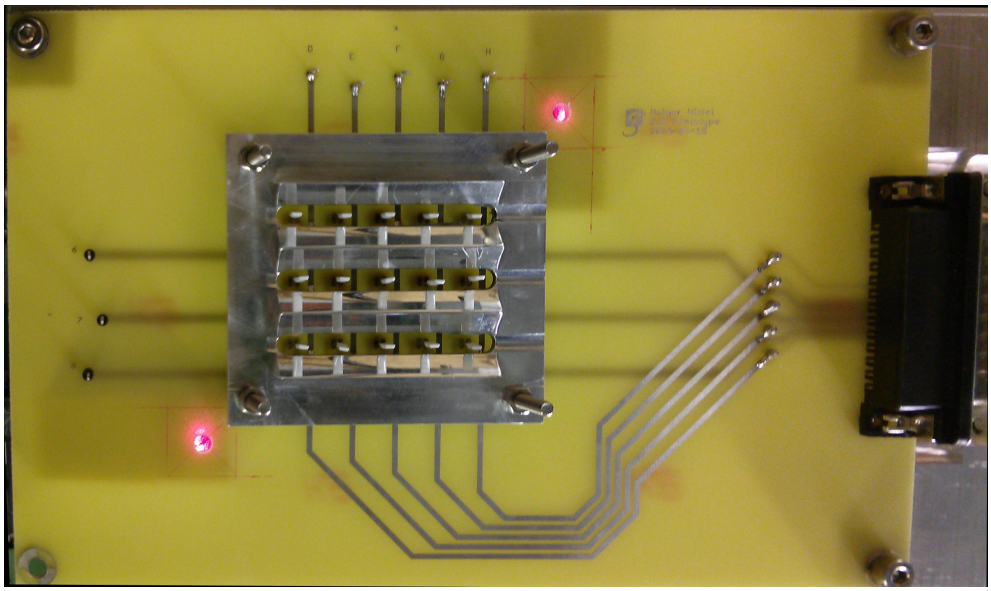

Figure A.3.: 5x3 Prototype with parabolic aluminum reflector. The bright red lights at the top right and bottom left corner are red laser diodes, which are used to help with the coarse alignment of the heater matrix to the beam splitter.

Figure A.4.: Alternate 3D-printed reflectors for 5x3 matrix.

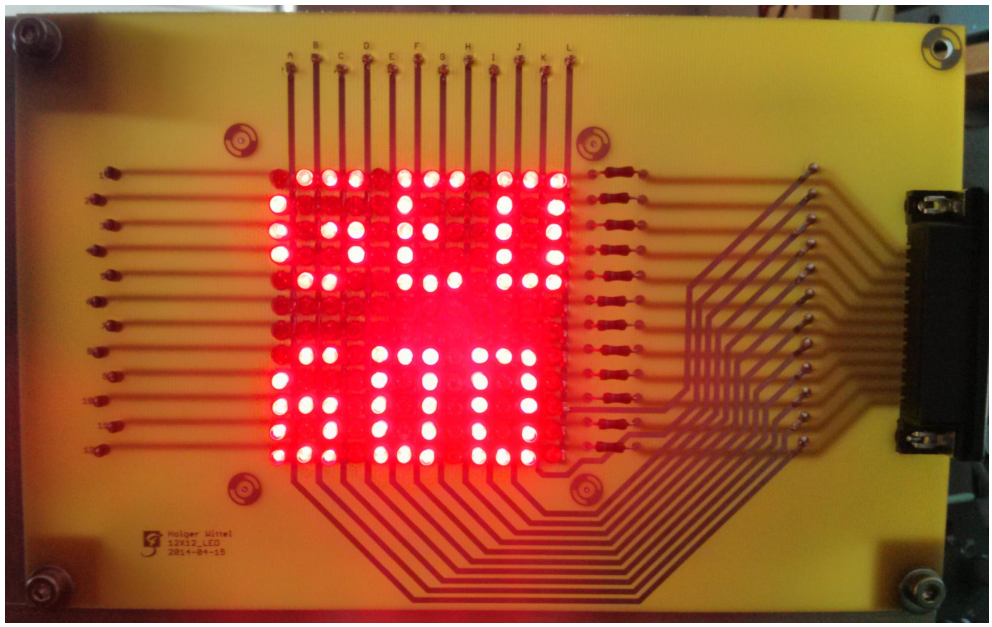

Figure A.5.: LED array for software development

A.1.2. Actuation matrix for thermal projector

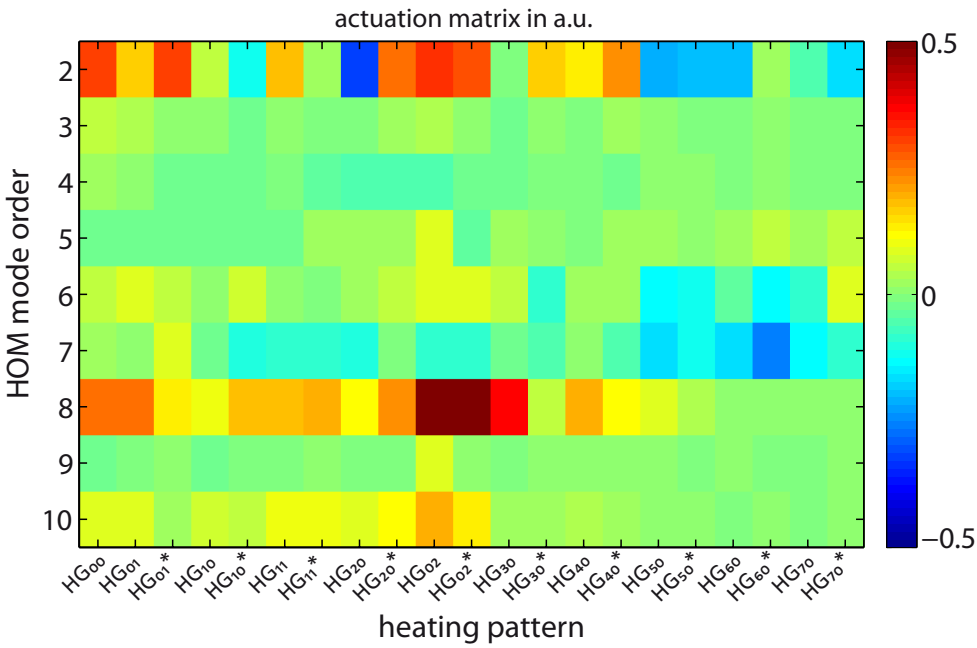

Figure A.6.: Actuation matrix for the thermal projector. The x-axis represents the heating patterns, where HG_{mn} represents heating with the spatial profile of the positive lobes of a Hermit Gauss mode, while HG_{mn}* represents heating the negative lobes of the same mode. The values have been measured by scanning the length of the OMC, and noting the power in modes of the different orders. Each value is the mean of three measurements in an OMC scan.

A.2. Baffle transfer function measurements

This section contains the transfer functions and coherence measurements that were used to produce the baffle noise projections in chapter 6.

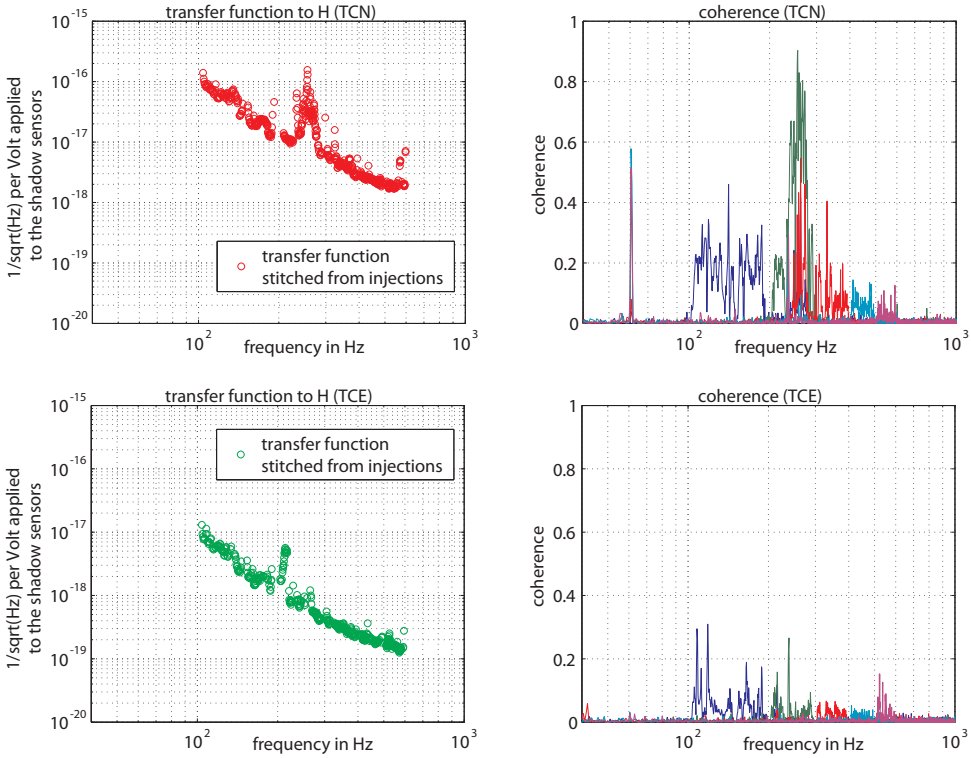

Figure A.7.: Transfer function measurements for the baffles in TCE and TCN, using the OSEMs in the baffle suspensions.

A.3. Spectrograms of acoustic injections

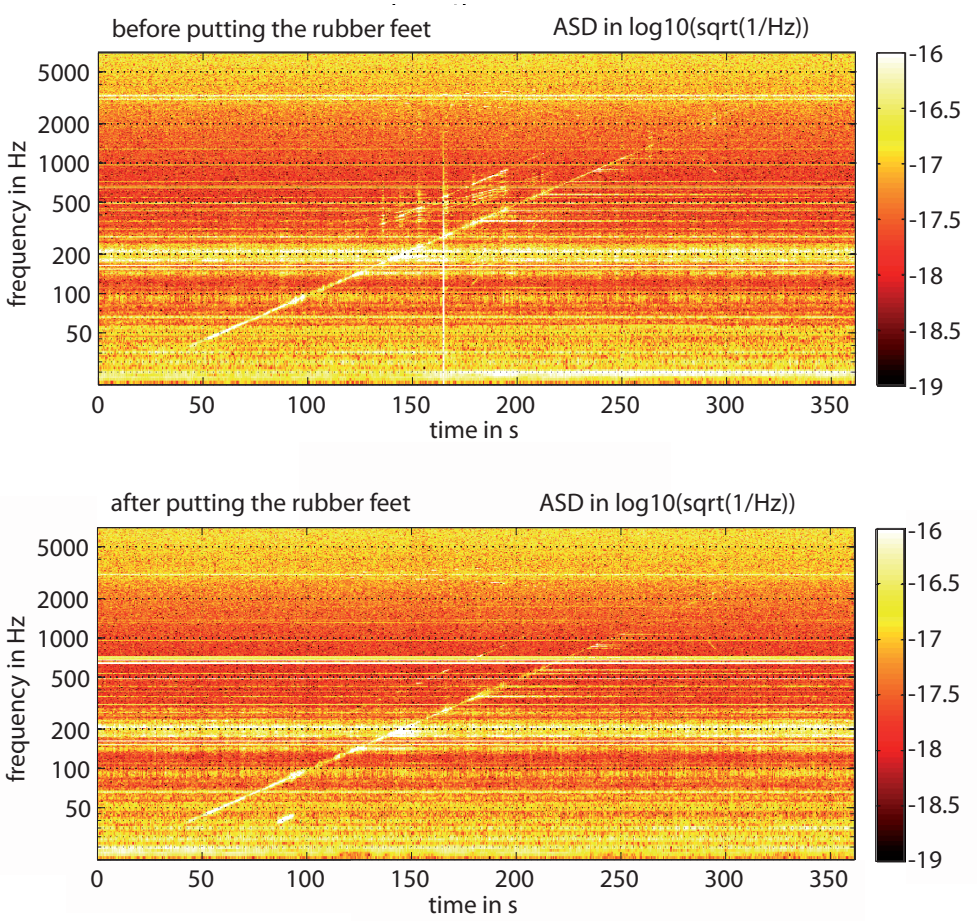

Figure A.8.: This figure shows spectrograms of the main gravitational wave signal, as amplitude spectral density (ASD), during the injection of a sweep signal (before (top) and after (bottom) putting the viton feet under the OMC). The data has been whitened by a 5th order high pass filter with a corner frequency of 150 Hz.

A.4. ANSYS code for new ESD geometry

Listing A.1: Ansys code for GEOweb

```
!Holger Wittel
!
!ESD SIMULATION for the
!AEI 10m Prototype

```

```
/CLEAR
/FILNAME,ESD,0
/TITLE, ESD simulation
/UNITS, SI

!------ build 3D model ---
/PREP7
/INPUT,'vars','txt','D:\ESD-local\ ' ,, 0 !read in the vars from a different file

!content of vars.txt (example):
!
!vlt=1000
!displ=-3.000000e-002
!meshsize=15
!ydispl=0
!xdispl=0
!rotz=0
!rotx=0
!roty=0


!---capacitor plates---
capacitor_sep   = 0.07  !separation of the plates
capacitor_thick = 0.005 !thickness of the plates
capacitor_length= 0.05  !length of the plates
capacitor_depth = 0.05  !depth of the plates

BLOCK, -capacitor_length/2, capacitor_length/2, capacitor_sep/2, capacitor_sep/2 +capacitor_thick , -capacitor_depth
      /2, capacitor_depth/2
BLOCK, -capacitor_length/2, capacitor_length/2, -capacitor_sep/2, -capacitor_sep/2 -capacitor_thick , -
      capacitor_depth/2, capacitor_depth/2


!---Dielectric (MIRROR)---
mirr_rad    = 0.0245    !radius of the mirror
mirr_depth  = 0.0245    !depth of the mirror

VSEL,ALL

!---------Rotation
!define local coord system
THZ     =rotz   !rotation in XY plane
THX     =rotx   !rotation in YZ plane
THY     =roty   !rotation in ZX plane

LOCAL, 11, 0, 0, 0, 0, THZ, THX, THY,,
CSYS, 11    !make this the actice coordinate system
WPCSYS,,11  ! define working plane

!CYL4, 0, 0, mirr_rad, , , , -mirr_depth
CYLIND, mirr_rad,,-mirr_depth/2, mirr_depth/2, ,

CSYS,0      !back to default coord system
WPCSYS,,0   !back t odefault working plane

VGEN, ,3, , , , ,-displ, , ,1
VGEN, ,3, , , ,ydispl ,, , ,1   !shift mirror towards one of the plates
VGEN, ,3, , , xdispl, ,, , ,1   !shift mirror towards one of the plates

!--- Vacuum---
BLOCK,-1.5*capacitor_length,1.5*capacitor_length,-1.5*capacitor_sep,1.5*capacitor_sep,-1.5*capacitor_depth,1.5*
      capacitor_depth

VSEL,ALL
VOVLAP, ALL
VGLUE,ALL   !Glue all Volumes

!---CAPACITOR PLATES ---- QUICK AND DIRTY VALUES
MP,PERX,1,1000
MP,PERY,1,1000
MP,RSVX,1,1.6e-8
MP,RSVY,1,1.6e-8
MP,LSST,1,1e-10

!---MIRROR - dielectric
MP,PERX,2,3.7
MP,PERY,2,3.7
MP,RSVX,2,1e18
MP,RSVY,2,1e18
MP,LSST,2,1e-4

!---VACUUM
MP,PERX,3,1
MP,PERY,3,1
!MP,RSVX,3,1e20
!MP,RSVY,3,1e20
MP,LSST,3,0

!---SET PROPERTIES
```

```
VSEL,ALL
VSEL, , , , 1
VATT,1,,1

VSEL,ALL
VSEL, , , , 2
VATT,1,,1

VSEL,ALL
VSEL, , , , 3
VATT,2,,1

VSEL,ALL
VSEL, , , , 5
VATT,3,,1

VSEL,ALL


!---MESHING----
ET,1,SOLID122,
!KEYOPT,1,4,0

!select the "short lines of the capacitor plates"
LSEL,S,,,1
LSEL,A,,,3
LSEL,A,,,6
LSEL,A,,,8

LSEL,A,,,18
LSEL,A,,,15
LSEL,A,,,13
LSEL,A,,,20

LESIZE,ALL,,,meshsize/4,
ALLSEL

!MSHAPE,0,3D
!SMRTSIZE,1
ESIZE, , meshsize
EXTOPT,VSWE,TETS,ON
VSWEEP,ALL

FINISH


/SOLU
!---DEFINE LOADS---
!vlt    = 1e3   !Potential betw electrodes

!---set Voltage
VSEL,ALL
VSEL, , , , 1
NSLV,S,0
D,ALL,VOLT,-vlt/2

VSEL,ALL
VSEL, , , , 2
NSLV,S,0
D,ALL,VOLT,vlt/2

VSEL,ALL
ASEL,ALL
SFA,ALL,MXWF    !FLAG for force
ASEL,ALL

!--- SOLVE ---
ALLSEL
ANTYPE,0
/STATUS,SOLU
BCSOPTION,,INCORE,,,,PERFORMANCE
SOLVE

/POST1
ALLSEL
/CONTOUR,1,256,AUTO,,
PLVECT,EF, , , ,VECT,ELEM,ON,0
!PLVECT,D, , , ,VECT,ELEM,ON,0

!---calculate capacitance---
ALLSEL
ETABLE,SENE,SENE
ETABLE,EFX,EF,X
ETABLE,EFY,EF,Y
SSUM
*GET,W,SSUM,,ITEM,SENE
C=(W*2)/((vlt)**2)
*status,C

```

```
ALLSEL
VSEL, , , , 3
NSLV,S,1
NSLV,U,0
ESEL,ALL
EMFT

*cfopen,'D:\ESD-local\ ','txt'
*vwrite,W,C
(E13.7,2X,E13.7)

FINISH
```

A.5. FINESSE model of GEO 600

Listing A.2: Finesse model of GEO 600

```
#----------------------------------------------------------------------
# based on the Finesse model geoHF_official.kat $Rev: 47 $
#----------------------------------------------------------------
## Laser bench ##
# Laser
# (distances on laser bench up to MMC1a are only approximately)
l i1 2.85 0 nLaser # power injected into MC1 (for 75deg, see page 803 GHFlog)
gauss beam_in i1 nLaser 1m -5.4
# beam size that fits into MC1, we assume "i1" includes the laser and
# mode matching lense as well as all the other components from the
# laser bench, except the modulator and the last table mounted mirror.
s s0 1 nLaser nEOM1in

## MU 1, modulation for PDH for locking laser to MC1
mod eom1 25M 0.1 1 pm 0 nEOM1in nEOM1out ## MC1 PDH locking frequency
s s1 1 nEOM1out nZ1
bs mZ 1 0 0 0 nZ1 nZ2 dump dump       # the last table mounted mirror
s s2 2.86 nZ2 nBDIMC1a

##-------------------------------------------------------------
## mode cleaners ##
#
# The mode cleaners are rougly adapted to fit the measured
# visibility, throughput or finesse, see labbok 4027
## MC1
bs1  BDIMC1 50u 30u 0 45 nBDIMC1a nBDIMC1b dump dump
s    mc1_sin 0.45 nBDIMC1b nMC1in
bs1  MMC1a 10000u 130u 0 44.45 nMC1in nMC1refl nMC1_0 nMC1_5
s    mc1_s0 0.15 nMC1_0 nMC1_1
bs1  MMC1b 35u 130u 0.0003 2.2 nMC1_3 nMC1_4 dump dump #3*10^-10m away from res.
attr MMC1b Rc 6.72
s    mc1_s1 3.926 nMC1_4 nMC1_5
bs1  MMC1c 10000u 130u 0 44.45 nMC1_1 nMC1_2 nMC1out dump
s    mc1_s2 3.926 nMC1_2 nMC1_3
s smcmc1 0.5 nMC1out nMU2in
## MU 2
mod  eom2 13M .1 1 pm 0 nMU2in nMU2_1a          # MC2 PDH locking frequency
s    s_eom2_eom3 0 nMU2_1a nMU2_1b
mod  eom3 $fPR $midxPR 1 pm 0 nMU2_1b nMU2_2a    # PRC  PDH locking frquency
s    s_eom3_d1 0 nMU2_2a nMU2_2b
isol d1 0 nMU2_2b nMU2out                       # Faraday Isolator
s    smcmc2 0.5 nMU2out nMC2in

## MC2
bs1  MMC2a 10000u 130u 0 44.45 nMC2in nMC2refl nMC2_0 nMC2_5
s    mc2_s  0.15 nMC2_0 nMC2_1
# inner surface of MMC2b:
bs1  MMC2bi 10000u 130u 0 2.2 nMC2_3 nMC2_4 nMC2bi dump
attr MMC2bi Rc 6.72
s    mc2_s1 3.9588 nMC2_4 nMC2_5
bs1  MMC2c 114u 130u 0.0003 44.45 nMC2_1 nMC2_2 dump dump #3*10^-10m away from res.
s    mc2_s2 3.9588 nMC2_2 nMC2_3
s    sMMC2b 0.05 1.44963 nMC2bi nMC2bo
# second surface of MMC2b:
m    MMC2bo 0 1 0 nMC2bo nMC2out
attr MMC2bo Rc 0.35
s    smcpr1 0.135 nMC2out nBDOMC2a
bs1  BDOMC2 50u 30u 0 45 nBDOMC2a nBDOMC2b dump dump
# Note:
# The length of 'smcpr2' and 'smcpr3' represent not the geometrical
# distance but the length of the space with respect to mode propagation.
# The values include the effects of the Faraday crystals and the
# modulator crystals which are not explicitely given here.
s    smcpr2 0.2825 nBDOMC2b nMU3in
```

```
65
66  ##-------------------------------------------------------------
67  ## MU 3
68  mod  eom4 $fSR $midxSR 2 pm 0 nMU3in nMU3_2a      # Schnupp1 (SR control)
69  s    s_eom4_eom5 0 nMU3_2a nMU3_2b
70  mod  eom5 $fMI $midxMI 2 pm 0 nMU3_2b nMU3_3a      # Schnupp2 (MI control)
71  s    s_eom5_lpr 0 nMU3_3a nMU3_3b
72  lens lpr 2.0 nMU3_3b nMU3_4a          # new lens since 2012, p.3538 GEO-HF
73  s    s_lpr_therm 0 nMU3_4a nMU3_4b
74  # some rather arbitrary thermal lense for the isolators and the EOMs:
75  lens therm 5.2 nMU3_4b nMU3_5a                      # ** to be checked **
76  s    s_therm_d2 0 nMU3_5a nMU3_5b
77  isol d2 120 nMU3_5b nMU3out                         # Faraday Isolator
78  s    smcpr3 4.391 nMU3out nBDIPR1
79  bs1  BDIPR 50u 30u 0 45 nBDIPR1 nBDIPR2 dump dump
80  s    smcpr4 0.11 nBDIPR2 nMPR1
81
82  ##-------------------------------------------------------------
83  ## main interferometer ##
84  m    mPRo 0 1 0 nMPR1 nMPRi1 #first (curved) surface of MPR
85  attr mPRo Rc -1.85
86  s    smpr 0.0718 1.44963 nMPRi1 nMPRi2
87  # second (inner) surface of MPR
88  m1   MPR 900u $LMPR 0. nMPRi2 nMPR2  # T=900 ppm, L=50 ppm
89  s    swest 1.1463 nMPR2 nBSwest     # new length with T_PR=900 ppm ** to be checked **
90
91  ##-------------------------------------------------------------
92  ## BS
93  ##                          nBSnorth      ,'-.
94  ##                                |      +     `.
95  ##                                |    ,'        :'
96  ##             nBSwest            |  +i1       +
97  ##          ----------------->    ,:._   i2 ,'
98  ##                              + \  `-. +        nBSeast
99  ##                            ,' i3\    ,' ---------------
100 ##                          +       \ +
101 ##                        ,'      i4.'
102 ##                       `._        ..
103 ##                          `._ ,' |nBSsouth
104 ##                             -   |
105 bs2   BS 0.485998 $LBS 0.0 42.834 nBSwest nBSnorth nBSi1 nBSi3
106 s    sBS1 0.091 1.44963 nBSi1 nBSi2
107 s    sBS2 0.091 1.44963 nBSi3 nBSi4
108 bs2   BS2 60u $LBSAR 0  27.9694 nBSi2 dump nBSeast nBSAR   # R=60 ppm, L=30ppm
109 bs2   BS3 60u $LBSAR 0 -27.9694 nBSi4 dump nBSsouth dump     # R=60 ppm, L=30ppm
110 # two measured values for R_AR: labbook page 2418 (44ppm), 3996 (64ppm)
111
112 ##-------------------------------------------------------------
113 # Thermal lens of beam splitter
114 ###################################################
115 s beforeTL 1n nBSeast nMTHERM1
116 lens BStherm 10k nMTHERM1 nBSeast0
117
118 ##-------------------------------------------------------------
119 ## north arm
120 s snorth1 598.5682 nBSnorth nMFN1  #Âă** to be checked **
121 bs1 MFN 8.3u $LMFN 0.0 0.0 nMFN1 nMFN2 dump dump  # T=8.3 ppm
122 attr MFN Rc 666
123 s snorth2 597.0241 nMFN2 nMCN1 # ** to be checked **
124 m1 MCN 13u $LMCN -$DFO nMCN1 dump                  # T=13 ppm
125 attr MCN Rc 636
126
127 ##-------------------------------------------------------------
128 ## east arm
129 s seast1 598.4497 nBSeast0 nMFE1
130 bs1 MFE 8.3u $LMFE 0.0 0.0 nMFE1 nMFE2 dump dump  # T=8.3 ppm
131 ##------NEW  see side GHF log 3760 (ring heater at 34.7W and side heaters at 2.5W)
132 attr MFE Rcx 661    # 34.7W + side heater 2.5W
133 attr MFE Rcy 661    # 34.7W + side heater 2.5W
134 #ring heater
135 #  power    MFE RoC X   MFE RoC Y   (without side heaters),  see Ghf logbook  3760
136 #  33.1W        667.5m      660.5m
137 #  34.7W        665.5m      658m
138 #  36.5W        663.5m      656m
139 s seast2 597.0630 nMFE2 nMCE1
140 m1 MCE 13u $LMCE $DFO nMCE1 dump                  # T=13ppm
141 attr MCE Rc 622
142
143 ##-------------------------------------------------------------
144 ## south arm
145 s ssouth 1.109 nBSsouth nMSR1
146 m MSR1 0.90 0.099 0 nMSR1 nMSR2         #####NEW MSR page 1410 ghf logbook
147 s s_MSR 75.E-3 1.44963 nMSR2 nMSR3          # MSR substrate
148 m MSR2 0.E0 998.E-3 0 nMSR3 nMSR4           #
149 pd outpower nMSR4
150
151 ##-------------------------------------------------------------
152 ## output optics telescope
153 s sout1 1.79606 nMSR4 nBDO1i
```

```
bs BDO1 990E-3 10E-3 0.0 3.55 nBDO1o nBDO1i dump dump    # T=1%
attr BDO1 Rc $BDO1_RofC

s sout2 1.5774 nBDO1o nBDO2i
bs BDO2 998.E-3 2.E-3 0 3.701 nBDO2i nBDO2o dump dump

s sout3 1.3501 1. nBDO2o nBDO3i
bs BDO3 998.E-3 2.E-3 0 44.896 nBDO3i nBDO3o dump dump

s rs14  1.11 1 nBDO3o nWTCOce1a          # Distance BDO3 -> Window east
m sf14a 0 998.E-3 0 nWTCOce1a nWTCOce1b
s rs14e 0.005 1.45 nWTCOce1b nWTCOce1c
m sf14b 0 998.E-3 0 nWTCOce1c nWTCOce1d

s rs14w 0.075 1 nWTCOce1d nTCOcL1a
lens l_L4a $F_L4a_fl nTCOcL1a nTCOcL1b

s rs14a 0.025 nTCOcL1b nTCOcPBS1a       # Distance L4a -> PBS1

m sf15a 0 990.E-3 0 nTCOcPBS1a nTCOcPBS1b
s rsPB1 0.017 1.45 nTCOcPBS1b nTCOcPBS1c
m sf15b 0 995.E-3 0 nTCOcPBS1c nTCOcPBS1d

s rsPBS1e 0.063 1 nTCOcPBS1d nTCOcFRa       # Distance PBS1 -> FR

m sf16a 0 998.E-3 0 nTCOcFRa nTCOcFRb
s rsFR  0.1 1.94 nTCOcFRb nTCOcFRc
m sf16b 0 998.E-3 0 nTCOcFRc nTCOcFRd

s rsFRe 0.055 1 nTCOcFRd nTCOcLama        # Distance FR -> Lambda plate

m sf17a 0 998.E-3 0 nTCOcLama nTCOcLamb
s rsLam 0.002 1.45 nTCOcLamb nTCOcLamc
m sf17b 0 998.E-3 0 nTCOcLamc nTCOcLamd

# the following lens is on a remote-control moveable stage
# and can be shifted by about +-10mm keeping the sum of rsLame and rsPB2s const.
s rsLame 0.077 1 nTCOcLamd nTCOcL2a         # Lambda plate -> L4b
lens l_L4b $F_L4b_fl nTCOcL2a nTCOcL2b
s rsPB2s 0.076 1 nTCOcL2b nTCOcBS2a     # L4b -> PBS2

m sf18a 0 995.E-3 0 nTCOcBS2a nTCOcBS2b
s rsPB2 0.017 1.45 nTCOcBS2b nTCOcBS2c
m sf18b 0 995.E-3 0 nTCOcBS2c nTCOcBS2da
s s_sf18b_sf18c 0 nTCOcBS2da nTCOcBS2db
bs sf18c 0.E-3 995.E-3 0 45 nTCOcBS2db dump nTCOcBS2e nTCOcBS2f
# nTCOcBS2e output node for the carrier
# nTCOcBS2f output node for the sqz beam
s rs16 0.0601 1 nTCOcBS2e nOMC1_AR_w    # Distance PBS2 -> OMC

#-------------------OMC---------------------------------
# This is the newly installed (May 2013), slightly longer OMC!
# See GHF log p. 2860 + 4712
# Convention about the name of the node
# nOMC1_AR_w =  first mirror of the OMC, AR coating side, coming from the left
#
#             /--\  OMCN
#
#        /          /
#   OMC1/          /    OMC2
#      /          /
#
#         \--/  OMCS
bs OMC1_AR 1.E-3 999.E-3 0 41.652 nOMC1_AR_w dump nOMC1_AR_e dump
s rs17 0.0135 1.44963 nOMC1_AR_e nOMC1_HR_w
bs OMC1_HR 980.E-3 20.E-3 0 27.288 nOMC1_HR_w nOMC1_HR_n nOMC1_HR_e nOMC1_HR_s
s rs18 73.22E-3 1. nOMC1_HR_e  nOMC2_HR_w
bs OMC2_HR 980.E-3 20.E-3 0 41.652 nOMC2_HR_w nOMC2_HR_n nOMC2_HR_e nOMC2_HR_s
s rs19 153.81E-3 1. nOMC2_HR_n nOMCN_HR_w
bs OMCN_HR 999.9E-3 100.E-6 0 6.702 nOMCN_HR_w nOMCN_HR_n nOMCN_HR_e dump
attr OMCN_HR Rc 2.35
s rs20 307.62E-3 nOMCN_HR_n nOMCS_HR_n
bs OMCS_HR 1 0 0 6.711949 nOMCS_HR_w nOMCS_HR_n dump dump
attr OMCS_HR Rc 2.35
# Last path to close the OMC
s rs21 153.81E-3 1. nOMCS_HR_w nOMC1_HR_s
# Transmitted beam through the east mirror
s rs22 13.490E-3 1.44963 nOMC2_HR_e nOMC2_AR_w
bs OMC2_AR 1.E-3 999.E-3 0 27.185 nOMC2_AR_w dump nOMC2_AR_e dump
s rs23 1 nOMC2_AR_e n_dump_east
m sf-5 0 0 0 n_dump_east dump

# Transmitted beam through the north mirror
s rs24 12.0419E-3 1.44963 nOMCN_HR_e nOMCN_AR_w
bs OMCN_AR 1.E-3 999.E-3 0 4.779 nOMCN_AR_w dump nOMCN_AR_e dump
s rs25 1 nOMCN_AR_e  n_dump_north
m sf-6 0 0 0 n_dump_north dump

# Reflected beam from the west mirror
```

```
s rs26 13.490E-3 1.44963 nOMC1_HR_n nOMC1_AR2_w
bs OMC1_AR2 1.E-3 999.E-3 0 27.185 nOMC1_AR2_w dump nOMC1_AR2_e dump
# Reflected beam going toward BDO5
s rs27 290.284E-3 1. nOMC1_AR2_e nBDO5_w
bs BDO5_HR 1.9E-3 0 0 38.226 nBDO5_w nBDO5_n dump dump
s rs28 297.866E-3 1. nBDO5_n nWin_east1

#Lens System for alignment
bs bsdet 0.5 0.5 0 0 nWin_east1 nd2 nd3 dump
s det1b 313.453E-3 1. nd2 nd2d

s det5 100E-3 1 nd3 nd8 #Hier der zweite #380
attr det1b g 0
attr det5 g 90

#For the sqz beam leaving PBS2
# 5 cm down, 4 cm south and then 43.9cm up to the window
s rs101 0.529 1 nTCOcBS2f nWTCOce2a

m sf102a 0 998.E-3 0 nWTCOce2a nWTCOce2b
s rs102w 0.006 1.45 nWTCOce2b nWTCOce2c
m sf102b 0 998.E-3 0 nWTCOce2c nWTCOce2d
##-----------------------------------------------------------
## further settings and commands
# Mode matching for OMC
const BDO1_RofC 6.27
const F_L4a_fl 0.25
const F_L4b_fl -0.0523   # this lens is on a moveable stage

# Modulation frquencies
const fSR 9017350    ## corresponding to tuned DC, crystal osc.
const fMI 14.904932M ## (2/2014 H. Grote), crystal osc.
const fPR  37.16M     # crystal oscillator
const midxPR 0.1      # best guess, reduced in 2012 after EOM replacement
const midxSR 0.06     # best guess
#const midxMI 0.2     # used for Lock acquisition & Heterodyne readout
const midxMI 0.05     # used for DC readout, dynamically reduced mod. index
# dark fringe offset for DC readout
const DFO 0.006       # should be about 6mW of carrier light for 2.85W into MC1

# Michelson losses
# tuned to give approx 2.x kW on BS and to match the observed PRC gain on GHF log p.5622
# these are at 130u in the 'official GHF finesse file'
const LMPR  142u
const LMCN  142u
const LMFN  142u
const LMCE  142u
const LMFE  142u
const LBS   142u
const LBSAR 142u

#cavities
cav mc1 MMC1a nMC1_0 MMC1a nMC1_5 # MC1 cavity
cav mc2 MMC2a nMC2_0 MMC2a nMC2_5 # MC2 cavity
cav src1 MSR1 nMSR1 MCN nMCN1  # SR cavity (north arm)
cav src2 MSR1 nMSR1 MCE nMCE1  # SR cavity (east arm)
cav prc1 MPR nMPR2 MCN nMCN1  # PR cavity (north arm)
cav prc2 MPR nMPR2 MCE nMCE1 # PR cavity (east arm)
cav OMC OMC1_HR nOMC1_HR_e OMC1_HR nOMC1_HR_s  # OMC cavity

##-----------------------------------------------------------
# power detectors
pd Ptrans nOMC2_AR_e              # Transmitted beam (for the carrier from the ifo)

##############################
##check the gain of the PRC
pd BSpow2 nBSwest
set power BSpow2 re
pd MPRin nMPR1*
set MPRinpow MPRin re
noplot MPRin
func PRCgain=$power/($MPRinpow+ 1E-15)
##############################
##darkport/intracav
pd darkport nMSR4
set dark darkport re
func dark/west=$dark/($power + 1E-15)
##############################

##-----------------------------------------------------------
## Simulation commands
xaxis i1 P lin 1 35 300  #scan input power
yaxis lin abs

maxtem 4
retrace
time
phase 3
trace 10
```

```
332 pause
333 gnuterm matlab
```

APPENDIX B

Seismic Tracking

B.1. Motivation

Seismic isolation is a key technology to earth-bound gravitational wave observatories. Insufficient isolation may result in excess noise at low frequencies or lead to instabilities and lock losses. Therefore, active and passive seismic isolation systems aim to suppress seismic disturbances. Generally the seismic isolation of GEO is good enough to allow lock durations of several tens of hours in good conditions. Seismic related lock-loss do happen though, and sometimes there are periods when seismic of local origin makes locks unstable. Some examples to mention here:

- A new gravel mine opened less than a kilometer form the east end building in early 2010. While it took the GEO crew some time to notice the new gravel mine, it led to increased ground motion, especially visible in the seismometer in the east end station during working hours. This general elevated seismic is sometimes accompanied by seismic transients, which can be best described as sine gaussians with a center frequency of 2 Hz. These transients do not only happen during working hours, but also during the night. They often cause lock losses. It is believed that these transients are caused by landslides in the gravel mine. In the meantime, the gravel mining has moved away from GEO and while the seismic disturbances are still there, they do not threaten the lock anymore.

- There has been an instance of high seismic in the east, which could be traced back to the stables of the veterinarian college (which is located 100-200 meters away from the east end building) being cleaned with a large high-pressure cleaner.

- Farming work, such as plowing and harvesting on the fields adjacent to GEO 600 is always a source for seismic induced instabilities.

These examples show that oftentimes local seismic events can be challenging. If local events can to be identified first though, then sometimes it is possible to try to cure the source, and not only the symptoms. To help commissioning, a tool was made that runs online and tells the origin of local seismic surface perturbations.

B.2. Principle

The working principle of this tool is simple, it works in the following steps:

1. download a few seconds of data from all seismometers (only z direction)
2. use a Fourier transform and pick a frequency band of interest
3. make cross correlations between each pair of seismometers to get arrival times
4. assume seismic plane wave and compute its speed and direction
5. with the speed and the arrival times, perform a trilateration, use a least squares solver
6. plot and save the results

Assuming we have the arrival time differences of the perturbation at the different seismometers, then we can directly compute its velocity. For that of course one has to assume a plane wave. Now be (x_e, y_e, t_e) the coordinates where the seismic perturbation originates. (x_0, y_0, t_0) denote the location of the TCC seismometer and the time when it registers the perturbation. The corresponding coordinates for TFE are (x_1, y_1, t_1) and for TFN (x_2, y_2, t_2).

Then we can set up the following system of equations:

$$(x_0 - x_e)^2 + (y_0 - y_e)^2 = (v * (t_e - t_0))^2 \tag{B.1}$$
$$(x_1 - x_e)^2 + (y_1 - y_e)^2 = (v * (t_e - t_1))^2 \tag{B.2}$$
$$(x_2 - x_e)^2 + (y_2 - y_e)^2 = (v * (t_e - t_2))^2 \tag{B.3}$$
$$\tag{B.4}$$

The above system can be solved for (x_e, y_e, t_e), which is the origin of the seismic perturbation.

One example output of the implemented real time seismic tracking algorithm is shown in figure B.1. It shows a satellite image[1] of GEO 600 and the surrounding. Seismic activity is portrayed as circles on the map, with the size representing the amplitude.

[1] The image was taken from Google Maps [Goo]

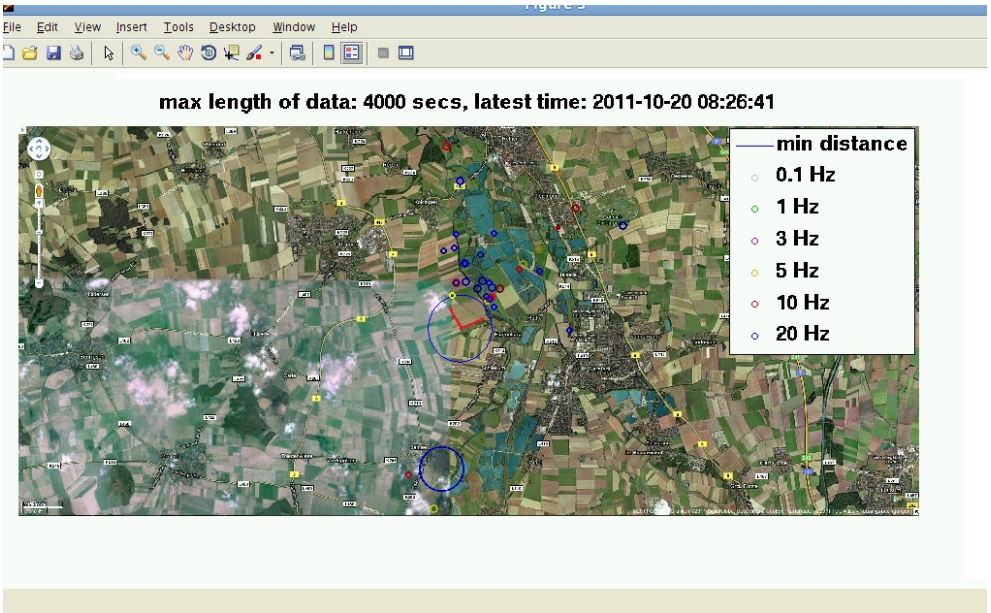

Figure B.1.: Sample output of the seismic tracker. The arms of GEO are printed in red. At this time, a big local seismic event happened in the south of GEO 600, which caused a lock loss. This event has been localized by the tool to be about 2 km south of GEO 600, and is shown as blue circle south on the map.

APPENDIX C

GEOweb - A remote status display using near real time data

This chapter describes a new online status display of GEO 600 in form of a website, which has been developed in the course of this work. It aims to provide near real time data, and is optimized for pc, tablet computers and smartphones.

C.1. Motivation and existing online status displays

During most of the work in this thesis the other large gravitational wave detectors are either being built or upgraded, while GEO 600 has been operating in astrowatch mode. In astrowatch, we still perform experimental work and maintenance on the detector during daytime, and try to maximize the science time during night and weekends. This way, typically we achieve a science duty cycle of 60-70% [DC+15].

Usually nobody is present on site during nighttime, weekends or holidays. Instead, the weekends and holidays are covered by remote shifts, with the responsible person checking the status of GEO remotely, and only driving to the site if necessary.

As GEO 600 is a very complex machine, the lock, i.e. the state where all mirrors are at their operating positions, can be disturbed in a multitude of ways. And while GEO 600 can automatically re-lock, this only works if the mirrors are sufficiently well aligned. Manual intervention is still necessary in some cases.

Those cases include situations when the mirrors are misaligned, after strong earthquakes[1], during storms or sometimes after heavy farming machinery drives close by the buildings of GEO 600. Strong temperature changes in outside temperature can have a similar effect. But not only external events can disturb the lock of GEO 600. Some further cases where manual intervention is necessary to restore the lock of the

[1] Large earthquakes can disturb the lock of GEO 600 even when their epicenter is located far away from GEO 600

optical cavities of GEO 600 are when an actuator of a mirror reaches the end of its range. Furthermore, breaking equipment, such as electronics, vacuum pumps, air conditioning and crashing computers are other cases where automated locking is not possible anymore.

There is a number of ways in which GEO 600 can end up in a state where it cannot automatically regain lock. Online tools, such as the one described in this chapter are essential to help whoever is on off-site on duty to judge the status of GEO 600.

C.1.1. Differences to existing status websites

It should be mentioned that two websites of such kind already exist, which will be called the 'old GEO summary pages' and the 'ATLAS summary pages'.

The ATLAS summary pages[2] are based on a python framework, which is also used by advanced LIGO[3]. It offers a broad overview of several interferometer channels. However, it is not well suited to check the online status of GEO 600, as it uses frame data which is typically 10 minutes delayed (see [Hew04] for the different data formats). Moreover, it is not suited for display on mobile devices, it can be properly used only on large display devices.

The old summary pages[4] are more useful for checking the current status of GEO 600, as they use raw data, which is available with a delay of only a few seconds. The data that is available on the old summary pages to judge the detector status is very basic, and limited though. The old summary page are not optimized for mobile devices either.

For these reasons, GEOweb[5], a new web-based status display of the detector status of GEO 600 was developed. It aims at being a tool that can be used off-site, to give an immediate (i.e. without the 10 minutes delay of the ATLAS summary pages) overview of the most relevant detector parameters, such as current and past sensitivity of the gravitational wave measurement, which can be well accessed from any device.

GEOweb also offers some unique information that is not offered by either of the other summary pages, and are important for the operation of the detector, such as mirror positions and temperatures inside and outside of the buildings. Earthquakes can affect GEO 600 as well, and therefore data on recent earthquakes and the arrival time of their seismic waves at GEO 600 is shown on GEOweb. Furthermore, screenshots of the control computers running Labview are automatically taken and uploaded to GEOweb, and also backed up and archived at regular time intervals. Many of the settings in the labview interface are not recorded in any other way, therefore the screenshots make it possible to better reconstruct the state of the interferometer at a given time.

Another feature of GEOweb is that it is optimized for use on both pc and mobile devices, which means that it can be used conveniently on a smartphone. This has proven to be a useful feature, especially for off-site shifts during the weekends.

[2] https://atlas1.atlas.aei.uni-hannover.de/~geodc/LSC/monitors/
[3] https://ldas-jobs.ligo-la.caltech.edu/~detchar/summary/
[4] http://www.geo600.uni-hannover.de/georeports/
[5] http://www.geo600.org/GEOweb/ or alternatively http://www.geo600.uni-hannover.de/GEOweb/

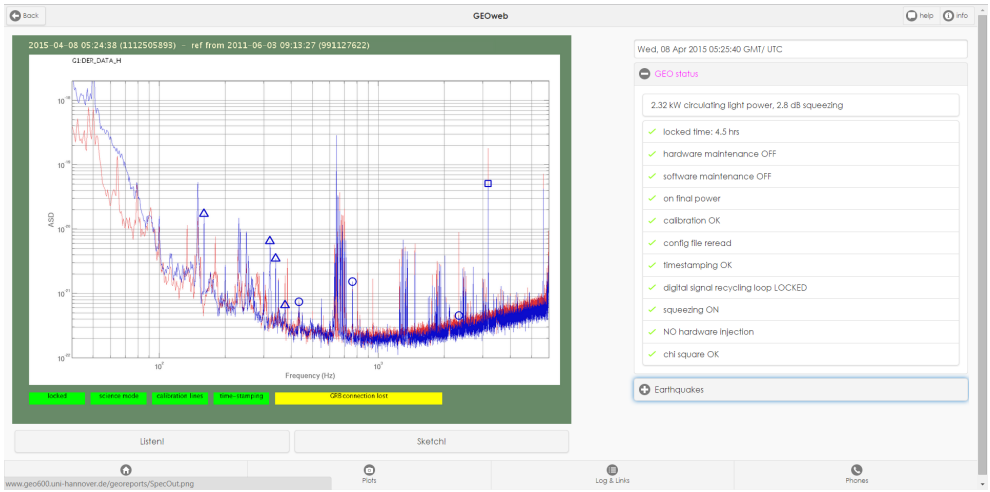

Figure C.1.: Screenshot of the front page of GEOweb.

C.2. Description

Figure C.1 shows the interface of the main page of GEOweb. On the left, a live spectrum of the sensitivity of GEO 600 is displayed, below it are two buttons: The 'Listen!' button plays a one minute long mp3 audio file of the detector output of the most recent minute. The audio file necessary for this is prepared by a Matlab [Mat] backend, which filters and encodes the audio file. The 'Sketch!' button allows to draw on the image of the sensitivity curve, and to save the result as image file. The functions of both buttons are implemented as HTML5 features, and have been tested with recent versions the web-browsers Chrome [Chr] and Firefox [Fir] at the time of writing this thesis.

On the right hand side in figure C.1 the top field shows the current UTC time, below that the expandable section 'GEO status' shows several important parameters of the detector (see figure C.1). The color of the writing 'GEO status' changes according to the detector status.

The following colors are implemented and will change from top to bottom during the locking procedure of all optical cavities in GEO 600[6]:

- black = GEO unlocked
- orange = final circulating light power
- blue = GEO fully locked without squeezing
- purple = GEO fully locked with squeezing

[6] This is inspired by an art installation ('Stardust' by Wilfried Behre [Beh]) at the site of GEO 600, which uses similar colors to show the detector state

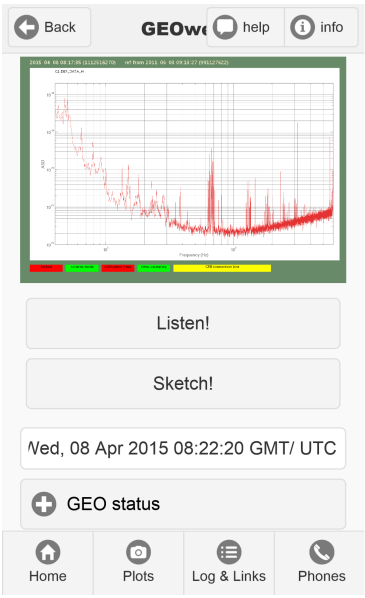

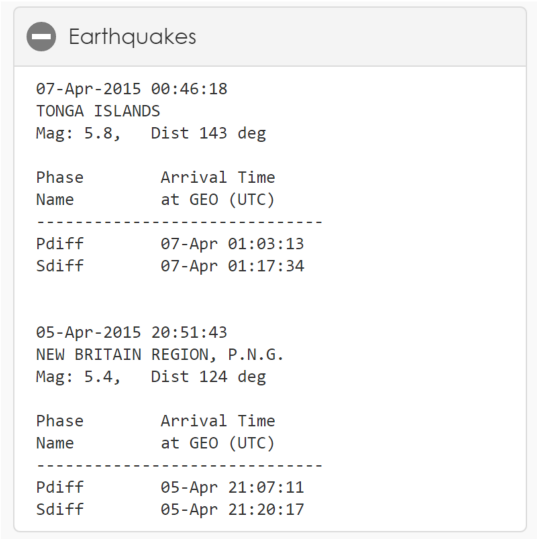

Figure C.2.: Mobile view (left) and earthquake section (right) of GEOweb.

Below the 'GEO status' is another expandable section called 'Earthquakes'. A sample output of this section is provided on the right in figure C.2. It shows the magnitude, epicenter and time of the most recent earthquakes, along with the arrival times of the seismic waves at GEO 600. This is again realized by a Matlab backend, using the mattaup framwork of the Project SEIZMO [Sei] and seismic data from [IRI].

The bottom of figure C.1 shows the navigation bar, with tabs 'Home', which is the page displayed in figure C.1. The tab 'Plots' (screenshot in figure C.3), which provides a multitude of plots that visualize subsystems of GEO 600. 'Log & Links' gives a collection of links to other useful webpages, like the electronic logbook of GEO 600. And finally 'Phones' provides a telephone list with numbers of most on-site telephones. The entries on the page 'Phones' are realized by using 'callto:' (on the desktop version) or 'tel:' (on the mobile version) links, therefore phone calls can be made directly from the webpage. The webpages for 'Log & Links' and 'Phones' are shown in figure C.4.

C.3. Implementation and source code

GEOweb is implemented as an HTML webpage, using JavaScript, jQuery mobile [jQu] and a custom css file. The data that is displayed on GEOweb is provided via a Matlab backend, which runs a computer at GEO 600. The source code for the server side of GEOweb is provided below, along with an example Matlab code which produces a plot for GEOweb.

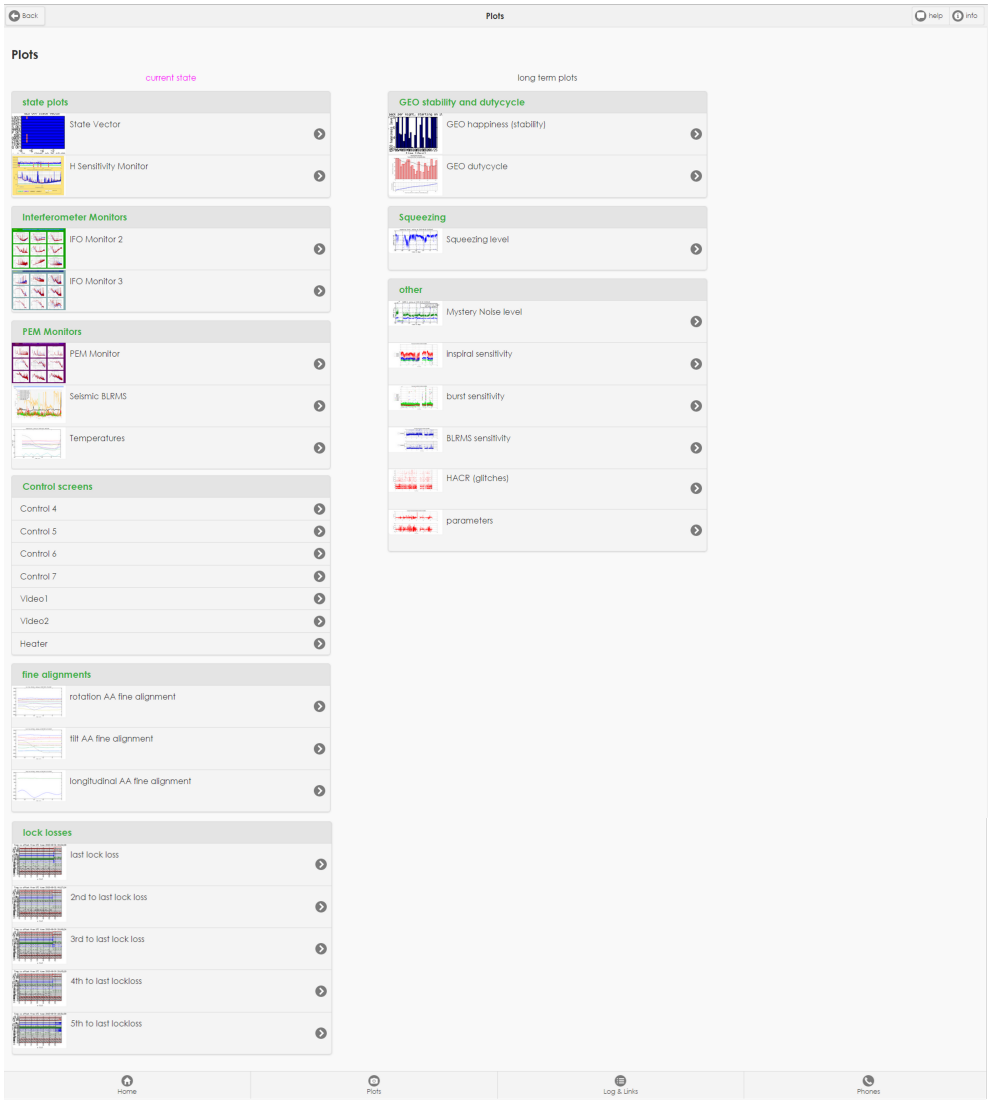

Figure C.3.: Plots page of GEOweb.

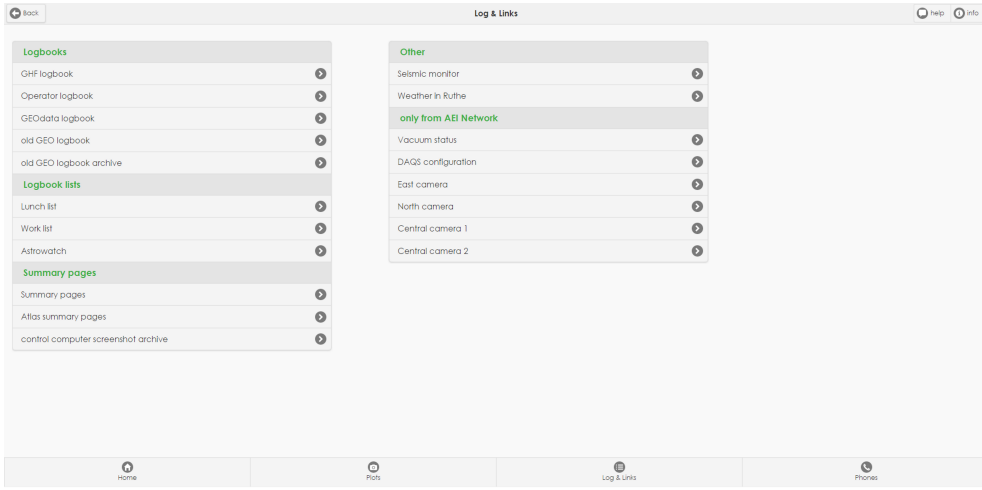

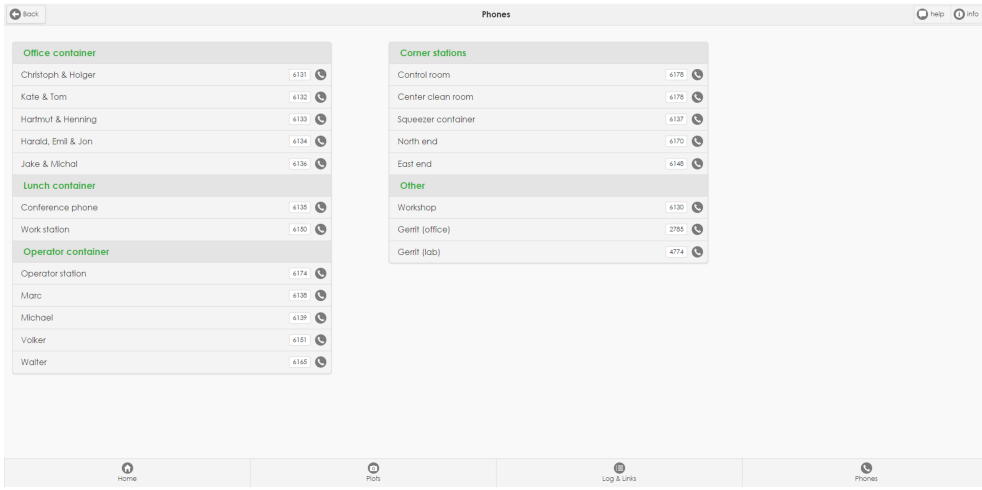

Figure C.4.: GEOweb pages for 'Log & Links' (top) and 'Phones' (bottom).

Listing C.1: HTML code for GEOweb

```
<!DOCTYPE html>
<!-- Holger Wittel 2014 -->
<html lang="en">
    <head>
        <meta HTTP-EQUIV="refresh" CONTENT="600">
        <meta charset="utf-8" />
        <title>GEOweb</title>

        <link rel="stylesheet" href="./plugin/jquery.mobile-1.4.0-rc.1.min.css">

        <link rel="stylesheet" href="./GEOweb.css"/>
        <link rel="stylesheet" type="text/css" href="./mobile_no_shadows.css" media="screen and (max-width: 14cm)"/>
              <!--fixes some slowness on android -->

        <script src="./plugin/jquery-2.0.3.min.js" type="text/javascript"></script>
        <script src="./plugin/jquery.mobile-1.4.0-rc.1.min.js" type="text/javascript"></script>

        <script src="./GEOweb.js" type="text/javascript"></script>
        <meta name="viewport" content="width=device-width, initial-scale=1, maximum-scale=1, user-scalable=no">

        <!-- Apple specific -->
        <meta name="apple-mobile-web-app-capable" content="no" />
        <link rel="apple-touch-startup-image" href="./IMG/GEOLogo.jpg" />
        <link rel="apple-touch-icon" href="./IMG/touch-icon-iphone4.png" />
    </head>

    <body>
<!-- ------------------------------------------------------------------- -->
        <div data-role="page" id="home"><!-- Page Home -->
            <div data-role="header" data-position="fixed">
                <a href="#" data-role="button" data-rel="back" data-inline="true" data-icon="arrow-l" data-direction
                      ="reverse" >Back</a>
                <h1>GEOweb</h1>
                <div data-type="horizontal" data-role="controlgroup" class="ui-btn-right">
                    <a href="#help_home" data-role="button" data-inline="true" data-icon="comment">help</a>
                    <a href="#info" data-role="button" data-inline="true" data-icon="info">info</a>
                </div>
            </div>

            <article data-role="content">
                <div class="ui-grid-a my-breakpoint">
                    <div class="ui-block-a">
                        <div id="wrapper1" style="text-align:center">
                            <a href="./SpecOut.png" rel="external" target="_blank">  <img src="./IMG/bad1.png" class
                                  ="fullscreen" alt="spectrum" id="spectrum"/></a>
                            <!-- inserting the javascript here is not so nice, but MUCH faster than using $doument.
                                  ready -->
                            <script type="text/javascript">
                                reload_spect();
                            </script>

                            <div class="ui-grid-a homebuttons">
                                <div class="ui-block-a">
                                    <a href="javascript:playaudio()" data-role="button" id="listenbuttonID">Listen!<
                                          /a>
                                </div>
                                <div class="ui-block-b">
                                    <a href="#drawing" data-role="button">Sketch!</a>
                                </div>
                            </div>
                        </div>
                    </div>

                    <div class="ui-block-b">
                        <form name="clock">
                            <input type="text" name="display" size="8" value="Loading...">
                        </form>

                        <!-- status vector -->
                        <div data-role="collapsible" data-theme="a" data-content-theme="a" data-inset="true" id="
                              status_header" data-collapsed="false">

                            <ul data-role="listview" id="currentpower"  data-inset="true">
                                <li>??? kW circulating light power, ??? dB squeezing</li>
                            </ul>

                            <h2> <div id="geo_status">GEO status</div></h2>
                            <ul data-role="listview" data-inset="true" id="geostats">
                            </ul>
                        </div><!-- status vector -->

                         <div data-role="collapsible" id="earthquake" data-collapsed="true">
                             <h3>Earthquakes</h3>
                            <code><div id="earthquake_text"><p> big earthquake here! </p></div></code>
                         </div>

                    </div><!-- /grid-a - block B-->
```

```
82                  </div>
83              </article>
84
85              <div data-role="footer" data-position="fixed">
86                  <nav data-role="navbar">
87                      <ul>
88                          <li><a href="#home" data-icon="home" data-transition="slideup" data-theme="a">Home</a></li>
89                          <li><a href="#plots" data-icon="camera" data-transition="slide">Plots</a></li>
90                          <li><a href="#links" data-icon="bullets" data-transition="slide">Log & Links</a></li>
91                          <li><a href="#phones" data-icon="phone" data-transition="slide">Phones</a></li>
92                      </ul>
93                  </nav>
94              </div>
95          </div><!-- /Page Home -->
96
97
98  <!-- ------------------------------------------------------------------ -->
99          <div data-role="page" id="plots"><!-- Page Plots -->
100             <div data-role="header" data-position="fixed">
101                 <a href="#" data-role="button" data-rel="back" data-inline="true" data-icon="arrow-l" data-direction
                        ="reverse">Back</a>
102                 <h1>Plots</h1>
103                 <div data-type="horizontal" data-role="controlgroup" class="ui-btn-right">
104                     <a href="#help_home" data-role="button" data-inline="true" data-icon="comment" >help</a>
105                     <a href="#info" data-role="button" data-inline="true" data-icon="info">info</a>
106                 </div>
107             </div>
108
109             <article data-role="content">
110
111             <!-- Plots -->
112             <h2>Plots</h2>
113             <div class="ui-grid-b my-breakpoint2">
114                 <div class="ui-block-a">
115                     <div id="current-state-textID" class="current-state-text" style="text-align:center">current
                            state</div>
116                     <ul data-role="listview" data-inset="true">
117                         <li data-role="list-divider">state plots</li>
118                         <li><a href="./live_IMG/statevect.png" target="_blank" rel="external"><img src="./live_IMG/
                                statevect_thumb.png" alt="State vector">State Vector </a></li>
119                         <li><a href="./live_IMG/hSensMon.png" target="_blank" rel="external"><img src="./live_IMG/
                                hSensMon_thumb.gif" alt="H Sens Mon">H Sensitivity Monitor </a></li>
120                     </ul>
121
122                     <ul data-role="listview" data-inset="true">
123                         <li data-role="list-divider">Interferometer Monitors</li>
124                         <li><a href="./live_IMG/ifoMon2.png" target="_blank" rel="external"><img class="load-delay"
                                src="./IMG/grey.png" data-original="./live_IMG/ifoMon2_thumb.gif" alt="ifoMon2">IFO
                                Monitor 2 </a></li>
125                         <li><a href="./live_IMG/ifoMon3.png" target="_blank" rel="external"><img class="load-delay"
                                src="./IMG/grey.png" data-original="./live_IMG/ifoMon3_thumb.gif" alt="H Sens Mon">
                                IFO Monitor 3 </a></li>
126                     </ul>
127
128                     <ul data-role="listview" data-inset="true">
129                         <li data-role="list-divider">PEM Monitors</li>
130                         <li><a href="./live_IMG/PEMMON.png" target="_blank" rel="external"><img class="load-delay"
                                src="./IMG/grey.png" data-original="./live_IMG/PEMMON_thumb.gif" alt="H Sens Mon">PEM
                                 Monitor </a></li>
131                         <!-- [...] other environment monitors omitted here -->
132                     </ul>
133
134                     <ul data-role="listview" data-inset="true">
135                         <li data-role="list-divider">Control screens</li>
136                         <li><a href="./live_IMG/Control5.png" target="_blank" rel="external"><img class="load-delay"
                                 src="./IMG/grey.png" data-original="./live_IMG/Control5_thumb.png" alt="Control 5">
                                Control 5</a></li>
137                         <!-- [...] other scrrenshots of contrl computers omitted here -->
138                     </ul>
139
140                     <ul data-role="listview" data-inset="true">
141                         <li data-role="list-divider">fine alignments</li>
142                         <li><a href="./finealign/rotAA.png" target="_blank" rel="external"><img class="load-delay"
                                src="./IMG/grey.png" data-original="./finealign/rotAA_thumb.png" alt="rot AA">
                                rotation AA fine alignment</a></li>
143                         <!-- [...] other alignement plots omitted here -->
144                     </ul>
145
146                     <ul data-role="listview" data-inset="true">
147                         <li data-role="list-divider">lock losses</li>
148                         <li><a href="./lockloss/L1.png" target="_blank" rel="external"><img class="load-delay" src="
                                ./IMG/grey.png" data-original="./lockloss/L1_thumb.png" alt="last lockloss">last lock
                                 loss </a></li>
149                         <!-- [...] other plots omitted here -->
150
151                     </ul>
152                 </div>
153
154                 <div class="ui-block-b">
```

```
155                 </div>
156
157                 <div class="ui-block-c">
158                 <div style="text-align:center">long term plots</div>
159                 <div id="monthlyplot">
160                     <ul data-role="listview" data-inset="true">
161                         <li data-role="list-divider">GEO stability and dutycycle</li>
162                         <li><a href="./live_IMG/GEOhappy.png" target="_blank" rel="external"><img class="load-delay"
                                src="./IMG/grey.png" data-original="./live_IMG/GEOhappy_thumb.png" alt="GEO
                               happiness">GEO happiness (stability)</a></li>
163                         <li><a href="./groups/georeports_September2013/reports/dutycycle_normal.gif" target="_blank"
                                rel="external"><img class="load-delay" src="./IMG/grey.png" data-original="./groups/
                               georeports_September2013/reports/dutycycle_thumb.gif" alt="GEO dutycycle">GEO
                               dutycycle</a></li>
164                     </ul>
165
166                     <ul data-role="listview" data-inset="true">
167                         <li data-role="list-divider">Squeezing</li>
168                         <li><a href="./live_IMG/SQZ.png" target="_blank" rel="external"><img class="load-delay" src=
                               "./IMG/grey.png" data-original="./live_IMG/SQZ_thumb.png" alt="Squeezing level">
                               Squeezing level</a></li>
169                     </ul>
170
171                     <ul data-role="listview" data-inset="true">
172                         <li data-role="list-divider">other</li>
173                         <li><a href="./live_IMG/midvisBLRMS.png" target="_blank" rel="external"><img class="load-
                               delay" src="./IMG/grey.png" data-original="./live_IMG/midvisBLRMS_thumb.png" alt="
                               inspiral">Mystery Noise level</a></li>
174                         <!-- [...] other plots omitted here -->
175                     </ul>
176                 </div>
177                 </div>
178             </div> <!-- grid a-->
179
180             </article>
181
182             <div data-role="footer" data-position="fixed">
183                 <nav data-role="navbar">
184                     <ul>
185                         <li><a href="#home" data-icon="home" data-transition="slide" data-direction="reverse">Home</
                                a></li>
186                         <li><a href="#plots" data-icon="camera" data-transition="slide" data-theme="a">Plots</a></li
                                >
187                         <li><a href="#links" data-icon="bullets" data-transition="slide">Log & Links</a></li>
188                         <li><a href="#phones" data-icon="phone" data-transition="slide">Phones</a></li>
189                     </ul>
190                 </nav>
191             </div>
192         </div><!-- /Page Help -->
193
194
195 <!-- ------------------------------------------------------------------ -->
196         <div data-role="page" id="links"><!-- Page Links -->
197             <div data-role="header" data-position="fixed">
198                 <a href="#" data-role="button" data-rel="back" data-inline="true" data-icon="arrow-l" data-direction
                        ="reverse">Back</a>
199                 <h1>Log & Links</h1>
200                 <div data-type="horizontal" data-role="controlgroup" class="ui-btn-right">
201                     <a href="#help_home" data-role="button" data-inline="true" data-icon="comment" >help</a>
202                     <a href="#info" data-role="button" data-inline="true" data-icon="info">info</a>
203                 </div>
204             </div>
205
206             <article data-role="content">
207
208             <div class="ui-grid-b my-breakpoint2">
209                 <div class="ui-block-a">
210                     <ul data-role="listview" data-inset="true">
211                         <li data-role="list-divider">Logbooks</li>
212                         <li><a href="https://intranet.aei.uni-hannover.de/geo600/geohflogbook.nsf" data-transition="
                                slide" rel="external" target="_blank">GHF logbook</a></li>
213                         <!-- [...] other list entries omitted here -->
214
215                         <li data-role="list-divider">Logbook lists</li>
216                         <li><a href="https://intranet.aei.uni-hannover.de/geo600/geohflogbook.nsf" data-transition="
                                slide" rel="external" target="_blank">Work list</a></li>
217                         <!-- [...] other list entries omitted here -->
218
219                         <li data-role="list-divider">Summary pages</li>
220                         <li><a href="http://www.geo600.uni-hannover.de/georeports/" data-transition="slide" rel="
                                external" target="_blank">Summary pages</a></li>
221                         <li><a href="https://atlas1.atlas.aei.uni-hannover.de/~geodc/LSC/monitors/" data-transition=
                                "slide" rel="external" target="_blank">Atlas summary pages</a></li>
222                         <li><a href="http://www.geo600.uni-hannover.de/georeports/screenshot_archive/" data-
                                transition="slide" rel="external" target="_blank">control computer screenshot archive
                                </a></li>
223                     </ul>
224                 </div>
225
```

```
226                 <div class="ui-block-b">
227                 </div>
228
229                 <div class="ui-block-c">
230                     <ul data-role="listview" data-inset="true">
231
232                         <li data-role="list-divider">Other</li>
233                         <li><a href="http://geofon.gfz-potsdam.de/eqinfo/seismon/globmon.php" data-transition="slide
                                " rel="external" target="_blank">Seismic monitor</a></li>
234                         <li><a href="http://www.muk.uni-hannover.de/wetter/wetterdaten.php" data-transition="slide"
                                rel="external" target="_blank">Weather in Ruthe</a></li>
235
236                         <li data-role="list-divider">only from AEI Network</li>
237                         <li><a href="http://130.75.117.140/" data-transition="slide" rel="external" target="_blank">
                                Vacuum status</a></li>
238                         <li><a href="https://info.geo600.uni-hannover.de/GEOStatus/CurrDAQSStat" data-transition="
                                slide" rel="external" target="_blank">DAQS configuration</a></li>
239                         <li><a href="http://130.75.117.171/" data-transition="slide" rel="external" target="_blank">
                                East camera</a></li>
240                         <!-- [...] other camera images omitted here -->
241                     </ul>
242                 </div>
243             </div>
244             </article>
245
246         <div data-role="footer" data-position="fixed">
247             <nav data-role="navbar">
248                 <ul>
249                     <li><a href="#home" data-icon="home" data-transition="slide" data-direction="reverse">Home</a></
                            li>
250                     <li><a href="#plots" data-icon="camera" data-transition="slide" data-direction="reverse">Plots</
                            a></li>
251                     <li><a href="#links" data-icon="bullets" data-transition="slideup" data-theme="a">Log & Links</a
                            ></li>
252                     <li><a href="#phones" data-icon="phone" data-transition="slide">Phones</a></li>
253                 </ul>
254             </nav>
255         </div>
256         </div><!-- /Page Links -->
257
258
259 <!-- ------------------------------------------------------------------- -->
260         <div data-role="page" id="phones"><!-- Page Phones -->
261             <div data-role="header" data-position="fixed">
262                 <a href="#" data-role="button" data-rel="back" data-inline="true" data-icon="arrow-l" data-direction
                        ="reverse">Back</a>
263                 <h1>Phones</h1>
264                 <div data-type="horizontal" data-role="controlgroup" class="ui-btn-right">
265                     <a href="#help_home" data-role="button" data-inline="true" data-icon="comment" >help</a>
266                     <a href="#info" data-role="button" data-inline="true" data-icon="info">info</a>
267                 </div>
268             </div>
269
270             <article data-role="content">
271
272             <div class="ui-grid-b my-breakpoint2">
273                 <div class="ui-block-a">
274                     <ul data-role="listview" data-inset="true">
275                         <li data-role="list-divider">Office container</li>
276                         <li data-icon="phone"><a href="tel:00495117626131">Christoph & Holger<span class="ui-li-
                                count">6131</span></a></li>
277                         <!-- [...] other phone list entries omitted here -->
278                     </ul>
279                 </div>
280
281                 <div class="ui-block-b">
282                 </div>
283
284                 <div class="ui-block-c">
285                     <ul data-role="listview" data-inset="true">
286                         <li data-role="list-divider">Corner stations</li>
287                         <li data-icon="phone"><a href="tel:00495117626178">Control room<span class="ui-li-count">
                                6178</span></a></li>
288                         <!-- [...] other list entries omitted here -->
289
290                         <li data-role="list-divider">Other</li>
291                         <li data-icon="phone"><a href="tel:00495117626130">Workshop<span class="ui-li-count">6130</
                                span></a></li>
292                         <!-- [...] other list entries omitted here -->
293                     </ul>
294                 </div>
295             </article>
296
297         <div data-role="footer" data-position="fixed">
298             <nav data-role="navbar">
299                 <ul>
300                     <li><a href="#home" data-icon="home" data-transition="slide" data-direction="reverse">Home</a></
                            li>
301                     <li><a href="#plots" data-icon="camera" data-transition="slide" data-direction="reverse">Plots</
```

```
                        a></li>
302                     <li><a href="#links" data-icon="bullets" data-transition="slide" data-direction="reverse">Log &
                            Links</a></li>
303                     <li><a href="#phones" data-icon="phone" data-transition="slide" data-theme="a">Phones</a></li>
304                 </ul>
305             </nav>
306         </div>
307         </div><!-- Page /Phones -->
308
309
310
311 <!-- ------------------------------------------------------------------ -->
312         <div data-role="page" id="drawing"><!-- drawing -->
313             <div data-role="content" id="theContent">
314                 <canvas id="theCanvas">
315                     <h1>Your browser does not support the HTML5 canvas element.</h1>
316                 </canvas>
317             </div>
318
319             <div data-role="footer" data-position="fixed">
320                 <nav data-role="navbar">
321                     <ul>
322                             <li><a href="#" data-rel="back" data-icon="arrow-l" data-direction="reverse">back</a></
                                    li>
323                             <li><a href="javascript: drawingUtil.clear()" data-icon="delete">Clear canvas</a></li>
324                             <li><a href="javascript: drawingUtil.toImage()" data-icon="camera">Open as image</a></li
                                    >
325                     </ul>
326                 </nav>
327             </div>
328
329             <div data-role="popup" id="popupPhoto" data-overlay-theme="a" data-corners="false">
330                 <a href="#" data-rel="back" data-role="button" data-theme="a" data-icon="delete"  class="ui-popup-
                        btn-close">Close</a><img src="" style="margin-bottom:-4px" id="thePopupImage">
331             </div>
332         </div><!-- /drawing -->
333
334
335
336 <!-- ------------------------------------------------------------------ -->
337         <div data-role="page" id="info"><!-- Page Info -->
338
339             <div data-role="header" data-position="fixed">
340                 <a href="#" data-role="button" data-rel="back" data-inline="true" data-icon="arrow-l" data-direction
                        ="reverse">Back</a>
341                 <h1>Info</h1>
342                 <a href="#info" data-role="button" data-inline="true" data-icon="info" data-theme="a">info</a>
343             </div>
344
345             <article data-role="content">
346             <b>GEO WebApp, Version 2.9.2, 11.April 2014 </b> <br> <br>
347
348                 <div data-role="collapsible" data-theme="a" data-content-theme="a" data-inset="true">
349                     <h2>version info</h2>
350                         <ul data-role="listview" data-inset="true" id="changelog">
351
352                                 <li data-role="list-divider">changelog</li>
353                                 <li><b>1.0</b>  initial version</li>
354                                 <li><b>1.1</b>  fixed typos and DAQS config link</li>
355                                 <li><b>1.2</b>  added link to Atlas state vector plot, Geo status refreshing, added
                                        caching</li>
356                                 <li><b>1.3</b>  added "annotate and save" button, also added help page</li>
357                                 <li><b>1.4</b>  added listen function</li>
358                                 <li><b>1.5</b>  (un-)locked time in proper units, general improvements</li>
359                                 <li><b>1.6</b>  error message when there is something wrong the audio, performance
                                        improvements</li>
360                                 <li><b>1.7</b>  added display of circulating power and squeezing</li>
361                                 <li><b>1.8</b>  added berta and month plots</li>
362                                 <li><b>1.9</b>  fixed error handling</li>
363                                 <li><b>2.0</b>  "GEO status" text changes color, as does the stone on site (not all
                                        colors supported yet) </li>
364                                 <li><b>2.1</b>  Plots open in new tab, lockloss plots</li>
365                                 <li><b>2.2</b>  Plots section!</li>
366                                 <li><b>2.3</b>  changed warning about old data, separate layout for mobile and
                                        desktop</li>
367                                 <li><b>2.4</b>  bigger thumbnails, images open in new tabs, easier logbook access,
                                        direct links to work and lunch list</li>
368                                 <li><b>2.5</b>  links to month plots auto-generated, desktop version: phone links &
                                        geo status color working now</li>
369                                 <li><b>2.6</b>  links to month plots auto-generated (and working), GEO happiness
                                        plot</li>
370                                 <li><b>2.7</b>  state vector plot, new jqm version (faster?), new design</li>
371                                 <li><b>2.7.1</b>  Same file for phones and desktop, fixed many issues </li>
372                                 <li><b>2.8</b>  made plots,links and phone lists "responsive", thumbs for the plots
                                        section </li>
373                                 <li><b>2.8.1</b> delayed loading of thumbnails, link to labview archive</li>
374                                 <li><b>2.9</b> earthquake arrival times at GEO</li>
375                                 <li><b>2.9.1</b> Mystery Noise plot</li>
376                                 <li><b>2.9.2</b>GEO data logbook</li>
```

```
                                <li data-role="list-divider">known issues</li>
                                <li>- annotated spectrum low quality on mobile phones</li>
                                <li>- audio not working on android</li>
                            </ul>
                        </div>

                <br><br>
                Author: Holger Wittel,<br> comments, bugs, and suggestions to
                <li><a href="mailto:holger.wittel@aei.mpg.de">holger.wittel@aei.mpg.de</a></li> <br><br>
                </article>

                <div data-role="footer" data-position="fixed">
                    <nav data-role="navbar">
                        <ul>
                            <li><a href="#home" data-icon="home" data-transition="slideup">Home</a></li>
                            <li><a href="#plots" data-icon="camera" data-transition="slide">Plots</a></li>
                            <li><a href="#links" data-icon="bullets" data-transition="slideup">Log & Links</a></li>
                            <li><a href="#phones" data-icon="phone" data-transition="slideup">Phones</a></li>
                        </ul>
                    </nav>
                </div>
            </div><!-- /Page Info -->


<!-- ------------------------------------------------------------------- -->
            <div data-role="page" id="help_home"><!-- /Page Help -->
                <div data-role="header" data-position="fixed">
                    <a href="#" data-role="button" data-rel="back" data-inline="true" data-icon="arrow-l" data-direction
                          ="reverse">Back</a>
                    <h1>Help</h1>
                    <div data-type="horizontal" data-role="controlgroup" class="ui-btn-right">
                        <a href="#help_home" data-role="button" data-inline="true" data-icon="comment" data-theme="a" >
                              help</a>
                        <a href="#info" data-role="button" data-inline="true" data-icon="info">info</a>
                    </div>
                </div>

                <article data-role="content">
                <b> The image at the top </b> usually shows two sensitivity curves.<br>
                A <span style="color:red"><b>red reference curve,</b></span> and <span style="color:blue"><b>the current
                      sensitivity as blue curve.</b></span> <br>
                If there is no blue curve, then GEO is not fully locked. <br>
                Some lines in the blue curve have markers on top, those lines are injected intentionally. <br><br>

                With the button "Sketch!" you can annotate and save the current spectrum.
                "Listen!" allows you to listen to the interferometer output. The audio is 90-150 seconds delayed.<br><br
                    >
                The field below shows the <b>current UTC time</b><br><br>

                <b>At the bottom</b> is an expandable list that shows for how long GEO has been (un-)locked and the
                      state of various subsystems.
                In normal science (data-taking) operation, all entries should have a <span style="color:lime"><b>green
                      ok sign.</b></span> <br><br>
            </article>

            <div data-role="footer" data-position="fixed">
                <nav data-role="navbar">
                    <ul>
                        <li><a href="#home" data-icon="home" data-transition="slideup">Home</a></li>
                        <li><a href="#plots" data-icon="camera" data-transition="slide">Plots</a></li>
                        <li><a href="#links" data-icon="bullets" data-transition="slideup">Log & Links</a></li>
                        <li><a href="#phones" data-icon="phone" data-transition="slideup">Phones</a></li>
                    </ul>
                </nav>
            </div>
            </div><!-- /Page Help -->

        </body>
</html>
```

Listing C.2: CSS code for GEOweb

```
 /* Holger Wittel*/
 img.fullscreen {
    max-height: 100%;max-width: 100%;
 }

@media all and (max-width: 60em) {
/* start page */
    .ui-grid-a.my-breakpoint .ui-block-a,
    .ui-grid-a.my-breakpoint .ui-block-b{width: 100%; float:none;}

  .ui-grid-a.homebuttons .ui-block-a,
  .ui-grid-a.homebuttons .ui-block-b{width: 100%; clear: none;}
    #wrapper1{width: 100%;}
```

```
/* PLOTS page */
  .ui-grid-b.my-breakpoint2 .ui-block-a,
  .ui-grid-b.my-breakpoint2 .ui-block-b,
  .ui-grid-b.my-breakpoint2 .ui-block-c{width: 100%; float:none;}
}

@media all and (min-width: 60.1em) {
/* start page */
    .ui-grid-a.my-breakpoint .ui-block-a{width: 64.95%;  clear: left;}
    .ui-grid-a.my-breakpoint .ui-block-b{width: 34.925%;}
  .ui-grid-a.homebuttons .ui-block-a,
  .ui-grid-a.homebuttons .ui-block-b{width: 50%; clear: none;}
   #wrapper1{width: 90%;}
/* PLOTS page */
  .ui-grid-b.my-breakpoint2 .ui-block-a{width: 33%;}
  .ui-grid-b.my-breakpoint2 .ui-block-b{width: 5.925%;}
  .ui-grid-b.my-breakpoint2 .ui-block-c{width: 33%;}
}

.in, .out {
    -webkit-animation-timing-function: ease-in-out;
    -webkit-animation-duration: 150ms !important;
}

.ui-content .ui-listview .ui-li-divider {
    font-size: 18px;
    color: #3eb249;
    background: #e4e4e4;
}

.ui-content, .ui-content .ui-block-b .ui-input-text input, .ui-btn, .ui-li-count, body {
  font-family: "Avant Garde", Avantgarde, "Century Gothic", CenturyGothic, "AppleGothic", sans-serif;
  font-weight: 300;
}

.ui-page-theme-a {
  font-weight: 500;
}

.ui-page-theme-a .ui-btn, html .ui-bar-a .ui-btn, html .ui-body-a .ui-btn, html body .ui-group-theme-a .ui-btn, html head+body .ui-btn.ui-btn-a, .ui-page-theme-a .ui-btn:visited, html .ui-bar-a .ui-btn:visited, html .ui-body-a .ui-btn:visited, html body .ui-group-theme-a .ui-btn:visited, html head+body .ui-btn.ui-btn-a:visited{
    background: #f4f4f4;
}

.ui-btn-icon-left:after, .ui-btn-icon-right:after, .ui-btn-icon-top:after, .ui-btn-icon-bottom:after, .ui-btn-icon-notext:after, html .ui-btn.ui-icon-checkbox-off:after, html .ui-btn.ui-icon-radio-off:after {
  background-color: rgba(0, 0, 0, 0.5) !important;
}

.ui-bar-a, .ui-page-theme-a .ui-bar-inherit, html .ui-bar-a .ui-bar-inherit, html .ui-body-a .ui-bar-inherit, html body .ui-group-theme-a .ui-bar-inherit {
  background: #e1e1e1;
  border-color: #ddd;
}

.ui-page-theme-a .ui-btn:hover, html .ui-bar-a .ui-btn:hover, html .ui-body-a .ui-btn:hover, html body .ui-group-theme-a .ui-btn:hover, html head+body .ui-btn.ui-btn-a:hover {
  background: #c8c8c8;
  border-color: rgba(0, 0, 0, 0.2);
}

.ui-bar-a, .ui-page-theme-a .ui-bar-inherit, html .ui-bar-a .ui-bar-inherit, html .ui-body-a .ui-bar-inherit, html body .ui-group-theme-a .ui-bar-inherit {
  background: none repeat scroll 0 0 #f1f1f1;
  border-color: #DDDDDD;
}

.arrowDown {
  border-top: 30px solid #aaa;
  border-left: 30px solid transparent;
  border-right: 30px solid transparent;
  font-size: 0;
  line-height: 0;
  width: 0;
 }

.bottom-space {
    margin-bottom: 100px;
  }

  .ui-li-thumb, .ui-li-icon {
    left: 1px;
    max-height: 100px;
    max-width: 100px;
    position: absolute;
    top: 0;
  }

```

```
97
98 .ui-listview > .ui-li-has-thumb > .ui-btn, .ui-listview > .ui-li-static.ui-li-has-thumb {
99     min-height: 3.625em;
100    padding-left: 7em;
101    }
102
103
104 .ui-listview .ui-li-has-thumb > img:first-child, .ui-listview .ui-li-has-thumb > .ui-btn > img:first-child, .ui-
        listview .ui-li-has-thumb .ui-li-thumb {
105   left: 0;
106   max-height: 6em;
107   max-width: 6.5em;
108   position: absolute;
109   top: 0;
110   min-height: 3em;
111   min-width: 3.5em;
112 }
```

Listing C.3: JavaScript code for GEOweb

```
1     //Holger Wittel
2
3     //<!-- UTC time clock -->
4     function clock(){
5         updateClock = new Date();
6         document.clock.display.value = updateClock.toGMTString() + "/ UTC";
7         setTimeout("clock()", 1000)
8     }
9
10   //<!-- reload spectrum every 30 secs -->
11    function reload_spect(){
12        d = new Date();
13        var myImageElement = document.getElementById('spectrum');
14        myImageElement.src ='SpecOut.png?' +Math.round(d.getTime()/1000);
15        setTimeout("reload_spect()", 30000)
16    }
17
18    // execute when page DOM is ready
19    $(document).ready(function() {
20        //reload_spect();
21        clock();
22        get_status(); //call function to get status vector
23        get_powerandsqueeze();
24
25        get_earthquake();
26        replace_links();
27        test_mobile_replace_tel();
28        load_images_delayed();
29        //$("#current-state-textID").css('color', '#FF00FF');
30        //$("#geo_status").css('color', '#FF00FF');
31    });
32
33
34    //read status vector from textfile
35    function replace_links() {
36    var year = d.getFullYear();
37
38    var monthNames = [ "January", "February", "March", "April", "May", "June",
39    "July", "August", "September", "October", "November", "December" ];
40    var month = monthNames[d.getMonth()];
41        document.getElementById('monthlyplot').innerHTML = document.getElementById('monthlyplot').innerHTML.replace
              (/georeports_September2013/g, 'georeports_'+ month + year);
42        //document.refresh();
43    }
44
45
46    function get_earthquake(){
47        d = new Date();
48        jQuery.get('earthquake.txt?'+d.getTime(), function(data1) {
49            $('#earthquake_text').text(data1);
50            document.getElementById('earthquake_text').innerHTML = document.getElementById('earthquake_text').
                  innerHTML.replace(/ /g, ' ');
51            document.getElementById('earthquake_text').innerHTML = document.getElementById('earthquake_text').
                  innerHTML.replace(/\n/g, '<br>');
52        });
53        setTimeout("get_earthquake()", 60000)
54    }
55
56
57    //read status vector from textfile
58    function addlist_ok(text) {
59        $("#geostats").append("<li><img src='./IMG/good1.png' class='ui-li-icon' alt='ok'>" + text + "</li>");
60    }
61
62    function addlist_bad(text) {
63        $("#geostats").append("<li><img src='./IMG/bad1.png' class='ui-li-icon' alt='no'>" + text + "</li>");
```

```
64      }
65
66      //read status vector from textfile
67      function get_status(){
68      d = new Date();
69      jQuery.get('stats.log?'+d.getTime(), function(data) {  // async
70          $('#geostats').empty(); // empty list
71
72          var myArray = data.split("\n");
73
74          // go through array
75          for(var i=0;i<myArray.length;i++) {
76             // save each elemet in array
77             localStorage.setItem(i, myArray[i]);
78          }
79
80              var time_in_s;  // holds the locked / unlocked time in seconds
81              var time_displ;
82              var time_unit;
83              var geo_color;
84
85              if (localStorage[4][localStorage[4].length-1]==0) {
86                  time_in_s=(localStorage[3].toString()).split('         ');
87
88                  //display secs
89                  time_displ=time_in_s[1];
90                  time_unit=' sec';
91
92                  // display minutes
93                  if (time_in_s[1]>=60)
94                  {
95                      time_displ=time_in_s[1]/60;
96                      time_unit=' min';
97                  }
98
99                   if (time_in_s[1]>=3600)
100                 {
101                     time_displ=time_in_s[1]/3600;
102                     time_unit=' hrs';
103                 }
104                 time_displ=Math.round(time_displ*10)/10; //round to 2 decimals
105                 addlist_bad('unlocked time: '+ time_displ + time_unit ); //unlocked secs
106                 //addlist_bad(localStorage[3]); //unlocked secs
107                 geo_color='black';
108
109             } else {
110                 time_in_s=(localStorage[2].toString()).split('           ');
111
112                 //display secs
113                 time_displ=time_in_s[1];
114                 time_unit=' sec';
115
116                 // display minutes
117                 if (time_in_s[1]>=60)
118                 {
119                     time_displ=time_in_s[1]/60;
120                     time_unit=' min';
121                 }
122
123                  if (time_in_s[1]>=3600)
124                 {
125                     time_displ=time_in_s[1]/3600;
126                     time_unit=' hrs';
127                 }
128
129                 time_displ=Math.round(time_displ*10)/10; //round to 2 decimals
130                 addlist_ok('locked time: '+ time_displ + time_unit ); //unlocked secs
131             }
132
133             if (localStorage[5][localStorage[5].length-1]==0) {
134                 addlist_ok("hardware maintenance OFF");
135             } else {
136                 addlist_bad("hardware maintenance ON");
137             }
138
139             if (localStorage[6][localStorage[6].length-1]==0) {
140                 addlist_ok("software maintenance OFF");
141             } else {
142                 addlist_bad("software maintenance ON");
143             }
144
145             if (localStorage[7][localStorage[7].length-1]==1) {
146                 addlist_ok("on final power");
147                 geo_color='orange';
148             } else {
149                 addlist_bad("NOT on final power");
150             }
151
152             if (localStorage[8][localStorage[8].length-1]==1) {
```

```
153                 addlist_ok("calibration OK");
154             } else {
155                 addlist_bad("calibration NOT ok");
156             }
157 
158             if (localStorage[9][localStorage[9].length-1]==0) {
159                 addlist_ok("config file reread");
160             } else {
161                 addlist_bad("config file NOT reread");
162             }
163 
164             if (localStorage[10][localStorage[10].length-1]==0) {
165                 addlist_ok("timestamping OK");
166             } else {
167                 addlist_bad("timestamping BAD");
168             }
169 
170             if (localStorage[11][localStorage[11].length-1]==1) {
171                 addlist_ok("digital signal recycling loop LOCKED");
172                 geo_color='blue';
173             } else {
174                 addlist_bad("digital signal recycling loop NOT locked");
175             }
176 
177             if (localStorage[12][localStorage[12].length-1]==1) {
178                 addlist_ok("squeezing ON");
179 
180                 // AND if DSR locked -
181                 if (localStorage[11][localStorage[11].length-1]==1) {
182                 geo_color='#FF00FF';
183                 }
184 
185             } else {
186                 addlist_bad("squeezing OFF")
187             }
188 
189             if (localStorage[13][localStorage[13].length-1]==0) {
190                 addlist_ok("NO hardware injection");
191             } else {
192                 addlist_bad("hardware injection running");
193             }
194 
195             if (localStorage[14][localStorage[14].length-1]==1) {
196                 addlist_bad("chi square BAD");
197             } else {
198                 addlist_ok("chi square OK");
199             }
200 
201 
202             $("#current-state-textID").css('color', geo_color);
203             $("#geo_status").css('color', geo_color);
204 
205 
206             $("#geostats").listview('refresh');
207     });
208             //$('#geostats').listview('refresh');
209             setTimeout("get_status()", 20000)
210     };
211 
212 
213     // Listen! button
214     var isplaying=0;
215     var geo_audio = document.createElement("audio");
216     function playaudio() {
217 
218     if (check_time()==1)
219     {
220         alert('The data is old! Please nake sure that your internet connection is ok. If that does not help, restart
                the Matlab script  /daqs/holger/streamingH/streamingH.m on Alaysis3');
221     }
222 
223     if (isplaying == 0)
224        {
225             isplaying=1;
226             d = new Date();
227             var source= document.createElement('source');
228 
229             if (geo_audio.canPlayType('audio/mpeg;')) {
230                 source.type= 'audio/mpeg';
231                 source.src= './sound/geosound.mp3?' +d.getTime();
232             } else {
233                 source.type= 'audio/ogg';
234                 source.src= './sound/geosound.ogg?' +d.getTime();
235             }
236 
237             geo_audio = new Audio(source.src);
238             geo_audio.load();
239             geo_audio.play();
240         }
```

```
241         else
242         {
243             isplaying=0;
244             geo_audio.pause();
245         }
246     }
247 
248 
249     function check_time(){
250         d = new Date();
251         jQuery.get('./sound/time.txt?'+d.getTime(), function(data) {  // async
252             var time_audio=data.toString();
253             if ( Math.abs(time_audio- d.getTime()) < 150000){
254                 return 0;
255             }
256             else
257             {
258                 return 1;
259             }
260         })
261         .fail(function(data) {
262         //alert('The audio is old! Please restart the Matlab script  /daqs/holger/streamingH/streamingH.m on
                Alaysis3:3');
263         return 1; });
264     }
265 
266 
267     function get_powerandsqueeze(){
268         d = new Date();
269         if (check_time()==1)
270         {
271             $('#currentpower').empty();
272             $('#currentpower').append("<li>" + 'Please restart the Matlab script  /daqs/holger/streamingH/streamingH
                    .m on Alaysis3' + "</li>");
273             $('#currentpower').listview('refresh');
274             return;
275         }
276 
277         jQuery.get('powerandsqueeze.txt?'+d.getTime(), function(data) {  // async
278             $('#currentpower').empty();
279             $('#currentpower').append("<li>" + data + "</li>");
280             $('#currentpower').listview('refresh');
281             });
282         setTimeout("get_powerandsqueeze()", 20000)
283     }
284 
285 
286     function test_mobile_replace_tel(){
287         var mobile = (/iphone|ipad|ipod|android|blackberry|mini|windows\sce|palm/i.test(navigator.userAgent.
                toLowerCase()));
288         if (mobile) {
289             return;
290         }
291         else     {
292             document.getElementById('phones').innerHTML = document.getElementById('phones').innerHTML.replace(/tel:/
                    g, 'callto:');
293         }
294     }
295 
296 
297     function load_images_delayed(){
298         setTimeout(function () {
299             $('.load-delay').each(function () {
300                 var imagex = $(this);
301                 var imgOriginal = imagex.data('original');
302                 $(imagex).attr('src', imgOriginal);
303             });
304         }, 1000);
305     }
306 
307 
308 //***********************
309 //Drawing
310 //modified from http://canvas.sjmorrow.com/script.js
311 var drawingUtil = null;
312 $(function() {
313     String.prototype.contains = function(it) { return this.indexOf(it) != -1; };
314     var theCanvas = document.getElementById("theCanvas");
315     drawingUtil = new DrawingUtil(theCanvas);
316 
317     theCanvas.width = window.innerWidth*0.7;
318     //theCanvas.height = window.innerHeight;
319     theCanvas.height = 1.00*0.7*window.innerWidth*1.408/2.027;
320     drawingUtil.setStrokeWeight(5);
321 });
322 
323 function DrawingUtil(aCanvas) {
324     var canvas = aCanvas;
325     var context = canvas.getContext("2d");
```

```
326     var isDrawing = false;
327     var headerHeight = $("#theHeader").height();
328     init();
329
330     function start(event) {
331         isDrawing = true;
332         context.beginPath();
333         context.moveTo(getX(event),getY(event));
334         event.preventDefault();
335     }
336
337     function draw(event) {
338         if(isDrawing) {
339             context.lineTo(getX(event),getY(event));
340             context.stroke();
341         }
342         event.preventDefault();
343     }
344
345     function stop(event) {
346         if(isDrawing) {
347             context.stroke();
348             context.closePath();
349             isDrawing = false;
350         }
351         event.preventDefault();
352     }
353
354     function getX(event) {
355         if(event.type.contains("touch")) {
356             return event.targetTouches[0].pageX;
357         }
358         else {
359             return event.layerX;
360         }
361     }
362
363     function getY(event) {
364         if(event.type.contains("touch")) {
365             return event.targetTouches[0].pageY-headerHeight;
366         }
367         else {
368             return event.layerY;
369         }
370     }
371
372     this.clear = function() {
373         context.clearRect(0,0,canvas.width,canvas.height);
374         draw_bg();
375     }
376
377     this.toImage = function() {
378         var imageData = canvas.toDataURL();
379         $("#thePopupImage").attr("src",imageData);
380         $.mobile.popup.prototype.options.initSelector = "#popupPhoto";
381         $('#popupPhoto').popup('open',0,0);
382     }
383
384     this.setStrokeWeight = function(weight) {
385         context.lineWidth = weight;
386     }
387
388     function init() {
389         draw_bg();
390         canvas.addEventListener("touchstart",start,false);
391         canvas.addEventListener("touchmove",draw,false);
392         canvas.addEventListener("touchend",stop,false);
393         canvas.addEventListener("mousedown",start,false);
394         canvas.addEventListener("mousemove",draw,false);
395         canvas.addEventListener("mouseup",stop,false);
396         canvas.addEventListener("mouseout",stop,false);
397         window.addEventListener("orientationchange", sizechange, false);
398         window.addEventListener("resize", sizechange, false);
399     }
400
401      function draw_bg(){
402         var img = new Image();
403         d = new Date();
404
405         img.srcset ="./SpecOut.png?" + Math.round(d.getTime()/1000)+" 2x";
406         img.src = './SpecOut.png?' +Math.round(d.getTime()/1000);
407
408         img.onload = function(){
409             context.drawImage(img, parseInt(0), parseInt(0),parseInt(canvas.width),parseInt(canvas.height));
410         };
411     }
412
413
414     function sizechange(){
```

```
            theCanvas.width = window.innerWidth*0.7;
            //theCanvas.height = window.innerHeight;
            theCanvas.height = 1.00*0.7*window.innerWidth*1.408/2.027;

            context.clearRect(0,0,canvas.width,canvas.height);
            draw_bg();
            context.lineWidth = 5;
    };
}
//end drawing
//************************
```

Listing C.4: Matlab sample code for producing a plot for GEOweb

```
%% make a plot of the stability of GEO locks
% use the longest lock duration per night
% Oct 2013,  Holger Wittel
%%
function GEO_happyness_GEOweb(obj, event, string_arg)

try
%% parameters
server='130.75.117.73';
port=9000;
frametype=2;
%   type          -   the trend type - 1 (for hour trends)
%                                    - 2 (for day trends)
%                                    - 3 (for hour control trends)
%                                    - 4 (for day control trends)
%                                    - 5 (for BLRMS trends)

%get latest time
%disp('getting latest time from server...')
latest_time = m2fserv(server, port, 'DAY');
%start_date='2012-01-01';
start_date=[datestr(now,'yyyy-mm-') '01'];
start_time=UTC2GPS([start_date ' 00:00:00']); %must start at midnight
nsecs= latest_time-start_time;
ndays = nsecs/(24*3600);
ndays=round(ndays);

channel='G1:ASC_MCN_SPOT-PWR';  % name of the desired channel

%% download data
disp('downloading data for GEOhappiness')

%precache
av_lock_time=zeros(1,ndays);
longest_lock_time=zeros(1,ndays);
download_problem=zeros(1,ndays);
time_locked=zeros(1,ndays);
idx=1:480;
lock_loss_times=0;

for temp=1:ndays
    % get day frames
    disp(['downloading data...' GPS2UTC(start_time)])
    try
        [t1, x1] = m2fserv(server, port,start_time, channel, 'av', frametype); %dl first day
        [t2, x2] = m2fserv(server, port,start_time+86400, channel, 'av', frametype); %dl 2nd day
    catch
        x1=zeros(1440,1);
        x2=zeros(1440,1);
        download_problem(temp)=1;
        disp('ERROR')
    end

    %join both days (to get the night in between)
    x_joined=[x1 x2];

    %get data from the night
    x_night=x_joined(1200:1680); %20:00 to 04:00 UTC
    x=x_night;

    %calibrate data
    x(x<0.6)=0;     %no lock
    x(x>=0.6)=1;    %lock

    %average lock length per day
    time_locked(temp)=sum(x/60);  %locked time that night in h

    %find times of lock losses
    diff_x=diff(x);
    lock_loss_times=[lock_loss_times, idx(diff_x==-1)]; %time in s since 20:00 UTC of the locklosses

    %find longest lock duration
```

```
    l1=0;
    l2=0;
    for i=1:length(x);
        l1=l1+x(i);
        if x(i)==0 || i==length(x)
            if l1>l2
                l2=l1;
            end
            l1=0;
        end
    end
    longest_lock_time(temp)=l2;    % duration of longest lock during that night

    % move to next day
    start_time=start_time+86400;
end

%% correct the data (fill gaps)
for i=1:length(longest_lock_time)
    if download_problem(i)==1
        longest_lock_time(i)=longest_lock_time(i-1);
    end
end

%% plot data
figure(1)
bar(longest_lock_time/60)
ylim([2 8.05])
title(['longest lock per night,' ' starting on ' start_date])
xlabel('time (days)')
ylabel({'max lock duration per night in h', '(GEO happiness level)'});

if length(longest_lock_time)>9
    hold on
    test2=c_avg(1,longest_lock_time/60);
    plot(3:length(longest_lock_time)-3,test2(3:length(test)-3),'r','Linewidth',2)
    hold off
    legend({'data','lowpassed'})
end

set(gca,'FontSize',10);
xlhand = get(gca,'xlabel');
set(xlhand,'fontsize',14);
ylhand = get(gca,'ylabel');
set(ylhand,'fontsize',14);
set(gca,'XTick',[1 5 10 15 20 25])
start_date(end-1:end)='00'; %dirty hack to get the labels right
dateaxis('x', 17, start_date)
set(gcf, 'PaperOrientation', 'portrait');
print -dpng -r100 ./live_IMG/GEOhappy.png
legend(gca,'off')
print -dpng -r20 ./live_IMG/GEOhappy_thumb.png
close all

catch
    return
end
```

APPENDIX D

Technical drawings

The design of the mechanical and electronic systems outlined in this thesis was part of this work as well. This chapter contains the technical drawings, which were made in the course of this work, and used to fabricate the parts for this thesis. The design was made by the author, and the manufacturing was done by the workshop staff of the AEI, unless noted otherwise.

This chapter only contains drawings of the parts that were actually installed into GEO 600. Several prototypes and design variants are omitted for the sake of brevity. All measures are in millimeter.

D.1. Reflector for ring heater

The technical drawings that were used to make the reflector for the ring heater are given in this section. The reflector dish was fabricated by entering the data of the 3D CAD model digitally to a CNC turning machine. For completeness though, a 2D drawing of it is supplied here.

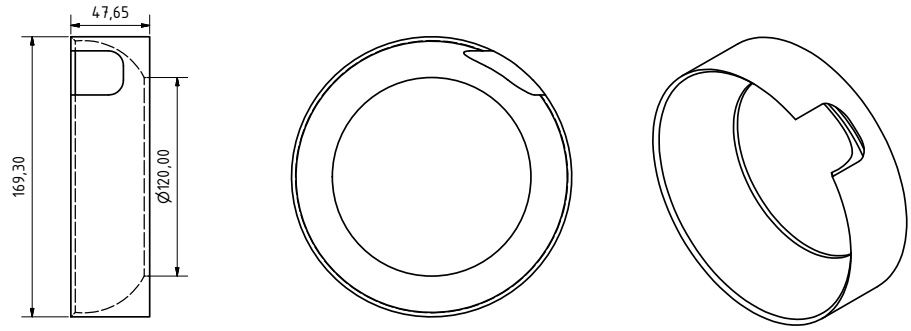

Figure D.1.: Drawing of the ring heater reflector dish.

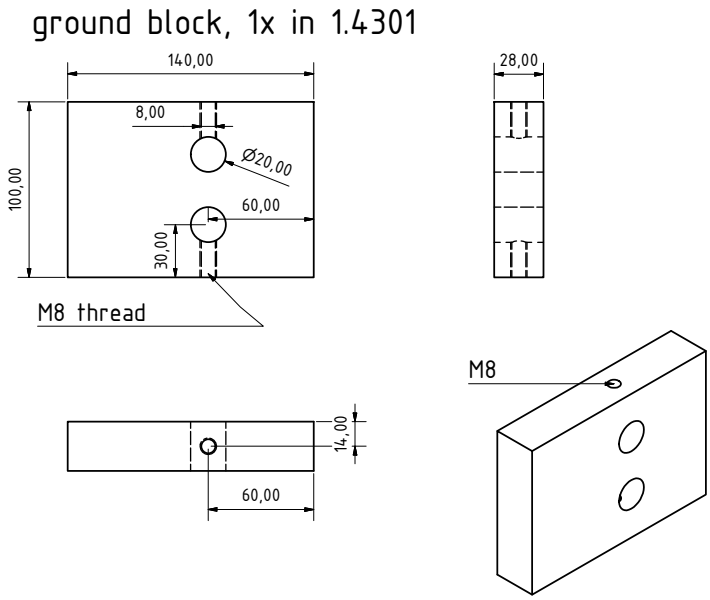

Figure D.2.: Drawing of the ring heater reflector foot.

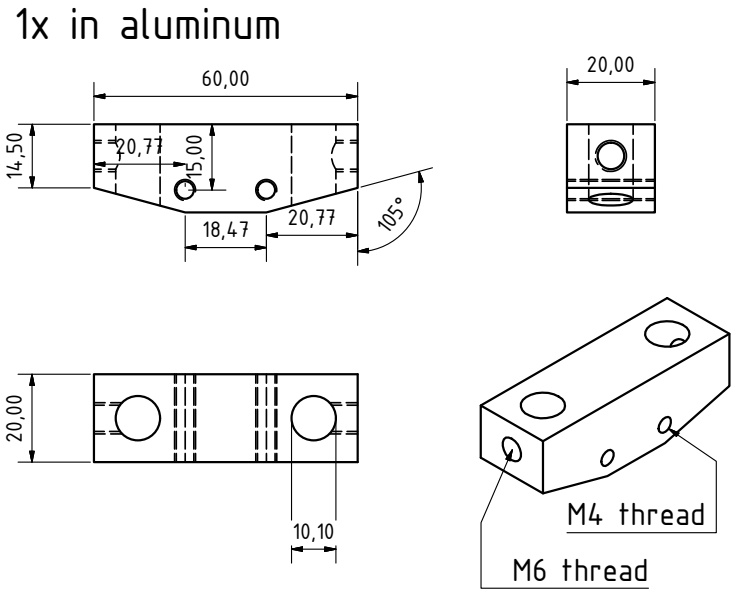

Figure D.3.: Drawing of the upper connection piece.

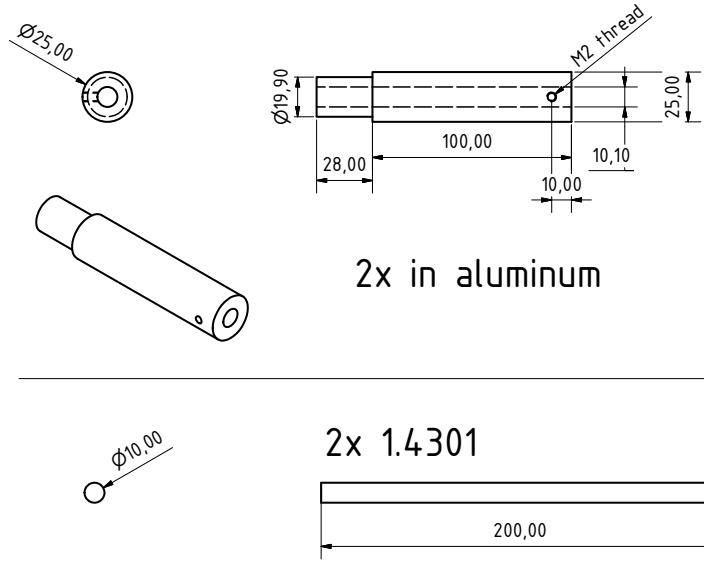

Figure D.4.: Drawing of the adjustable height stage for the ring heater reflector.

D.2. Side heaters

The drawings that were used to fabricate the side heaters are attached as the following pages. Note that the stand is omitted here for brevity, it is made of a 30mmx30mm non-anodized aluminum profile from the company ITEM [iIG14].

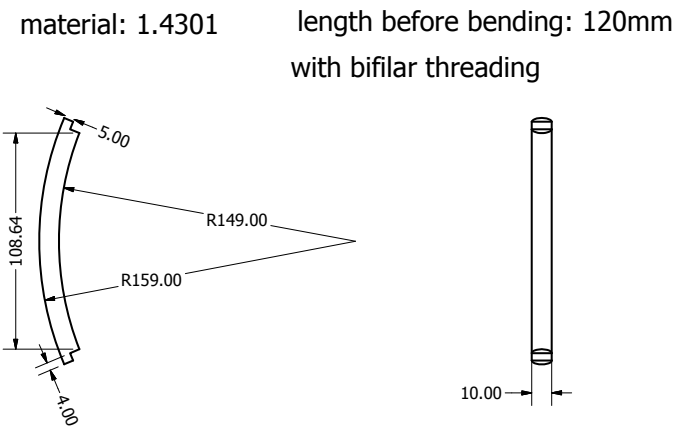

Figure D.5.: Drawing of the side heater rod.

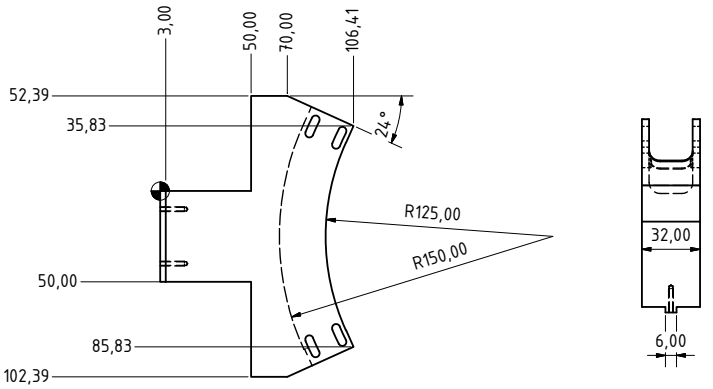

Figure D.6.: Drawing of the side heater reflector.

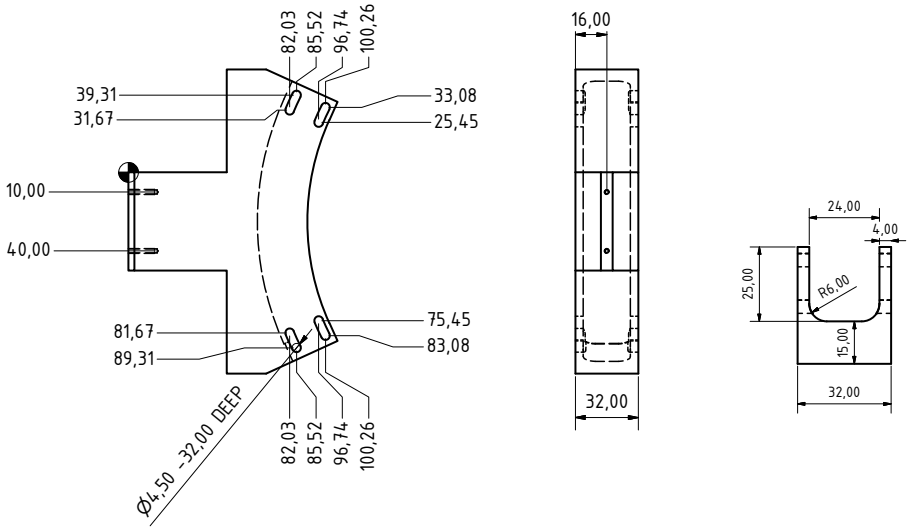

Figure D.7.: Drawing of the side heater reflector(2).

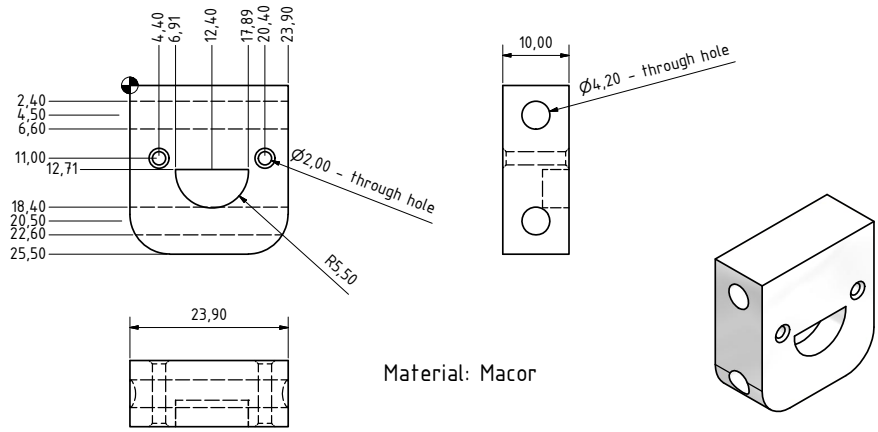

Figure D.8.: Drawing of the Macor endcaps for the side heaters.

D.3. Matrix heater

This section contains drawings of the parts that were designed and made for the thermal projection system. All were designed by the author, except for the electronics - where Andreas Weidner has modified the author's original design. Not shown here is the drawing of the parabolic mirror used for the projection system, as it exists only in electronic format, and has been milled directly from the 3D-CAD file by [Rum] from a solid piece of aluminum. Also not shown here are the drawings of the many prototype heaters (see appendix A.1.1) as they are not permanently installed into GEO 600.

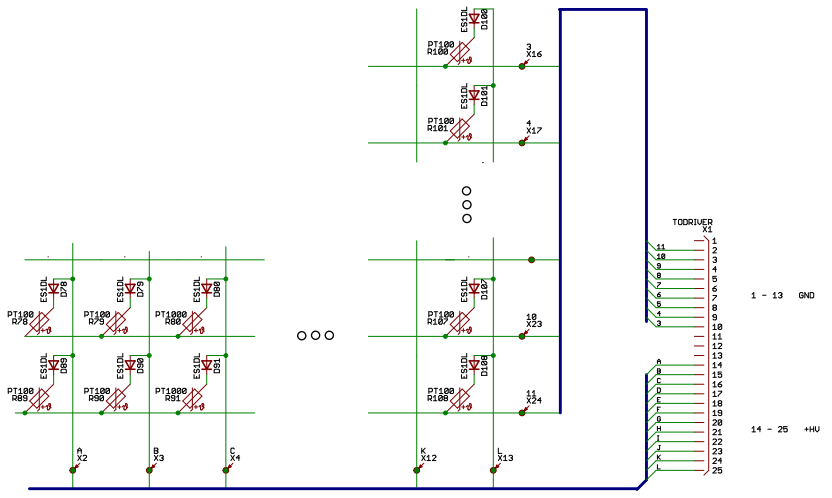

Figure D.9.: Schematic for the heater array of the thermal projector.

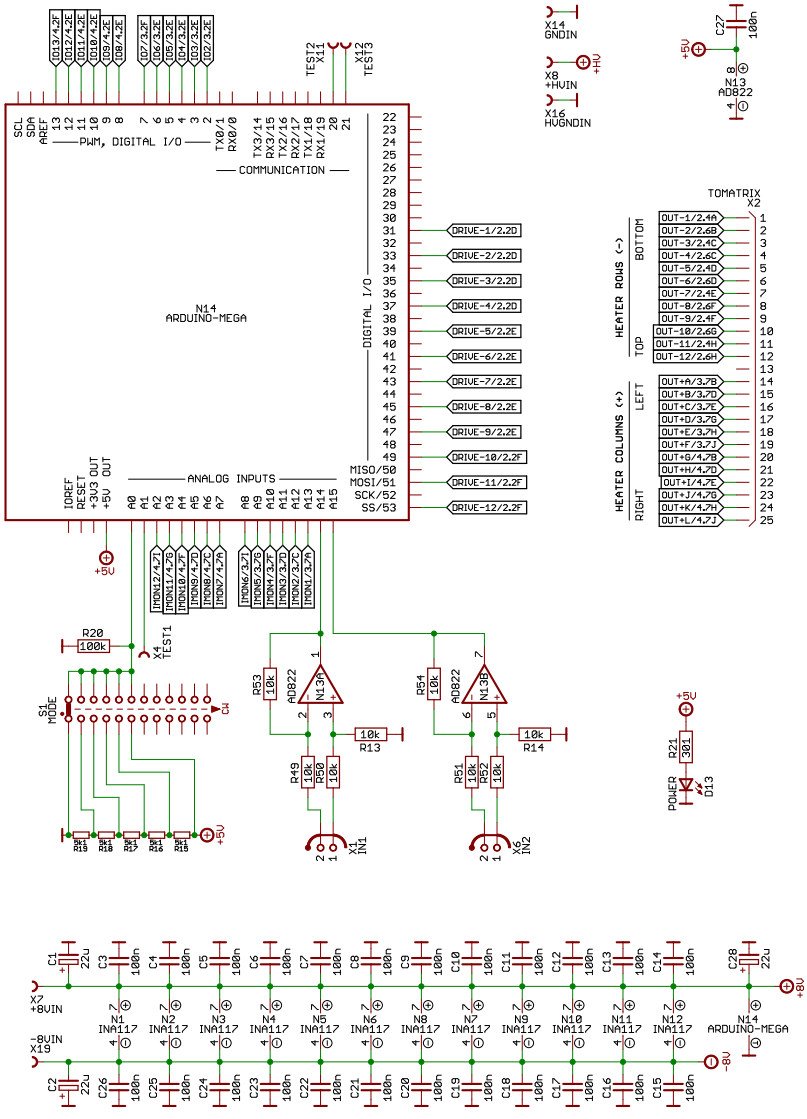

Figure D.10.: Schematic: thermal projector driver (1).

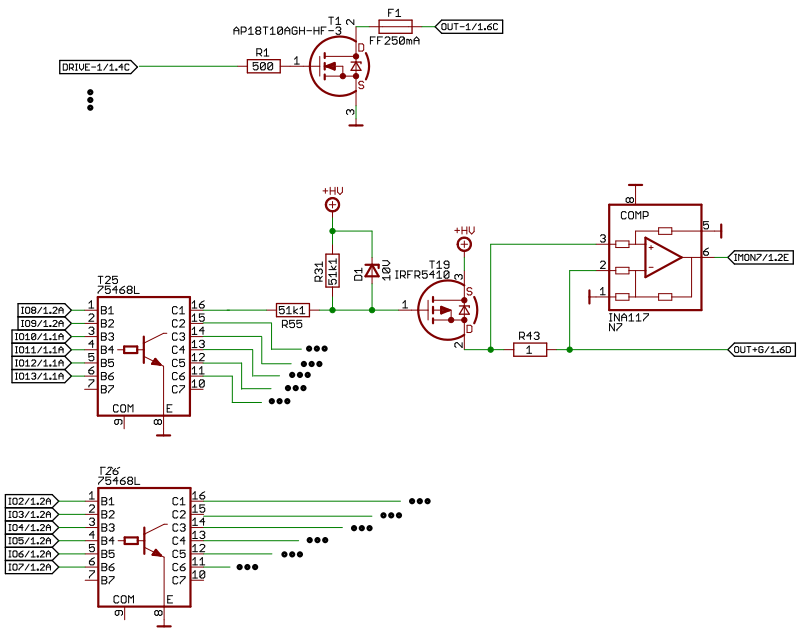

Figure D.11.: Schematic: thermal projector driver (2).

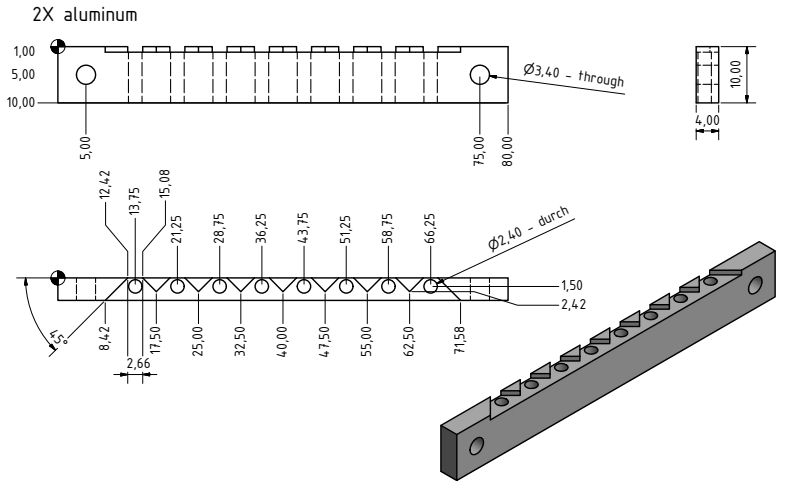

Figure D.12.: Drawing of the reflector grill (1).

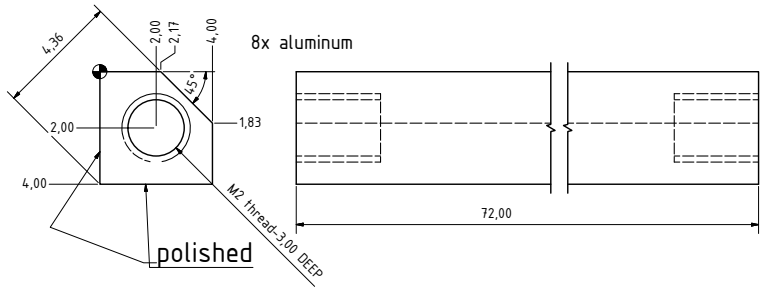

Figure D.13.: Drawing of the reflector grill (2).

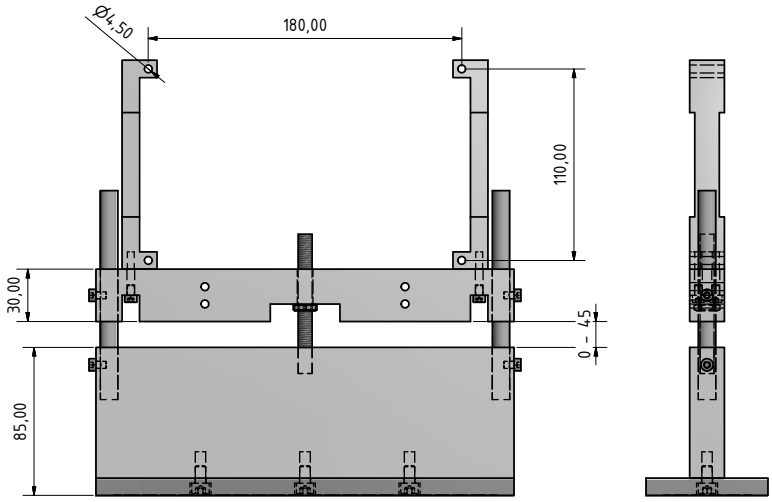

Figure D.14.: Drawing of the stand for the heater array.

D.4. Baffles

D.4.1. TFE baffle assembly

The parts for the baffle assembly in TFE are presented here. The ITEM profiles were bought from the company ITEM [iIG14], and are not anodized, with a cross section of 30 mm x 30 mm.

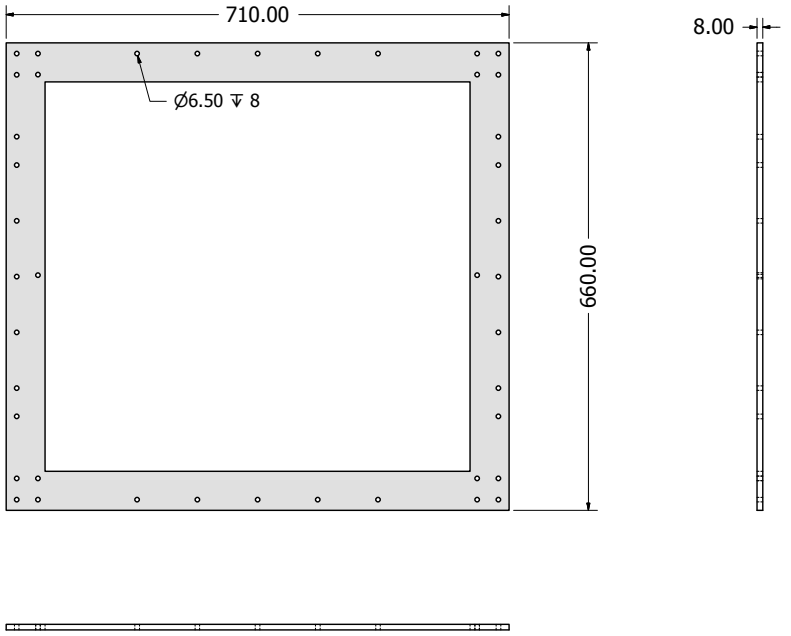

Figure D.15.: Drawing of the frame for the TFE baffle.

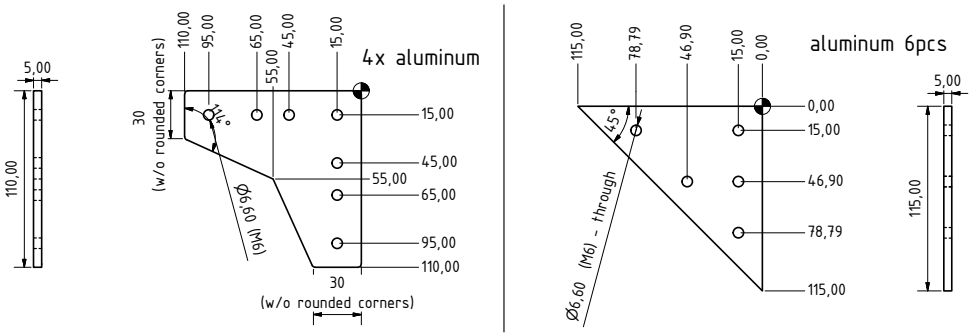

Figure D.16.: Drawing of the braces.

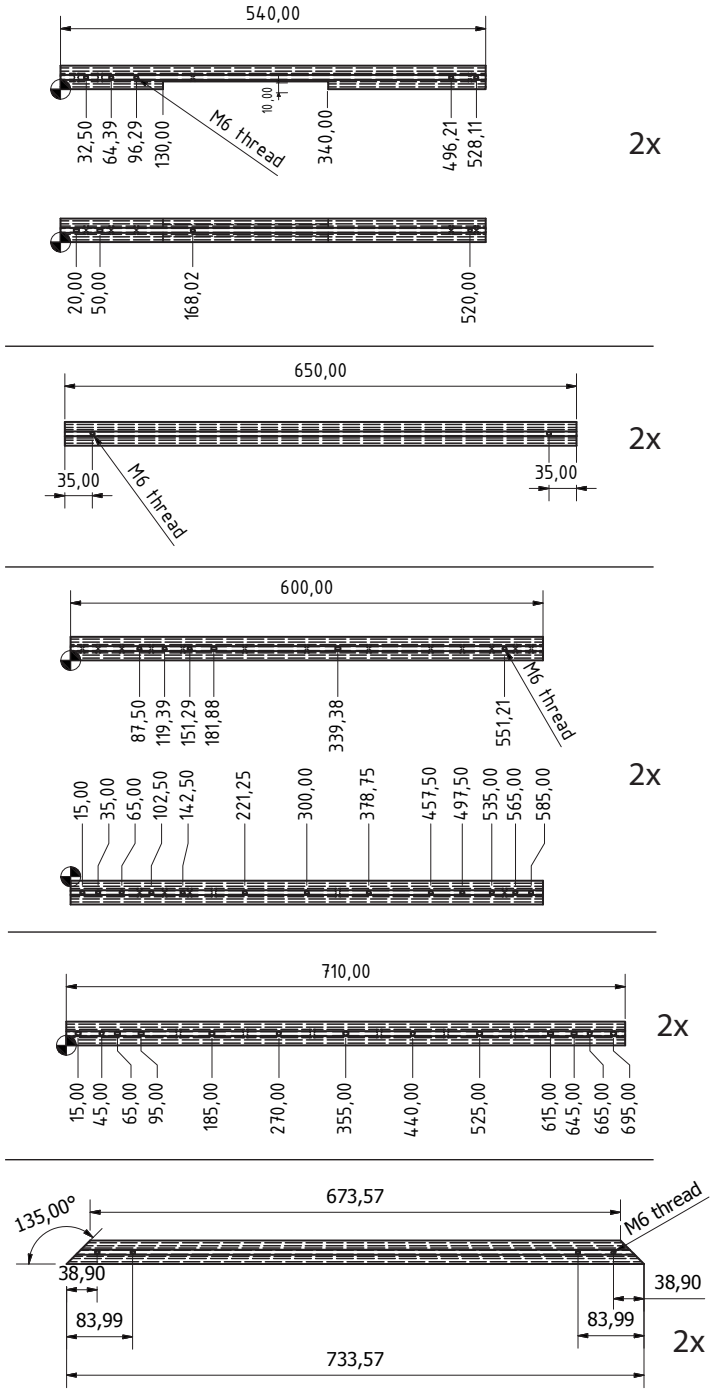

Figure D.17.: Drawing of the ITEM profiles.

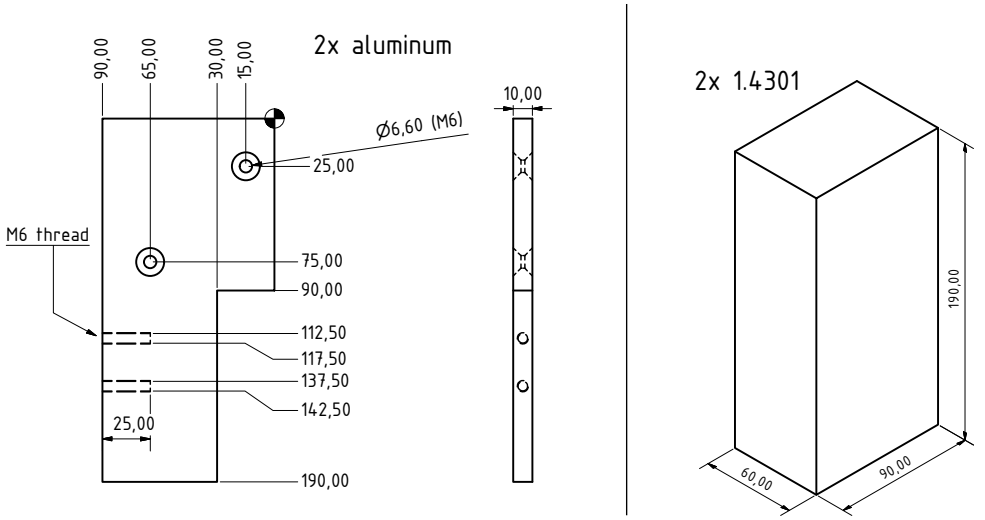

Figure D.18.: Drawing of the weights (right) and their supports (left).

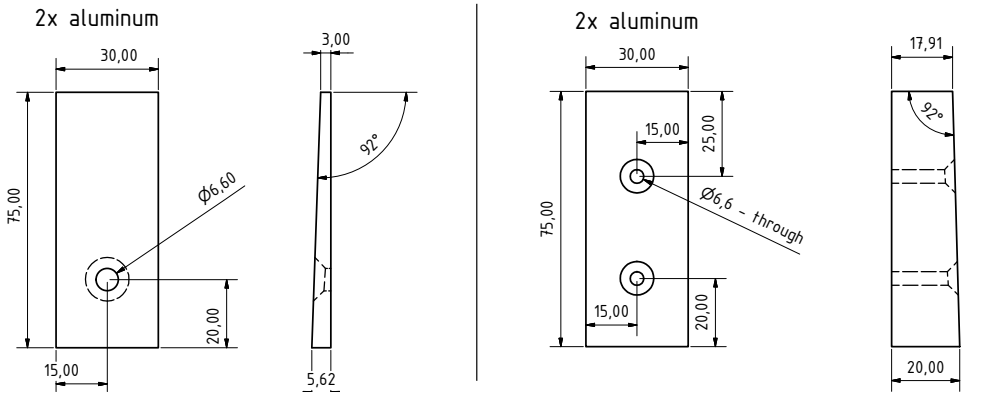

Figure D.19.: Drawing of the feet for the TFE baffle assembly.

D.4.2. TCE and TCN baffle assemblies

This section shows the technical drawings that were used to manufacture the baffle holders in TCE and TCN. Furthermore, additional constructions, like a mount for the shadow sensors, which are used for sensing and actuating on the baffles, are provided here.

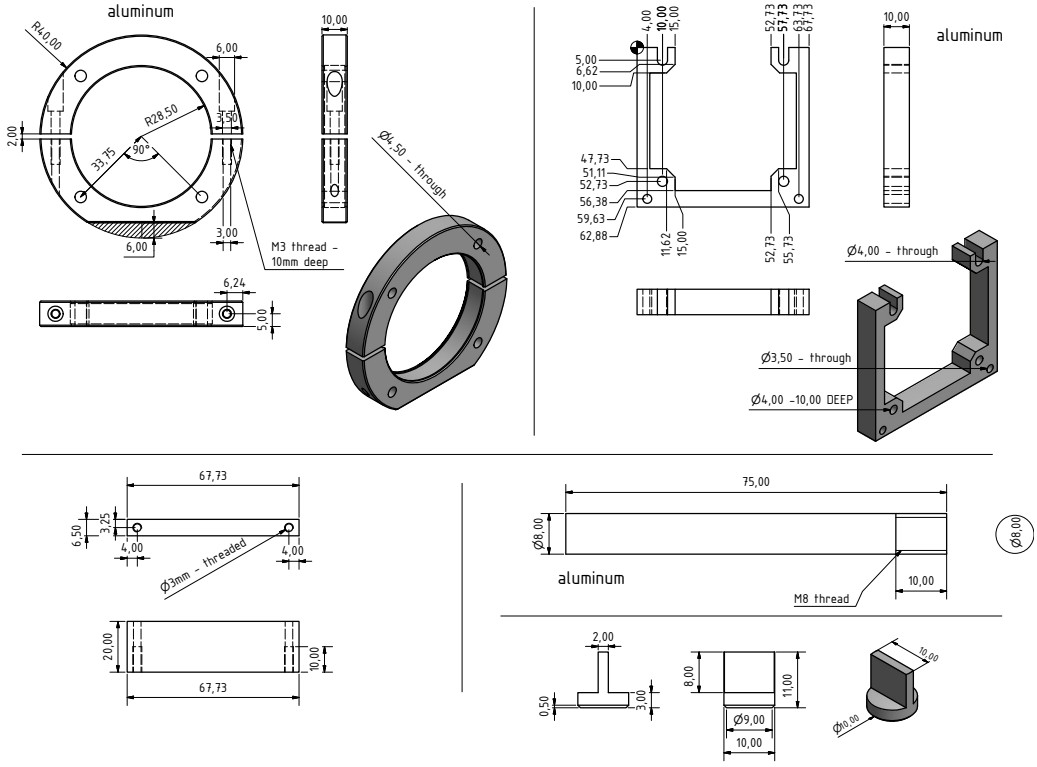

Figure D.20.: Drawing of the OSEM related parts. The top row and the bottom left image show a holder for the OSEM, while th bottom right drawings show the flag and pole for the shadow sensing of the OSEM.

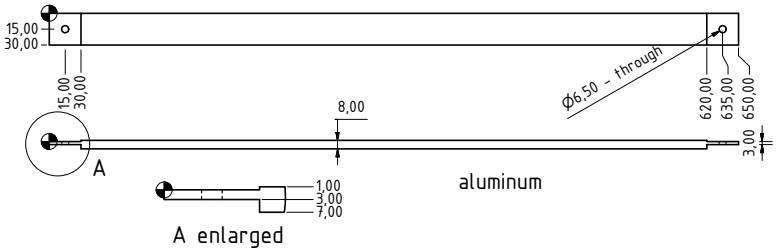

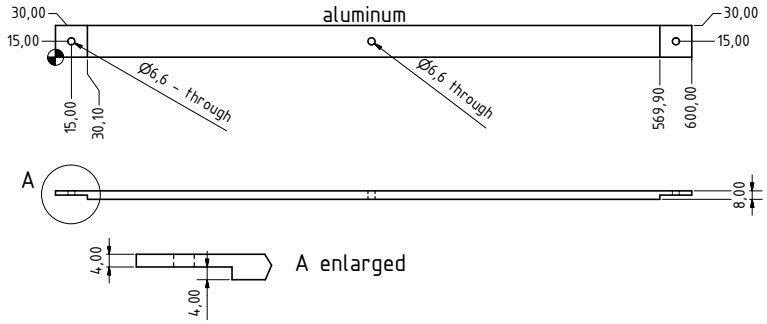

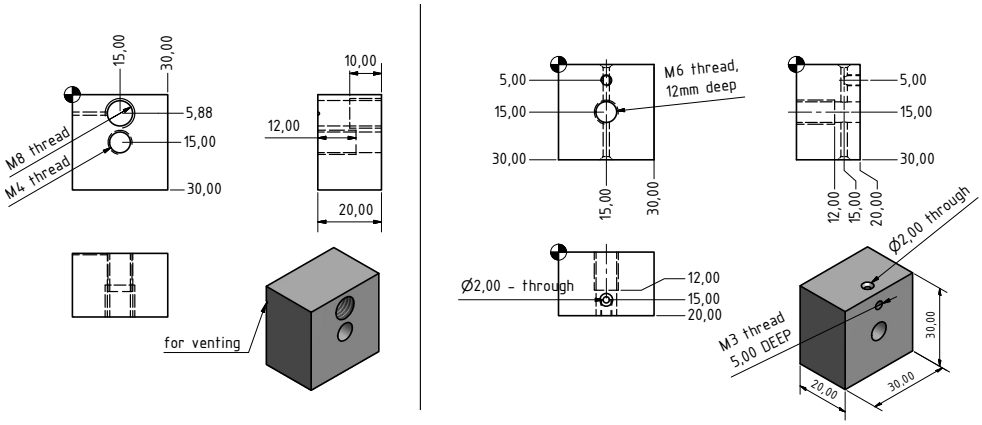

Figure D.21.: Drawing of the parts for the frames of the baffles in TCE and TCN.

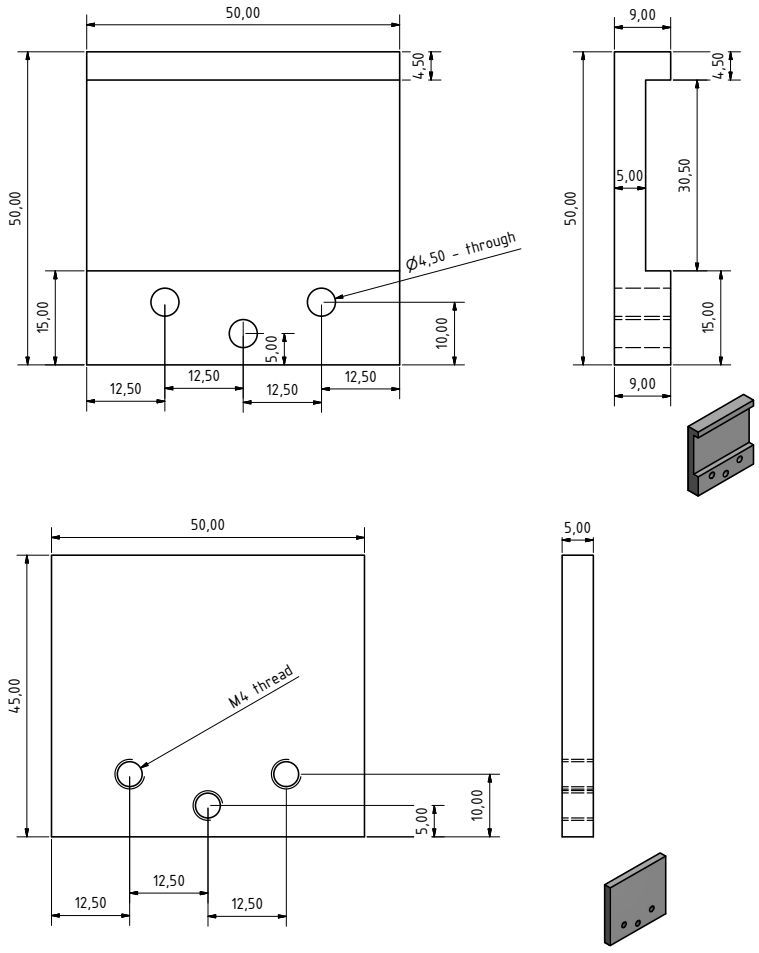

Figure D.22.: Drawing of the clamps for the baffles in TCE and TCN.

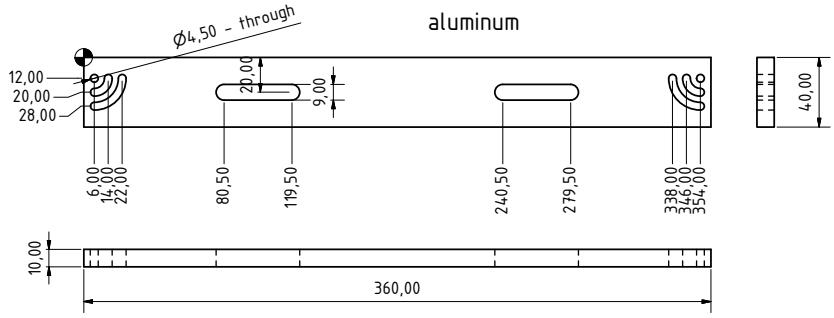

Figure D.23.: Drawing of the connection piece to the stacks in the vacuum chamber.

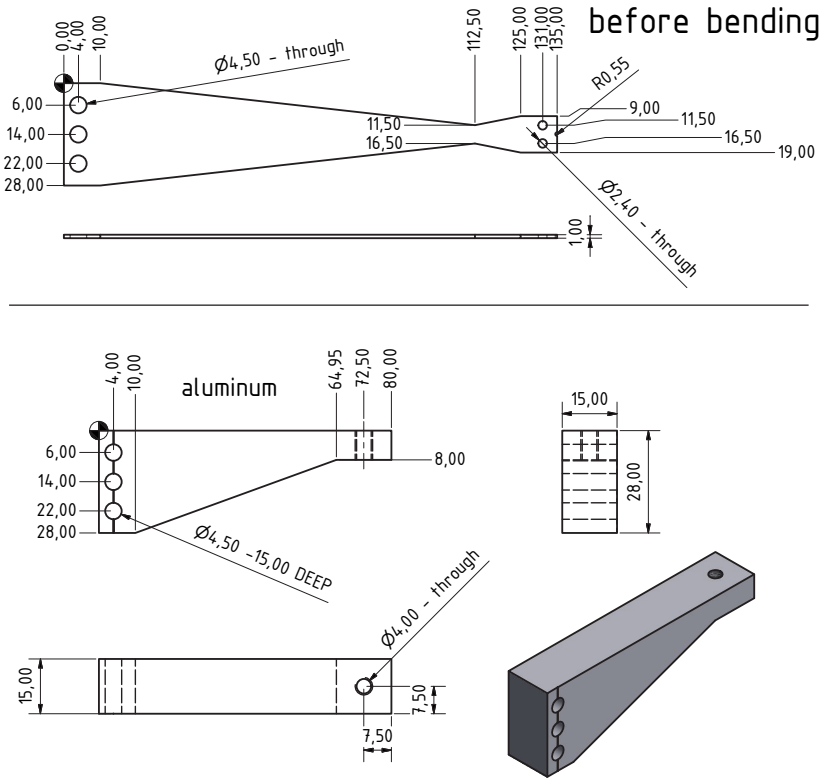

Figure D.24.: Drawing of the blade spring assembly(1).

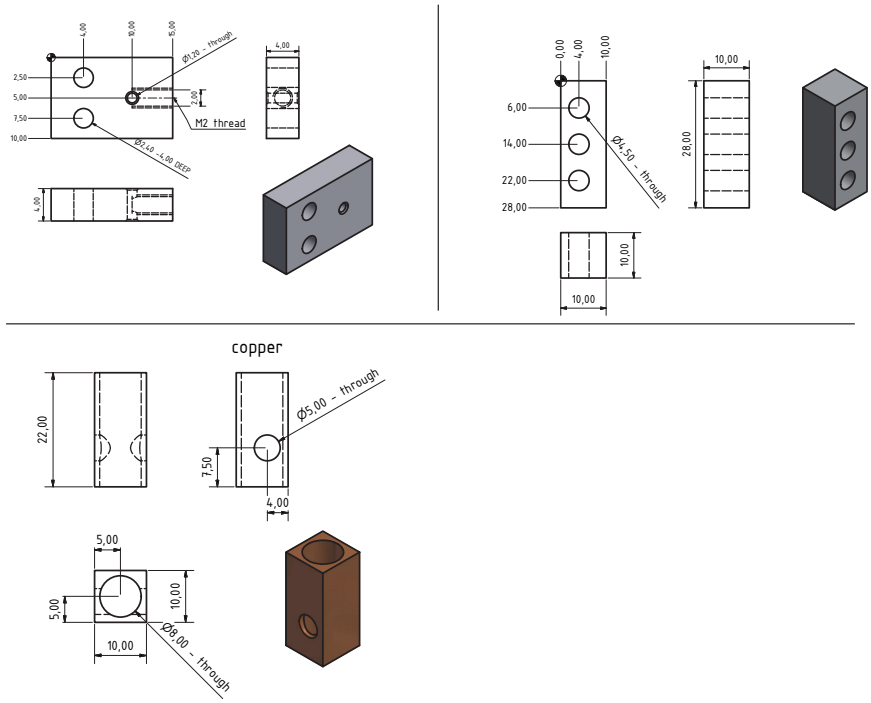

Figure D.25.: Drawings of the blade spring assembly(2)

D.5. OMC

This section shows the technical drawings of the new OMC, including drawings of the individual parts, such as the baseplate and the mirrors. Parts of the same dimensions have been used already for the original OMC, but the drawings had to be remade to allow a complete model of the new OMC. The individual parts have been assembled such that the resulting optical path length is as designed, with the help of a template. The template was designed as part of this work, and its drawing is attached below as well. It has several drill holes, small metal balls are put in those drill holes, and act as defined touching point for the optics.

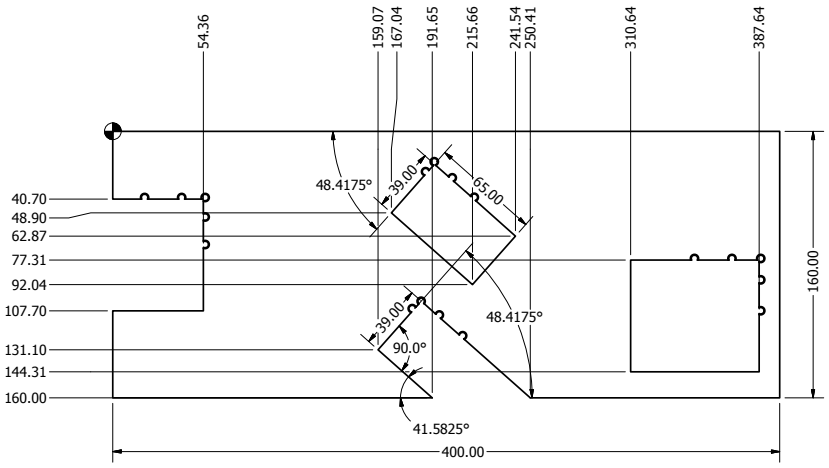

Figure D.26.: Drawing of the template for the new OMC (1).

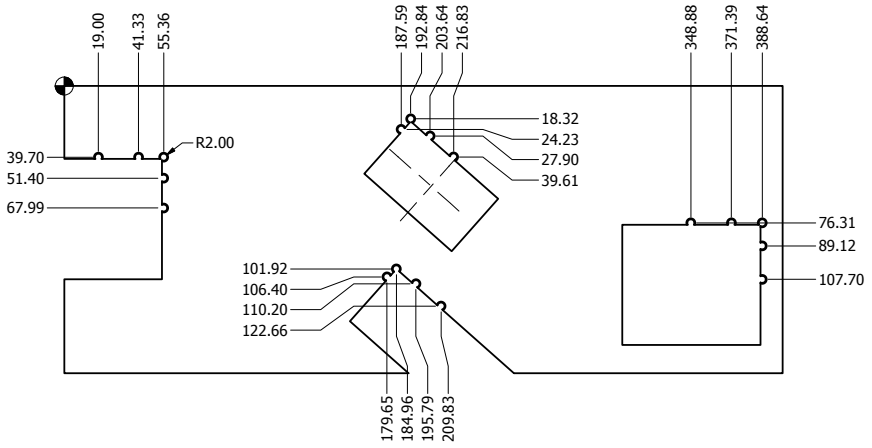

Figure D.27.: Drawing of the template for the new OMC (2).

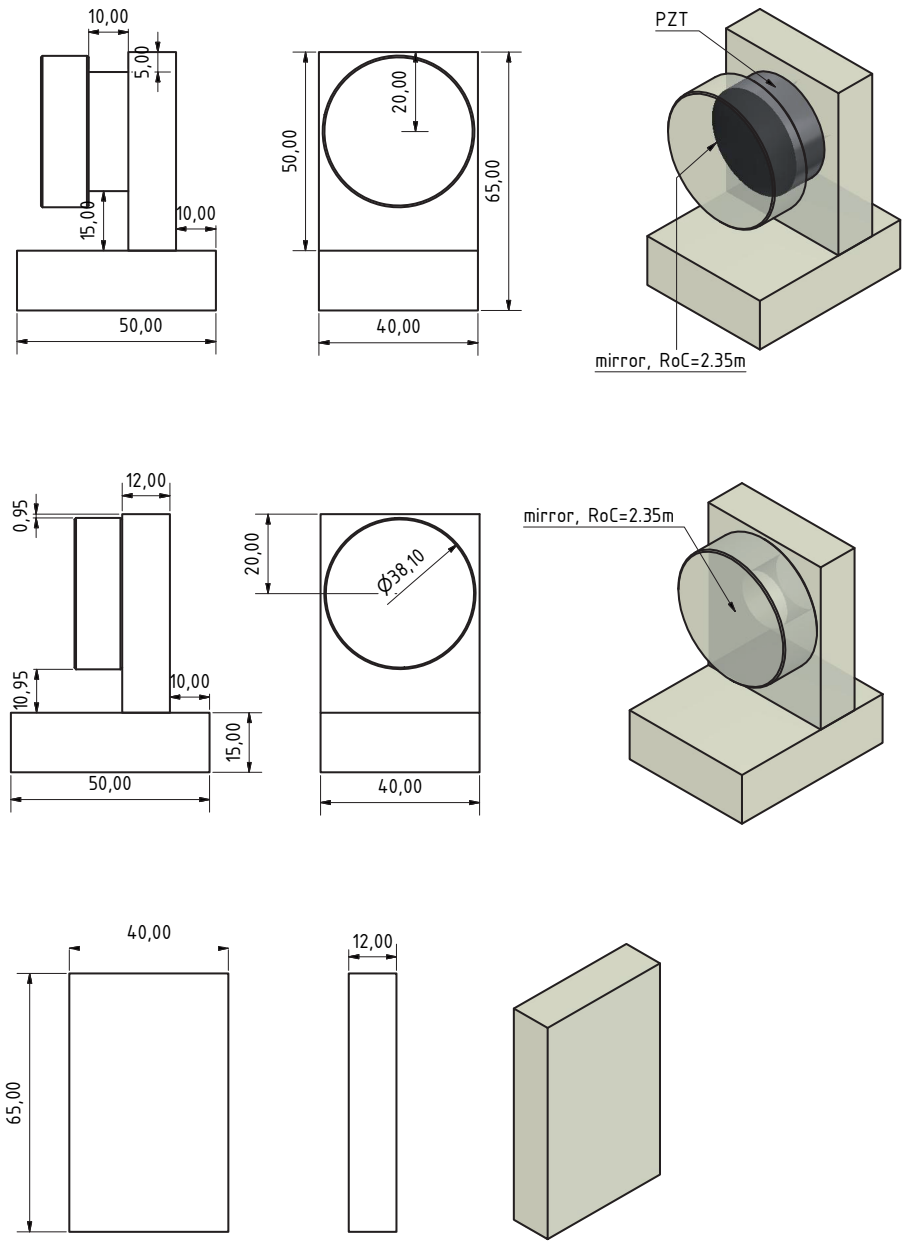

Figure D.28.: Drawing of the OMC optics. The baseplate, on which the optics above are glued with UV-curable epoxy, is not shown here. It has the dimensions 400 mm x 160 mm x 38 mm.

Bibliography

[AAA+07] Fausto Acernese, P Amico, M Alshourbagy, F Antonucci, S Aoudia, P Astone, Saverio Avino, D Babusci, G Ballardin, Fabrizio Barone, et al., *Measurement of the optical parameters of the Virgo interferometer*, Applied optics **46** (2007), 3466–3484.

[AAA+09a] BP Abbott, R Abbott, F Acernese, R Adhikari, P Ajith, B Allen, G Allen, M Alshourbagy, RS Amin, SB Anderson, et al., *An upper limit on the stochastic gravitational-wave background of cosmological origin*, Nature **460** (2009), no. 7258, 990–994.

[AAA+09b] BP Abbott, R Abbott, R Adhikari, P Ajith, Bruce Allen, G Allen, RS Amin, SB Anderson, WG Anderson, MA Arain, et al., *LIGO: the laser interferometer gravitational-wave observatory*, Reports on Progress in Physics **72** (2009), no. 7, 076901.

[AAA+09c] T. Accadia, F. Acernese, F. Antonucci, K.G. Arun, P. Astone, et al., *A thermal compensation system for the gravitational wave detector VIRGO*, Conference Proceedings of the 12th Marcel Grossmann Meeting on General Relativity (MG 12) (C09-07-12) (2009), 1652–1656.

[AAA+10a] Jea Abadie, BP Abbott, R Abbott, M Abernathy, T Accadia, F Acernese, C Adams, R Adhikari, P Ajith, B Allen, et al., *Predictions for the rates of compact binary coalescences observable by ground-based gravitational-wave detectors*, Classical and Quantum Gravity **27** (2010), no. 17, 173001.

[AAA+10b] T Accadia, F Acernese, F Antonucci, P Astone, G Ballardin, F Barone, M Barsuglia, Th S Bauer, MG Beker, A Belletoile, et al., *Noise from scattered light in Virgo's second science run data*, Classical and Quantum Gravity **27** (2010), no. 19, 194011.

[AAA+11] T Accadia, F Acernese, F Antonucci, P Astone, G Ballardin, F Barone, M Barsuglia, A Basti, Th S Bauer, M Bebronne, et al., *Status of the virgo project*, Classical and Quantum Gravity **28** (2011), no. 11, 114002.

[AAA+13] T Accadia, F Acernese, M Agathos, A Allocca, P Astone, G Ballardin, F Barone, M Barsuglia, A Basti, Th S Bauer, et al., *Central heating radius of curvature correction (CHRoCC) for use in large scale gravitational wave interferometers*, Classical and Quantum Gravity **30** (2013), no. 5, 055017.

[AAA+15a] J Aasi, BP Abbott, R Abbott, T Abbott, MR Abernathy, K Ackley, C Adams, T Adams, P Addesso, RX Adhikari, et al., *Advanced LIGO*, Classical and quantum gravity **32** (2015), no. 7, 074001.

[AAA+15b] F Acernese, M Agathos, K Agatsuma, D Aisa, N Allemandou, A Allocca, J Amarni, P Astone, G Balestri, G Ballardin, et al., *Advanced Virgo: a second-generation interferometric gravitational wave detector*, Classical and Quantum Gravity **32** (2015), no. 2, 024001.

[ABB+02] P Astone, D Babusci, M Bassan, P Bonifazi, P Carelli, G Cavallari, E Coccia, C Cosmelli, S D'Antonio, V Fafone, et al., *Study of the coincidences between the gravitational wave detectors EXPLORER and NAUTILUS in 2001*, Classical and Quantum Gravity **19** (2002), no. 21, 5449.

[ADD+14] C Affeldt, K Danzmann, K L Dooley, H Grote, M Hewitson, S Hild, J Hough, J Leong, H Lück, M Prijatelj, S Rowan, A Rüdiger, R Schilling, R Schnabel, E Schreiber, B Sorazu, K A Strain, H Vahlbruch, B Willke, W Winkler, and H Wittel, *Advanced techniques in GEO 600*, Classical and Quantum Gravity **31** (2014), no. 22, 224002.

[Aff13] Christoph Affeldt, *Post baffle installation stray light measurement*, Internal note, GEO HF logbook page 4650, September 2013.

[Aff14] Christoph Affeldt, *Laser power increase for GEO 600 - Commissioning aspects towards an operation of GEO 600 at high laser power*, Ph.D. thesis, Gottfried Wilhelm Leibniz Universität Hannover, 2014.

[AME] *AMETEK Process Instruments*, http://www.ametekpi.com/, AMETEK GmbH, Rudolf-Diesel-Strasse 16, D-40670 Meerbusch Germany.

[AMS+13] Yoichi Aso, Yuta Michimura, Kentaro Somiya, Masaki Ando, Osamu Miyakawa, Takanori Sekiguchi, Daisuke Tatsumi, and Hiroaki Yamamoto, *Interferometer design of the kagra gravitational wave detector*, Physical Review D **88** (2013), no. 4, 043007.

[And84] Dana Z Anderson, *Alignment of resonant optical cavities*, Applied Optics **23** (1984), no. 17, 2944–2949.

[ANDF+09] T Accadia, F Nocera, L Di Fiore, G Vajente, F Marchesoni, V Moscatelli, A Vicere, M Granata, F Paoletti, G Pagliaroli, et al., *A thermal compensation system for the gravitational wave detector Virgo*, To appear in the proceedings of Conference: 12th Marcel Grossmann Meeting on General Relativity (MG 12) C09-07-12, p.1652-1656 Proceedings, 2009, pp. 1652–1656.

[ANS] ANSYS Inc., *ANSYS Mechanical*, http://www.ansys.com/, Southpointe, 2600 ANSYS Drive, Canonsburg, PA 15317, USA.

[Ard] Arduino, *Mega ADK*, http://arduino.cc/en/Main/ArduinoBoardADK, accessed in May 2015.

[ASAB+12] Pau Amaro-Seoane, Sofiane Aoudia, Stanislav Babak, Pierre Binétruy, Emanuele Berti, Alejandro Bohe, Chiara Caprini, Monica Colpi, Neil J Cornish, Karsten Danzmann, et al., *Low-frequency gravitational-wave science with eLISA/NGO*, Classical and Quantum Gravity **29** (2012), no. 12, 124016.

[Ast02] Pia Astone, *Resonant mass detectors: present status*, Classical and Quantum Gravity **19** (2002), no. 7, 1227.

[Bal06] Stefan W Ballmer, *LIGO interferometer operating at design sensitivity with application to gravitational radiometry*, Ph.D. thesis, Massachusetts Institute of Technology, 2006.

[BBB+08] L Baggio, M Bignotto, M Bonaldi, M Cerdonio, M De Rosa, P Falferi, S Fattori, P Fortini, G Giusfredi, M Inguscio, et al., *A joint search for gravitational wave bursts with AURIGA and LIGO*, Classical and Quantum Gravity **25** (2008), no. 9, 095004.

[BCF09] B Bland, D Coyne, and J Fauver, *LIGO Clean and Bake Methods and Procedures E960022-v25*, https://dcc.ligo.org/LIGO-E960022/public, 2009, [Online; accessed 01-Aug-2011].

[BCH+15] Aidan Brooks, Ayodele Cole, Alastair Heptonstall, Mindy Jacobson, Alexander Lynch, Stephen O'Connor, Zhenhua Shao, and Cheryl Vorvick, *Thermal Compensation System (TCS): CO2 Laser Projection System (CO2P) Final Design Document*, LIGO Document T1100570-v5 https://dcc.ligo.org/LIGO-T1100570/public, 2011 - revised 2015, [Online; accessed 09-Sept-2015].

[Beh] *Behre*, http://www.stoneart-behre.de/, Wilfried Behre, Willmerstr. 20c, D-30519 Hannover, Germany.

[BFC+12] C Bond, P Fulda, L Carbone, K Kokeyama, and A Freise, *The effect of mirror surface distortions on higher order Laguerre-Gauss modes*, Journal of Physics: Conference Series, vol. 363, IOP Publishing, 2012, p. 012005.

[BFL+04] Stefan Ballmer, Valery Frolov, Ryan Lawrence, William Kells, Gerado Moreno, Ken Mason, David Ottaway, Mike Smith, Cheryl Vorvick, Phil Willems, et al., *Thermal Compensation System Description*, Optics Letters **29** (2004), no. 22, 2635–2637.

[Bla05] David G Blair, *The detection of gravitational waves*, Cambridge university press, 2005.

[Boy82] Robert W Boyd, *Photon bunching and the photon-noise-limited performance of infrared detectors*, Infrared Physics **22** (1982), no. 3, 157–162.

[Bro07] Aidan Brooks, *Enhanced and Advanced LIGO TCS*, Presentation LSC/Virgo Collaborations Meeting, October 22-25 2007, Hannover Germany, slides at https://dcc.ligo.org/LIGO-G070634/public, 2007, [Online; accessed 01-Aug-2015].

[C+11] LIGO Scientific Collaboration et al., *A gravitational wave observatory operating beyond the quantum shot-noise limit*, Nature Physics **7** (2011), no. 12, 962–965.

[CAC+12] L Carbone, SM Aston, RM Cutler, A Freise, J Greenhalgh, J Heefner, D Hoyland, NA Lockerbie, D Lodhia, NA Robertson, et al., *Sensors and actuators for the Advanced LIGO mirror suspensions*, Classical and Quantum Gravity **29** (2012), no. 11, 115005.

[CBC+97] Massimo Cerdonio, M Bonaldi, D Carlesso, E Cavallini, S Caruso, A Colombo, P Falferi, G Fontana, PL Fortini, R Mezzena, et al., *The ultracryogenic gravitational-wave detector AURIGA*, Classical and Quantum Gravity **14** (1997), no. 6, 1491.

[Chi12] Antonino Chiummo, *Computation of AdV arm-cavity baffle displacement noise projection*, https://dcc.ligo.org/LIGO-G1200633/public, 2012, Slides of a talk given at GWADW, held on 14 May 2012 in Waikoloa Marriott Resort, Hawaii
slides availiable as LIGO Document G1200633-v1.

[Chr] *Chrome browser*, https://www.google.de/chrome/browser/desktop/, Google Inc.

[Col11] LIGO Scientific Collaboration, *A gravitational wave observatory operating beyond the quantum shot-noise limit*, Nature Physics **7** (2011), no. 12, 962–965.

[Coy96] Dennis C Coyne, *The Laser Interferometer Gravitational-Wave Observatory (LIGO) Project*, Aerospace Applications Conference, 1996. Proceedings., 1996 IEEE, vol. 4, IEEE, 1996, pp. 31–61.

[DC+15] Katherine L Dooley, LIGO Scientific Collaboration, et al., *Status of GEO 600*, Journal of Physics: Conference Series, vol. 610, IOP Publishing, 2015, pp. 12015–12018.

[DCN+92] Karsten Danzmann, J Chen, PG Nelson, TM Niebauer, Albrecht Rüdiger, Roland Schilling, L Schnupp, Kenneth A Strain, H Walther, Walter Winkler, et al., *The GEO–project a long-baseline laser interferometer for the detection of gravitational waves*, Relativistic Gravity Research with Emphasis on Experiments and Observations, Springer, 1992, pp. 184–209.

[Deg06] Jérôme Degallaix, *Compensation of strong thermal lensing in advanced interferometric gravitational waves detectors*, Ph.D. thesis, University of Western Australia, 2006.

[Deg08] Jerome Degallaix, *Measuring the beam splitter absorption (new try)*, Internal note, GEO logbook page 5177, July 2008.

[DGP+10] J Degallaix, H Grote, M Prijatelj, M Hewitson, S Hild, C Affeldt, A Freise, J Leong, H Lück, KA Strain, et al., *Commissioning of the tuned DC readout at GEO 600*, Journal of Physics: Conference Series, vol. 228, IOP Publishing, 2010, p. 012013.

[DHN+11] R Dolesi, M Hueller, D Nicolodi, D Tombolato, S Vitale, PJ Wass, WJ Weber, M Evans, P Fritschel, R Weiss, et al., *Brownian force noise from molecular collisions and the sensitivity of advanced gravitational wave observatories*, Physical Review D **84** (2011), no. 6, 063007.

[DSV+15] Katherine L Dooley, Emil Schreiber, Henning Vahlbruch, Christoph Affeldt, Jonathan R Leong, Holger Wittel, and Hartmut Grote, *Phase control of squeezed vacuum states of light in gravitational wave detectors*, Optics express **23** (2015), no. 7, 8235–8245.

[DVKM13] RA Day, G Vajente, M Kasprzack, and J Marque, *Reduction of higher order mode generation in large scale gravitational wave interferometers by central heating residual aberration correction*, Physical Review D **87** (2013), no. 8, 082003.

[eC+15] eLISA Consortium et al., *LISA and its pathfinder*, Nature Physics **11** (2015), no. 8, 613–615.

[Ein16] Albert Einstein, *Die Grundlage der allgemeinen Relativitätstheorie*, Annalen der Physik **354** (1916), no. 7, 769–822.

[ELE] *Pulsable Infrared Array for Asset Identification*, http://www.eoc-inc.com/pulsable-infrared-array.htm.

[FHL+04] A Freise, G Heinzel, H Lück, R Schilling, B Willke, and K Danzmann, *Frequency-domain interferometer simulation with higher-order spatial modes*, Classical and Quantum Gravity **21** (2004), no. 5, S1067.

[Fir] *Firefox browser*, https://www.mozilla.org/de/firefox/new/, The Mozilla Foundation.

[Fre03] Andreas Freise, *The Next Generation of Interferometry: Multi-Frequency Optical Modelling, Control Concepts and Implementation*, Ph.D. thesis, Universität Hannover, 2003.

[FS10] Andreas Freise and Kenneth A. Strain, *Interferometer Techniques for Gravitational-Wave Detection*, Living Reviews in Relativity **13** (2010), no. 1.

[Ful14] Paul Fulda, *Laguerre-Gauss Beams for Test Mass Thermal Noise Reduction*, Precision Interferometry in a New Shape, Springer, 2014, pp. 17–39.

[GBB+10] S Goßler, A Bertolini, M Born, Y Chen, K Dahl, D Gering, C Gräf, G Heinzel, S Hild, F Kawazoe, et al., *The AEI 10 m prototype interferometer*, Classical and quantum gravity **27** (2010), no. 8, 084023.

[GBB+14] C Gräf, BW Barr, AS Bell, F Campbell, AV Cumming, SL Danilishin, NA Gordon, GD Hammond, J Hennig, EA Houston, et al., *Design of a speed meter interferometer proof-of-principle experiment*, Classical and quantum gravity **31** (2014), no. 21, 215009.

[GBF+10] M Granata, M Barsuglia, R Flaminio, A Freise, S Hild, and J Marque, *Design of the Advanced Virgo non-degenerate recycling cavities*, Journal of Physics: Conference Series, vol. 228, IOP Publishing, 2010, p. 012016.

[GC+08] Hartmut Grote, LIGO Scientific Collaboration, et al., *The status of GEO 600*, Classical and Quantum Gravity **25** (2008), no. 11, 114043.

[GFM+04] H Grote, A Freise, M Malec, G Heinzel, B Willke, H Lück, KA Strain, J Hough, and K Danzmann, *Dual recycling for GEO 600*, Classical and Quantum Gravity **21** (2004), no. 5, S473.

[GHF+04] H Grote, G Heinzel, A Freise, S Goßler, B Willke, H Lück, H Ward, MM Casey, KA Strain, DI Robertson, et al., *Alignment control of GEO 600*, Classical and Quantum Gravity **21** (2004), no. 5, S441.

[GHL+12] Christian Gräf, Stefan Hild, Harald Lück, Benno Willke, Kenneth A Strain, Stefan Goßler, and Karsten Danzmann, *Optical layout for a 10 m Fabry–Perot Michelson interferometer with tunable stability*, Classical and quantum gravity **29** (2012), no. 7, 075003.

[GL73] Richard L Garwin and James L Levine, *Single gravity-wave detector results contrasted with previous coincidence detections*, Physical Review Letters **31** (1973), no. 3, 176.

[Goo] *Google Maps*, https://maps.google.de/, Google Inc.

[Gor] *W. L. Gore and Associates*, http://www.schott.com/, 91785 PLEINFELD, Germany.

[Goß04] Stefan Goßler, *The suspension systems of the interferometric gravitational-wave detector GEO 600*, Ph.D. thesis, Universität Hannover, 2004.

[Grä13] Christian Gräf, *Optical design and numerical modeling of the AEI 10 m Prototype sub-SQL interferometer*, Ph.D. thesis, Universität Hannover, 2013.

[Gro03] Hartmut Grote, *Making it Work: Second Generation Interferometry in GEO 600!*, Ph.D. thesis, Universität Hannover, 2003.

[GSSS96] Joseph Giaime, Partha Saha, David Shoemaker, and Lisa Sievers, *A passive vibration isolation stack for LIGO: design, modeling, and testing*, Review of scientific instruments **67** (1996), no. 1, 208–214.

[Gum] *Gummi Hansen GmbH*, http://gummi-hansen.de/, Stellvertr. Laborleiter, Am Eisenwerk 5 - 9, 30519 Hannover.

[HAA+03] Martin Hewitson, Peter Aufmuth, Carsten Aulbert, Stanislav Babak, R Balasubramanian, BW Barr, S Berukoff, G Cagnoli, CA Cantley, Morag M Casey, et al., *A report on the status of the GEO 600 gravitational wave detector*, Classical and Quantum Gravity **20** (2003), no. 17, S581.

[HAA+11] S Hild, M Abernathy, F Acernese, P Amaro-Seoane, N Andersson, K Arun, F Barone, B Barr, M Barsuglia, M Beker, et al., *Sensitivity studies for third-generation gravitational wave observatories*, Classical and Quantum Gravity **28** (2011), no. 9, 094013.

[Ham] *G. Hammond*, Publication in preparation.

[HBB+14] Eiichi Hirose, Dan Bajuk, GariLynn Billingsley, Takaaki Kajita, Bob Kestner, Norikatsu Mio, Masatake Ohashi, Bill Reichman, Hiroaki Yamamoto, and Liyuan Zhang, *Sapphire mirror for the KAGRA gravitational wave detector*, Physical Review D **89** (2014), no. 6, 062003.

[HC+10] Gregory M Harry, LIGO Scientific Collaboration, et al., *Advanced LIGO: the next generation of gravitational wave detectors*, Classical and Quantum Gravity **27** (2010), no. 8, 084006.

[HCG+14] D Heinert, K Craig, H Grote, S Hild, H Lück, R Nawrodt, DA Simakov, DV Vasilyev, SP Vyatchanin, and H Wittel, *Thermal noise of folding mirrors*, Physical Review D **90** (2014), no. 4, 042001.

[HD14] Gerhard Heinzel and Karsten Danzmann, *LISA in 2012 and Beyond: 20 Years After the First Proposal*, General Relativity, Cosmology and Astrophysics, Springer, 2014, pp. 477–481.

[HDG+07] M Hewitson, K Danzmann, H Grote, S Hild, J Hough, H Lück, S Rowan, JR Smith, KA Strain, and B Willke, *Charge measurement and mitigation for the main test masses of the GEO 600 gravitational wave observatory*, Classical and Quantum Gravity **24** (2007), no. 24, 6379.

[Hera] Heraeus, *Heraeus Holding GmbH*, http://heraeus.de/, Heraeusstrasse 12-14, D-63450 Hanau - Germany.

[Herb] Heraeus Quarzglas, *Transmission Calculator v0.75WE*, http://optik.heraeus-quarzglas.de/, accessed in May 2015.

[Herc] Heraeus Sensor Technology, *Produktbroschüre: Platin-Temperatursensoren, die überzeugen*, http://heraeus-sensor-technology.de/media/webmedia_local/media/pdfs/hstproduktbroschuere.pdf, accessed in May 2015.

[Hew04] Martin R. Hewitson, *On aspects of characterising and calibrating the interferometric gravitational wave detector, GEO 600*, Ph.D. thesis, Department of Physics and Astronomy, University of Glasgow, 2004.

[HFG+02] Gerhard Heinzel, Andreas Freise, Hartmut Grote, Kenneth Strain, and Karsten Danzmann, *Dual recycling for GEO 600*, Classical and Quantum Gravity **19** (2002), no. 7, 1547.

[HGS+06] Stefan Hild, Hartmut Grote, JR Smith, Martin Hewitson, et al., *Towards gravitational wave astronomy: Commissioning and characterization of GEO600*, Journal of Physics: Conference Series, vol. 32, IOP Publishing, 2006, p. 66.

[HGW+07] Yu Hu, JiaoBo Gao, Jun Wang, YaWei Zheng, JiLong Wang, and JunHu Xie, *Study of dynamic infrared scene projection technology based on Digital Micro-mirror Device (DMD)*, Photonics Asia 2007, International Society for Optics and Photonics, 2007, pp. 68350T–68350T.

[HH05] Daniel E Holz and Scott A Hughes, *Using gravitational-wave standard sirens*, The Astrophysical Journal **629** (2005), no. 1, 15.

[HHP14] Giles Hammond, Stefan Hild, and Matthew Pitkin, *Advanced technologies for future ground-based, laser-interferometric gravitational wave detectors*, Journal of modern optics **61** (2014), no. sup1, S10–S45.

[Hil07] Stefan Hild, *Beyond the first Generation: Extending the Science Range of the Gravitational Wave Detector GEO 600.*, Ph.D. thesis, Gottfried Wilhelm Leibniz Universität Hannover, 2007.

[HLW+06] Stefan Hild, Harald Lück, Walter Winkler, Ken Strain, Hartmut Grote, Joshua Smith, Michaela Malec, Martin Hewitson, Benno Willke, James Hough, and Karsten Danzmann, *Measurement of a low-absorption sample of oh-reduced fused silica*, Appl. Opt. **45** (2006), no. 28, 7269–7272.

[HMY+11] T Hong, J Miller, H Yamamoto, Y Chen, and R Adhikari, *Effects of mirror aberrations on Laguerre-Gaussian beams in interferometric gravitational-wave detectors*, Physical Review D **84** (2011), no. 10, 102001.

[HT75] RA Hulse and JH Taylor, *Discovery of a pulsar in a binary system*, Neutron stars, black holes, and binary X-ray sources **48** (1975), 433.

[iIG14] item Industrietechnik GmbH, *Item*, http://www.item24.de/, 2014, [Online; accessed 19-July-2014].

[IRI] *IRIS INCORPORATED RESEARCH INSTITUTIONS FOR SEISMOLOGY*, http://ds.iris.edu/ds/nodes/dmc/.

[JKKPD09] Carl Justin Kamp, Hinata Kawamura, Roberto Passaquieti, and Riccardo DeSalvo, *Directional radiative cooling thermal compensation for gravitational wave interferometer mirrors*, Nuclear Instruments and Methods in Physics Research Section A: Accelerators, Spectrometers, Detectors and Associated Equipment **607** (2009), no. 3, 530–537.

[jQu] *jQuery mobile - A Touch-Optimized Web Framework*, https://jquerymobile.com/.

[KL66] H Kogelnik and Tingye Li, *Laser beams and resonators*, Applied Optics **5** (1966), no. 10, 1550–1567.

[Kog65] Herwig Kogelnik, *Imaging of optical modes - resonators with internal lenses*, Bell System Technical Journal **44** (1965), no. 3, 455–494.

[Kor] *Korth Kristalle GmbH*, www.korth.de, Am Jagersberg 3, D-24161 Altenholz (Kiel).

[KPJ07] Rei Kitamura, Laurent Pilon, and Miroslaw Jonasz, *Optical constants of silica glass from extreme ultraviolet to far infrared at near room temperature*, Applied optics **46** (2007), no. 33, 8118–8133.

[Law03] Ryan Christopher Lawrence, *Active Wavefront Corection in Laser Interferometric Gravitational Wave Detectors*, Ph.D. thesis, Massachusetts Institute of Technology, 2003.

[LB03] Vincent Loriette and Claude Boccara, *Absorption of low-loss optical materials measured at 1064 nm by a position-modulated collinear photothermal detection technique*, Applied optics **42** (2003), no. 4, 649–656.

[LC+12] Harald Lück, LIGO Scientific Collaboration, et al., *The Upgrade of GEO 600*, Marcel Grossmann Meeting on Recent Developments in Theoretical and Experimental General Relativity, Astrophysics and Relativistic Field Theories; 12 (MG12), World Scientific, 2012, pp. 1726–1728.

[LFG+04] H Lück, A Freise, S Goßler, S Hild, K Kawabe, and K Danzmann, *Thermal correction of the radii of curvature of mirrors for GEO 600*, Classical and Quantum Gravity **21** (2004), no. 5, S985.

[LG73] James L Levine and Richard L Garwin, *Absence of gravity-wave signals in a bar at 1695 Hz*, Physical Review Letters **31** (1973), no. 3, 173.

[LG74] James L Levine and Richard L Garwin, *New negative result for gravitational wave detection, and comparison with reported detection*, Physical Review Letters **33** (1974), no. 13, 794.

[Los15] Giovanni Losurdo, *Advanced Virgo News*, https://dcc.ligo.org/LIGO-G1501147, 2015, Slides of a talk given at the LSC collaboration meeting, held on the 26 Aug 2015 to 03 Sep 2015 in Budapest, Hungary slides availiable as LIGO Document G1501147-v1.

[LSF+09] I Leonor, Patrick J Sutton, R Frey, Gareth Jones, S Marka, and Z Marka, *Estimating detection rates for the LIGO–Virgo search for gravitational-wave burst counterparts to gamma-ray bursts using inferred local GRB rates*, Classical and Quantum Gravity **26** (2009), no. 20, 204017.

[LZF+02] Ryan Lawrence, Michael Zucker, Peter Fritschel, Phil Marfuta, and David Shoemaker, *Adaptive thermal compensation of test masses in advanced LIGO*, Classical and Quantum Gravity **19** (2002), no. 7, 1803.

[M+76] Lucio F Mondolfo et al., *Aluminum alloys: structure and properties*, vol. 5, Butterworths London, 1976.

[Mar84] S Margulies, *Force on a dielectric slab inserted into a parallel-plate capacitor*, Am. J. Phys **52** (1984), no. 6.

[Mat] *Matlab*, https://www.mathworks.com/, MathWorks.

[MTG15] Christopher J Moore, Stephen R Taylor, and Jonathan R Gair, *Estimating the sensitivity of pulsar timing arrays*, Classical and Quantum Gravity **32** (2015), no. 5, 055004.

[Mue] *Dr. D Mueller GmbH*, Zeppelinring 1B, D-26197 Ahlhorn.

[OFW12] David J Ottaway, Peter Fritschel, and Samuel J Waldman, *Impact of upconverted scattered light on advanced interferometric gravitational wave detectors*, Optics express **20** (2012), no. 8, 8329–8336.

[Orf04] Sophocles Orfanidis, *"multidiel.m" from "Electromagnetic Waves and Antennas Toolbox"*, http://www.mathworks.com/matlabcentral/fileexchange/4456-electromagnetic-waves-antennas-toolbox/content/multidiel.m, 2004, [Online; accessed 25-July-2013].

[PDG+12] M Prijatelj, J Degallaix, H Grote, J Leong, C Affeldt, S Hild, H Lück, J Slutsky, H Wittel, K Strain, et al., *The output mode cleaner of GEO 600*, Classical and Quantum Gravity **29** (2012), no. 5, 055009.

[Pri12] Mirko Prijatelj, *Gravitational wave detection with refined light*, Ph.D. thesis, Universität Hannover, 2012.

[PRRH11] Matthew Pitkin, Stuart Reid, Sheila Rowan, and James Hough, *Gravitational Wave Detection by Interferometry (Ground and Space)*, Living Reviews in Relativity **14** (2011), no. 5.

[PTH+00] MV Plissi, CI Torrie, ME Husman, NA Robertson, KA Strain, H Ward, H Lück, and J Hough, *GEO 600 triple pendulum suspension system: Seismic isolation and control*, Review of scientific instruments **71** (2000), no. 6, 2539–2545.

[RMS+09] Jocelyn S Read, Charalampos Markakis, Masaru Shibata, Kōji Uryū, Jolien DE Creighton, and John L Friedman, *Measuring the neutron star equation of state with gravitational wave observations*, Physical Review D **79** (2009), no. 12, 124033.

[Rum] Rump, *Feinmechanische Werkstatt Präzisions Dreh- u. Fräßteile, Inh. Peter Rump*, Kurt-Schumacher-Allee 1, 30851 Langenhagen.

[SAC+14] Yusuke Sakakibara, Tomotada Akutsu, Dan Chen, Aleksandr Khalaidovski, Nobuhiro Kimura, Shigeaki Koike, Tatsuya Kume, Kazuaki Kuroda, Toshikazu Suzuki, Chihiro Tokoku, et al., *Progress on the cryogenic system for the KAGRA cryogenic interferometric gravitational wave telescope*, Classical and Quantum Gravity **31** (2014), no. 22, 224003.

[SC+09] Joshua R Smith, LIGO Scientific Collaboration, et al., *The path to the enhanced and advanced LIGO gravitational-wave detectors*, Classical and Quantum Gravity **26** (2009), no. 11, 114013.

[Sch] *SCHOTT AG*, http://www.schott.com/, Hattenbergstrasse 10, 55122 Mainz, Germany.

[Sch99] Bernard F Schutz, *Gravitational wave astronomy*, Classical and Quantum Gravity **16** (1999), no. 12A, A131.

[SDM+94] KA Strain, K Danzmann, J Mizuno, PG Nelson, A Rüdiger, R Schilling, and W Winkler, *Thermal lensing in recycling interferometric gravitational wave detectors*, Physics Letters A **194** (1994), no. 1, 124–132.

[Sei] *Project SEIZMO - passive seismology toolbox for Matlab and GNU Octave*, https://github.com/g2e/seizmo and http://epsc.wustl.edu/~ggeuler/codes/m/seizmo/.

[Sie86] Anthony E. Siegman, *Lasers*, University Science Books, 1986.

[SLO+09] Kevin Sparkman, Joe Laveigne, Jim Oleson, Greg Franks, Steve McHugh, John Lannon, Brian Woode, Derek Greer, and Nicole Bui, *MIRAGE WF infrared scene projector system, with 1536 x 768 wide format resistive array, performance data*, SPIE Defense, Security, and Sensing, International Society for Optics and Photonics, 2009, pp. 73010F–73010F.

[Smi06] J Smith, *Formulation of instrument noise analysis techniques and their use in the commissioning of the Gravitational Wave Observatory, GEO600*, Ph.D. thesis, Gottfried Wilhelm Leibniz Universität Hannover, 2006.

[SMYT11] Brett Shapiro, Nergis Mavalvala, and Kamal Youcef-Toumi, *Actuator sizing of a quadruple pendulum for advanced gravitational wave detectors*, American Control Conference (ACC), 2011, IEEE, 2011, pp. 1358–1363.

[SPF+14] Leo P Singer, Larry R Price, Ben Farr, Alex L Urban, Chris Pankow, Salvatore Vitale, John Veitch, Will M Farr, Chad Hanna, Kipp Cannon, et al., *The first two years of electromagnetic follow-up with Advanced LIGO and Virgo*, The Astrophysical Journal **795** (2014), no. 2, 105.

[SS09] B.S. Sathyaprakash and Bernard F. Schutz, *Physics, Astrophysics and Cosmology with Gravitational Waves*, Living Reviews in Relativity **12** (2009), no. 2.

[SSHK10] B Sorazu, KA Strain, IS Heng, and R Kumar, *Violin mode amplitude glitch monitor for the presence of excess noise on the monolithic silica suspensions of GEO 600*, Classical and Quantum Gravity **27** (2010), no. 15, 155017.

[SSSMS15] Rudolf Saathof, Gerrit Jan M Schutten, Jo W Spronck, and Robert H Munnig Schmidt, *Actuation profiles to form zernike shapes with a thermal active mirror*, Optics letters **40** (2015), no. 2, 205–208.

[Str06] K A Strain, *Electrostatic drive (ESD) results from GEO and application in Advanced LIGO*, Tech. report, LIGO Document Control Center, Feb 2006, LIGO Document T060015-x0.

[TAKS04] Ryutaro Takahashi, Koji Arai, Seiji Kawamura, and Michael R. Smith, *Direct measurement of the scattered light effect on the sensitivity in TAMA300*, Phys. Rev. D **70** (2004), 062003.

[TCH+12] KV Tokmakov, A Cumming, J Hough, R Jones, R Kumar, S Reid, S Rowan, NA Lockerbie, A Wanner, and G Hammond, *A study of the fracture mechanisms in pristine silica fibres utilising high speed imaging techniques*, Journal of Non-Crystalline Solids **358** (2012), no. 14, 1699–1709.

[TI] *Texas Instruments Incorporated*, http://www.ti.com/, 12500 TI Boulevard, Dallas, Texas 75243 USA.

[TSM+02] Takayuki Tomaru, Toshikazu Suzuki, Shinji Miyoki, Takashi Uchiyama, CT Taylor, Akira Yamamoto, Takakazu Shintomi, Masatake Ohashi, and Kazuaki Kuroda, *Thermal lensing in cryogenic sapphire substrates*, Classical and Quantum Gravity **19** (2002), no. 7, 2045.

[TW82] Joseph H Taylor and Joel M Weisberg, *A new test of general relativity-Gravitational radiation and the binary pulsar PSR 1913+ 16*, The Astrophysical Journal **253** (1982), 908–920.

[UFRW14] Dennis Ugolini, C Fitzgerald, I Rothbarth, and J Wang, *Discharging fused silica optics occluded by an electrostatic drive*, Review of Scientific Instruments **85** (2014), no. 3, 034502.

[VBB96] Jean-Yves Vinet, Violette Brisson, and Stefano Braccini, *Scattered light noise in gravitational wave interferometric detectors: Coherent effects*, Physical Review D **54** (1996), no. 2, 1276.

[VM13] Henning Vahlbruch and Moritz Mehmet, *Old OMC as good as new OMC*, Internal note, GEO HF logbook page 4451, September 2013.

[WAA+02] Benno Willke, Peter Aufmuth, Carsten Aulbert, Stanislav Babak, R Balasubramanian, BW Barr, S Berukoff, Sukanta Bose, G Cagnoli, Morag M Casey, et al., *The GEO 600 gravitational wave detector*, Classical and Quantum Gravity **19** (2002), no. 7, 1377.

[WAA+06] Benno Willke, P Ajith, B Allen, P Aufmuth, C Aulbert, S Babak, Ramachandran Balasubramanian, BW Barr, S Berukoff, A Bunkowski, et al., *The GEO-hF project*, Classical and Quantum Gravity **23** (2006), no. 8, S207.

[WBB+12] A Wanner, G Bergmann, A Bertolini, T Fricke, H Lück, CM Mow-Lowry, KA Strain, S Goßler, and K Danzmann, *Seismic attenuation system for the AEI 10 meter Prototype*, Classical and quantum gravity **29** (2012), no. 24, 245007.

[WDG+07] W Winkler, K Danzmann, H Grote, M Hewitson, S Hild, J Hough, H Lück, M Malec, A Freise, K Mossavi, et al., *The GEO 600 core optics*, Optics Communications **280** (2007), no. 2, 492–499.

[Web63] J Weber, *Remarks on gravitational experiments*, Il Nuovo Cimento **29** (1963), no. 4, 930–934.

[Web66] Joseph Weber, *Observation of the thermal fluctuations of a gravitational-wave detector*, Physical Review Letters **17** (1966), no. 24, 1228.

[Web68] Joseph Weber, *Gravitational-wave-detector events*, Physical Review Letters **20** (1968), no. 23, 1307.

[Web69] Joseph Weber, *Evidence for discovery of gravitational radiation*, Physical Review Letters **22** (1969), no. 24, 1320.

[WG+14] Holger Wittel, Hartmut Grote, et al., *GEO finesse file*, Internal note, GEO HF logbook page 5000, February 2014.

[WH10] Christian Wagner and Noreen Harned, *EUV lithography: Lithography gets extreme*, Nature Photonics **4** (2010), no. 1, 24–26.

[WHB+15] H Wittel, S Hild, G Bergmann, K Danzmann, and KA Strain, *New Design of Electrostatic Mirror Actuators for Application in High-Precision Interferometry*, Class. Quantum Grav. 32, 175021. (2015).

[Wil09] Phil Willems, *Thermal compensation in the ligo gravitational-wave interferometers*, Frontiers in Optics 2009/Laser Science XXV/Fall 2009 OSA Optics & Photonics Technical Digest, Optical Society of America, 2009, p. AOThA5.

[Wil11] Phil Willems, *TCS Actuator Noise Couplings*, LIGO Document T060224-v7 https://dcc.ligo.org/LIGO-T060224, 2011, [Online; accessed 09-Sept-2015].

[Wit09] Holger Wittel, *Compensation of thermal lensing in the GEO 600 beam splitter*, Diplomarbeit, 2009.

[Wit13] Holger Wittel, *Side heaters off -> H gets worse*, Internal note, GEO HF logbook page 4902, December 2013.

[WL12] Holger Wittel and Jonathan Leong, *Baffle AR coating*, Internal note, GEO HF logbook page 3555, November 2012.

[WLA+14] Holger Wittel, Harald Lück, Christoph Affeldt, Katherine L Dooley, Hartmut Grote, Jonathan R Leong, Mirko Prijatelj, Emil Schreiber, Jacob Slutsky, K Strain, et al., *Thermal correction of astigmatism in the gravitational wave observatory GEO 600*, Classical and Quantum Gravity **31** (2014), no. 6, 065008.

Curriculum vitae

Name	**Holger Wittel**
Date of birth	June 16th 1984
Place of birth	Hannover, Germany
Marital status	unmarried

02.2010–present	Doctoral studies at Albert-Einstein-Institute, Max-Planck-Institute for Gravitational Physics, Cluster of Excellence QUEST, and Gottfried Wilhelm Leibniz Universität, Hannover
04.2009–present	Member of the International Max Planck Research School (IMPRS) on Gravitational Wave Astronomy
2011–present	Member of the LIGO Scientific Collaboration

6. Publications with immediate relation to this thesis

P15 Emil Schreiber, Kathrine L Dooley, Henning Vahlbruch, Christoph Affeldt, Aparna Bisht, Jonathan R Leong, James Lough, Mirko Prijatelj, Jacob Slutsky, Michal Was, **Holger Wittel**, Karsten Danzmann, Hartmut Grote
Alignment sensing and control for squeezed vacuum states of light
arXiv preprint arXiv:1507.06468, 2015.

P14 **H Wittel**, S Hild, G Bergmann, K Danzmann, and K A Strain
New design of electrostatic mirror actuators for application in high-precision interferometry
Class. Quantum Grav. 32 (2015) 175021., 2015.

P13 Katherine L Dooley, Emil Schreiber, Henning Vahlbruch, Christoph Affeldt, Jonathan R Leong, **Holger Wittel**, and Hartmut Grote
Phase control of squeezed vacuum states of light in gravitational wave detectors
Optics express 23 (7), 8235-8245, 2015.

P12 D Heinert, K Craig, H Grote, S Hild, H Lück, R Nawrodt, DA Simakov, DV Vasilyev, SP Vyatchanin, and **H Wittel**
Thermal noise of folding mirrors
Physical Review D, 90(4):042001, 2014.

P11 **Holger Wittel**, Harald Lück, Christoph Affeldt, Katherine L Dooley, Hartmut Grote, Jonathan R Leong, Mirko Prijatelj, Emil Schreiber, Jacob Slutsky, K Strain, M Was, B Willke and K Danzmann
Thermal Correction of Astigmatism in the Gravitational Wave Observatory GEO 600
Classical and Quantum Gravity, 31(6):065008, 2014.

P10 C Affeldt, K Danzmann, K L Dooley, H Grote, M Hewitson, S Hild, J Hough, J Leong, H Lück, M Prijatelj, S Rowan, A Rüdiger, R Schilling, R Schnabel,

E Schreiber, B Sorazu, K A Strain, H Vahlbruch, B Willke, W Winkler and **H Wittel**
Advanced Techniques in GEO 600
Classical and quantum gravity, 31(22):224002, 2014.

P9 Yan Wang, David Keitel, Stanislav Babak, Antoine Petiteau, Markus Otto, Simon Barke, Fumiko Kawazoe, Alexander Khalaidovski, Vitali Müller, Daniel Schütze, **Holger Wittel**, Karsten Danzmann, and Bernard F. Schutz
Octahedron configuration for a displacement noise-cancelling gravitational wave detector in space
Physical Review D, 88(10):104021, 2013.

P8 J R Leong, M Hewitson, H Lück, H Grote, S Hild, C Affeldt, J Degallaix, A Freise, M Prijatelj, K Strain, **H Wittel**, B Willke and K Danzmann
A new method for the absolute amplitude calibration of GEO 600
Classical and Quantum Gravity, 29(6):065001, 2012.

P7 M Prijatelj, J Degallaix, H Grote, J Leong, C Affeldt, S Hild, Harald Lück, J Slutsky, **H Wittel**, K Strain and K Danzmann
The output mode cleaner of GEO 600
Classical and quantum gravity, 29(5):055009, 2012.

P6 LIGO Scientific Collaboration et al.
A gravitational wave observatory operating beyond the quantum shot-noise limit
Nature Physics, 7(12):962–965, 2011.

P5 Alexey G Gurkovsky, Daniel Heinert, Stefan Hild, Ronny Nawrodt, Kentaro Somiya, Sergey P Vyatchanin, and **Holger Wittel**
Reducing Thermal Noise in future Gravitational Wave Detectors by employing Khalili Etalons
Physics Letters A, 375(46):4147–4157, 2011.

P4 J Degallaix, H Grote, M Prijatelj, M Hewitson, S Hild, C Affeldt, A Freise, J Leong, H Lück, K A Strain, **H Wittel**, B Willke and K Danzmann
Commissioning of the tuned dc readout at GEO 600
Journal of Physics: Conference Series, 228(1):012013, 2010.

P3 H Lück, C Affeldt, J Degallaix, A Freise, H Grote, M Hewitson, S Hild, J Leong, M Prijatelj, K A Strain, B Willke, **H Wittel** and K Danzmann
The upgrade of GEO 600
Journal of Physics: Conference Series, 228(1):012012, 2010.

P2 Harald Lück, Christoph Affeldt, J Degallaix, A Freise, H Grote, M Hewitson, S Hild, Jonathan Leong, M Prijatelj, K A Strain, B Willke, **H Wittel**, K Danzmann. **The transition to GEO hf**
J. Phys.: Conf. Ser.(Proc. of the 8th Amaldi conference), 2010.

P1 M Prijatelj, H Grote, J Degallaix, M Hewitson, S Hild, C Affeldt, A Freise, J Leong, H Lück, KA Strain, **H Wittel**, B Willke and K Danzmann
Control and automatic alignment of the output mode cleaner of GEO 600
Journal of Physics: Conference Series, 228(1):012014, 2010.

7. Further publications

2015 J Aasi, J Abadie, BP Abbott, R Abbott, T Abbott, MR Abernathy, T Accadia, F Acernese, C Adams, T Adams, ... , Holger Wittel, others,
Searching for stochastic gravitational waves using data from the two colocated LIGO Hanford detectors
Physical Review D, American Physical Society, volume 91, pp. 022003, 2015.

2015 J Aasi, BP Abbott, R Abbott, T Abbott, MR Abernathy, F Acernese, K Ackley, C Adams, T Adams, P Addesso, ... , Holger Wittel, others),
Narrow-band search of continuous gravitational-wave signals from Crab and Vela pulsars in Virgo VSR4 data
Physical Review D, American Physical Society, volume 91, pp. 022004, 2015.

2015 J Aasi, BP Abbott, R Abbott, T Abbott, MR Abernathy, F Acernese, K Ackley, C Adams, T Adams, P Addesso, ... , Holger Wittel, others,
Directed search for gravitational waves from Scorpius X-1 with initial LIGO data
Physical Review D, American Physical Society, volume 91, pp. 062008, 2015.

2015 J Aasi, J Abadie, BP Abbott, R Abbott, T Abbott, MR Abernathy, T Accadia, F Acernese, C Adams, T Adams, ... , Holger Wittel, others,
Characterization of the LIGO detectors during their sixth science run
Classical and Quantum Gravity, IOP Publishing, volume 32, pp. 115012, 2015.

2015 J Aasi, BP Abbott, R Abbott, T Abbott, MR Abernathy, K Ackley, C Adams, T Adams, P Addesso, RX Adhikari, ... , Holger Wittel, others,
Advanced ligo
Classical and quantum gravity, IOP Publishing, volume 32, pp. 074001, 2015.

2014 B Farr, R Poggiani, Y Levin, C Belczynski, D Hoske, T Prestegard, M Factourovich, A Giazotto, R Bonnand, ED Harstad, ... , Holger Wittel, others,
Methods and results of a search for gravitational waves associated with gamma-ray bursts using the GEO 600, LIGO, and Virgo detectors
PHYSICAL REVIEW D, PARTICLES, FIELDS, GRAVITATION, AND COSMOLOGY, volume 89, pp. 122004-1, 2014.

2014 J Aasi, BP Abbott, R Abbott, T Abbott, MR Abernathy, F Acernese, K Ackley, C Adams, Thomas Adams, P Addesso, ... , Holger Wittel, others,
Search for gravitational waves associated with γ-ray bursts detected

by the interplanetary network
Physical review letters, American Physical Society, volume 113, pp. 011102, 2014.

2014 Junaid Aasi, BP Abbott, Rich Abbott, Thomas Abbott, MR Abernathy, Timothee Accadia, F Acernese, Kendall Ackley, Carl Adams, Thomas Adams, ... , Holger Wittel, others,
The NINJA-2 project: detecting and characterizing gravitational waveforms modelled using numerical binary black hole simulations
Classical and quantum gravity, IOP Publishing, volume 31, pp. 115004, 2014.

2014 J Aasi, BP Abbott, R Abbott, T Abbott, MR Abernathy, F Acernese, K Ackley, C Adams, Thomas Adams, P Addesso, ... , Holger Wittel, others,
Methods and results of a search for gravitational waves associated with gamma-ray bursts using the GEO 600, LIGO, and Virgo detectors
Physical Review D, American Physical Society, volume 89, pp. 122004, 2014.

2014 J Aasi, BP Abbott, R Abbott, T Abbott, MR Abernathy, T Accadia, F Acernese, K Ackley, C Adams, Thomas Adams, ... , Holger Wittel, others,
Improved upper limits on the stochastic gravitational-wave background from 2009–2010 Ligo and Virgo data
Physical review letters, American Physical Society, volume 113, pp. 231101, 2014.

2014 Junaid Aasi, BP Abbott, Rich Abbott, Thomas Abbott, MR Abernathy, Timothee Accadia, F Acernese, Kendall Ackley, Carl Adams, Thomas Adams, ... , Holger Wittel, others,
Implementation of an F-statistic all-sky search for continuous gravitational waves in Virgo VSR1 data
Classical and quantum gravity, IOP Publishing, volume 31, pp. 165014, 2014.

2014 J Aasi, J Abadie, BP Abbott, R Abbott, T Abbott, MR Abernathy, T Accadia, F Acernese, C Adams, T Adams, ... , Holger Wittel, others,
Gravitational waves from known pulsars: results from the initial detector era
The Astrophysical Journal, IOP Publishing, volume 785, pp. 119, 2014.

2014 J Aasi, BP Abbott, R Abbott, T Abbott, MR Abernathy, T Accadia, F Acernese, K Ackley, C Adams, Thomas Adams, ... , Holger Wittel, others,
First all-sky search for continuous gravitational waves from unknown sources in binary systems
Physical Review D, American Physical Society, volume 90, pp. 062010, 2014.

2014 J Aasi, J Abadie, BP Abbott, R Abbott, T Abbott, MR Abernathy, T Accadia, F Acernese, C Adams, T Adams, ... , Holger Wittel, others,
Constraints on cosmic detectors strings from the LIGO-Virgo gravitational-wave

Physical Review Letters, American Physical Society, volume 112, pp. 131101, 2014.

2014 J Aasi, J Abadie, BP Abbott, R Abbott, T Abbott, MR Abernathy, T Accadia, F Acernese, C Adams, T Adams, ... , Holger Wittel, others,
Application of a Hough search for continuous gravitational waves on data from the fifth LIGO science run
Classical and quantum gravity, IOP Publishing, volume 31, pp. 085014, 2014.

2014 MG Aartsen, M Ackermann, J Adams, JA Aguilar, M Ahlers, M Ahrens, D Altmann, T Anderson, C Arguelles, TC Arlen, ... , Holger Wittel, others,
Multimessenger search for sources of gravitational waves and high-energy neutrinos: Initial results for LIGO-Virgo and IceCube
Physical Review D, American Physical Society, volume 90, pp. 102002, 2014.

2013 S Adrián-Martínez, I Al Samarai, A Albert, M André, M Anghinolfi, G Anton, S Anvar, M Ardid, T Astraatmadja, JJ Aubert, ... , Holger Wittel, others,
A first search for coincident gravitational waves and high energy neutrinos using LIGO, Virgo and ANTARES data from 2007
Journal of Cosmology and Astroparticle Physics, IOP Publishing, volume 2013, pp. 008, 2013.

2013 J Aasi, J Abadie, BP Abbott, R Abbott, T Abbott, MR Abernathy, T Accadia, F Acernese, C Adams, T Adams, ... , Holger Wittel, others,
Search for long-lived gravitational-wave transients coincident with long gamma-ray bursts
Physical Review D, American Physical Society, volume 88, pp. 122004, 2013.

2013 J Aasi, J Abadie, BP Abbott, R Abbott, TD Abbott, M Abernathy, T Accadia, F Acernese, C Adams, T Adams, ... , Holger Wittel, others,
Parameter estimation for compact binary coalescence signals with the first generation gravitational-wave detector network
Physical Review D, American Physical Society, volume 88, pp. 062001, 2013.

2013 J Aasi, J Abadie, BP Abbott, R Abbott, TD Abbott, MR Abernathy, C Adams, Thomas Adams, P Addesso, RX Adhikari, ... , Holger Wittel, others,
Enhanced sensitivity of the LIGO gravitational wave detector by using squeezed states of light
Nature Photonics, Nature Publishing Group, volume 7, pp. 613-619, 2013.

2013 J Aasi, J Abadie, BP Abbott, R Abbott, TD Abbott, M Abernathy, T Accadia, F Acernese, C Adams, T Adams, ... , Holger Wittel, others,
Einstein@Home all-sky search for periodic gravitational waves in LIGO S5 data
Physical Review D, American Physical Society, volume 87, pp. 042001, 2013.

2013 J Aasi, J Abadie, BP Abbott, R Abbott, T Abbott, MR Abernathy, T Accadia, F Acernese, C Adams, T Adams, ... , Holger Wittel, others,

Directed search for continuous gravitational waves from the Galactic center
Physical Review D, American Physical Society, volume 88, pp. 102002, 2013.

2012 PA Evans, JK Fridriksson, N Gehrels, J Homan, JP Osborne, M Siegel, A Beardmore, P Handbauer, J Gelbord, JA Kennea, ... , Holger Wittel, others,
Swift follow-up observations of candidate gravitational-wave transient events
The Astrophysical Journal Supplement Series, IOP Publishing, volume 203, pp. 28, 2012.

2012 J Abadie, BP Abbott, R Abbott, TD Abbott, M Abernathy, T Accadia, F Acernese, C Adams, R Adhikari, C Affeldt, ... , Holger Wittel, others,
Upper limits on a stochastic gravitational-wave background using LIGO and Virgo interferometers at 600–1000 Hz
Physical Review D, American Physical Society, volume 85, pp. 122001, 2012.

2012 J Abadie, BP Abbott, R Abbott, TD Abbott, M Abernathy, T Accadia, F Acernese, C Adams, R Adhikari, C Affeldt, ... , Holger Wittel, ... , others,
Sensitivity achieved by the LIGO and Virgo gravitational wave detectors during LIGO's sixth and Virgo's second and third science runs
arXiv preprint arXiv:1203.2674, 2012.

2012 J Abadie, BP Abbott, R Abbott, TD Abbott, M Abernathy, T Accadia, F Acernese, C Adams, R Adhikari, C Affeldt, ... , Holger Wittel, ... , others,
Search for gravitational waves from intermediate mass binary black holes
Physical Review D, American Physical Society, volume 85, pp. 102004, 2012.

2012 J Abadie, BP Abbott, R Abbott, TD Abbott, M Abernathy, T Accadia, F Acernese, C Adams, R Adhikari, C Affeldt, ... , Holger Wittel, others,
Implementation and testing of the first prompt search for gravitational wave transients with electromagnetic counterparts
Astronomy & Astrophysics, EDP Sciences, volume 539, pp. A124, 2012.

2012 J Abadie, BP Abbott, R Abbott, TD Abbott, M Abernathy, T Accadia, F Acernese, C Adams, R Adhikari, C Affeldt, ... , Holger Wittel, ... , others,
First low-latency LIGO+ Virgo search for binary inspirals and their electromagnetic counterparts
Astronomy & Astrophysics, EDP Sciences, volume 541, pp. A155, 2012.

2012 J Abadie, BP Abbott, R Abbott, TD Abbott, M Abernathy, T Accadia, F Acernese, C Adams, R Adhikari, C Affeldt, ... , Holger Wittel, others,
All-sky search for periodic gravitational waves in the full S5 LIGO data
Physical Review D, American Physical Society, volume 85, pp. 022001, 2012.

2012 J Aasi, J Abadie, BP Abbott, R Abbott, TD Abbott, M Abernathy, T Accadia, F Acernese, C Adams, T Adams, ... , Holger Wittel, others,
The characterization of Virgo data and its impact on gravitational-wave searches
Classical and quantum gravity, IOP Publishing, volume 29, pp. 155002, 2012.

Acknowledgments

I had the privilege to work with a lot of bright minds and great people at the AEI over last years. I want to thank Karsten Danzmann for giving me the opportunity to work in this environment.

Also a big thank you goes to supervisors Harald Lück and Hartmut Grote for many fruitful discussions. Thanks to the whole GEO 600 team: Aparna Bisht, Christoph Affeldt, James Lough, Emil Schreiber and the operators Michael Weinert, Marc Brinkmann, Walter Grass and Volker Kringel!

Also thanks again for proofreading parts of this work to Hartmut, Harald, Christoph, Aparna, Emil, Jim and Jonathan Leong. All remaining errors are in my responsibility.

Thank you Dmitry for a great office atmosphere.

I have to thank my parents for their support, without it this would not have been possible. And finally, thank you Madalina for everything!